

# BULGARIAN CHEMICAL COMMUNICATIONS

2015 Volume 47 / Special Issue C

Selected papers from presentations delivered at  
the 11<sup>th</sup> International Symposium on Heterogeneous Catalysis  
September 6–9, 2015, Varna, Bulgaria

*Journal of the Chemical Institutes  
of the Bulgarian Academy of Sciences  
and of the Union of Chemists in Bulgaria*



## *Preface*

The present Special issue of the journal Bulgarian Chemical Communications contains selected papers from presentations delivered at the 11<sup>th</sup> International Symposium on Heterogeneous Catalysis, held in Varna, Bulgaria, from 6<sup>th</sup> to 9<sup>th</sup> September 2015. This forum was also selected to be a satellite event of the 12<sup>th</sup> European Congress on Catalysis (Europacat-12) held in Kazan, Russia, from 31<sup>st</sup> August to 4<sup>th</sup> September 2015.

International symposia on heterogeneous catalysis organized by the Bulgarian catalysis community have a long history. They have been organized periodically since 1967.

Traditionally the organizers of these symposia have attempted to provide wide access to presented scientific results and we are happy that we could realize this once again.

Most of submitted papers included in this issue come from Bulgarian authors or report results of international cooperation between Bulgarian and foreign scientists. To some extent, the contents of this issue represent a current picture of the Bulgarian catalysis science.

14<sup>th</sup> December 2015

*Guest editors*



## Enhancement of the activity of TiO<sub>2</sub>-based photocatalysts: a review

V. Iliev\*, D. Tomova, A. Eliyas, S. Rakovsky, M. Anachkov, L. Petrov<sup>1</sup>

*Institute of Catalysis, Bulgarian Academy of Sciences, Acad. G. Bonchev St., Block 11, 1113 Sofia, Bulgaria*

<sup>1</sup> *SABIC Chair in Catalysis, King Abdulaziz University, P.O. Box 80204, Jeddah 21589, Saudi Arabia*

Received: September 30, 2015; Revised: November 12, 2015

Titania is one of the most widely used standard reference photocatalysts in the field of environmental applications. However, the wide anatase band gap and high degree of recombination between photogenerated charge carriers is limiting titania overall photocatalytic efficiency in water and air purification. This paper reviews recent studies on semiconductor photocatalysis, carried out at the Institute of Catalysis of the Bulgarian Academy of Sciences, aimed at enhancing the efficiency of TiO<sub>2</sub>-based photocatalysts and obtaining novel photocatalytic systems for sunlight utilization and application of methods improving the overall performance of the photocatalytic processes.

**Keywords:** semiconductor photocatalysis, photochemical oxidation, water purification, environmental remediation, solar light.

### INTRODUCTION

In parallel with the ever-growing amount of persistent organic contaminants accumulating in air, wastewaters, and soil, the ecological legislation and the respective normative restrictions are becoming more and more severe [1]. In many cases, standard oxidation processes (biological, chemical, or physical) for removal of pollutants are still economically unfavourable; moreover, they do not achieve complete mineralization of organic and inorganic pollutants [2]. One of the modern methods for removal of organic and inorganic compounds, persistent towards conventional means of neutralization, is destruction by applying the so-called ‘advanced oxidation processes (AOPs)’. These processes are based on generation of highly reactive particles of radical type, mainly HO• radicals, which destroy a large variety of organic and inorganic chemical compounds [3].

Among the AOP processes, heterogeneous photocatalysis appears to be one of the basic and most efficient approaches for degradation of organic contaminants in water, air, and soil [4]. Various oxides, chalcogenides, and composite materials and alloys are finding application in classical heterogeneous photocatalysis manifesting semiconductor properties. One of the most intensively studied photocatalysts is titanium dioxide (TiO<sub>2</sub>) [5], in whose presence photocatalytic processes occur under UV light irradiation, however, a high degree of recombination between the photogenerated charge carriers is lowering its efficiency as photocatalyst.

Aimed at overcoming the disadvantages of the photocatalysts based on TiO<sub>2</sub> and promoting the efficiency of the photocatalytic processes some new semiconducting materials are being developed, excited simultaneously by both the UV and visible components of the solar radiation [6], as well as such materials, in which the charges are separated more efficiently [7]. The increase in photonic efficiency of the processes of destruction of water and air pollutants as well as the utilization of solar light for this purpose is driving forward to realization of large-scale projects solving ecological problems and achieving at the same time improvement of the quality of light.

### I. TITANIA-BASED PHOTOCATALYSTS MODIFIED SUPERFICIALLY WITH NOBLE METAL NANOPARTICLES

Photocatalysts based on titania were modified superficially (0.1–1 wt.%) with nanoparticles (Ag, Au, Pd, Pt) aimed at increasing the quantum yield of the processes of destruction of organic and inorganic compounds [8–13]. The photocatalysts have been characterized by physical methods.

It was found that the sizes of noble metal nanoparticles attached to the surface of TiO<sub>2</sub> have a substantial influence on their photocatalytic activity. A remarkable influence of the pH of the medium during synthesis on Au particle size was registered upon attaching gold on the titania surface by photo-reduction, which exerts an effect also on adsorption capacity with respect to oxalic acid (Fig. 1A). Thus for one and the same quantity of gold deposited on TiO<sub>2</sub> (1 wt.%), when the size of the nanoparticles was decreased from 18 nm down to 4 nm, the rate

\* To whom all correspondence should be sent:  
E-mail: iliev@ic.bas.bg

constants of the photocatalytic destruction of oxalic acid were increased more than twice (Fig. 1B) [11]. It has been shown that the photocatalytic activity is affected by the quantity of metal nanoparticles attached on the surface of TiO<sub>2</sub> (Fig. 2) [10]. The reason for this is that two factors acting in opposite

directions are influencing photocatalyst efficiency: (i) the metal nanoparticles improve charge carrier separation and (ii) they decrease the adsorption capacity of TiO<sub>2</sub> because of partial blocking of adsorption sites on its surface.

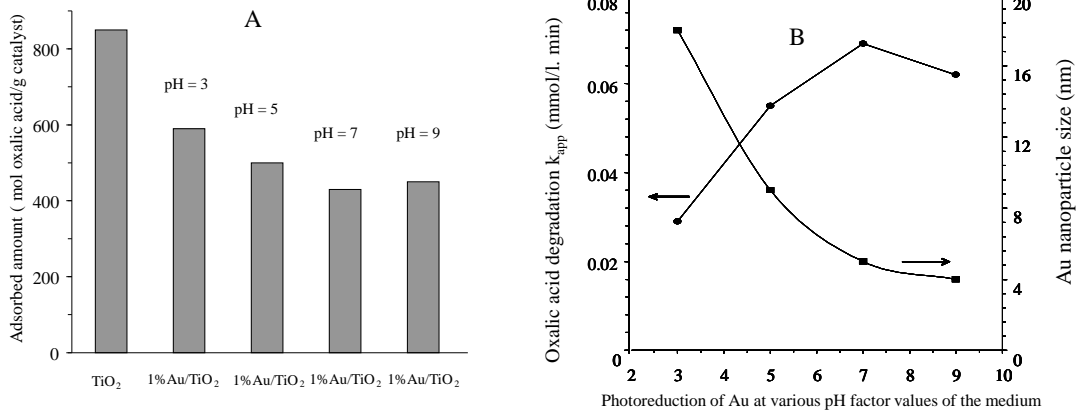


**Fig. 1.** A – total amount of oxalic acid adsorbed at pH 3 on TiO<sub>2</sub> photocatalysts prepared at various pH factor values of the medium; B – dependence of the rate constants of photocatalytic degradation of oxalic acid on Au<sup>0</sup> nanoparticle size.

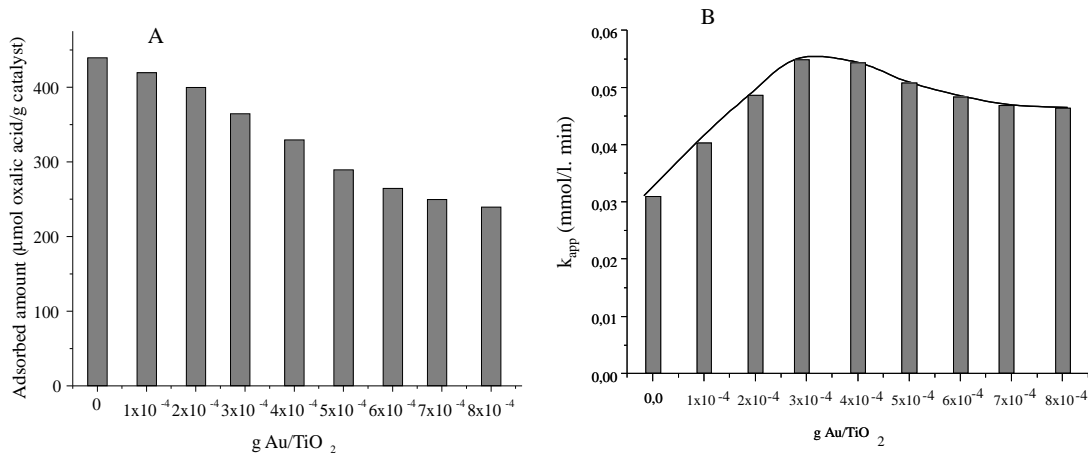


**Fig. 2.** A – total amount of oxalic acid adsorbed on TiO<sub>2</sub> at pH 3 and on Au-modified TiO<sub>2</sub> materials; B – dependence of the rate of photocatalytic degradation of oxalic acid on gold loading.

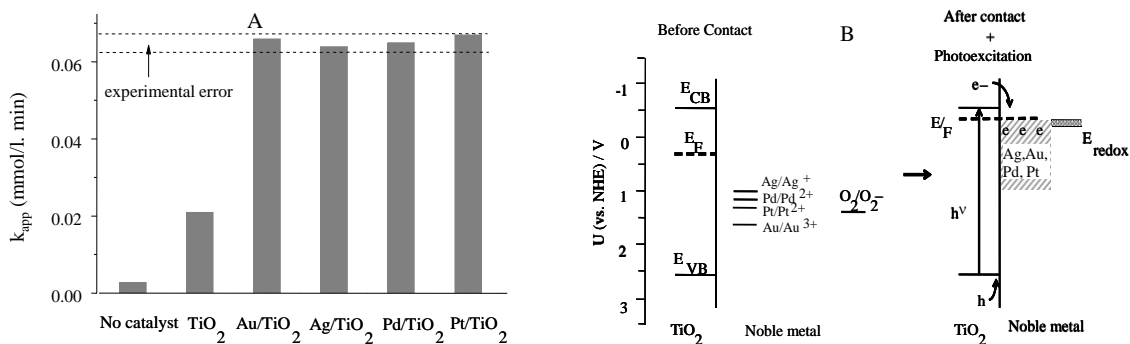


**Fig. 3.** A – dependence of the rate constants of photocatalytic degradation of oxalic acid on the nature of the noble metal particles on TiO<sub>2</sub>; B –Fermi level energies of the TiO<sub>2</sub>/noble metal composites upon photoexcitation.

It was also ascertained that the chemical nature of the noble metal attached on the surface of TiO<sub>2</sub> does not influence photocatalyst efficiency [13]. In this aspect at the same size of noble metal nanoparticles ( $\approx 5$  nm), deposited on the surface of TiO<sub>2</sub>, the rate constants of destruction of the pollutants in water are approximately the same (Fig. 3A).

Photo-physical investigations on titania/noble metal systems explain the obtained results. It has been shown [14] that as a result of equilibrated process of electron transfer from oxide semiconductors to the metal nanoparticles the life-time of the photoexcited electron is increased in the conduction band of the semiconductor (Fig. 3B). The lifetimes of the excited states are approximately the same in cases of attaching Ag, Au, Pd or Pt on the semiconductor [15], and for this reason the photocatalytic activity is varying within the framework of the experimental error (Fig. 3A) [13].

## II. INORGANIC OXIDES WITH SEMI-CONDUCTING PROPERTIES: PHOTOCATALYSTS FOR UTILIZATION OF SOLAR LIGHT

Two types of photocatalytic systems have been prepared and studied, which are able of being excited simultaneously under irradiation with UV and visible light. One type of systems is coupled composites of two oxides: one with a wide band gap and another one with a narrow band gap [16–18]. The second type of materials is prepared by doping the titania and a WO<sub>3</sub>/TiO<sub>2</sub> composite with nitrogen by means of anionic replacement of oxygen atoms by nitrogen entities in the crystal lattices of TiO<sub>2</sub> or WO<sub>3</sub>) [19–21]. The photocatalysts have been characterized by physical methods.

### II. 1. Coupled semiconductors

The photocatalytic activity of WO<sub>3</sub>/TiO<sub>2</sub> and CeO<sub>2</sub>/TiO<sub>2</sub> composites was studied in the degrada-

tion of 4-chlorophenol and oxalic acid under irradiation with visible [16] and ultraviolet light in separate and under combined UV-vis light irradiation [17,18]. The photocatalytic oxidation of both contaminants occurs completely leading to total mineralization: formation of CO<sub>2</sub>, H<sub>2</sub>O, and HCl. The band gap of anatase TiO<sub>2</sub> is about 3.2 eV and because of that, it is excited only by UV light. However, the band gaps of WO<sub>3</sub>  $\approx 2.8$  eV and CeO<sub>2</sub>  $\approx 2.75$  eV enable their photo-excitation by visible light, i.e. photons of energy  $E_{hv} \geq$  higher or equal to the energy of the band gap of the semiconductor.

It has been observed that under irradiation with UV light of the coupled photocatalyst systems the rate constants of destruction of oxalic acid are much higher than those registered under irradiation with visible light (Fig. 4A). Visible light illumination of WO<sub>3</sub>, CeO<sub>2</sub> and of the binary composites WO<sub>3</sub>/TiO<sub>2</sub> and CeO<sub>2</sub>/TiO<sub>2</sub> does not lead to high activity due to a small amount of tungsten or cerium oxides in the composites (4–6 wt.%) [17,18].

Under irradiation with UV or visible light the rate constants of destruction of oxalic acid or 4-chlorophenol photocatalysed by WO<sub>3</sub>/TiO<sub>2</sub> or CeO<sub>2</sub>/TiO<sub>2</sub> are higher than those registered with the individual oxides (Figs. 4A,B). This fact can be attributed to more efficient separation of surface charge carriers, i.e. to an increase in the quantum yield of the formed HO<sup>•</sup> radicals in the valence bands of both components in the composite photocatalyst (Fig. 4C). Thus under irradiation with UV light the rate constant of the process of oxalic acid destruction catalysed by WO<sub>3</sub>/TiO<sub>2</sub> is  $\sim 1.5$  times higher than that on pure titania [17], while in the case of photo-oxidation of 4-chlorophenol under irradiation with visible light it is 2.5 times higher than that on pure tungsta [16]. Under UV-A light irradiation the CeO<sub>2</sub>/TiO<sub>2</sub> photocatalyst showed a 0.44-fold increase in the rate of oxalic acid mineralization compared to that over the TiO<sub>2</sub> photocatalyst [18].

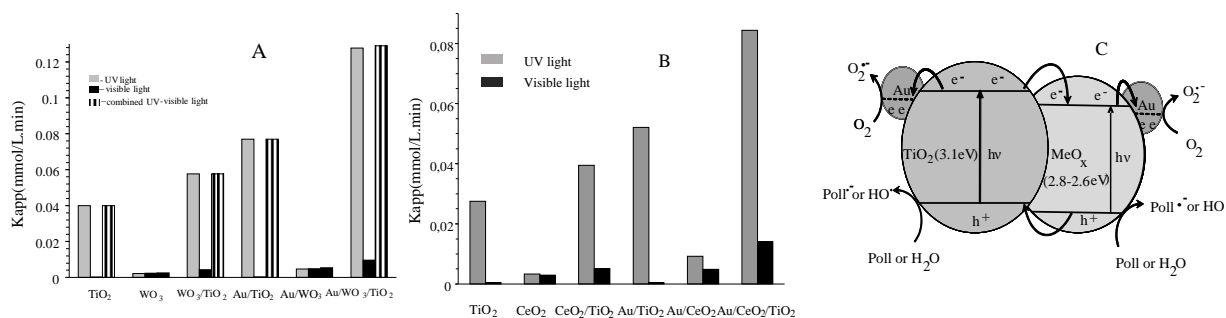


**Fig. 4.** Dependence of the apparent rate constants  $k_{app}$  of photocatalytic degradation of oxalic acid on irradiation type: A – WO<sub>3</sub>/TiO<sub>2</sub> photocatalyst; B – CeO<sub>2</sub>/TiO<sub>2</sub> photocatalyst; C – schematic representation of charge carrier separation in the photoexcited photocatalysts.

Modifying the surface of the studied semiconductors with Au nanoparticles is leading to a manifold increase in the rate constants of destruction of 4-chlorophenol or oxalic acid both in the cases of UV light irradiation and visible light irradiation (Figs. 4A,B). The enhancement of the photocatalytic activity is owing to a more efficient separation of the charge carriers in the photoactivated catalysts thus leading to an increase in the quantum yield of formation of the HO<sup>•</sup> radicals (Fig. 4C). Especially efficient is the charge separation in the case of Au/WO<sub>3</sub>/TiO<sub>2</sub> photocatalyst under irradiation with UV or combined UV-visible light, where the rate constants of destruction of the oxalic acid are approximately 1.7 times higher than that of the process catalysed by Au/TiO<sub>2</sub> and 3 times higher than that catalysed by pure titania [17]. In the case of photocatalytic destruction of 4-chlorophenol, occurring under irradiation with visible light, the rate constant of the process catalysed by Au/WO<sub>3</sub>/TiO<sub>2</sub> is 3 times higher than that of the process catalysed by tungsta [16]. Particularly efficient is the charge separation process in the Au/CeO<sub>2</sub>/TiO<sub>2</sub> material upon irradiation with UV light (Fig. 4B). In this case, the rate constants of oxalic acid decomposition were approximately twice higher than those over the Au/TiO<sub>2</sub> material and three times higher than those catalysed by pure titania.

## II. 2. Nitrogen-doped semiconductors

Nitrogen-doped titania (N-TiO<sub>2</sub>) and tungsta/titania (N-WO<sub>3</sub>/TiO<sub>2</sub>) catalysts have been synthesized using sol-gel technology. XPS studies established that the atomic concentration of the nitrogen atoms in the crystal lattices of TiO<sub>2</sub> and WO<sub>3</sub>/TiO<sub>2</sub> is ≈ 1.2%. All the photocatalysts have been additionally modified superficially with gold nanoparticles (0.5–1 wt.%) by the method of photo-reduction.

The photocatalytic destruction reactions of 2-propanol, oxalic acid, and 2,4,6-trinitrotoluene (TNT) in the presence of TiO<sub>2</sub>, N-TiO<sub>2</sub>, WO<sub>3</sub>/TiO<sub>2</sub>, N-WO<sub>3</sub>/TiO<sub>2</sub>, and superficially modified with Au nanoparticles photocatalysts have been investigated under irradiation with UV, visible, and combined UV-visible light [19–21]. It was proved that there occurs a complete destruction of the substrates, which is due most of all to the generated HO<sup>•</sup> radicals.

The ability of nitrogen-doped titania to be photo-excited simultaneously under irradiation with UV and visible light is owing to the fact that, in case of replacing the oxygen atoms in the crystal lattice of TiO<sub>2</sub> by nitrogen atoms, new admixture electron

energy levels are being formed resulting in a narrower band gap. This explains the possibility to excite simultaneously a photocatalyst under UV and visible light irradiation (Fig. 5B).

Concerning the photocatalytic activity of nitrogen-doped catalysts (Fig. 5A) the following conclusions can be drawn.

1. N-doped TiO<sub>2</sub> and N-doped WO<sub>3</sub>/TiO<sub>2</sub> as well as samples modified by nanosized Au particles are efficient photocatalysts for removal of organic contaminants from water under irradiation with UV and visible light.

2. Under irradiation with UV light, the photonic efficiencies of N-doped TiO<sub>2</sub> and N-doped WO<sub>3</sub>/TiO<sub>2</sub> are one order of magnitude higher than the efficiency under irradiation with visible light. This is because of the nitrogen atoms (1.2 at.%) incorporated in the crystal lattice of N-doped photocatalysts. Higher rate constant values for organic contaminants decomposition upon irradiation with UV light are due to the photocatalytic processes occurring simultaneously on N-doped TiO<sub>2</sub>, N-doped WO<sub>3</sub>, and coupled N-doped WO<sub>3</sub>/TiO<sub>2</sub> photocatalysts.

3. An increased photocatalytic activity of N-doped TiO<sub>2</sub> and N-doped WO<sub>3</sub>/TiO<sub>2</sub> under irradiation with visible light is owing to the formation of a new impurity electron energy level leading to narrowing of the band gap of the photocatalysts. Thus, under irradiation with visible light the rate constant values for TNT photooxidation, catalyzed by N-doped WO<sub>3</sub>/TiO<sub>2</sub> or N-doped TiO<sub>2</sub>, are 2-fold and 5-fold higher, respectively, than those for undoped WO<sub>3</sub>/TiO<sub>2</sub> or TiO<sub>2</sub> samples, accordingly.

4. The photocatalytic activities of gold-modified N-doped TiO<sub>2</sub> and N-doped TiO<sub>2</sub>/WO<sub>3</sub> photocatalysts under irradiation with UV or visible light is increased more than twice compared with that of unmodified samples. The higher rate of photocatalytic destruction of the pollutant in the case of deposited nanosized Au particles on the surface of the catalysts is a result of more efficient charge separation, increased lifetime of the charge carriers, and enhanced efficiency of the interphase charge transfer to adsorbed pollutants.

## III. PROMOTING THE EFFICIENCY OF PHOTOCATALYTIC PROCESSES OCCURRING WITH THE PARTICIPATION OF OZONE

Efficiency enhancement of the photocatalytic processes of destruction in aqueous medium has been studied with oxalic acid as pollutant [22] and also with 2,4,6-trinitrotoluene [23] under irradiation with UV-A or UV-C and visible light in the

presence of oxygen-ozone mixture. The concentration of ozone in the mixture was  $6.7 \times 10^{-4} \text{ mol.L}^{-1}$ . A parallel is made in these studies between the efficiency of the photocatalytic processes occurring in the presence of oxygen with that of the processes accomplished involving the participation of ozone. In both cases, it was found that the photocatalytic destruction of the contaminants is reaching a complete decomposition of their organic structure with the formation of CO<sub>2</sub>, H<sub>2</sub>O, and NO<sub>3</sub><sup>-</sup>.

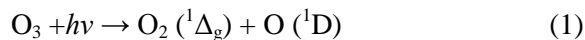
It was shown that in the absence of illumination the ozone does not react directly with the oxalic acid [22], while in the case of TNT some degree of destruction is registered occurring at a very low rate constant (Fig. 6A) as a result of formation of HO• radicals from the ozone in aqueous medium at pH 7 [23].

Under irradiation with ultraviolet or visible light in the presence of ozone the rate constants of destruction of the pollutants are much higher than those registered in the presence of oxygen only and they depend on the illumination intensity of the UV light source [22,23] (Fig. 6A).

A higher efficiency of the photocatalytic pro-

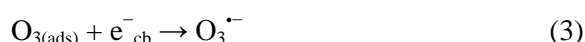
cesses of organic molecules destruction in the presence of ozone is due to generation of HO• radicals from ozone (Fig. 6B) by the following mechanism (equations 1–5):

- Direct photolysis of ozone under irradiation with UV-C light ( $\lambda = 254 \text{ nm}$ )



where O<sub>2</sub> (<sup>1</sup>Δ<sub>g</sub>) is singlet oxygen and O (<sup>1</sup>D) is an oxygen atom in excited state.

- Generation of HO• radicals from adsorbed ozone molecules on the conduction band of the semiconductors



The hydroxyl radicals are among the most reactive free radicals and they are strong oxidizing agents capable of causing destruction of organic compounds.

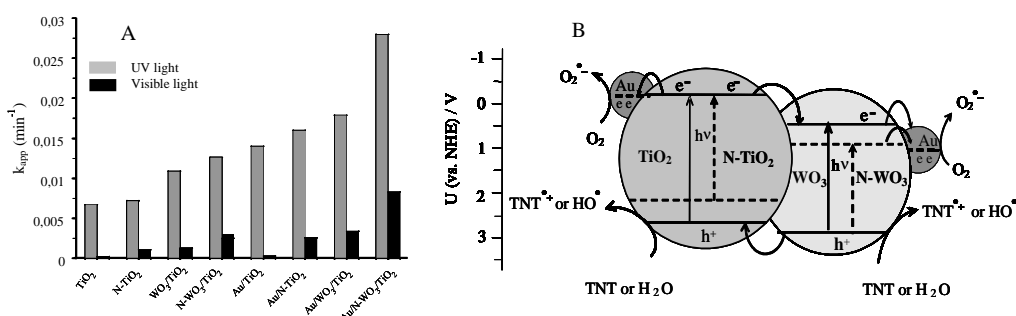


Fig. 5. A – dependence of apparent rate constants of TNT degradation; B – schematic representation of charge carrier separation in photoexcited Au/N-WO<sub>3</sub>/TiO<sub>2</sub> photocatalyst.

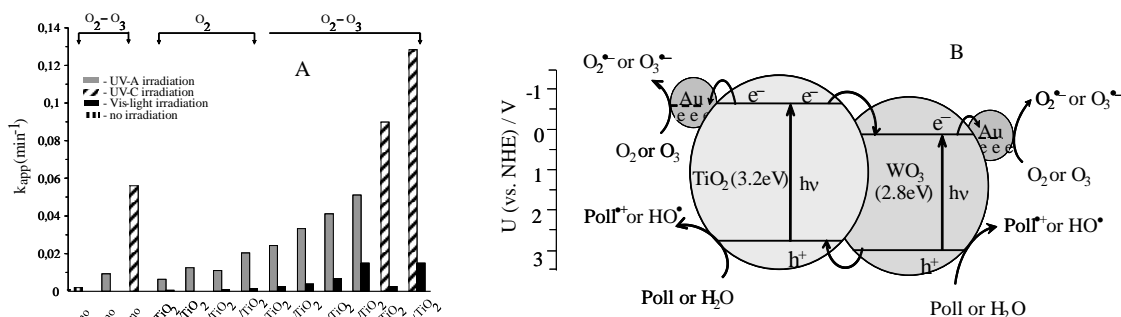


Fig. 6. A – dependence of the rate constants of photocatalytic degradation of TNT under the experimental conditions; B – schematic representation of charge carrier separation in the photoexcited Au/WO<sub>3</sub>/TiO<sub>2</sub> photocatalyst.

It is seen in Fig. 6A that under irradiation with UV light in the presence of ozone the rate constants of TNT photooxidation catalyzed by Au/WO<sub>3</sub>/TiO<sub>2</sub> are 6 times higher, while under visible light irradiation they are 11 times higher than those of the processes occurring in the presence of oxygen only [23]. An analogous tendency of increase in the rate constants (4–14 times) is also observed in the case of photocatalytic destruction of oxalic acid [22]. An additional increase was registered for the rate constants of destruction of TNT in the presence of ozone, which can be interpreted as appearance of synergistic effect [23].

The efficiency of the processes of destruction of TNT in the presence of ozone depends also on the type of photocatalyst (Fig. 6A). Thus in the case of irradiation with UV-A, UV-C, and visible light in the presence of ozone the rate constants of TNT photooxidation catalyzed by Au/WO<sub>3</sub>/TiO<sub>2</sub> are respectively 2.1, 1.4, and 6.2 times higher than those registered with pure titania [23]. Promoting the activity of the studied photocatalysts, Au/TiO<sub>2</sub>, WO<sub>3</sub>/TiO<sub>2</sub>, and Au/WO<sub>3</sub>/TiO<sub>2</sub>, is due to more efficient charge carrier separation during photoexcitation leading to an increase in the quantum yield of HO<sup>•</sup> radicals' formation (Fig. 6B).

During irradiation with UV or visible light the efficiency of the photocatalytic processes, occurring in the presence of catalysts superficially modified with noble metal nanoparticles, is 1.5–3 times higher than that in the case of non-modified catalysts (Fig. 6A). The increase in the rate constants of destruction of pollutants in water is owing to more efficient charge carrier separation in these materials during photoexcitation (Fig. 6B).

## CONCLUSIONS

Increasing the efficiency of titania-based photocatalysts and enhancing the photocatalytic processes, taken as a whole, is a top priority task for establishing the photocatalysis as one of the basic and most efficient processes of neutralization of the harmful effect of organic contaminants in wastewater, air, and soil. It has been shown that by modifying superficially TiO<sub>2</sub> with noble metals the activity of the catalysts is growing up by 2 to 4 times. Using coupled or doped photocatalytic materials, in addition to promoting the photocatalytic activity, is creating also conditions for more efficient utilization of solar radiation. A considerable growth in efficiency of the photocatalytic processes is registered in the case of accomplishing processes involving ozone as oxidizing agent, whereupon the rate constants of

destruction of the organic contaminants in water is being enhanced by 4 to 14 times.

*Acknowledgements: The authors gratefully acknowledge financial support by the Bulgarian Science Fund (Contract DFNI-T02/16).*

## REFERENCES

1. US EPA, National Emission Standards for Hazardous Air Pollutants, 40 CFR, part 63, 2006.
2. L. I. Dapeng, Q. U. Jiuhui, *J. Environ. Sci.*, **21**, 713 (2009).
3. M. Pera-Titus, V. Garcia-Molina, M. A. Banos, J. Giménez, S. Esplugas, *Appl. Catal. B-Environ.*, **47**, 219 (2004).
4. J. Disdier, J.-M. Herrmann, C. Lehaut, T. Chopin, S. Malato, J. Blanco, *Catal. Today*, **54**, 217 (1999).
5. M. A. Henderson, *Surf. Sci. Rep.*, **66**, 185 (2011).
6. M. Pelaez, N. T. Nolan, S. C. Pillai, M. K. Seery, P. Falaras, A. G. Kontos, P. S. M. Dunlop, J. W. J. Hamilton, J. A. Byrne, K. O'Shea, M. H. Entezari, D. D. Dionysiou, *Appl. Catal. B: Environ.*, **125**, 331 (2012).
7. S. G. Kumar, L. G. Devi, *J. Phys. Chem. A*, **115**, 13211 (2011).
8. V. Iliev, D. Tomova, L. Bilyarska, L. Petrov, *Catal. Commun.*, **5**, 759 (2004).
9. V. Iliev, D. Tomova, L. Bilyarska, A. Eliyas, L. Petrov, *Appl. Catal. B-Environ.*, **63**, 266 (2006).
10. V. Iliev, D. Tomova, R. Todorovska, D. Oliver, L. Petrov, D. Todorovsky, M. Uzunova-Bujnova, *Appl. Catal. A-Gen.*, **313**, 115 (2006).
11. V. Iliev, D. Tomova, L. Bilyarska, G. Tyuliev, *J. Mol. Catal. A-Chem.*, **263**, 32 (2007).
12. L. Petrov, V. Iliev, A. Eliyas, D. Tomova, G. L. Puma, *J. Environ. Prot. Ecology*, **8**, 881 (2007).
13. V. Iliev, D. Tomova, A. Eliyas, S. Rakovsky, *Nanosci. Nanotechnol.*, **10**, 102 (2010).
14. P. V. Kamat, *Pure Appl. Chem.*, **74**, 1693 (2002).
15. C. Damm, G. Israel, *Z. Phys. Chem.*, **223**, 719 (2009).
16. D. Tomova, V. Iliev, *Nanosci. Nanotechnol.*, **8**, 204 (2008).
17. V. Iliev, D. Tomova, S. Rakovsky, A. Eliyas, G. Li Puma, *J. Mol. Catal. A-Chem.*, **327**, 51 (2010).
18. D. Tomova, V. Iliev, A. Eliyas, S. Rakovsky, *Separ. Purif. Technol.*, in press.
19. V. Iliev, D. Tomova, *Nanosci. Nanotechnol.*, **9**, 118 (2009).
20. V. Iliev, D. Tomova, S. Rakovsky, *Desalination*, **260**, 101 (2010).
21. M. Daous, V. Iliev, L. Petrov, *J. Mol. Catal. A-Chem.*, **392**, 194 (2014).
22. D. Tomova, V. Iliev, S. Rakovsky, M. Anachkov, A. Eliyas, G. Li Puma, *Nanosci. Nanotechnol.*, **11**, 146 (2011).
23. D. Tomova, V. Iliev, S. Rakovsky, M. Anachkov, A. Eliyas, G. Li Puma, *J. Photochem. Photobiol. A-Chem.*, **231**, 1 (2012).

## ПОВИШАВАНЕ НА АКТИВНОСТТА НА ФОТОКАТАЛИЗАТОРИ НА ОСНОВАТА НА TiO<sub>2</sub>: ОБЗОРНА СТАТИЯ

В. Илиев \*, Д. Томова, Ал. Елияс, Сл. Раковски, М. Аначков, Л. Петров<sup>1</sup>

*Институт по катализ, Българска академия на науките, ул. „Акад. Г. Бончев“, бл. 11, 1113 София, България*

*<sup>1</sup> Катедра „Катализ“ на Саудитската основна индустриална корпорация, Департамент по инженерна химия и материали, Факултет по инженерство, Университет Крал Абдулазис, п.к. 80204, Джеда 21589, Саудитска Арабия*

Постъпила на 30 септември 2015 г.; Преработена на 12 ноември 2015 г.

(Резюме)

Титановият диоксид е един от стандартните фотокатализатори използван широко в областта на опазване на околната среда. Въпреки това, широката забранена зона на титановия диоксид и високата степен на рекомбинация на фотогенерираните носители на заряди ограничават неговата ефективност като фотокатализатор при пречистване на води и въздух. В тази статия се прави преглед на последните изследвания върху фотокатализа с полупроводникови материали провеждани в Института по катализ, БАН, целящи повишаване ефективността на фотокатализатори на базата на TiO<sub>2</sub>, получаване на фотокаталитични системи за утилизация на слънчева светлина, както и прилагане на методи влияещи върху повишаване на ефективността на фотокаталитичните процеси като цяло.

## Unconventional ‘chemisorption-hydrolysis’ vs ‘impregnation’ technique for preparation of nanodispersed copper on mesoporous ceria and zirconia

T. S. Tsoncheva<sup>1\*</sup>, I. G. Genova<sup>1</sup>, N. Scotti<sup>2</sup>, V. Dal Santo<sup>2</sup>, N. Ravasio<sup>2</sup>

<sup>1</sup> Institute of Organic Chemistry with Centre of Phytochemistry, Bulgarian Academy of Sciences, 1113 Sofia, Bulgaria

<sup>2</sup> CNR-Istituto di Scienze e Tecnologie Molecolari, Milano, Italy

Received: September 12, 2015; Revised December 7, 2015

Mesoporous nanostructured zirconia and ceria were synthesized by a template-assisted hydrothermal technique and used as a host matrix of nanosized copper oxide species. A ‘chemisorption-hydrolysis’ strategy was applied for ZrO<sub>2</sub> and CeO<sub>2</sub> modification with copper. The obtained materials were characterized by XRD, nitrogen physisorption, FTIR, UV-Vis, and temperature-programmed reduction with hydrogen and compared with analogues prepared by conventional incipient wetness impregnation method. The catalytic activity was tested in methanol decomposition. Copper deposition on zirconia by the ‘chemisorption-hydrolysis’ approach ensures formation of highly active and selective catalysts for methanol decomposition to carbon monoxide and hydrogen, which is provoked by a synergistic effect between copper and zirconia components.

**Keywords:** Copper-modified mesoporous ZrO<sub>2</sub> and CeO<sub>2</sub>, ‘chemisorption-hydrolysis’ method, methanol decomposition

### INTRODUCTION

Copper-based materials are low cost and are considered effective catalysts in a number of redox processes, such as dehydrogenation of alcohols, isomerization and hydrogenation of hydrocarbons, hydrogenation of carbonyl compounds, hydrogenolysis of carbon-carbon and carbon-silicon bonds, *etc.* [1 and refs. therein]. A strong control on dispersion and oxidation state of the copper species is needed, which could be achieved by copper deposition on various porous supports with tunable surface and texture characteristics as well as by the preparation procedure used [2]. Recently, mesoporous silicas revealed good prospects for a host matrix of nanoscale metal/metal oxide particles due to their unequal pore structure characteristics [3, 4]. Advantages of zirconia as a catalyst support originate from its strong interaction with the active phase, a high thermal stability, and a unique combination of acidic, basic, and redox ability [5]. It has been established that ZrO<sub>2</sub> surface properties depend strongly on zirconia polymorphs, which could easily be controlled by particle size [6]. Effects on the interaction between copper and zirconia are concerned about and a higher dispersion and catalytic activity were reported for copper supported on a tetragonal rather than amorphous or monoclinic ZrO<sub>2</sub> support. Alternatively, ceria also possesses promising properties. Due to high oxygen storage/ transport capacity,

ceria alone, or combined with other elements, is recognized as an efficient catalyst for various environmental processes, namely NO reduction and CO oxidation, light hydrocarbons combustion, removal of diesel soot, water-gas shift reaction, and VOCs oxidation. A superior catalytic activity of the copper-ceria binary system in different reactions has been a subject of intense investigation and controversial discussion. Generally, a synergistic coupling of the redox properties of both metal oxides is assumed and it is assigned to a strong interaction between CuO and CeO<sub>2</sub>, which facilitates CuO introduction into the ceria lattice to form a solid solution and to disperse over the surface [7 and refs. therein].

Nowadays, advanced technologies, such as sol-gel, chemical vapour synthesis, and combustion and precipitation procedures have been developed to produce nanopowder metal oxides, which can be used for catalyst supports. Among them, a hydrothermal process is reported to be a soft chemical route to prepare phase-pure products at a low temperature and enable easy control of crystal size by altering process conditions [8]. Much attention is paid to the synthesis of nanostructured mesoporous oxides of high surface area and uniform pore size distribution using a surfactant-assisted route [9, 10 and refs therein]. It has been established that direct synthesis for modification of mesoporous silica supports typically results in deposition of a relatively low copper loading, while the traditional impregna-

\* To whom all correspondence should be sent  
E-mail: tsoncheva@orgchm.bas.bg

tion method [11] provides an undesirable agglomeration of copper species. A common grafting method causes the formation of  $\text{Cu}^+$  ions [12]. A predominant formation of oligomeric Cu-O-Cu species has been found using a molecular design method [13], while isolated  $\text{Cu}^{2+}$  ions dominate when an impregnation method is applied [13]. In a previous study [14] we reported that copper oxide species deposited by a ‘chemisorption-hydrolysis’ (CH) procedure is finely divided and interact strongly with the silica support. It was further demonstrated that this method, if applied to ordered mesoporous silicas, essentially improves the catalytic activity and stability of copper materials for methanol decomposition.

In the present study we report our attempts to apply the ‘chemisorption-hydrolysis’ strategy to deposition of copper oxide nanoparticles on mesoporous  $\text{ZrO}_2$  and  $\text{CeO}_2$  supports and to compare their properties with similar composites obtained by a conventional incipient wetness impregnation technique. The catalytic behaviour of the prepared materials was tested in methanol decomposition. Recently, fossil fuel depletion and large  $\text{CO}_2$  emissions focused the attention on biomass as renewable environmentally friendly feedstock, the latter resulting in no net increase in atmospheric carbon dioxide. Methanol, which can be produced from biomass, is regarded as an attractive alternative fuel and hydrogen release from methanol can be obtained through various techniques, such as simple decomposition, steam reforming, partial oxidation, and oxidative steam reforming [15].

## EXPERIMENTAL

### Materials

Mesoporous zirconia and ceria were prepared by a hydrothermal procedure using  $\text{ZrCl}_4$  or  $\text{CeCl}_3 \cdot 7\text{H}_2\text{O}$  as a precursor and CTAB as a structure-directing agent as described in Ref. 14. Zirconia and ceria samples were calcined at 573 K in air for 15 h. Samples denoted as Cu/ $\text{CeO}_2$ \_CH and Cu/ $\text{ZrO}_2$ \_CH were prepared by a ‘chemisorption-hydrolysis’ method which included: (i) impregnation of the supports with an aqueous solution of a tetramine copper complex ( $[\text{Cu}(\text{NH}_3)_4]^{2+}$ , pH = 9) at room temperature for 20 min; (ii) hydrolysis of the obtained product with water at 273 K; (iii) filtration and drying at 373 K overnight. Alternatively, samples denoted as Cu/ $\text{CeO}_2$ \_WI and Cu/ $\text{ZrO}_2$ \_WI were prepared by conventional incipient wet impregnation with an aqueous solution of  $\text{Cu}(\text{NO}_3)_2 \cdot 3\text{H}_2\text{O}$ . The obtained CH and WI samples were calcined in air at 623 K for 4 and 2 h, respectively. Copper content in the studied materials,

determined by atomic absorption spectroscopy, is given in table 1.

### Methods of investigation

Atomic absorption analyses were performed on a Pye Unicam SP 192 instrument. The porous structure of selected modifications was studied by nitrogen physisorption at 77 K, which was carried out in an ASAP 2020 Micromeritics automatic volumetric apparatus. The isotherms were used to calculate specific surface area,  $S_{\text{BET}}$ , and pore volumes of the obtained materials. Powder X-ray diffraction patterns were collected within the range of  $5.3$  to  $80^\circ$   $2\theta$  on a Bruker D8 advance diffractometer with  $\text{Cu K}\alpha$  radiation and a LynxEye detector. Scherrer equation was used to evaluate average crystallite size. UV-Vis spectra of powder samples were recorded on a Jasco V-650 apparatus. FTIR spectra in the region of skeletal vibrations were recorded on a Bruker Vector 22 spectrometer at a resolution of  $1$ – $2$   $\text{cm}^{-1}$  by accumulating 64–128 scans and using the KBr pellet technique. TPR/TG (temperature-programmed reduction/thermogravimetric) analyses were performed on a Setaram TG92 instrument in a flow of 50 vol.%  $\text{H}_2$  in Ar ( $100$   $\text{cm}^3 \cdot \text{min}^{-1}$ ) at a heating rate of  $5$   $\text{grad} \cdot \text{min}^{-1}$ .

Methanol conversion was carried out in a fixed bed flow reactor (0.055 g of catalyst) using argon as a carrier gas ( $50$   $\text{cm}^3 \cdot \text{min}^{-1}$ ). Methanol partial pressure was 1.57 kPa. The catalysts were tested under conditions of a temperature-programmed regime within the range of 350–770 K at a heating rate of  $1$   $\text{grad} \cdot \text{min}^{-1}$ . Online gas chromatographic analyses were performed by means of an HP apparatus equipped with flame ionization and thermal conductivity detectors and a PLOT Q column using an absolute calibration method and carbon-based material balance.

## RESULTS AND DISCUSSION

Nitrogen physisorption isotherms of  $\text{ZrO}_2$  and  $\text{CeO}_2$  supports (Fig. 1, Table 1) exhibit a sharp jump in the relative pressure region of 0.6–0.8 and above 0.8, respectively, which, according to IUPAC classification, is typical of mesoporous materials. The specific surface area was about 5 times higher for zirconia as compared to ceria support (Table 1). Hysteresis loop shape reveals presence of nearly cylindrical mesopores for  $\text{ZrO}_2$  with an average pore diameter ( $D_{\text{av}}$ ) of 6 nm, while slit-like mesopores of much broader pore size distribution ( $D_{\text{av}}$  about 26 nm) dominate with  $\text{CeO}_2$ . In general, after modification with copper a decrease in BET surface area, total pore volume, and average pore diameter was

observed without substantial changes of the isotherms. This effect was more significant with the WI-obtained materials and could be assigned to pore blocking due to deposition of copper phase into the mesopores without considerable textural collapse. However, an extremely strong decrease in BET surface area and pore volume combined with a shift of the maximum of pore size distribution to higher values was observed for Cu/ZrO<sub>2</sub>\_WI and for that reason, structure changes of zirconia due to high temperature treatment during modification are not excluded.

**Table 1.** Copper content, specific surface area ( $S_{\text{BET}}$ ), total pore volume ( $V_{\text{tot}}$ ), and average pore diameter ( $D_{\text{av}}$ ) of studied samples.

Sample	Cu %??	$S_{\text{BET}}$ , $\text{m}^2\cdot\text{g}^{-1}$	$V_{\text{tot}}$ , $\text{cm}^3\cdot\text{g}^{-1}$	$D_{\text{av}}$ , nm
ZrO <sub>2</sub>	-	300	0.42	6.0
Cu/ZrO <sub>2</sub> _CH	9.83	200	0.31	4.5
Cu/ZrO <sub>2</sub> _WI	9.83	80	0.23	8.8
CeO <sub>2</sub>	-	58	0.27	26.4
Cu/CeO <sub>2</sub> _CH	9.65	62	0.21	16.0
Cu/CeO <sub>2</sub> _WI	9.65	44	0.17	16.0

The XRD pattern of pure ZrO<sub>2</sub> represents a broad hump typical of amorphous materials (Fig. 2a). Bands at around 750, 650, and 550  $\text{cm}^{-1}$  in the FTIR spectrum of ZrO<sub>2</sub> (not shown) reveal coexistence of monoclinic and tetragonal phases. This phase compo-

sition of the support was preserved after modification by the CH procedure (Fig. 2a), while the WI method resulted in the formation of a well-crystallized tetragonal zirconia phase with average crystallite size of 9 nm. XRD patterns of pure and copper-modified ceria (Fig. 2b) represent typical reflections of a fluorite type structure with average particle size of 12 nm. No additional reflections of a copper containing phase could be distinguished for Cu/CeO<sub>2</sub>\_CH, while small reflections at 35.6 and 38.5° 2 $\theta$ , characteristic of CuO tenorite phase with average crystallite size of 3–5 nm, were registered for all other modifications of ceria and zirconia.

Fig. 3 displays UV-Vis spectra of parent and copper-modified ZrO<sub>2</sub> and CeO<sub>2</sub>. The electronic spectra of ceria and zirconia are very sensitive to cation coordination environment [17]. A blue shift observed in the UV-Vis spectrum of ceria (Fig. 3b) and a red shift in the spectrum of zirconia (Fig. 3a) as compared to the bulk materials (400 and 275 nm, respectively) disclose a decrease in coordination number of the Ce and Zr ions incorporated in highly defective finely dispersed crystallites. Absorption in the region of 300–500 nm and above 720 nm for all copper modifications is associated with the presence of oligomeric Cu-O-Cu species and well-crystallized CuO particles, the highest amount of the former being in Cu/CeO<sub>2</sub>\_CH in agreement with XRD data.

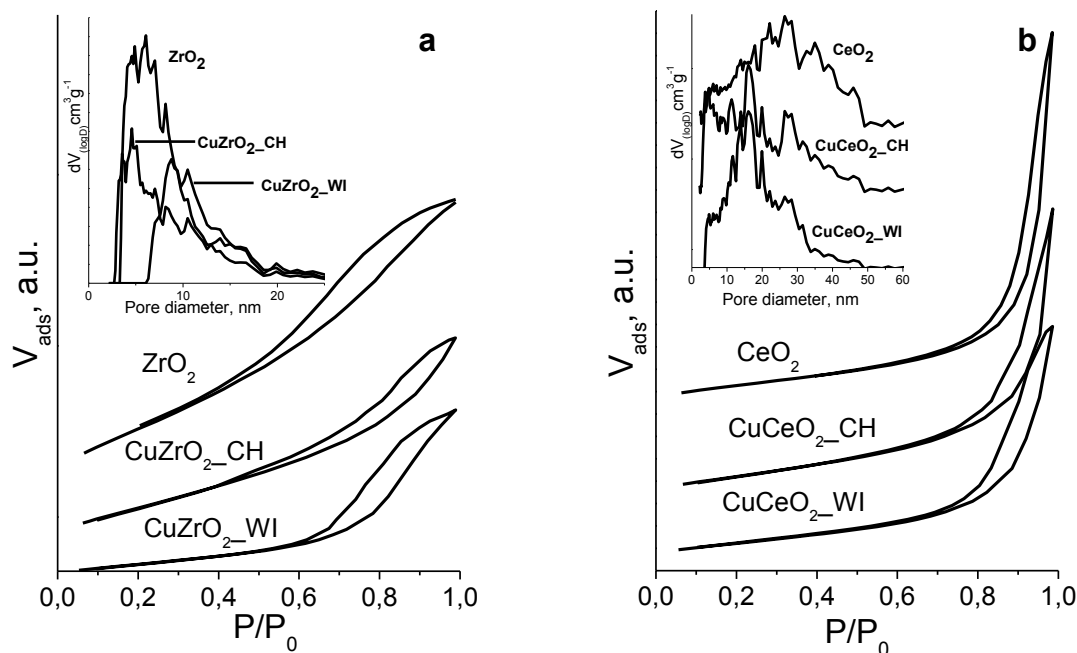


**Fig. 1.** Nitrogen physisorption isotherms and pore size distribution (inset) for parent and copper-modified ZrO<sub>2</sub> (a) and CeO<sub>2</sub> (b).

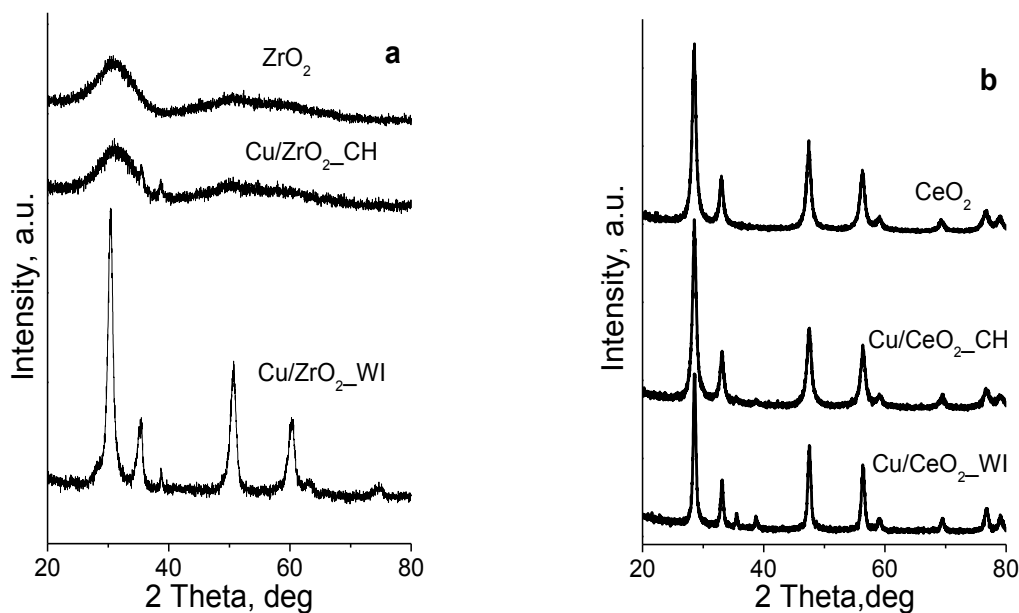


**Fig. 2.** XRD patterns of parent and copper-modified  $\text{ZrO}_2$  (a) and  $\text{CeO}_2$  (b) materials.

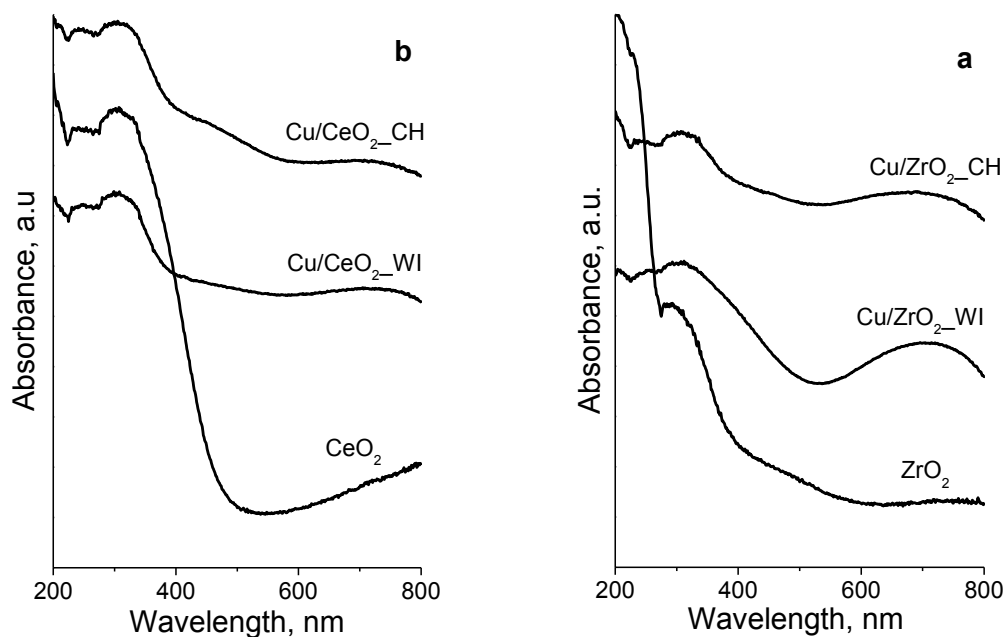


**Fig. 3.** UV-Vis spectra of parent and copper-modified  $\text{ZrO}_2$  (a) and  $\text{CeO}_2$  (b) materials.

Further information about the state of the copper species was gained by temperature-programmed reduction (TPR) experiments with hydrogen (Fig. 4). In principle, this method could provide useful data on metal ion oxidation state and environment, but usually interpretation of the results is rather complicated due to superposition of various effects. TPR profiles of pure  $\text{CeO}_2$  show a slight weight loss above 650 K which corresponds to about 80% reduction of  $\text{Ce}^{4+}$  to  $\text{Ce}^{3+}$  ions at the surface [18]. In accordance with our previous study [14], the observed weight loss for pure  $\text{ZrO}_2$  in the completely

studied temperature range could be related to a release of surface hydroxyl groups. Two reduction effects with maxima at 430 and 516 K appeared in the TPR profile of  $\text{Cu/ZrO}_2\text{-WI}$ . According to Liu *et al.* [19] they can be assigned to stepwise reduction ( $\text{Cu}^{2+} \rightarrow \text{Cu}^{1+} \rightarrow \text{Cu}^0$ ) of bulk  $\text{CuO}$  particles. However, taking into account XRD and FTIR data (see above), reduction of  $\text{CuO}$  particles, which are in intimate contact with different zirconia phases (amorphous, monoclinic, and tetragonal) cannot be fully disregarded, as reported in Refs. 20 and 21. Calculations based on these two reduction effects gave a

reduction degree of about 95%. Only one reduction effect in the 350–430 K range with a maximum at about 400 K was observed with Cu/ZrO<sub>2</sub>\_CH. It is related to a complete Cu<sup>2+</sup>→Cu<sup>0</sup> transition of more finely divided particles as compared with Cu/ZrO<sub>2</sub>\_WI. It should be noted that weight losses observed in the whole temperature interval exceeded theoretical values of Cu<sup>2+</sup> total reduction to metallic copper and the effect was much more pronounced for Cu/ZrO<sub>2</sub>\_CH. We assign this phenomenon to a release of OH groups from the ZrO<sub>2</sub> surface, which are continually restored *via* spillover of hydrogen from finely divided copper particles to the zirconia surface [22].

TPR-TG profiles of both ceria modifications consist of only one TPR effect. It is narrower and centred at a lower temperature as compared to their ZrO<sub>2</sub> analogues, and is consistent with a 90–100% reduction degree of Cu<sup>2+</sup> to Cu<sup>0</sup>. This indicates that CuO species on CeO<sub>2</sub> is more finely and uniformly dispersed as compared to that on the ZrO<sub>2</sub> support. This effect was more pronounced for Cu/CeO<sub>2</sub>\_CH indicating that the CH procedure ensures formation of a finely dispersed CuO phase.

Fig. 5a shows temperature dependencies of methanol conversion over various materials. Selectivity to CO, its formation being closely related to the production of hydrogen from methanol, is presented in Fig. 5b. Methane, dimethyl ether (DME), and carbon dioxide are also registered as by-products. Both CeO<sub>2</sub> and ZrO<sub>2</sub> supports exhibit own catalytic activity above 650 K, which exceeds about 50% at 725 K. CO selectivity for both supports

is below 40% due to formation of DME, the latter being provoked by the presence of Lewis and Brønsted acidic sites. Modification of both supports with copper increased not only their catalytic activity in methanol decomposition (Fig. 5a), but also improved the selectivity to CO formation (Fig. 5b). These effects were more pronounced if the CH procedure was used. ZrO<sub>2</sub>-supported copper modifications manifested a higher catalytic activity as compared to their ceria-based analogues. Bearing in mind XRD, UV-Vis, and TPR data, we assume a synergistic effect between ZrO<sub>2</sub> support and deposited copper species. Formation of methoxy intermediates seems to be promoted by interaction between methanol and hydroxyl groups from the zirconia surface, while hydrogen transfer assists further transformation of the latter to and from the copper species. It seems that this mechanism is facilitated by higher dispersion of the copper entities, which is achieved during the ‘chemisorption-hydrolysis’ procedure. According to TPR data, they not only promote recovery of a ‘OH group reservoir’ on the zirconia surface but also demonstrate a high redox activity. The conversion curve of Cu/ZrO<sub>2</sub>\_WI shows a complicated behaviour that can be due to agglomeration of reduced copper species by the influence of reaction medium. Obviously, on increasing copper dispersion this effect is suppressed to a higher extent. This could be achieved using a ‘chemisorption-hydrolysis’ procedure or by copper deposition on ceria, where formation of an interface layer between CeO<sub>2</sub> and CuO prevents copper particles from agglomeration [23].

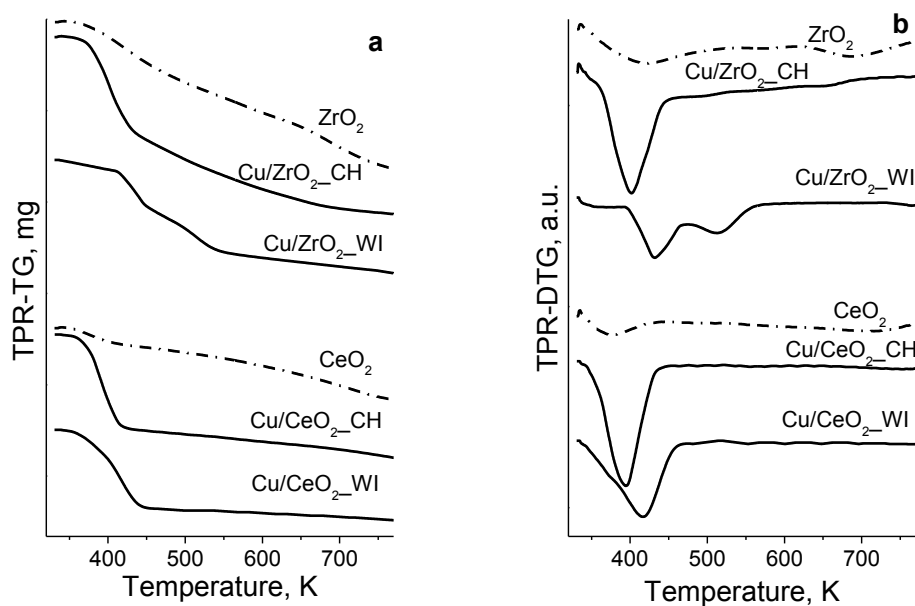


Fig. 4. TPR-TG (a) and TPR-DTG (b) profiles of copper modifications of ZrO<sub>2</sub> and CeO<sub>2</sub>.

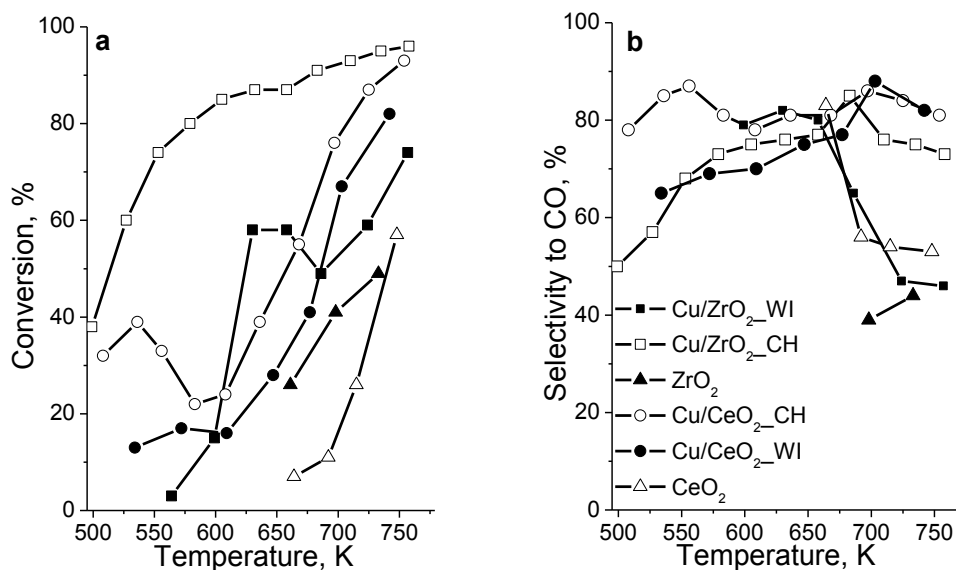


Fig. 5. Temperature profiles of methanol conversion (a) and CO selectivity (b) for various materials.

## CONCLUSIONS

A ‘chemisorption-hydrolysis’ method was applied to prepare nanosize copper oxide supported on nanostructured mesoporous  $\text{CeO}_2$  and  $\text{ZrO}_2$ . In comparison with conventional incipient wetness impregnation technique, this method provided deposition of readily reducible and highly active copper species in methanol decomposition. A higher catalytic activity achieved with zirconia-supported copper catalyst prepared by ‘chemisorption-hydrolysis’ procedure is assigned to a synergism between copper species and  $\text{ZrO}_2$ .

*Acknowledgements:* Financial support by Consiglio Nazionale delle Ricerche and Bulgarian Academy of Sciences through bilateral projects (2013–2015) and Bulgarian Science Fund under Project DFNI-E-02-2/2014 are gratefully acknowledged.

## REFERENCES

1. A. Yin, X. Guo, W.-L. Dai, K. Fan, *Catal. Commun.*, **12**, 412 (2011).
2. N. B. Linder, R. Besse, F. Audonnet, S. LeCaer, J. Deschamps, M. I. Clerc, C. A. Simionescu, *Micropor. Mesopor. Mater.*, **132**, 518 (2010).
3. A. Kong, H. W. Wang, X. Yang, Y. W. Hou, Y. K. Shan, *Micropor. Mesopor. Mater.*, **118**, 348 (2009).
4. T. Tsoncheva, I. Genova, M. Stoyanova, M.-M. Pohl, R. Nickolov, M. Dimitrov, E. Sarcadi-Priboczki, M. Mihaylov, D. Kovacheva, K. Hadjiivanov, *Appl. Catal. B-Environ.*, **147**, 684 (2014).
5. Z.-Y. Ma, C. Yang, W. Wei, W.-H. Li, Y.-H. Sun, *J. Mol. Catal. A-Chem.*, **231**, 75 (2005).
6. K. T. Jung, A. T. Bell, *Catal. Lett.*, **80**, 63 (2002).
7. T. Caputo, L. Lisi, R. Pirone, G. Russo, *Appl. Catal. A-Gen.*, **348**, 42 (2008).
8. A. Behbahani, S. Rowshanzamir, A. Esmaeilifar, *Proc. Eng.*, **42**, 908 (2012).
9. M. Rezaei, S. M. Alavi, S. Sahebdehfar, Z.-F. Yan, *Powder Technol.*, **168**, 59 (2006).
10. V. I. Pârvulescu, H. Bonnemant, V. Pârvulescu, U. Endruschat, A. Rufinska, Ch. W. Lehmann, B. Tesche, G. Poncelet, *Appl. Catal. A-Gen.*, **214**, 273 (2001).
11. K. M. Parida, D. Rath, *Appl. Catal. A-Gen.*, **321**, 101 (2007).
12. L.-F. Chen, P.-J. Guo, L.-J. Zhu, M.-H. Qiao, W. Shen, H.-L. Xu, K.-N. Fan, *Appl. Catal. A-Gen.*, **356**, 129 (2009).
13. L. Chmielarz, P. Kustrowski, R. Dziembaj, P. Cool, E. F. Vansant, *Appl. Catal. B-Environ.*, **62**, 369 (2006).
14. T. Tsoncheva, V. Dal Santo, A. Gallo, N. Scotti, M. Dimitrov, D. Kovacheva, *Appl. Catal. A-Gen.*, **406**, 13 (2011).
15. S. T. Yong, C. W. Ooi, S. P. Chai, X. S. Wu, *Int. J. Hydrogen Energy*, **38**, 9541 (2013).
16. F. Boccuzzi, S. Coluccia, G. Martra, N. Ravasio, *J. Catal.*, **184**, 316 (1999).
17. A. Kambolis, H. Matralis, A. Trovarelli, Ch. Papadopoulou, *Appl. Catal. A-Gen.*, **377**, 16 (2010).
18. G. Rao, B. G. Mishra, *Bull. Catal. Soc. India*, **2**, 122 (2003).
19. Z. Liu, M. Amiridis, Y. Chen, *J. Phys. Chem. B*, **109**, 1251 (2005).
20. Y. Zhao, K. Tao, H. L. Wan, *Catal. Commun.*, **5**, 249 (2004).
21. Z.-Y. Ma, C. Yang, W. Wei, W.-H. Li, Y.-H. Sun, *J. Mol. Catal. A-Chem.*, **231**, 75 (2005).
22. S. Esposito, M. Turco, G. Bagnasco, C. Cammarano, P. Pernice, *Appl. Catal. A-Gen.*, **403**, 128 (2011).
23. T. Tsoncheva, G. Issa, J. M. López-Nieto, T. Blasco, P. Concepcion, M. Dimitrov, G. Atanasova, D. Kovacheva, *Micropor. Mesopor. Mater.*, **180**, 156 (2013).

НЕСТАНДАРТЕН МЕТОД НА „ХЕМИСОРБЦИЯ-ХИДРОЛИЗА“ И МЕТОД НА  
„ИМПРЕГНИРАНЕ“ ЗА ПОЛУЧАВАНЕ НА НАНОДИСПЕРСНА МЕД ВЪРХУ МЕЗОПОРЕСТИ  
ЦЕРИЕВ ДИОКСИД И ЦИРКОНИЕВ ДИОКСИД

Т. С. Цончева<sup>1\*</sup>, Из. Г. Генова<sup>1</sup>, Н. Скоти<sup>2</sup>, В. Дал Санто<sup>2</sup>, Н. Равазио<sup>2</sup>

<sup>1</sup> *Институт по органична химия с Център по фитохимия, Българска академия на науките, 1113 София, България*

<sup>2</sup> *CNR-Институт по молекулярна наука и технология, Милано, Италия*

Постъпила на 12 септември 2015 г.; Преработена на 7 декември 2015 г.

(Резюме)

Синтезирани са мезопорести наноразмерни циркониев диоксид и цериев диоксид чрез темплейтен хидротермален синтез, които са използвани като матрица за нанасяне и стабилизиране на наноразмерни меднооксидни частици. Приложен е метод на „хемисорбция-хидролиза“ за получаване на медни модификации на  $ZrO_2$  и  $CeO_2$ . Получените материали са охарактеризирани с прахова рентгенова дифракция, азотна физисорбция, ИЧ и УВ спектроскопии и температурно програмирана редукция с водород и са сравнени с техни аналози, получени чрез традиционен метод на „импрегниране“. Каталитичната активност на така получените материали е изследвана в разлагането на метанол. Показано е, че чрез прилагане на метода на „хемисорбция-хидролиза“ за отлагане на медни частици върху  $ZrO_2$  се получават високо активни и селективни катализатори за разлагане на метанол до въглероден оксид и водород, което се дължи на синергичен ефект между медния и циркониевооксидния компоненти.

## Redox properties of ceria-alumina oxides

R. Palcheva<sup>1</sup>, B. Pawelec<sup>2</sup>, E. Gaigneaux<sup>3</sup>, J. L. Fierro<sup>2</sup>, S. Damyanova<sup>1\*</sup>

<sup>1</sup>*Institute of Catalysis, Bulgarian Academy of Sciences, G. Bonchev St., Bldg. 11, 1113 Sofia, Bulgaria*

<sup>2</sup>*Instituto de Catálisis y Petroleoquímica, CSIC, Cantoblanco, 28049 Madrid, Spain*

<sup>3</sup>*Université Catholique de Louvain, Institute of Matter Condensed and Nanosciences (IMCN), Molecules, Solids and Reactivity (MOST), Croix du Sud, 2/L17.05.17, B-1348 Louvain la Neuve, Belgium*

Received 15 October 2015; Revised 4 November 2015

A series of  $x\text{CeO}_2\text{-Al}_2\text{O}_3$  samples of different  $\text{CeO}_2$  loading ( $x = 1\text{--}12$  wt.%) were prepared by impregnation of  $\gamma$ -alumina with aqueous solution of  $(\text{NH}_4)_3[\text{Ce}(\text{NO}_3)_6]$ . The effect of  $\text{CeO}_2$  content on the structure, textural and redox properties of  $x\text{CeO}_2\text{-Al}_2\text{O}_3$  samples was studied by using  $\text{N}_2$  adsorption-desorption isotherms, XRD, and TPR. It was shown that the increase of  $\text{CeO}_2$  content leads to a decrease in surface area and pore volume of mixed oxides caused by filling the pores with cerium oxide particles. XRD measurements detected an increase of  $\text{CeO}_2$  average particle size on increasing ceria content. The redox properties of  $x\text{CeO}_2\text{-Al}_2\text{O}_3$  oxides were modified by a consecutive reduction and oxidation treatment, which was more evident for 6- and 12-wt.%  $\text{CeO}_2$  samples. An enhanced reducibility upon reduction-oxidation treatment of  $x\text{CeO}_2\text{-Al}_2\text{O}_3$  oxides was revealed by formation of a phase of high oxygen mobility reduced at a lower temperature.

**Key words:** mixed  $\text{CeO}_2\text{-Al}_2\text{O}_3$  oxides, redox properties, XRD, TPR.

### INTRODUCTION

Cerium(IV) oxide and  $\text{CeO}_2$ -containing materials have a great importance as catalysts and as structural and electronic promoters in catalysts for different heterogeneous catalytic reactions. The  $\text{CeO}_2\text{-Al}_2\text{O}_3$  system is of special interest in catalysis because of its technological importance in auto exhaust catalysis [1, 2], in reforming processes of ethanol and methane to hydrogen production [3, 4], or in water-gas shift reaction and selective CO oxidation in the presence of a large excess of hydrogen (PROX) [5]. In spite of the great importance of ceria as an active catalyst component, a more detailed mechanistic understanding on how cerium affects catalytic processes is still a matter of considerable debate, although some key findings are well established.

Several works have been devoted to studies of the physical and chemical features of ceria deposited on  $\text{Al}_2\text{O}_3$ , with the aim of improving ceria properties through a better knowledge of the nature of interaction between  $\text{CeO}_2$  and  $\text{Al}_2\text{O}_3$ . Some authors believe that the structural and morphological modifications operated by ceria on  $\text{Al}_2\text{O}_3$  play a minor role in relation to chemical effects as modification of acid-base properties, which is much more important for determining the properties of the system. Other authors proposed that the stabilization effect of ceria

in terms of modification of the structural and textural features of alumina is a major factor [1, 6]. Usually, these discrepancies may originate from different experimental conditions that are employed in the studies, such as temperature range investigated, durability of thermal treatment and pretreatment as well as use of some additional promoters.

One of the most important beneficial effects of ceria is the ability to oxidize deposited carbon species over catalytic metal centres and to increase catalyst stability due to its high oxygen storage capacity (OSC) caused by the redox couple  $\text{Ce}^{4+} \leftrightarrow \text{Ce}^{3+}$  under oxidation and reduction conditions [7, 8]. Nanostructured mixed metal oxides supported on alumina have been prepared by impregnation of  $\gamma\text{-Al}_2\text{O}_3$  with cerium/zirconium citrate solutions, which exhibit a high OSC [8]. It was shown [10] that the following types of cerium oxides as  $\text{CeO}_2$ ,  $\text{CeO}_{2-x}/\text{Al}_2\text{O}_3$ , and  $\text{CeAlO}_3/\text{Al}_2\text{O}_3$  exhibit a decrease of OSC value in the order: finely-divided  $\text{CeO}_{2-x} > \text{CeAlO}_3 > \text{small-sized CeO}_2 > \text{large CeO}_2$  crystallites.

To improve catalyst performance, further knowledge of the interaction between ceria and alumina in mixed  $\text{CeO}_2\text{-Al}_2\text{O}_3$  oxides is essential, because they are potential carriers for supported Ni catalysts for ethanol or methane reforming to hydrogen. In the present work, it was attempted to investigate the effect of  $\text{CeO}_2$  content on the structure and reductive properties of mixed  $x\text{CeO}_2\text{-Al}_2\text{O}_3$  oxides by using different techniques:  $\text{N}_2$  adsorption-desorption iso-

\* To whom all correspondence should be sent:  
E-mail: soniad@ic.bas.bg

therms, X-ray diffraction (XRD) and temperature programmed reduction (TPR). Studies related to subjecting mixed  $\text{CeO}_2\text{-Al}_2\text{O}_3$  oxides to consecutive reducing and oxidizing conditions at different reoxidation temperatures were performed.

## EXPERIMENTAL

### Sample preparation

$\text{CeO}_2\text{-Al}_2\text{O}_3$  supports were obtained by impregnation of  $\gamma\text{-Al}_2\text{O}_3$  (Topsøe) with an aqueous solution of  $(\text{NH}_4)_3[\text{Ce}(\text{NO}_3)_6]$ , a 99.99% product of Degussa, with an appropriate concentration of  $\text{CeO}_2$ . The solution with alumina was stirred at  $50^\circ\text{C}$  for 4 h and after that the water was evaporated by a Rotavapor. The obtained samples were dried in air at  $100^\circ\text{C}$  for 12 h and calcined at  $600^\circ\text{C}$  for 4 h. Nominal  $\text{CeO}_2$  content was in the range of 1–12 wt.%. The samples were denoted as  $x\text{Ce-Al}$ , where  $x$  is the theoretical amount of  $\text{CeO}_2$ . For comparative purposes, ceria was obtained by calcination of  $(\text{NH}_4)_3[\text{Ce}(\text{NO}_3)_6]$  in air at  $650^\circ\text{C}$  for 2 h.

### Methods

$\text{N}_2$  adsorption-desorption isotherms of calcined samples were recorded at 77 K on a Micromeritics TriStar 3000 apparatus. Beforehand the samples were outgassed at  $150^\circ\text{C}$  for 24 h under vacuum ( $10^{-4}$  mbar) to obtain a relatively clean surface. Specific surface area ( $S_{\text{BET}}$ ), pore volume ( $V_p$ ), and average pore diameter ( $D_p$ ) of  $x\text{CeO}_2\text{-Al}_2\text{O}_3$  samples were evaluated from the  $\text{N}_2$  adsorption-desorption isotherms. Surface area were calculated according to the BET method using nitrogen adsorption data taken in the relative equilibrium pressure interval of  $0.03 < P/P_0 < 0.3$ .

XRD analysis was performed in  $2\theta$  range between  $10$  and  $90^\circ$  by a computerized Seifert 3000 diffractometer, using Ni-filtered  $\text{CuK}\alpha$  ( $\lambda = 0.15406$  nm) radiation and a PW 2200 Bragg-Brentano  $\theta/2\theta$  goniometer equipped with a bent graphite monochromator and an automatic slit. A step size of  $0.02$  and a step scan of  $2$  s were used to identify samples structure. Phase identification was carried out by comparison with JCPDF database cards.  $\text{CeO}_2$  average crystallite size was estimated by Debye-Scherrer equation using the X-ray diffraction pattern at  $2\theta = 28.8^\circ$ .

TPR experiments were conducted on a Micromeritics TPD/TPR 2900 equipment provided with a TCD and interfaced to a data station. Samples of  $0.100$  g were reduced in a flowing gas containing 10 vol.%  $\text{H}_2$  in Ar up to a final temperature of  $1000^\circ\text{C}$  at a total flow rate of  $50$  ml.min $^{-1}$  and heating rate of

$15$  deg.min $^{-1}$ . The samples were subjected to redox treatment at  $500^\circ\text{C}$  ( $\text{R-O}_{500}$ ) and  $700^\circ\text{C}$  ( $\text{R-O}_{700}$ ), which involved  $\text{H}_2$ -TPR to  $1000^\circ\text{C}$  followed by cooling to  $500^\circ\text{C}/700^\circ\text{C}$  under argon and *in situ* oxidation by an oxygen flow ( $70$  ml.min $^{-1}$ ) at  $500^\circ\text{C}/700^\circ\text{C}$  for 2 h. After each oxidation run, the reactor was cooled to r.t. in Ar flow and the samples were subjected to TPR (from r.t. to  $1000^\circ\text{C}$ ).

## RESULTS AND DISCUSSION

### Textural properties and structure

$\text{N}_2$  adsorption-desorption isotherms of calcined  $x\text{CeO}_2\text{-Al}_2\text{O}_3$  samples of different  $\text{CeO}_2$  content shown in figure 1 have hysteresis loops that belong to H1 type according to IUPAC, typical for mesoporous materials [11]. Textural characteristics of the samples are given in Table 1.

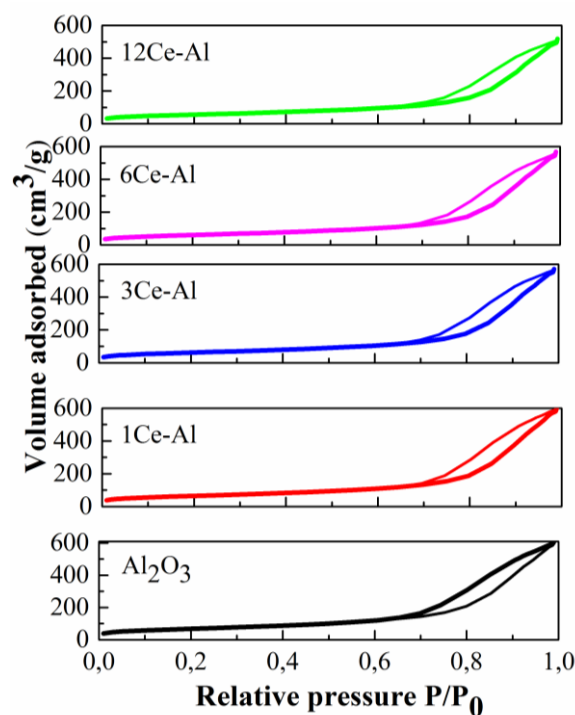


**Fig. 1.**  $\text{N}_2$  adsorption-desorption isotherms of  $\gamma\text{-Al}_2\text{O}_3$ , bulk  $\text{CeO}_2$ , and mixed  $x\text{CeO}_2\text{-Al}_2\text{O}_3$  oxides of different  $\text{CeO}_2$  content.

Introduction of small amount of  $\text{CeO}_2$  (1 wt.%) to alumina led to a slight decrease of the  $S_{\text{BET}}$ . However, increasing the  $\text{CeO}_2$  content to 12 wt.% causes a significant decrease in  $S_{\text{BET}}$  and  $V_p$ . Lower surface area and pore volume values of  $x\text{CeO}_2\text{-Al}_2\text{O}_3$  oxides compared to those of alumina can be related to a blockage of alumina pores by cerium oxide species [12] due to easy-going agglomeration of  $\text{CeO}_2$  over alumina. In addition, ceria agglomeration may develop some porosity, which contributes to measured

textural properties [13]. The mean pore diameter of  $x\text{CeO}_2\text{-Al}_2\text{O}_3$  samples is higher than that of alumina (Table 1). This is probably caused by the presence of particles with larger pores and possible blockage of small diameter pores by cerium oxide species.

**Table 1.** Textural properties and particle size ( $D_{\text{XRD}}$ ) of  $\text{CeO}_2\text{-Al}_2\text{O}_3$  oxides

Samples	$S_{\text{BET}}$ ( $\text{m}^2\cdot\text{g}^{-1}$ )	$V_{\text{p}}$ ( $\text{cm}^3\cdot\text{g}^{-1}$ )	Pore diameter (nm)	$D_{\text{XRD}}$ (nm)
$\text{Al}_2\text{O}_3$	248	0.92	14.6	–
1Ce-Al	228	0.91	15.7	–
3Ce-Al	217	0.87	15.7	5.3
6Ce-Al	213	0.86	15.7	7.2
12Ce-Al	198	0.79	15.4	9.2

XRD patterns of  $\text{Al}_2\text{O}_3$  and calcined  $x\text{CeO}_2\text{-Al}_2\text{O}_3$  oxides of different  $\text{CeO}_2$  content are shown in figure 2. For comparison, XRD data on bulk  $\text{CeO}_2$  is also included. The XRD patterns indicate that all  $\text{CeO}_2$ -containing samples demonstrate peaks at  $2\theta = 28.8, 32.6, 47.4, 56.1,$  and  $76.5^\circ$  characteristic of a  $\text{CeO}_2$  phase with fluorite structure (JCPDS 34-0394). These peaks become more intense on increasing the ceria content in  $x\text{CeO}_2\text{-Al}_2\text{O}_3$  samples.  $\text{CeO}_2$  average crystallite size ( $D_{\text{XRD}}$ ) increases from 5.3 nm to 9.2 nm for 1- and 12-wt.%  $\text{CeO}_2$  samples, respectively (Table 1). Reflections at  $2\theta = 33.4, 37.6, 40.5, 45.8,$  and  $67.1^\circ$  (JCPDS 10-425) are assigned to  $\gamma\text{-Al}_2\text{O}_3$ . The intensity of the main line of alumina support ( $2\theta = 67.1^\circ$ ) decreases upon increasing cerium oxide loading, which is most visible with 12 wt.%  $\text{CeO}_2$ . This could be explained by existence of some interaction between cerium and aluminium or increased coverage of  $\text{CeO}_2$  crystallites on alumina. Ferreira *et al.* [14] observed a small amount of cerium oxide species at low  $\text{CeO}_2$  content ( $x \leq 3$  wt.%), which interacts with the alumina support surface to form non-stoichiometric  $\text{CeO}_{2-x}$ .

#### TPR and redox properties

TPR profiles of bulk  $\text{CeO}_2$  and calcined  $x\text{CeO}_2\text{-Al}_2\text{O}_3$  samples, and effects of subsequent oxidation and reduction cycles are compared in figure 3. The TPR shape of bulk  $\text{CeO}_2$  is very similar to that reported in the literature and it can be interpreted as a stepwise reduction process. Bulk  $\text{CeO}_2$  manifests two well-known peaks [15]: a small peak at about  $508^\circ\text{C}$  and a large peak at  $749^\circ\text{C}$ . The low-temperature peak is due to reduction of most easily reducible surface capping oxygen of  $\text{CeO}_2$ , while removal

of bulk oxygen is registered by the high-temperature TPR pattern. A good correlation between surface area and  $\text{H}_2$  consumption of the first peaks has been found [16]. Variations between surface area and  $\text{H}_2$  consumption are linear indicating that at first ceria reduction occurs on the surface and then progressively affects the bulk. Thus, the initial progress of reduction is highly sensitive to the surface area and bulk reduction, favoured by high oxygen mobility in the  $\text{CeO}_2$  lattice, is beginning when all surface sites are fully reduced. The low-temperature peak is due to reduction of readily reduced surface capping oxygen of  $\text{CeO}_2$  followed by generation of vacancies and surface  $\text{Ce}^{3+}$  ions, which can easily be oxidized to  $\text{Ce}^{4+}$  under oxidation conditions [17]. At the second step, the reduction process is associated with creation of oxygen vacancies in the bulk of  $\text{CeO}_2$ . Therefore, the high temperature peak at  $749^\circ\text{C}$  can be attributed to complete reduction of  $\text{Ce}^{4+}$  to  $\text{Ce}^{3+}$  by removing  $\text{O}^{2-}$  anions of the ceria lattice and formation of  $\text{Ce}_2\text{O}_3$ . Due to low surface area of the bulk  $\text{CeO}_2$  sample ( $18 \text{ m}^2\cdot\text{g}^{-1}$ ) prepared by decomposition of  $(\text{NH}_4)_3[\text{Ce}(\text{NO}_3)_6]$ , the low-temperature signal is very weak, and the majority of hydrogen consumption originates from the reduction of large ceria crystallites (Fig. 3).

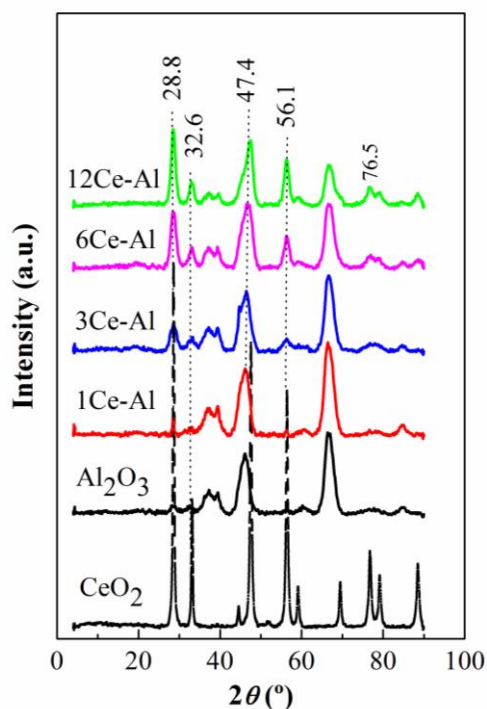


**Fig. 2.** XRD of bulk  $\text{CeO}_2$  and mixed  $x\text{CeO}_2\text{-Al}_2\text{O}_3$  oxides of different  $\text{CeO}_2$  content.

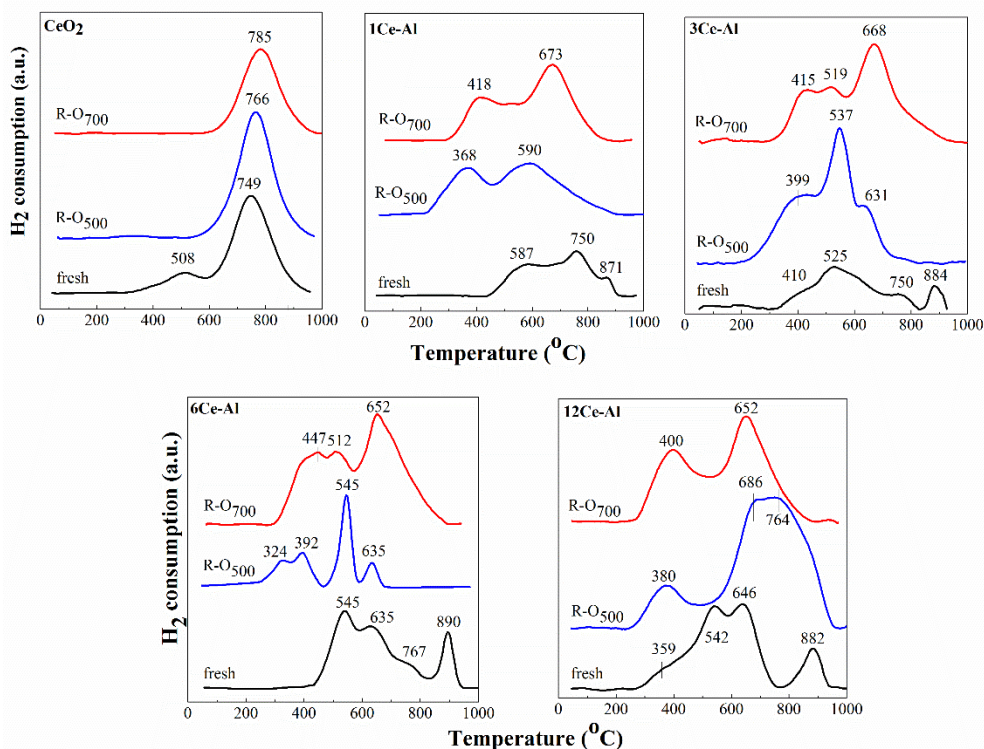


Fig. 3. TPR of bulk  $\text{CeO}_2$  and mixed  $x\text{CeO}_2\text{-Al}_2\text{O}_3$  oxides subjected to R-O<sub>500</sub> and R-O<sub>700</sub>.

As was previously discussed [18], surface and bulk reduction cannot easily be distinguished by the conventional TPR technique, since both processes occur almost simultaneously during the TPR experiment. As can be seen in Fig. 3, reductive behaviour of alumina-supported  $\text{CeO}_2$  of different concentration is modified depending on the extent and nature of interaction between ceria and alumina. The TPR profiles of mixed  $x\text{CeO}_2\text{-Al}_2\text{O}_3$  oxides show new characteristics: (i) TPR peak shape depends on crystallite size of deposited  $\text{CeO}_2$ ; (ii) significant shifts of peak temperatures are apparent; (iii) apparent  $\text{H}_2$  consumption continues even after the main peaks characteristic of bulk ceria; (iv) low temperature features, assigned to surface oxygen reduction, fall in a wide temperature range, and (v) effectiveness of  $\text{Ce}^{4+}$  reduction increases upon increasing  $\text{CeO}_2$  loading at all reduction temperatures, as revealed by an increase of peak intensity.

Regardless of  $\text{CeO}_2$  loading, the TPR profiles of calcined  $x\text{CeO}_2\text{-Al}_2\text{O}_3$  samples can be divided into three temperature regions: region I (200–500°C), region II (500–800°C), and region III (> 800°C) (Fig. 3). Region I peaks are generally associated with reduction of small ceria crystallites and/or surface cerium oxide species weakly interacting with support, whereas region II is ascribed to reduction of large/bulk  $\text{CeO}_2$  crystallites or cerium oxide species or cerium atoms that interact strongly with alumina [19]. A high-temperature peak at 882–

890°C observed with all samples may be caused by formation of surface  $\text{CeAlO}_3$  species associated with  $\text{Ce}^{4+}$  reduction to  $\text{Ce}^{3+}$ . It has been shown [20, 21] that, depending on ceria loading, ceria reduction on alumina under hydrogen involves at least two reactions: formation of non-stoichiometric cerium oxides and cerium aluminate ( $\text{CeAlO}_3$ ). It should be noted that an increase in  $\text{CeAlO}_3$  peak intensity is accompanied by a decrease in high-temperature peak intensity due to bulk ceria reduction (Fig. 3).

TPR profiles of fresh  $\text{CeO}_2$  samples of  $\geq 3$ -wt.% content show features in the low-temperature region (< 500°C) due to well dispersed very small ceria particles on alumina surface (Fig. 3). However, there is still reduction of large  $\text{CeO}_2$  crystallites of different size in the profile of 12-wt.%  $\text{CeO}_2$  sample as revealed by peaks at 542 and 640°C. Shifting of reduction peaks to low temperatures is in agreement with a suggestion that a high concentration of ions of redox character (i.e.  $\text{Ce}^{4+}$  ions) favours an electron transfer as  $\text{Ce}^{4+} \leftrightarrow \text{Ce}^{3+}$ . Prevailing peaks in the TPR profile of a sample of the lowest  $\text{CeO}_2$  content (1 wt.%) in the medium temperature range may be mainly caused by reduction of cerium oxide species that interacts strongly with alumina due to high ceria dispersion. The lowest intensity of the  $\text{CeAlO}_3$  peak at 882°C is due to the smallest number of cerium oxide species in  $1\text{CeO}_2\text{-Al}_2\text{O}_3$ .

After R-O<sub>500</sub> and R-O<sub>700</sub> treatment of bulk  $\text{CeO}_2$  the small peak caused by surface shell reduction of

CeO<sub>2</sub> disappeared, while the peak due to bulk reduction of ceria was shifted to higher temperatures (from 749°C for fresh samples to 766 and 785°C for R-O<sub>500</sub> and R-O<sub>700</sub>, respectively).

The TPR profiles of all  $x\text{CeO}_2\text{-Al}_2\text{O}_3$  samples of different CeO<sub>2</sub> content subjected to R-O<sub>500</sub> show a marked enhancement of low-temperature reducibility relative to that of fresh samples (Fig. 3). Improved low-temperature reducibility was observed for a mixed oxide of 6 wt.% expressed by a small peak at a lower temperature of 324°C, probably due to formation of a small fraction of non-stoichiometric cerium oxides species. Regardless of CeO<sub>2</sub> loading, some agglomeration of cerium oxide species was observed after R-O<sub>500</sub> treatment, as revealed by the peaks in the 537–590°C range. On the other hand, one cannot exclude a partial segregation of species of low oxidation state, such as Ce<sup>3+</sup>, on the ceria surface owing to the higher ionic radius of Ce<sup>3+</sup> (1.1 Å) compared to that of Ce<sup>4+</sup> (0.97 Å) [22]. Thus, segregation may lead to complete disappearance of the peak characteristic of CeAlO<sub>3</sub> in the TPR profiles of all samples. It is well known [21] that well dispersed CeO<sub>x</sub> entities can be precursors for surface CeAlO<sub>3</sub> formation under reduction, while they are readily transferred to CeO<sub>2</sub> after oxidation.

However, some distinct features characterize the TPR profile of the sample of the highest CeO<sub>2</sub> loading (12 wt.%). Besides the presence of small well-dispersed ceria particles, a broad high intensity peak in the high temperature region between 600 and 900°C was observed attributed to reduction of large CeO<sub>2</sub> crystallites. This indicates that reoxidation at 500°C affects ceria crystallites size in the 12CeO<sub>2</sub>-Al<sub>2</sub>O<sub>3</sub> sample, although there is still a fraction of highly reducible ceria in low-loaded samples (Fig. 3).

Subjecting the R-O<sub>500</sub> samples to R-O<sub>700</sub> leads to a shift of the TPR peaks to higher temperatures (Fig. 3), which could mean that the average oxidation state in non-stoichiometric ceria approaches +4. The low-temperature peak maxima are almost identical for all oxides, while the higher temperature peaks are shifted to lower values due to bulk ceria reduction detected for high-loaded ceria samples (6 and 12 wt.%) caused by a higher oxygen mobility.

## CONCLUSIONS

TPR analysis showed that hydrogen uptake for mixed CeO<sub>2</sub>-Al<sub>2</sub>O<sub>3</sub> samples is dependent on reoxidation temperature and CeO<sub>2</sub> content. It can be assumed that the amount of initially present cerium in a lower oxidation state formed during sample pre-

paration is higher for samples of lower CeO<sub>2</sub> loading, where the stability of non-stoichiometric ceria is higher. This is in agreement with a lower average size of CeO<sub>2</sub> crystallites of fluorite type structure. Partially reduced cerium oxide entities can be precursors for surface CeAlO<sub>3</sub> formation under reduction conditions, the amount being increased upon increasing the CeO<sub>2</sub> content. However, increasing the reoxidation temperature led to disappearance of the surface CeAlO<sub>3</sub> due to agglomeration of the cerium oxide species. A higher oxygen mobility was observed for samples of high CeO<sub>2</sub> content (6 and 12 wt.%) due to agglomeration of ceria particles.

**Acknowledgments:** The authors kindly acknowledge financial support by the Bulgarian Science Fund through project FNI E02/16 as well as by bilateral collaborations of the Institute of Catalysis with Catholic University of Louvain la Neuve (Belgium) and Institute of Catalysis and Petrochemistry, Madrid (Spain).

## REFERENCES

1. M. Ozawa, M. Kimura, *J. Mater. Sci. Lett.*, **9**, 291 (1990).
2. A. Holmgren, B. Andersson, D. Duprez, *Appl. Catal. B: Environ.*, **22**, 215 (1999).
3. A. C. S. F. Santos, S. Damyanova, G. N. R. Teixeira, L. V. Mattos, F. B. Noronha, F. B. Passos, J. M. C. Bueno, *Appl. Catal. A: Gen.*, **290**, 123 (2005).
4. L. S. F. Feio, C. E. Hori, S. Damyanova, F. B. Noronha, W. H. Cassinelli, C. M. P. Marques, J. M. C. Bueno, *Appl. Catal. A: Gen.*, **316**, 107 (2006).
5. L. Ilieva, T. Tabakova, G. Pantaleo, I. Ivanov, R. Zanella, D. Paneva, N. Velinov, J. W. Sobczak, W. Lisowski, G. Avdeev, A. M. Venezia, *Appl. Catal. A: Gen.*, **467**, 76 (2013).
6. A. Piras, A. Trovarelli, G. Dolcetti, *Appl. Catal. B: Environ.*, **28**, L77 (2000).
7. S. Bose, Y. Wu, *J. Am. Ceram. Soc.*, **88**, 1999 (2005).
8. D. Andreeva, R. Nedyalkova, L. Ilieva, M. Abrashev, *Appl. Catal. B: Environ.*, **52**, 157 (2004).
9. R. Di Monte, P. Fornasiero, J. Kaspar, M. Graziani, *Stud. Surf. Sci. Catal.*, **140**, 229 (2001).
10. M. Haneda, T. Mizushima, N. Kakuta, A. Ueno, Y. Sato, S. Matsuura, K. Kasahara, M. Sato, *Bull. Chem. Soc. Jpn.*, **66**, 1279 (1993).
11. G. Leofanti, M. Padovan, G. Tozzola, B. Venturelli, *Catal. Today*, **41**, 207 (1998).
12. C. Morterra, G. Magnacca, V. Bolis, G. Gerrato, M. Baricco, A. Giachello, M. Fuciale, *Stud. Surf. Sci. Catal.*, **96**, 361 (1995).
13. V. B. Mortola, S. Damyanova, D. Zanchet, J. M. C. Bueno, *Appl. Catal. B: Environ.*, **107**, 221 (2011).
14. A. P. Ferreira, D. Zanchet, J. C. S. Araujo, J. W. C. Liberatori, E. F. Souza-Aguiar, F. B. Noronha, J. M. C. Bueno, *J. Catal.*, **263**, 335 (2009).
15. H. C. Yao, Y. F. Yu Yao, *J. Catal.*, **86**, 254 (1984).

16. V. Perrichon, A. Laachir, G. Beregeret, R. Frety, L. Tounayan, *J. Chem. Soc., Faraday Trans.*, **90**, 773 (1994).
17. G. Jacobs, U. M. Graham, E. Chenu, P. M. Patterson, A. Dozier, B. A. Davis, *J. Catal.* **229**, 499 (2005).
18. G. Balducci, J. Kaspar, P. Fornasiero, M. Graziani, M. S. Islam, *J. Phys. Chem. B*, **102**, 557 (1998).
19. F. Giordano, A. Trovarelli, C. de Leitenburg, M. Giona, *J. Catal.*, **193**, 273, (2000).
20. S. Geller, P. M. Raccach, *Phys. Rev. B*, **2**, 1167 (1970).
21. A. Piras, S. Colussi, A. Trovarelli, V. Sergo, J. Llorca, R. Psaro, L. Sordelli, *J. Phys. Chem. B*, **109**, 11110 (2005).
22. A. I. Kozlov, D. H. Kim, A. Yezerets, P. Andersen, H. H. Kung, M. C. Kung, *J. Catal.*, **209**, 417 (2002).

## ОКИСЛИТЕЛНО-РЕДУКЦИОННИ СВОЙСТВА НА $\text{CeO}_2\text{-Al}_2\text{O}_3$ ОКСИДИ

Р. Палчева<sup>1</sup>, Б. Павелец<sup>2</sup>, Е. Геньо<sup>3</sup>, Х. Л. Г. Фиеро<sup>2</sup>, С. Дамянова<sup>1\*</sup>

<sup>1</sup> *Институт по катализ, Българска академия на науките, 1113 София, България*

<sup>2</sup> *Институт по катализ и нефтохимия, Кантобланко, 28049 Мадрид, Испания*

<sup>3</sup> *Католически университет на Льовен, В-1348 Льовен-ла-Ньов, Белгия*

Постъпила на 15 октомври 2015 г.; Преработена на 4 ноември 2015 г.

(Резюме)

Получени са  $x\text{CeO}_2\text{-Al}_2\text{O}_3$  оксиди с различно съдържание на  $\text{CeO}_2$  ( $x = 1\text{--}12$  тегл.%) чрез импрегниране на  $\gamma\text{-Al}_2\text{O}_3$  с воден разтвор на  $(\text{NH}_4)_3[\text{Ce}(\text{NO}_3)_6]$ . Ефектът на съдържанието на  $\text{CeO}_2$  върху структура, текстура и окислително-редукционни свойства на  $x\text{CeO}_2\text{-Al}_2\text{O}_3$  образци с помощта на адсорбционно-десорбционни изотерми на азот, рентгенова дифракционна спектроскопия (РДС) и температурно-програмирана редукция (ТПР). Показано е, че средният размер на частиците на  $\text{CeO}_2$  на повърхността на  $\gamma\text{-Al}_2\text{O}_3$  нараства с увеличаване на концентрацията му. Окислително-редукционните свойства на  $x\text{CeO}_2\text{-Al}_2\text{O}_3$  са модифицирани чрез последователна обработка в редукционни и окислителни условия, което е по-ярко забележимо за образци с 6 и 12 тегл.%  $\text{CeO}_2$ . Повишената редуцируемост на образците при окислително-редукционното им третиране се проявява чрез образуването на фаза, редуцираща се при по-ниска температура, което се дължи на по-високата мобилност на кислорода.

## Role of Mn in supported Au-Mn/TOS catalysts

A. M. Ali<sup>1</sup>, M. A. Daous<sup>1</sup>, L. A. Petrov<sup>2\*</sup>

<sup>1</sup> Department of Chemical and Materials Engineering, Faculty of Engineering, King Abdulaziz University, P.O. Box 80204, Jeddah 21589, Saudi Arabia

<sup>2</sup> SABIC Chair of Catalysis, King Abdulaziz University, P.O. Box 80204, Jeddah 21589, Saudi Arabia

Received: October 29, 2015; Revised: December 10, 2015

In this study, a complete catalytic propane oxidation was investigated by using four different supported Au-Mn catalytic systems. Results showed that addition of manganese to a supported gold catalyst promoted lattice oxygen activity in metal oxides, such as ceria, zirconia, and titania, which resulted in an enhanced catalytic activity of an Au-Mn catalyst because of formation of a dinuclear compound, either Au<sub>5</sub>Mn<sub>2</sub> or Au<sub>2</sub>Mn. A competition between Au and Mn to capture free lattice oxygen, dominated by manganese, was observed. In general, Ce 3d<sub>3/2</sub>, Au 4f<sub>7/2</sub>, and Mn 2p<sub>1/2</sub> orbitals are related to dominant elemental species that are responsible for the enhanced catalytic activity of the Au-Mn catalyst in the complete oxidation of propane.

**Keywords:** gold catalysts, gold-manganese catalysts, XPS, propane oxidation

### INTRODUCTION

Since the discovery of the high catalytic ability of Au nanoparticles, supported on a high surface area metal oxide support, gold has been extensively studied as a heterogeneous catalyst in both liquid and gaseous phases. In the last two decades, much attention is paid to the treatment, management, and ultimate elimination of toxic and hazardous materials [1] and effluent gases [2] from various toxic sources. Volatile organic compounds (VOCs), such as propane, are one of the main concerned pollutants [3]. For its abatement, direct combustion, a least efficient and high cost method, was used [4].

In recent decade, most scientists [5–12] had preferred catalytic oxidation to eliminate VOCs emissions and to meet stringent environmental quality standards (EQS). Various combinations of metal oxides and metals (both precious and nonprecious metals) were investigated for their potential as efficient oxidation catalysts. Among them, ceria-supported catalysts [5, 13–16] were mostly used for the catalytic oxidation of VOCs. Combinations between mixed ceria- and zirconia-based catalyst carriers were also tested and were found to be catalytically efficient because of possible changes of catalyst surface area [17]. Presence of each titania [18, 19], ceria, and zirconia [20] with an optimum amount of manganese oxide has shown an enhanced catalytic ability because of both enlarged surface area and redox qualities.

Supporting Au nanoparticles on ceria-titania [21]

and ceria-zirconia [22] was found to be productive to eliminate VOC compounds owing to gold activity and influence of Au on the reduction of ceria-titania or ceria-zirconia supports. However, gold was not enough efficient as compared to platinum because of the very good dispersion of Pt on the ceria-zirconia support. It is generally believed that excellent dispersion of Au nanoparticles on a metal oxide(s) support play a key role for observed high catalytic activity of the prepared Au catalysts.

Potentially well-dispersed Au nanoparticles on the metal oxide(s) support could increase lattice oxygen mobility and cause weakening of Ce-O bonds. This may lead to the release of surface capping oxygen [23, 24] that could participate in a Mars-Van Krevelen type of oxidation reaction mechanism [23, 25–28].

Among many transition metal oxides, manganese oxide has a huge range of various types of liable oxygen sources, such as MnO, MnO<sub>2</sub>,  $\alpha$ -Mn<sub>2</sub>O<sub>3</sub>, Mn<sub>2</sub>O<sub>3</sub>,  $\gamma$ -Mn<sub>2</sub>O<sub>3</sub>, Mn<sub>3</sub>O<sub>4</sub>, MnO<sub>2</sub>, and  $\beta$ -MnO<sub>2</sub> that may participate in an oxidation process in a competitive way. Lahousse *et al.* have summarised that  $\gamma$ -MnO<sub>2</sub> catalyst is favourable for abatement of volatile organic compounds [3]. Few studies were also conducted attempting to explain the importance of the presence of Mn on CeO<sub>2</sub> [29].

Based on own experimental data and published papers [7–23], it is fairly to presume that Au-Mn catalysts supported on mixed oxide carriers composed of CeO<sub>2</sub>, ZrO<sub>2</sub>, and TiO<sub>2</sub> could possibly have an increased catalytic activity in oxidation of VOCs, such as propane, the latter being one of the stringent and difficult organic compound to get oxidized. As

\* To whom all correspondence should be sent  
E-mail: lpetrov@kau.edu.sa

per authors' knowledge, so far none of the published studies has been reported on the possible role of Mn in supported Au-Mn catalysts especially through a detailed investigation carried out by XPS, which is a highly reliable way to identify possible orbital and/or suborbital overlapping to induce a synergistic effect of this system. This study was aimed at identifying how each elemental orbital does participate in such a catalytic system.

## EXPERIMENTAL

### Catalyst preparation and characterisation

An Au-Mn/TOS catalyst was prepared in three steps: (i) preparation of a triple oxide support (TOS) of  $5.5\text{CeO}_2:2.5\text{ZrO}_2:2\text{TiO}_2$  composition, (ii) manganese impregnation of the triple oxide support (1% Mn/TOS), and (iii) gold deposition-precipitation on Mn/TOS (1% Au-1% Mn/TOS). For comparative purposes, a 1% Au/TOS catalyst was prepared by deposition-precipitation method. Both a list of all the chemicals used and detailed catalyst preparations as well as XPS and XRD analysis details can be found in a previously reported article [30].

### Catalyst testing

Catalytic activity measurements in complete propane oxidation were carried out in a PID micro-activity reference reactor system. A schematic diagram of the experimental setup is shown in Figure 1. The experiments were exactly performed under the reaction conditions carried out by Ali *et al.* [30].

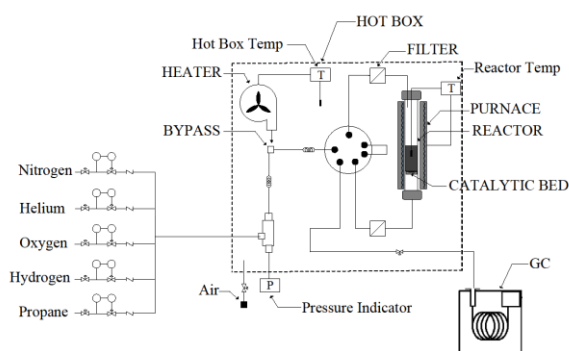


**Fig. 1.** Schematic diagram of the experimental setup.

The only components in the reaction mixture at the reactor exit in all experiments were propane, oxygen, carbon dioxide, and water. An Agilent 7890A GC system, equipped with a flame ionisation detector (FID) and a thermal conductivity detector (TCD), was used to identify and monitor the propane and the reaction products. Data processing was acquired by applying GC ChemStation® B.04.03 (54). 0.5-cm<sup>3</sup> gas samples, an Agilent DB1/122-1063 (1 μm, 60 m × 0.25 mm) column, an Hp-8ft

HAYSEP Q column, and He and N<sub>2</sub> carrier gases used for FID and TCD, respectively. Chromatographic oven temperature profiles are summarised in Table 1.

**Table 1.** Oven temperature profile

	Rate, °C.min <sup>-1</sup>	Temperature	Hold time
initial		40	3
ramp 1	30	130	0
ramp 2	20	220	0.5

## RESULTS AND DISCUSSION

In order to investigate a possible association between gold and manganese in the presence of TOS support, freshly prepared catalyst samples were analysed for catalytic ability in the complete oxidation of propane.

### Catalytic activity

Results of the catalytic tests are discussed and summarised in the following sections. Fig. 2 shows a detailed comparison of the catalytic activity of the Au-Mn, Au, and Mn catalysts and of the support (TOS).

The results showed that the triple oxide support itself exhibited a certain catalytic ability. Up to 300°C, less than 5% conversion of the propane took place. It reached 10% at 400°C and then shot up to nearly 90% at 450°C. As previously published [9, 31], we consider this conversion as being due mostly to cerium oxide.

The catalytic activity of the supported Mn catalyst at temperatures up to 350°C was practically the same as that of the catalyst carrier. At temperatures above 350°C, the Mn catalyst manifested a slightly higher catalytic activity than catalyst support. These results show that Mn is practically non-active in the reaction of propane oxidation at temperatures up to 500°C.

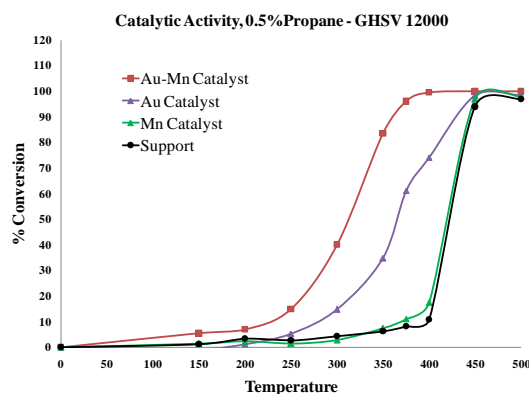


**Fig. 2.** Catalytic activity of the Au, Mn, and Au-Mn catalysts and the support in propane complete oxidation.

The Au catalyst had a moderate catalytic activity. Oxidation started after 200°C and a nearly 95% propane conversion was achieved at 400°C. The catalytic activity of the supported Au catalyst was substantially higher in comparison with Mn catalyst and triple oxide support in the temperature interval from 300 to 375°C. However, a 95%-conversion of propane was observed at the same temperature for the Mn catalyst. These results clearly indicate that the gold catalyst is relatively active in the reaction of propane total oxidation at moderate temperatures.

The catalytic conversion of propane over the Au-Mn catalyst started below 150°C and then strongly accelerated at temperatures above 225°C. A 95%-conversion was accomplished at 375°C. A complete conversion of propane over the Au-Mn catalyst was attained at 400°C. The catalytic activity of the Au-Mn catalyst was much higher than the activities of the rest studied samples. Obviously, it may be concluded from these results that manganese strongly enhanced the catalytic activity of the supported gold catalyst.

A synergism was observed due to interaction between Au and Mn in the presence of TOS and, as per authors' knowledge, so far no evidence is found in the literature. The nature and mechanism of such an interaction is yet to be studied and understood.

In order to investigate any interaction between Au and Mn and possible impacts of each of the metal oxides present in the support, a detailed XPS analysis was carried out before and after catalytic measurements.

#### *XPS study*

To study the possibility of any association between Au and Mn as well as their individual or collective role on enhanced catalytic activity, an XPS study was conducted in detail. Results are discussed and summarised below.

#### *Impact of introduction of Au and/or Mn to the support*

##### *Before reaction*

Figure 3 shows an overall comparison of survey XPS spectra of the triple oxide support, Au, Mn, and Au-Mn samples before catalytic reaction. In triple oxide support, oxygen (O 1s and O 2s), titanium (Ti 2s, Ti 2p, Ti 3s, and Ti 3p), cerium (Ce 4p, Ce 4d, Ce 3p, and Ce 3d), and zirconium (Zr 3d, Zr 3p, and Zr 3s) were found to be present. Among these peaks O 1s, Ti 2p, Ce 3d, and Zr3p are identified as the main peaks. Addition of either gold or manganese did not change much the spectra, however, bearing in mind the following three main differences:

(i) Au 4f and Mn 2p peaks were identified upon addition of gold and manganese, respectively.

(ii) Upon introduction of gold or manganese separately to the triple oxide support, a significant and clear peak of Ce 4s was found.

(iii) Addition of manganese to the gold catalyst (Au/TOS) gave rise to a significant and clear Mn 2s peak, which was not present when only manganese was added to the triple oxide support.

It is evident that Mn introduced to the Au catalyst has considerably affected the Ce component of the triple oxide support. This effect could be observed because of any possible synergism and/or any other interaction between gold and manganese that may have resulted in an enormous increase in catalytic activity of the gold catalyst.

In order to investigate any change in the results summarised in the previous section before and after catalytic reactions, a detailed XPS study of all the catalysts was also performed after the catalytic activity tests.

Figure 4 shows an overall comparison of survey overlaid XPS spectra before and after the catalytic reaction. Some of the key results are presented below.

(i) In triple oxide support (Fig. 4B), before and after the catalytic reaction, O 1s, Ti 2p and Zr 3p peaks were nearly the same in terms of intensity except for a significant change of binding energy (BE) in the range of 800–1200 eV. The Ce 3d peak was among those that seemed greatly affected. This change could be because of either partial reduction of Ce<sup>4+</sup> to Ce<sup>3+</sup> or due to its exposure to X-ray irradiation.

(ii) The surface scan spectra of the Mn catalyst (Fig. 4D) remained almost the same before and after reaction excepting negligible intensity variations after 800–1200 eV. Manganese presence did not cause any noticeable changes to the support except for a negligible change of the Ce ions. This could be explained as a possible reason that manganese alone on the support did not affect significantly the catalytic activity (see Fig. 2).

(iii) Considering the Au catalyst (Fig. 4B), a clear change can be seen after the binding energy range of 550–1200 eV. This variation is quite large as compared to the changes of the Mn catalyst and ceria. It might be because of the active role of gold for increasing the catalytic activity of the Au catalyst, as it was much higher than that of the Mn catalyst and ceria.

(iv) The highest variation was found in the overall survey laid XPS spectra of the Au-Mn catalyst (Fig. 4A), before and after the reaction, in the binding energy range of 200–1200 eV. This differ-

ence clearly indicates that the introduction of manganese to the Au catalyst is really affecting greatly in comparison with the Au and Mn catalysts. The highest catalytic activity of the Au-Mn catalyst might be associated with a possible interaction between gold and manganese.

The nature of this interaction can be a key aspect to better understanding of the enhanced catalytic activity and possible role of each of the mobile oxygen resources present in the catalysts. Further subsections describe possible reasons about this key aspect.

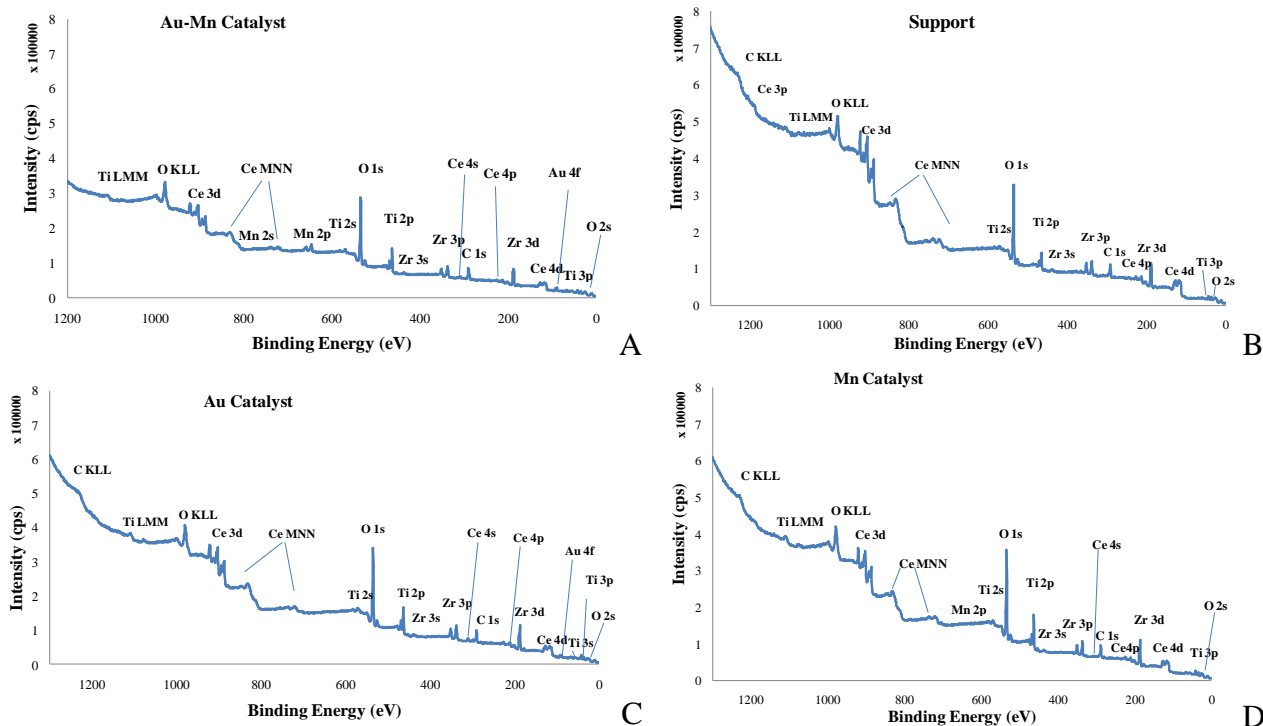


Fig. 3. Overall comparison of survey XPS spectra: A – Au-Mn catalyst, B – support, C – Au catalyst, D – Mn catalyst.

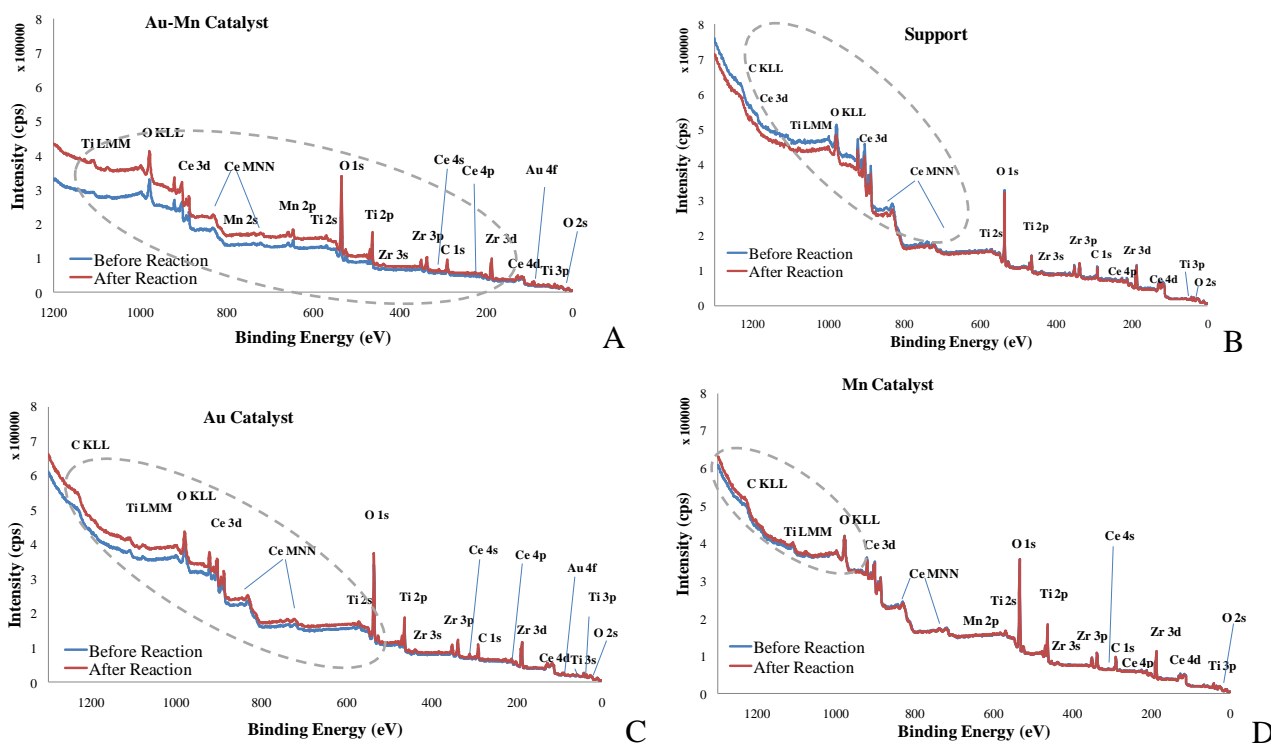


Fig. 4. Overall comparison of survey overlaid XPS spectra before and after catalytic reaction: A – Au-Mn catalyst, B – support, C – Au catalyst, D – Mn catalyst.

*After reaction*

*Role of Au, Mn, and triple oxide support in the catalytic reaction*

It is seen (Fig. 4A) that titanium and zirconium regions are not changed much before and after the catalytic reaction for the highly active Au-Mn catalyst. This could be because the presence of manganese may affect cerium significantly and/or due to a possible interaction between gold and manganese. To investigate this interaction between Au and Mn as well as the role cerium, a deconvolution study of Ce, Au, and Mn was carried out before and after catalysis.

*Role of ceria*

Figure 5 shows a detailed comparison of deconvoluted XPS spectra of CeO<sub>2</sub>, before and after the reaction, for each catalyst (Au-Mn/TOS, Au/TOS, Mn/TOS), support, and pure CeO<sub>2</sub>.

*Before reaction*

Figure 5A shows an in-depth comparison of the cerium deconvoluted XPS spectra for all the catalysts before reaction. A most probable oxidation state of cerium (Ce<sup>4+</sup>) in Au-Mn, Mn, and Au catalysts was observed [32]. Almost all the peaks, V, V'', V''' of Ce 3d<sub>5/2</sub> and U, U'', U''' of Ce 3d<sub>3/2</sub>, remained nearly the same excepting V'-Ce 3d<sub>5/2</sub> and U'-Ce 3d<sub>3/2</sub>. Table 2 shows a summary of the binding energies (eV) for the V' and U' peaks of all the catalysts and support.

Compared with the Au-Mn catalyst, the V'-Ce 3d<sub>5/2</sub> peak of the support and of the Mn catalyst remained constant. A significant difference of 0.66 eV was observed between the V'-Ce 3d<sub>5/2</sub> peaks of the Au-Mn and Au catalysts. A similar pattern was also detected for U'-Ce 3d<sub>3/2</sub> where the difference was found to be 0.80 eV. This might be owing to a partial reduction of Ce<sup>4+</sup> to Ce<sup>3+</sup> in the ceria upon addition of manganese to the Au catalyst as well as due to a favourable variation in the activation energies.

*After reaction*

Figure 5B shows V'-Ce 3d<sub>5/2</sub> and U'-Ce 3d<sub>3/2</sub> peak positions of deconvoluted XPS spectra of Ce after the catalytic reaction. No changes in associated oxidation states of cerium were observed after the reaction. Also, a similar change in BE of 0.30 eV (see Table 3) for the V'-Ce 3d<sub>5/2</sub> peak existed between the Au-Mn and Au catalysts, i.e. nearly half of the difference found before reaction. However, the difference between the U'-Ce 3d<sub>3/2</sub> peak values of the Au-Mn and Au catalysts was much smaller, nearly by two thirds, as to that before reaction. This

may lead to a conclusion that U'-Ce 3d<sub>3/2</sub> perhaps played a key role for the enhanced catalytic activity of the Au-Mn catalyst as to cerium belonging to the V' peak of Ce 3d<sub>5/2</sub>.

*Role of gold*

Figure 6 shows deconvoluted XPS spectra of gold for the Au-Mn and Au catalysts before and after catalytic reaction.

*Before reaction*

Three peaks W, W', W'' of Au 4f<sub>7/2</sub> and two peaks X, X' of Au 4f<sub>5/2</sub> were identified with possible Au<sup>1+</sup> oxidation state of the gold in the Au-Mn and Au catalysts (Fig. 6B). Each of the three peaks of Au 4f<sub>7/2</sub> (W, W', W'') and one of Au 4f<sub>5/2</sub> (X) were found to be identical in terms of binding energy except for the X' peak of Au 4f<sub>5/2</sub> for the gold containing catalysts before reaction (0.33 eV, see Table 3). This perhaps could be because of non-metallic gold in the Au-Mn catalyst as compared to slightly higher metallic nature of gold in the Au catalyst.

*After reaction*

After the catalytic reaction, two Au 4f<sub>7/2</sub> peaks (W and W'') and one Au 4f<sub>5/2</sub> peak (X') were slightly changed (see Fig. 6B) for the Au-Mn and Au catalysts contrary to the change of only one Au 4f<sub>5/2</sub> peak (X') before reaction. This may further indicate that during the catalytic reaction gold existed in a higher oxidation state (1+) in the Au-Mn catalyst as compared to the Au catalyst. This can also be related to the presence of Mn that did promote the non-metallic nature of gold because of its higher number of available unpaired valence shell electrons.

**Table 2.** Binding energies of the V'-Ce 3d<sub>5/2</sub> and U'-Ce 3d<sub>3/2</sub> cerium peaks before and after catalytic reaction

Catalyst	Binding energy, eV			
	before reaction		after reaction	
	V'-Ce 3d <sub>5/2</sub>	U'-Ce 3d <sub>3/2</sub>	V'-Ce 3d <sub>5/2</sub>	U'-Ce 3d <sub>3/2</sub>
Au-Mn	885.40	902.45	885.54	903.03
Au	886.06	903.25	885.84	902.70
Mn	885.50	902.30	885.60	902.40
support	885.50	902.70	885.70	902.80
CeO <sub>2</sub>	885.20	902.70	885.20	902.70

**Table 3.** Binding energies of the W-Au4f<sub>7/2</sub>, W''-Au4f<sub>7/2</sub>, and X'-Au 4f<sub>5/2</sub> gold peaks before and after catalytic reaction

Catalyst	Binding energy, eV			
	before reaction		after reaction	
	X'-Au4f <sub>5/2</sub>	W-Au4f <sub>7/2</sub>	W''-Au4f <sub>7/2</sub>	X'-Au4f <sub>5/2</sub>
Au-Mn	89.50	82.15	85.94	89.25
Au	89.17	82.40	85.25	89.42

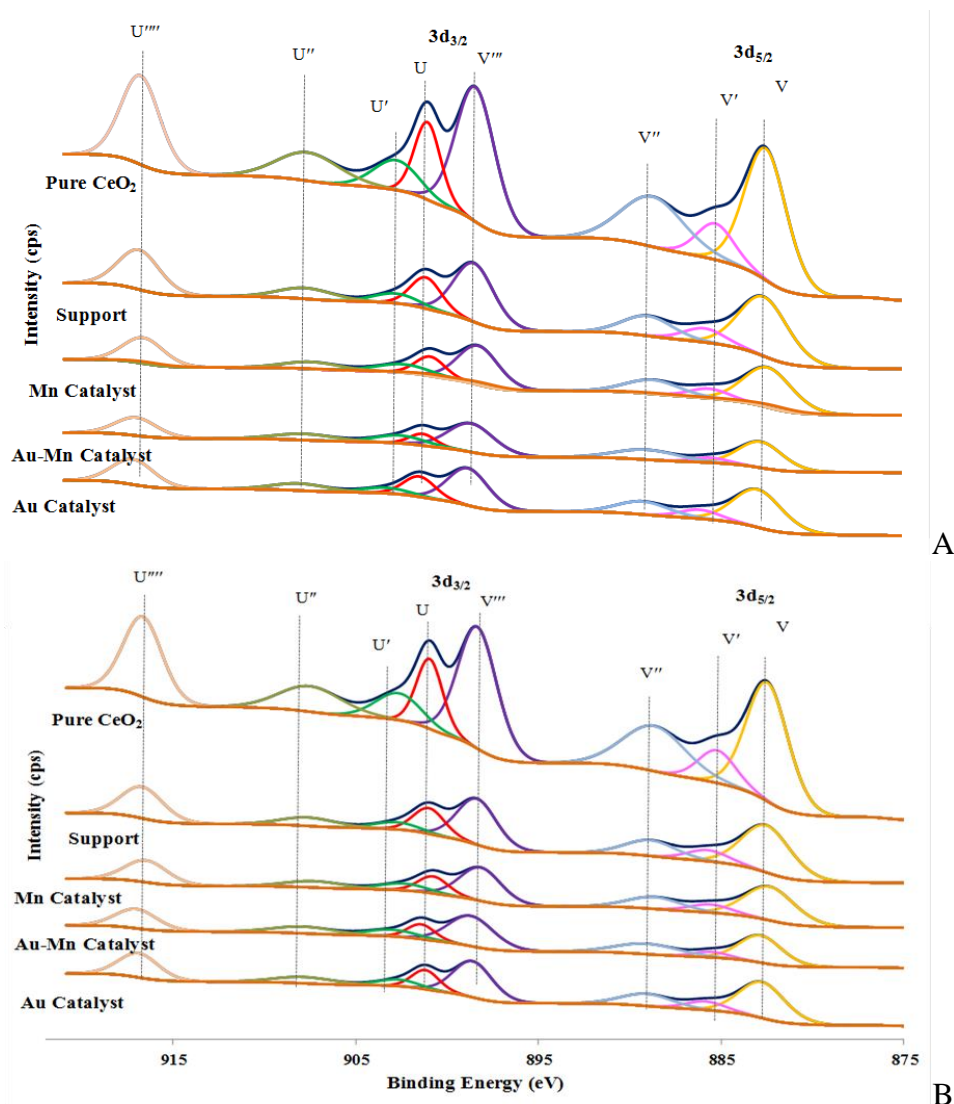


**Fig. 5.** Overall comparison of overlaid deconvoluted Ce XPS spectra: A – before reaction; B – after reaction.

### Role of manganese

The catalytic activity of the Au catalyst was moderate, whereas the catalytic activity of the Mn catalyst did not differ from that of the triple oxide support, i.e. Mn is not active in propane oxidation reaction. However, the catalytic activity of the Au-Mn catalyst was substantially increased compared to other two catalyst compositions. Apparently, this increase in catalytic activity is mainly due to an occurring synergism between catalyst components. Both the Au and Mn catalysts exhibited a much lower activity in the complete propane oxidation than the Au-Mn catalyst. It might be an indication that there existed a synergism (promotion of Au activity by Mn).

Based on the catalytic activity of the Au-Mn catalyst in comparison with the catalytic activity of

the Au and Mn catalysts it was assumed that it might be because of an efficient behaviour of Mn as promoter. Further, a detailed deconvoluted XPS study of manganese was also conducted. Fig. 7 shows an overall comparison of overlaid deconvoluted XPS spectra of the Mn catalyst before and after reaction.

### Before reaction

Two peaks of Mn  $2p_{3/2}$  (Y, Y') and two peaks (Z, Z') belonging to Mn  $2p_{1/2}$  with possible oxidation states of Mn<sup>+3</sup> and Mn<sup>+4</sup> in the Au-Mn catalyst were observed (Fig. 7) in comparison with single Y and Z peaks, ascribed to Mn  $2p_{3/2}$  and Mn  $2p_{1/2}$ , respectively, in the Mn catalyst [33].

This shows that the simultaneous presence of Au and Mn on the support gives rise to an entirely different behaviour of the Au-Mn catalyst in cata-

lysis in contrast to sole Mn on the support. The peaks Y' and Z' were identified as Au peaks within the main peaks Y and Z of the manganese. Possibly these sub-peaks (Y' and Z') within the main peaks of Mn belong to dinuclear (Au-Mn) compounds [34].

**Table 4.** Binding energies of the Y, Y'-Mn 2p<sub>3/2</sub> and Z, Z'-Mn 2p<sub>1/2</sub> manganese peaks before and after catalytic reaction

Condition	Binding energy, eV					
	Mn		Au-Mn			
	Mn 2p <sub>3/2</sub>	Mn 2p <sub>1/2</sub>	Mn 2p <sub>3/2</sub>	Mn 2p <sub>1/2</sub>		
	Y	Z	Y	Y'	Z	Z'
before reaction	641.20	653.3	641.64	644.84	653.20	655.66
after reaction	641.28	653.35	641.80	644.98	652.40	653.80

#### After reaction

The Mn 2p<sub>3/2</sub> and Mn 2p<sub>1/2</sub> peaks remained the same before and after the reaction (Table 4). Whereas, in the case of Au-Mn catalyst the Y and Y' peaks of Mn2p<sub>3/2</sub> did not change at all as to those of Z and Z' peaks of Mn2p<sub>1/2</sub>, which showed the largest shift (Table 5). This clearly indicates that both the dinuclear (Au-Mn) peak (Z') and the main peak (Z) of Mn2p<sub>1/2</sub> played an important role for the enhanced catalytic activity of the Au-Mn catalyst. Based on both XPS and catalytic activity results, it can be summarised that manganese is a key component for the increased catalytic activity of the gold catalyst. The presence of manganese as a promoter enhanced the catalytic activity by interacting with gold in the form of Au-Mn active system.

#### Identification of Au-Mn interaction

XPS studies have shown a unique association between Au and Mn that had caused an enhanced catalytic activity because of a dinuclear compound formation. In order to cross verify results, a thorough XRD study was conducted for all the catalysts before and after catalytic tests. Some results have already been reported by Ali *et al.* [30] showing that fresh and spent Au-Mn catalyst samples remained exactly the same, which is an indication that the Au-Mn catalyst was highly stable. Based on Au-Mn lattice parameters of Au solid solution *versus* composition, the expected structure contained more than 25% Mn but less than 35%. From the Au-Mn phase diagram, it was found that there could be two most probable structures: Au<sub>5</sub>Mn<sub>2</sub> and Au<sub>2</sub>Mn having a crystallite size of 7 nm.

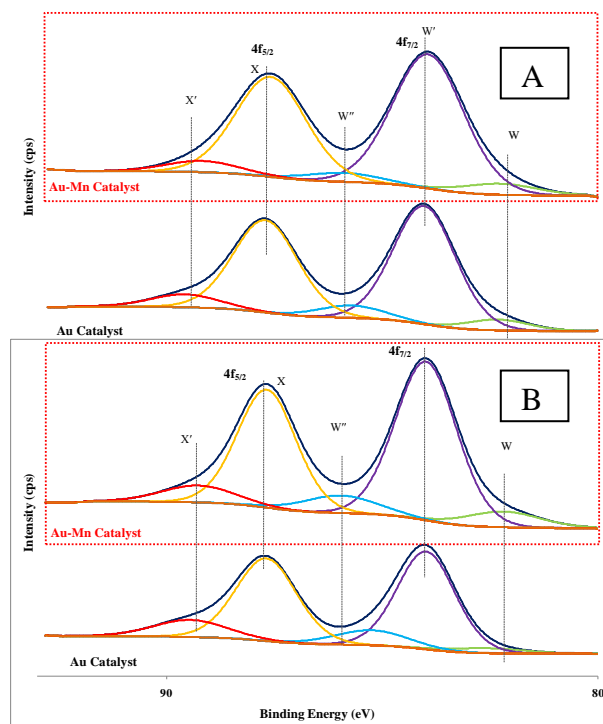


**Fig. 6.** Overall comparison of deconvoluted Au XPS spectra: A – before reaction, B – after reaction.

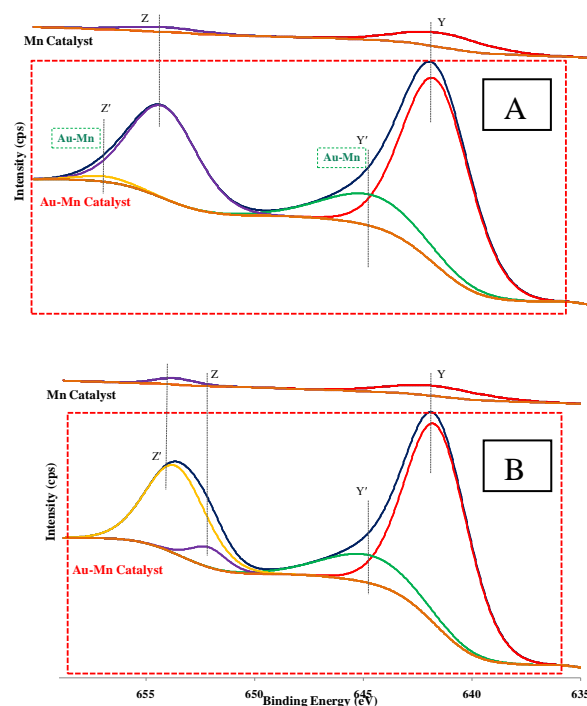


**Fig. 7.** Overall comparison of deconvoluted Mn XPS spectra: A – before reaction, B – after reaction.

Hence, based on XRD and XPS results the enhanced catalytic activity of Au-Mn could be due to the presence of dinuclear compound: Au<sub>5</sub>Mn<sub>2</sub> or Au<sub>2</sub>Mn.

## CONCLUSIONS

In conclusion, a supported Au-Mn catalyst has shown the highest catalytic ability in the complete oxidation of propane in comparison with Au and Mn catalysts. Manganese introduction to a gold catalyst promoted mobilization of lattice oxygen species of metal oxides of cerium, zirconium, and titanium that resulted in an enhanced catalytic activity of the Au-Mn catalyst. Enhanced lattice oxygen or adsorbed oxygen mobility was attributed to formation of a dinuclear Au-Mn compound: Au<sub>5</sub>Mn<sub>2</sub> or Au<sub>2</sub>Mn. In the absence of manganese, a moderate catalytic activity of Au catalyst was due to participation of ceria and titania lattice oxygens only. A competition between Au and Mn for free lattice oxygen, dominated by manganese, was also observed. In general, Ce 3d<sub>3/2</sub>, Au 4f<sub>7/2</sub>, and Mn 2p<sub>1/2</sub> orbitals were found to be related to dominating elemental species for enhanced catalytic activity of the Au-Mn catalyst in propane complete oxidation.

*Acknowledgement: The authors would like to acknowledge the Deanship of Scientific Research of King Abdulaziz University in Jeddah, Saudi Arabia, for funding this project under grant No. D-005/431. The authors, therefore, kindly acknowledge financial and technical support of university authorities. The authors would like also to thank R. Ahmad, H. Driss, and F. Trovela for technical support and assistance.*

## REFERENCES

- U. I. Gaya, A. H. Abdullah, Z. Zainal, M. Z. Hussein, *J. Hazard. Mater.*, **168**, 57 (2009).
- S. Deng, Z. Li, J. Huang, G. Yu, *J. Hazard. Mater.*, **179**, 1014 (2010).
- C. Lahousse, C. Cellier, B. Delmon, P. Grange, in *Stud. Surf. Sci. Catal.*, Vol. 130, A. Corma, J. L. G. Fierro, Eds., Elsevier, 2000.
- M. McGrath, *Appl. Catal. B-Environ.*, **5**, 25 (1995).
- Z. Abbasi, M. Haghighi, E. Fatehifar, S. Saedy, *J. Hazard. Mater.*, **186**, 1445 (2011).
- D. A. Aguilera, A. Perez, R. Molina, S. Moreno, *Appl. Catal. B-Environ.*, **104**, 144 (2011).
- S. S. T. Bastos, S. A. C. Carabineiro, J. J. M. Órfão, M. F. R. Pereira, J. J. Delgado, J. L. Figueiredo, *Catal. Today*, **180**, 148 (2012).
- M. Ousmane, L. F. Liotta, G. D. Carlo, G. Pantaleo, A. M. Venezia, G. Deganello, L. Retailleau, A. Boreave, A. Giroir-Fendler, *Appl. Catal. B-Environ.*, **101**, 629 (2011).
- S. Scirè, L. F. Liotta, *Appl. Catal. B-Environ.*, **125**, 222 (2012).
- T. Tabakova, D. Dimitrov, M. Manzoli, F. Vindigni, P. Petrova, L. Ilieva, R. Zanella, K. Ivanov, *Catal. Commun.*, **35**, 51 (2013).
- Z.-X. Yu, W. Zheng, W.-L. Xu, P. Zhang, H.-Y. Fu, Y.-H. Zhang, *Trans. Nonferrous Met. Soc. China*, **21**, (Suppl 2) 405 (2011).
- D. Vitry, J.-L. Dubois, W. Ueda, *J. Mol. Catal. A-Chem.*, **220**, 67 (2004).
- X. Liu, Z. Zhan, X. Meng, W. Huang, S. Wang, T. Wen, *J. Power Sources*, **199**, 138 (2012).
- J. Okal, M. Zawadzki, L. Krajczyk, *Catal. Today*, **176**, 173 (2011).
- V. Balcaen, H. Poelman, D. Poelman, G. B. Marin, *J. Catal.*, **283**, 75 (2011).
- D. B. Dadyburjor, T. K. Das, E. L. Kugler, *Appl. Catal. A-Gen.*, **392**, 127 (2011).
- G. Picasso, M. Gutiérrez, M. P. Pina, J. Herguido, *Chem. Eng. J.*, **126**, 119 (2007).
- G. Qi, R. T. Yang, *Appl. Catal. B-Environ.*, **44**, 217 (2003).
- M. Baldi, F. Milella, J. M. Gallardo-Amores, G. Busca, *J. Mater. Chem.*, **8**, 2525 (1998).
- B. Shen, X. Zhang, H. Ma, Y. Yao, T. Liu, *J. Environ. Sci.*, **25**, 791 (2013).
- C. Gennequin, M. Lamalle, R. Cousin, S. Siffert, F. Aïssi, A. Aboukais, *Catal. Today*, **122**, 301 (2007).
- J. Gaalova, P. Topka, L. Kaluza, O. Solcova, *Catal. Today*, **175**, 231 (2011).
- S. Scirè, S. Minicò, C. Crisafulli, C. Satriano, A. Pistone, *Appl. Catal. B-Environ.*, **40**, 43 (2003).
- G. C. Bond, C. Louis, D. T. Thompson, *Catalysis by Gold*, Imperial College Press, London, 2006.
- A. M. Ali, E. A. C. Emanuelsson, D. A. Patterson, *Appl. Catal. B-Environ.*, **106**, 323 (2011).
- A. M. Ali, E. A. C. Emanuelsson, D. A. Patterson, *Appl. Catal. B-Environ.*, **97**, 168 (2010).
- S. Minicò, S. Scirè, C. Crisafulli, R. Maggiore, S. Galvagno, *Appl. Catal. B-Environ.*, **28**, 245 (2000).
- C. Doornkamp, V. Ponc, *J. Mol. Catal. A-Chem.*, **162**, 19 (2000).
- L. E. Gómez, E. E. Miró, A. V. Boix, *Int. J. Hydrogen Energy*, **38**, 5645 (2013).
- A. M. Ali, M. A. Daous, A. A. M. Khamis, H. Driss, R. Burch, L. A. Petrov, *Appl. Catal. A-Gen.*, **489**, 24 (2015).
- L. Delannoy, K. Fajerweg, P. Lakshmanan, C. Potvin, C. Méthivier, C. Louis, *Appl. Catal. B-Environ.*, **94**, 117 (2010).
- B. Skårman, L. R. Wallenberg, P.-O. Larsson, A. Andersson, J.-O. Bovin, S. N. Jacobsen, U. Helmersson, *J. Catal.*, **181**, 6 (1999).
- J. Papavasiliou, G. Avgouropoulos, T. Ioannides, *J. Catal.*, **251**, 7 (2007).
- Modern Supramolecular Gold Chemistry: Gold-Metal Interactions and Applications, A. Laguna, Ed., Wiley-VCH, 2008.

## РОЛЯ НА МАНГАНА В НАНЕСЕНИ Au-Mn/TOS КАТАЛИЗАТОРИ

А. М. Али<sup>1</sup>, М. А. Даус<sup>1</sup>, Л. А. Петров<sup>2\*</sup>

<sup>1</sup> *Департамент по инженерна химия и материали, Факултет по инженерство, Университет Крал Абдулазис, п.к. 80204, Джеда 21589, Саудитска Арабия*

<sup>2</sup> *Катедра „Катализ“ на Саудитската основна индустриална корпорация, Департамент по инженерна химия и материали, Факултет по инженерство, Университет Крал Абдулазис, п.к. 80204, Джеда 21589, Саудитска Арабия*

Постъпила на 29 октомври 2015 г.; Преработена на 10 декември 2015 г.

(Резюме)

Изследвано е пълното каталитично окисление на пропан върху четири каталитични системи. Получените резултати показват, че добавянето на манган към нанесен златен катализатор промотира подвижността на решетъчния кислород в носителя – смесени оксиди  $\text{CeO}_2$ ,  $\text{ZrO}_2$  и  $\text{TiO}_2$  (TOS). В резултат на това се увеличава каталитичната активност на катализаторите. Установено е образуването на двуядрени съединения между златото и мангана със състав  $\text{Au}_5\text{Mn}_2$  и  $\text{Au}_2\text{Mn}$ . Установено е, че свободният решетъчен кислород се захваща както от златото, така и предимно от мангана. Намерено е, че орбиталите  $\text{Ce } 3d_{3/2}$ ,  $\text{Au } 4f_{7/2}$  и  $\text{Mn } 2p_{1/2}$  са свързани с преобладаващите активни форми на елементите на повърхността на Au-Mn катализатори.

## XANES and EXAFS study of supported CoNi catalysts for ethanol steam reforming

A. Braga<sup>1</sup>, J. B. dos Santos<sup>1</sup>, S. Damyanova<sup>2\*</sup>, J. M. C. Bueno<sup>1</sup>

<sup>1</sup> Departamento de Engenharia Química, Universidade Federal de São Carlos, Box 676, 13565-905 São Carlos, SP, Brazil

<sup>2</sup> Institute of Catalysis, Bulgarian Academy of Sciences, Acad. G. Bonchev St. Block 11, 1113 Sofia, Bulgaria

Received October 10, 2015; Revised November 17, 2015

Monometallic nickel and cobalt and bimetallic CoNi catalysts supported on MgAl<sub>2</sub>O<sub>4</sub> were synthesized. The electronic structure of the catalysts was characterized by in situ X-ray absorption near edge structure and extended X-ray absorption fine structure techniques. It was shown that the reduction of cobalt oxide species in Co-containing samples involved two reduction steps: the first one is reduction of Co<sub>3</sub>O<sub>4</sub> to CoO and the second one is transformation of CoO to Co<sup>0</sup>. For the bimetallic CoNi system, there was a coexisting of Co<sup>3+</sup>, Co<sup>2+</sup>, and Co<sup>0</sup>, as the first step was completed at a higher reduction temperature of 750°C. The presence of cobalt in the bimetallic CoNi catalyst suppressed the reduction of nickel oxide species at lower temperatures. Different reaction pathways were running in parallel during ethanol steam reforming as revealed by product distribution changes as a function of reaction temperature. The last one was related to a change of the fractions of the oxidic and metallic Co and Ni species under reaction conditions. At a low reaction temperature of about 400°C, the highest selectivity to hydrogen was observed with the bimetallic CoNi catalyst due to an intimate contact between cobalt and nickel, which stabilizes catalytically active metallic centres.

**Keywords:** CoNi catalyst, hydrogen, ethanol steam reforming, XANES, EXAFS.

### INTRODUCTION

Recent developments indicate that in the near future hydrogen will be used largely as a secondary energy carrier to produce electricity for mobile and small-to-medium scale stationary applications [1]. Hydrogen is an ideal energy carrier for sustainable energy development because the only product upon its burning is water. Hydrogen has the potential to solve two major challenges: restrict dependence on imported petroleum and reduce pollution and greenhouse emissions. Currently hydrogen is mainly produced from a fossil source (natural gas) that gives large amounts of CO<sub>2</sub> emissions. Developing technologies based on renewable resources have received much attention due to increasing costs of fossil resources, possibilities to carry out processes in more friendly conditions, and environmental appeal. Bioethanol, produced by biomass fermentation, is a promising feedstock for hydrogen production. Ethanol is advantageous over other conventional substrates because it is readily available, easy to obtain from biomass and to transport, CO<sub>2</sub> neutral and safe to handle. Ethanol steam reforming (ESR) (Eq. 1) is one of the possible industrial processes for hydrogen production:



Depending on catalyst used and operating conditions employed, several reactions may run in parallel, such as ethanol decomposition, dehydrogenation and dehydration, methane reforming, water-gas shift (WGS) and hydrogenation reactions producing acetaldehyde, hydrogen, methane, carbon oxides, and ethylene [2].

One of the major problems in ESR is coke formation on the catalyst surface, which may take place via several processes, such as ‘Boudouard’ reaction [3], methane decomposition, and cracking of ethylene produced by ethanol dehydration [4]. Carbon deposition can be avoided at high reaction temperatures (> 400°C), by using suitable catalyst, support, and promoter. However, high reaction temperatures enhance formation of by-product carbon monoxide, due to thermodynamically favoured reverse WGS and dry methane reforming. It is well known that CO concentration in PEM fuel cell systems should be reduced to less than 50 ppm [5].

Ethanol can also be reformed at low reaction temperatures (300–400°C) giving a gaseous mixture of H<sub>2</sub>, CH<sub>4</sub>, carbon monoxide, and carbon dioxide. CO content can be significantly reduced by involving a WGS activity function in the catalyst for-

\* To whom all correspondence should be sent:  
E-mail: soniad@ic.bas.bg

mulation or by a decrease of CH<sub>4</sub> selectivity by retarding CO methanation.

The mechanism of ethanol steam reforming has been extensively studied. Catalysts based on Ni, Co, Ir, Pt, Pd, Rh, and Ru dispersed on different supports, such as Al<sub>2</sub>O<sub>3</sub>, CeO<sub>2</sub>, La<sub>2</sub>O<sub>3</sub>, ZrO<sub>2</sub>, TiO<sub>2</sub>, and MgO have been examined [6–9]. However, there are controversial opinions about the role of the surface oxidation state of metals in the different pathways of ESR reaction, carbon deposition, and catalyst deactivation [2]. It was proposed that some reaction pathways are favoured, depending on the nature of support, resulting in a different product distribution in the gas phase.

In this work, it was attempted to discuss the different reaction pathways of ESR over monometallic nickel and cobalt as well as over bimetallic CoNi catalysts as a function of metal composition and reaction temperature. MgAl<sub>2</sub>O<sub>4</sub> was used as a catalyst carrier due to its high basicity. A detailed characterization of the samples was performed to point structural and electronic modification of MgAl<sub>2</sub>O<sub>4</sub>-supported nickel catalyst by cobalt addition. X-ray adsorption near edge structure (XANES) and extended X-ray absorption fine structure (EXAFS) methods were used for sample characterization.

## EXPERIMENTAL

### Sample preparation

MgAl<sub>2</sub>O<sub>4</sub> carrier was prepared by sol-gel method described elsewhere [10]. MgAl<sub>2</sub>O<sub>4</sub>-supported nickel and cobalt catalysts were prepared by incipient wetness impregnation of carrier with aqueous solution of Ni(NO<sub>3</sub>)<sub>2</sub>·6H<sub>2</sub>O (Aldrich, 99%) and Co(NO<sub>3</sub>)<sub>2</sub>·6H<sub>2</sub>O (Aldrich, 99%), respectively. The obtained solids were dried and calcined in airflow at 110 and 500°C for 12 and 6 h, respectively. The total metal loading was 8 wt.%. The samples were labelled as 8Ni, 4Co4Ni, and 8Co, where numbers represent amount of respective metal.

### Sample characterization

XANES analyses were performed at the K edge of Co (7709 eV) and Ni (8333 eV) using D06A-DXAS beamlines of Brazilian Synchrotron Light Laboratory at Campinas. Each sample was first crushed and sieved to particle sizes smaller than 20 μm and pressed into self-supporting pellets. Then the pellets were placed inside a tubular quartz reactor equipped with refrigerated kapton windows that were transparent to the X-ray beam. Temperature-resolved XANES spectra were acquired during reduction of the samples, which was achieved by heating at a rate of 10 deg.min<sup>-1</sup> from room temperature

to 750°C, with a holding time of 60 min, under a 200 ml.min<sup>-1</sup> flow of H<sub>2</sub>/He (5 vol.%). Energy calibration of the XANES spectra was performed by means of open source ATHENA/IFEFFIT software. A linear combination analysis was performed using Co<sup>0</sup>, CoO, Co<sub>3</sub>O<sub>4</sub>, Ni<sup>0</sup>, and NiO references [10].

In situ XANES spectra at the K edge of cobalt and nickel catalysts under ethanol steam reforming conditions were realized. The reactor with samples reduced at 750°C was cooled to room temperature under He flow and then switched to a flow of 3.9 ml.min<sup>-1</sup> of ESR mixture (water/ethanol at a molar ratio of 3:1), diluted in 133 ml.min<sup>-1</sup> of helium. The samples were heated from room temperature to 750°C at 10 deg.min<sup>-1</sup> and the XANES spectra were acquired 10 min after reaching a steady state.

EXAFS analyses at the K edge of Co (7709 eV) and Ni (8333 eV) were performed at the D04B-XAFS1 beamlines of LNLS. A general description of these beamlines can be found elsewhere [11]. The samples placed in the quartz reactor were reduced under 200 ml.min<sup>-1</sup> flow of H<sub>2</sub>/He (5 vol.%) by heating to 750°C at a heating rate of 10 deg.min<sup>-1</sup>. The samples remained at the reduction temperature for 1 h followed by acquisition of EXAFS spectra at room temperature. Background subtraction, normalization, and alignment of the EXAFS data were performed by the ATHENA/IFEFFIT software [12]. Structural parameters were obtained from a non-linear least squares fitting of the EXAFS data processed by ARTE-MIS/IFEFFIT software [12]. Coordination numbers (CN) were fixed for all references (Co<sup>0</sup>, CoO, Ni<sup>0</sup>, and NiO) and floated for the samples. Average interatomic distance (R) and structural Debye-Waller factor ( $\Delta\sigma_s^2$ ) values were allowed to float during the fitting. Table 1 provides fitting results of EXAFS spectra acquired at the K edge of Co and Ni of the samples reduced at 750°C.

**Table 1.** EXAFS parameters for reduced samples at 750°C.

Sample	Metal-metal		Metal-oxygen	
	CN	R(Å)	CN	R(Å)
Ni/NiO	12	2.48 ± 0.002	6	2.093 ± 0.003
Co/CoO	12	2.496 ± 0.003	6	2.130 ± 0.020
8Ni	9.6 ± 0.5	2.485 ± 0.001		
4Co4Ni	6.7 ± 0.3	2.481 ± 0.001	1.0 ± 0.1	1.949 ± 0.006
4Co4Ni	6.5 ± 0.6	2.485 ± 0.002	2.2 ± 0.9	1.978 ± 0.021
8Co	3.4 ± 0.2	2.490 ± 0.002	3.0 ± 0.2	1.973 ± 0.005

### Ethanol steam reforming reaction

The steam reforming of C<sub>2</sub>H<sub>5</sub>OH was carried out in a vertical fixed-bed reactor made of quartz tube under atmospheric pressure at temperatures of 250–750°C with a molar H<sub>2</sub>O to C<sub>2</sub>H<sub>5</sub>OH ratio of 3/1.

Catalyst loaded sample was 120 mg. Before reaction test, the catalyst was reduced in situ by heating at 750°C in a 10% H<sub>2</sub>/N<sub>2</sub> flow at a rate of 10 deg.min<sup>-1</sup> and keeping the temperature for 1 hour. The reaction products were analysed by a VARIAN 3400CX gas chromatograph equipped with a Chromosorb 102 packed column, while hydrogen was detected by mass spectrometry (Preiffer PrismaPlus).

## RESULTS AND DISCUSSION

### *XANES analysis*

An insight regarding metal oxidation state of metal components in MgAl<sub>2</sub>O<sub>4</sub>-supported monometallic Co(Ni) and bimetallic CoNi samples was investigated by in situ temperature-resolved XANES spectroscopy at K-edge of nickel and cobalt during sample reduction under hydrogen atmosphere up to 750°C. The percentage change of nickel and cobalt species in monometallic and bimetallic CoNi systems is shown in Fig. 1. There is no significant alteration in percentage of Ni species in the Ni sample at a low reduction temperature (up to 300°C). A change that is more visible is observed above 300°C: the percentage of NiO species decreases on increasing the reduction temperature, while that of metallic nickel (Ni<sup>0</sup>) component is increased. The reduction of Ni oxide species on the surface of the bimetallic CoNi system is characterized by a higher reduction temperature compared to that of the Ni sample (above 400°C). The latter suggests that the presence of cobalt suppresses nickel oxide reduction at lower temperatures, which is possibly caused by coexistence of Co<sup>3+</sup>, Co<sup>2+</sup>, and Co<sup>0</sup> ions (see below). This could be related to a strong interaction between nickel and cobalt, probably due to formation of a phase similar to NiCo<sub>2</sub>O<sub>4</sub> [13].

The reduction process of cobalt oxide species involves two reduction steps, as seen in Fig. 1: reduction of Co<sub>3</sub>O<sub>4</sub> to CoO and transformation of CoO to metallic cobalt (Co<sup>0</sup>). Co<sub>3</sub>O<sub>4</sub> reduction to CoO for the Co sample is finished at 410°C with a maximum percentage of CoO (95%) achieved at this temperature. The maximum rate of transformation of Co<sub>3</sub>O<sub>4</sub> to CoO started at the inflection point of the CoO percentage curve at 349°C (Fig. 1). The second reduction process of CoO to Co<sup>0</sup> has occurred at a temperature higher than 410°C.

For the bimetallic CoNi sample, inflection point temperature decreases from 349 to 332°C (Fig. 1). There is a coexisting of Co<sub>3</sub>O<sub>4</sub> → CoO and CoO → Co<sup>0</sup> transitions. The maximum percentage of CoO (67%) occurs at 453°C accompanied with the presence of Co<sub>3</sub>O<sub>4</sub> (18%). The first step of CoNi reduc-

tion is finished at a higher temperature of 750°C compared to monometallic Co (Fig. 1). It is interesting to note that both the CoO and Co<sup>0</sup> species in the Co-containing samples are present at the end of reduction process (Fig. 1). In addition, the fraction of metallic Co in the monometallic Co is high at a lower reduction temperature interval (300–500°C) as well as at the end of reduction process.

Reduction of Co<sup>2+</sup> species to Co<sup>0</sup> for the bimetallic system starts at a lower temperature (300°C) if compared to the monometallic Co sample (360°C). The latter is due to H<sub>2</sub> activation over the surface of metallic nickel species as the hydrogen atoms are transferred to cobalt oxide by spillover effect. It can be concluded that Co oxide is more easily reduced to Co<sup>0</sup> in the presence of nickel.

The percentage change of oxidic and metallic Co and Ni species in the monometallic and bimetallic systems as a function of reaction temperature up to 750°C during ethanol steam reforming reaction was analysed by in situ XANES-ESR at K edge of Ni and Co, as seen in Fig. 2. There is some equilibrium for Co<sup>0</sup> and Co<sup>2+</sup> species in the monometallic Co sample up to a reaction temperature of about 450°C and then the fraction of CoO species decreases at higher temperatures, while that of Co<sup>0</sup> increases. For both Co-containing catalysts, CoO is present at the end of reaction, whereas with the Ni-containing samples a small portion of NiO is detected only for monometallic nickel. The Ni sample exhibits a high amount of metallic nickel species (80%) at the beginning of reaction, which reaches 100% with increasing the reaction temperature to 500°C. The behaviour of the bimetallic CoNi system is different in relation to the monometallic systems. At the beginning of reaction up to 200°C the fraction of nickel oxide species (35%) for CoNi is higher than that observed for monometallic Ni (16%), which indicates that metal particle oxidation takes place at low reaction temperatures in the presence of cobalt. Metallic nickel fraction in CoNi increases at the expense of cobalt oxide species at a reaction temperature over 300°C. Above 400°C the NiO in the bimetallic system is totally reduced to Ni<sup>0</sup> (100%) (Fig. 2).

### *EXAFS analysis*

Magnitudes of the Fourier transformation of each sample together with the corresponding fits are shown in Fig. 3. Results of the fitting analysis in terms of coordination number, CN, interatomic distance, R, for references and samples are summarised in Table 1. The absorption spectra (Fig. 3) indicate that supported nickel and cobalt oxide species are not fully reduced after reduction at 750°C.

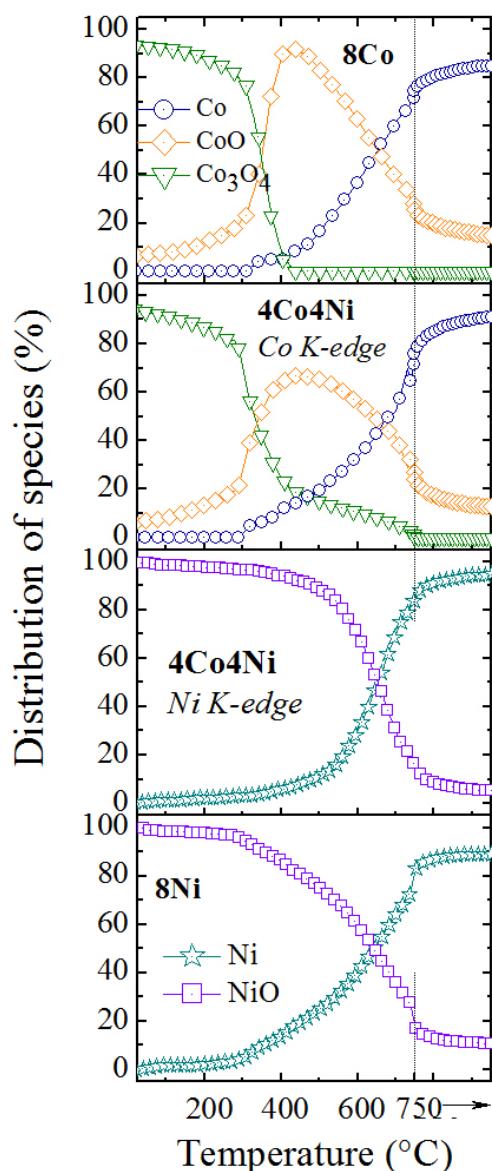


**Fig. 1.** Percentage change of species as a function of reduction temperature defined by in situ temperature-resolved XANES spectra of monometallic Co and Ni and bimetallic CoNi samples during reduction.

Both peaks of Co K-edge spectra at around 1.5 and 2.2 Å signify Co-O and Co-Co distances, respectively [14]. Peaks of Ni K-edge spectra at about 1.5 and 2.2 Å mean the atomic distance of Ni-O and Ni-Ni, respectively [15]. It should be noted that the values of the EXAFS parameters for references CoO, NiO, Co<sup>0</sup>, and Ni<sup>0</sup> are in agreement with those reported in the literature. Values of interatomic distances  $R_{\text{Ni-Ni}}$  and  $R_{\text{Co-Co}}$  for reduced samples related to the Ni-Ni distance in bulk Ni<sup>0</sup> and Co-Co distance in bulk Co<sup>0</sup>, respectively, indicate that the local structure of supported Ni and Co

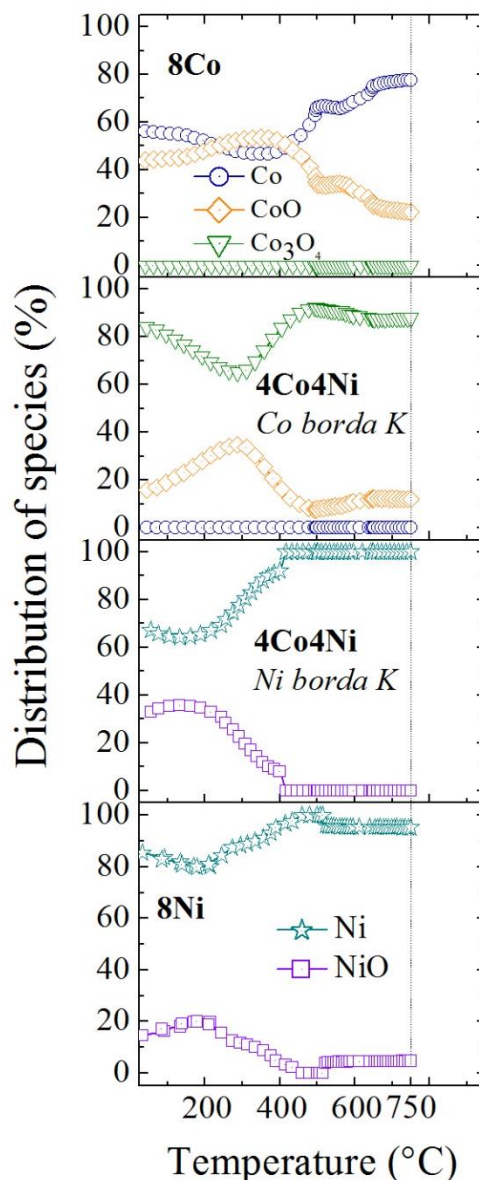


**Fig. 2.** Percentage change of species as a function of reaction temperature defined by in situ temperature-resolved XANES spectra of monometallic Co and Ni and bimetallic CoNi catalysts under ethanol steam reforming.

species is similar to that of the bulk samples. Co-Co and Ni-Ni atomic distances for the bimetallic CoNi system are lower compared to those of monometallic Co and Ni, which implies a strong interaction between the cobalt and nickel species. A decrease of the CN value from 9.6 to 6.7 for Ni and CoNi, respectively, is also evidence for a strong Co-Ni interaction. The highest CN value for the monometallic Ni sample is associated with Ni particle agglomeration on the MgAl<sub>2</sub>O<sub>4</sub> support. The Ni-O bond distance for Ni was not found, since the EXAFS technique is limited to large particles.

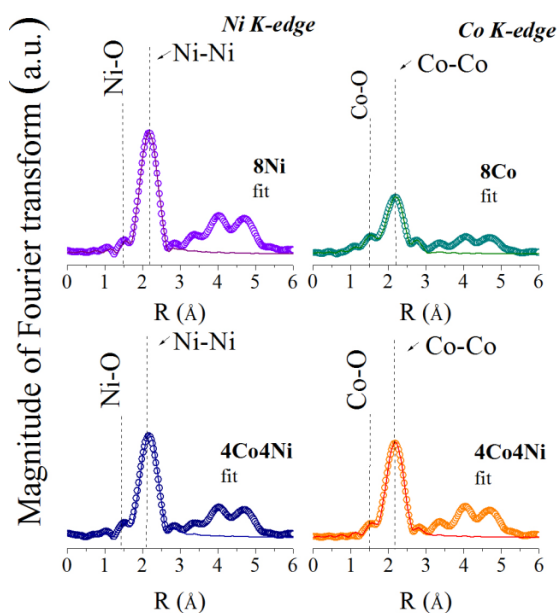


**Fig. 3.** EXAFS results at K edge of Co and Ni for reduced monometallic cobalt and nickel and bimetallic CoNi samples.

The Co sample has the smallest metallic nucleus revealed by the lowest CN value of Co-Co (3.4) (Table 1). In addition, the reduced monometallic Co catalyst possesses the highest oxidized surface shown by the highest CN value of Co-O (3.0, Table 1). The monometallic Co sample manifests the lowest Co-Co coordination number (3.4) to which cor-

responds the highest Co-O coordination number (3.0) that means more cobalt oxide species (Table 1). Changes in coordination number and interatomic distance of the bimetallic CoNi system relative to monometallic samples indicates a strong interaction between Ni and Co atoms that leads to a change of the electronic structure. It has been shown [16] that nickel species preferentially insert into octahedral sites in  $\text{Co}_3\text{O}_4$  spinel structure resulting in formation of tetrahedrally coordinated cobalt species in a structure similar to  $\text{NiCo}_2\text{O}_4$  spinel.

#### Catalytic test reaction

The effect of catalyst composition and metal component oxidation state on the catalytic performance of  $\text{MgAl}_2\text{O}_4$ -supported monometallic Co and Ni and bimetallic CoNi catalysts at various reaction temperatures was studied by means of ESR. Results are summarised in Fig. 4, where ethanol conversion and products distribution as a function of reaction temperature are shown. For all samples ethanol conversion increased on increasing the reaction temperature, as the maximum value of 100% was reached for the bimetallic CoNi catalyst at a lower reaction temperature of  $450^\circ\text{C}$  accompanied by the highest selectivity to hydrogen (70%). Higher temperatures were required for monometallic 8Ni ( $600^\circ\text{C}$ ) and 8Co ( $500^\circ\text{C}$ ) to achieve conversions over 90%.

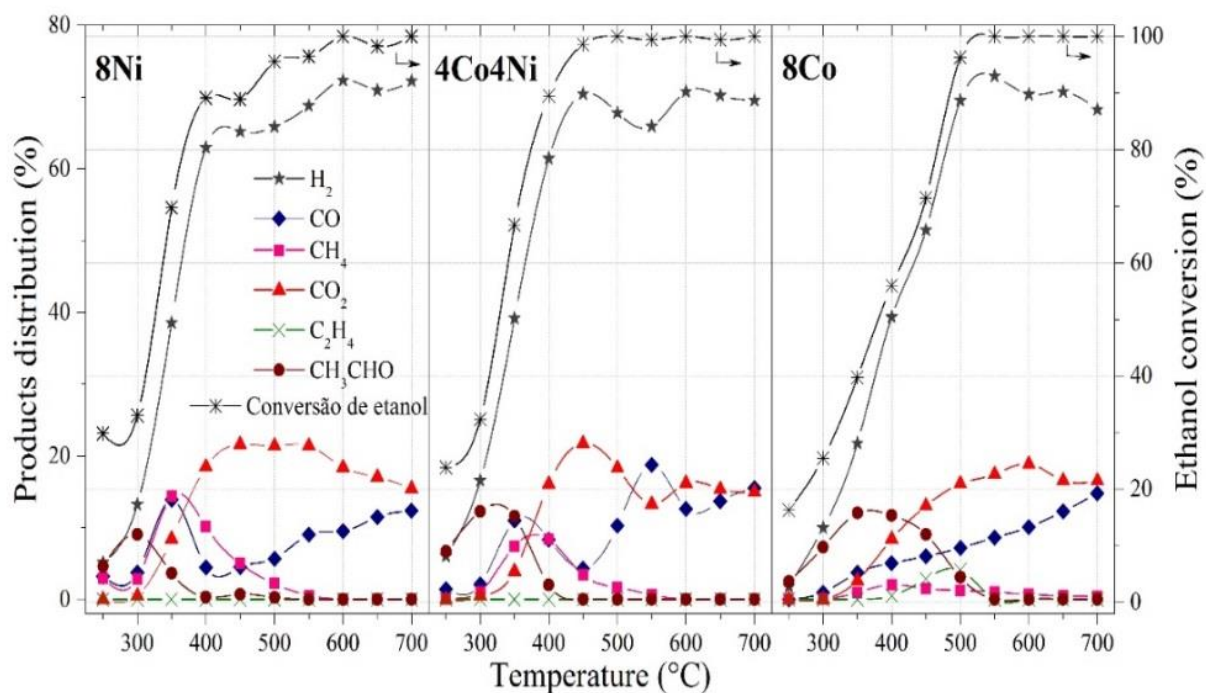
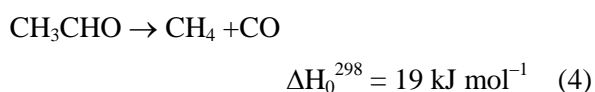
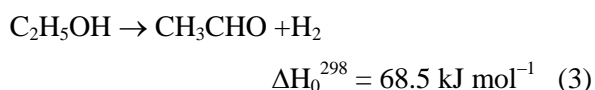
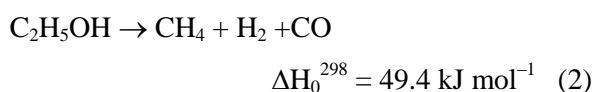
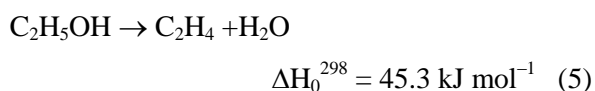


**Fig. 4.** Products distribution as a function of reaction temperature in ethanol steam reforming over monometallic cobalt and nickel and bimetallic CoNi catalysts.

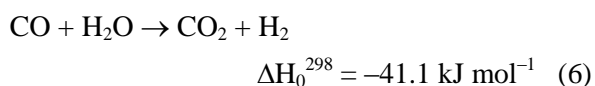
Reaction pathways of ethanol steam reforming at lower temperatures strongly depended on the capacity of the active metals to break the C-C bond in ethanol molecule. Over the Ni catalyst, at a low reaction temperature of 300°C ethanol was first dehydrogenated to acetaldehyde and hydrogen. By increasing the temperature up to 350°C, in parallel to hydrogen abstraction from the ethanol molecule, C-C bond scission and acetaldehyde decomposition were also observed resulting in formation of CH<sub>4</sub>, CO, and H<sub>2</sub> at a CO to CH<sub>4</sub> ratio of about unity. The production of H<sub>2</sub>, CH<sub>4</sub>, and CO may be attributed to ethanol decomposition, which can occur either directly (Eq. 2) or via intermediate formation of acetaldehyde as a sum of reactions (Eq. 3) and (Eq. 4) [3]:



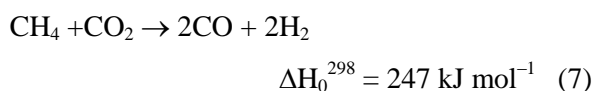
Traces of ethylene (< 0.05%) were detected as the formation of this product might take place via the dehydration reaction (Eq. 5):



CO selectivity for the Ni catalyst was comparable to that of hydrogen at 350°C, while at a higher temperature it decreased substantially. Contrary to this, raising the temperature above 400°C led to an increase in CO<sub>2</sub> production due to water-gas shift reaction (WGSR) (Eq. 6), the latter being caused by increased number of nickel metal centres, as seen in Fig. 2:



In the case of Ni catalyst, a maximal concentration of CH<sub>4</sub> may be associated with increasing the CO concentration up to 350°C, which indicates that ethanol decomposition reaction (Eq. 4) takes place on metallic nickel sites. Above 500°C, CH<sub>4</sub> is completely converted to CO and H<sub>2</sub> by dry methane reforming reaction (Eq. 7):



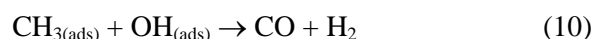
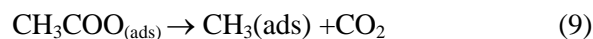
Detected decrease of CO<sub>2</sub> production at a temperature over 550°C can be related to occurrence of reverse WGSR. Above 500°C, H<sub>2</sub> and CO fractions continue to increase showing that ethanol steam reforming (Eq. 1) is dominating (Fig. 4).

Up to 300°C, the Co catalyst exhibits the formation of acetaldehyde and hydrogen products only, which is mainly due to the ethanol dehydrogenation, involving O-H bond cleavage in ethanol molecule (Fig. 3). Over Co surface, however, in spite of the low concentrations of produced CO, CO<sub>2</sub>, and H<sub>2</sub> up to 400°C, a high amount of CH<sub>3</sub>CHO is still present due to the high concentration of the cobalt oxide species that decrease catalyst ability for C-C bond breaking. As was suggested [17] both the Co<sup>0</sup> and CoO species are active for partial oxidation of adsorbed ethoxide species to produce acetaldehyde. Above 400°C, there is an increase of the CO and CO<sub>2</sub> products formation that can be related to an increased fraction of metallic cobalt species. The latter is accompanied by a decrease in acetaldehyde formation. It should be noted that traces of CH<sub>4</sub> and C<sub>2</sub>H<sub>4</sub> were formed at temperatures within 350–500°C (Fig. 4).

For the Co catalyst, increased concentrations of CO<sub>2</sub> and CO up to 500°C can mainly be attributed to formation of acetate species, which can be oxidized to carbonate species and after that decomposed to CO<sub>2</sub> or CO [18, 19]. It could be proposed that the produced acetaldehyde over the 8Co catalyst is oxidized by OH groups of support as well as by the metal oxide species to form surface acetate species (Eq. 8) in agreement with Refs. [18, 19].



According to Dömök *et al.* [19] the acetate species can be decomposed to CH<sub>3(ads)</sub> species (eq. 9), which may further react with surface OH groups to produce CO and H<sub>2</sub> (Eqs. 9, 10):



The catalytic performance of the 4Co4Ni catalyst at lower temperatures is between that of the monometallic catalysts (Fig. 4). At lower temperatures acetaldehyde was mainly formed on the surface of the bimetallic system, however, its amount was much lower compared to that observed with the Co catalyst. This means a better reducibility of the bimetallic catalyst, as confirmed by XANES and EXAFS analyses. Above 300°C, the behaviour of CoNi is similar to that of Ni in spite of the lower amount of CH<sub>4</sub>.

## SUMMARY

The results show that applied MgAl<sub>2</sub>O<sub>4</sub> carrier was a suitable support for the monometallic cobalt and nickel and bimetallic CoNi catalysts for ethanol steam reforming. XANES and EXAFS analyses show that introduction of nickel to a cobalt catalyst caused a change of the electronic structure and improved the redox properties.

The main difference in catalyst performance is related to variations of CH<sub>3</sub>CHO, CH<sub>4</sub>, CO, and CO<sub>2</sub> products distribution at different reaction temperatures. The results demonstrate that the main reaction pathway for ethanol steam reforming over supported catalysts at low temperatures (up to 400°C) is ethanol dehydrogenation to acetaldehyde, which is further decomposed to methane, hydrogen, and carbon dioxide. WGS and reforming reactions dominate at higher reaction temperatures (above 400–450°C).

Different catalyst performance can be related to differences in electronic properties. Dominating agglomerated nickel metal particles in the monometallic Ni catalyst are responsible for high activity in hydrogenation of CH<sub>x</sub> radicals caused by C-C cleavage. In contrast to this, Co particles in the monometallic Co catalyst, probably smaller than 4 nm, could easily be oxidized by steam in ethanol steam reforming that causes a decrease of the number of active metal centres. The latter led to a lower catalyst capacity for C-C bond breaking and formation of acetaldehyde involving O-H bond scission. Introduction of nickel to cobalt catalyst caused a strong interaction between Co and Ni, which stabilized the oxidation state of cobalt to Co<sup>0</sup> in the bimetallic CoNi catalyst under reaction conditions, thus stabilizing the highest hydrogen selectivity at a lower reaction temperature.

*Acknowledgements:* The authors kindly acknowledge FAPESP and project FNI E02/16 for financial support and Brazilian Synchrotron Light Laboratory for XAS beamline experiments.

## REFERENCES

1. P. E. Dodds, I. Staffel, A. D. Hawkes, F. Li, F. Grünewald, W. McDowall, P. Ekins, *Int. J. Hydrogen Energy*, **40**, 2065 (2015).
2. D. Zanchet, J. B. O. Santos, S. Damyanova, J. M. C. Bueno, *ACS Catalysis*, **5**, 3841 (2015).
3. A. C. Basagiannis, P. Panagiotopoulou, X. E. Verykios, *Top. Catal.*, **51**, 2 (2008).
4. G. P. Szijjarto, A. Tompos, J. L. Margitfavi, *Appl. Catal. A: Gen.*, **1-2**, 417 (2010).
5. A. F. Ghenciu, *Curr. Opin. Solid State Mater. Sci.*, **6**, 389 (2002).
6. P. Ciambelli, V. Palma, A. Ruggiero, *Appl. Catal. B: Environ.*, **96**, 18 (2010).
7. Q. Shi, C. Liu, W. Chen, *J. Rare Earths*, **27**, 948 (2009).
8. A. Casanovas, C. Leitenburg, A. Trovarrelli, J. Llorca, *Catal. Today*, **138**, 187 (2008).
9. J. Sun, X.P. Qiu, F. Wu, W. T. Zhu, *Int. J. Hydrogen Energy*, **30**, 437 (2005).
10. C. N. Avila-Neto, J. W. C. Liberatori, A. M. da Silva, D. Zanchet, C. E. Hori, F. B. Noronha, J. M. C. Bueno, *J. Catal.*, **287**, 124 (2012).
11. H. C. N. Tolentino, A. Y. Ramos, M. C. M. Alves, R. A. Barrea, E. Tamura, J. C. Cezar, N. Watanabe, *J. Synchrotron Radiat.*, **8**, 1040 (2001).
12. J. Mustre de Leon, J. J. Rehr, S. I. Zabinsky, R. C. Albers, *J. Am. Chem. Soc.*, **113**, 5135, (1991).
13. S. Verma, A. Kumar, D. Pravarthana, A. Deshpande, S. B. Ogale, S. M. Yusuf, *J. Phys. Chem. C*, **118**, 16246 (2014).
14. Tae Hwan Lim, Sung June Cho, Hee Sung Yang, M. H. Engelhardt, Do Heui Kim, *Appl. Catal. A: Gen.*, **505**, 62 (2015).
15. J. Rosan, G. S. Hutchings, F. Jiao, *J. Catal.*, **310**, 2 (2014).
16. C. F. Windisch, C. J. Exarhos, R. R. Owings, *J. Appl. Phys.*, **95**, 5435 (2004).
17. E. Martono, J. M. Vohs, *J. Catal.*, **291**, 79 (2012).
18. S. M. Lima, A. M. Silva, L. O. O. Costa, G. Jacobs, B. H. Davis, *J. Catal.*, **268**, 268 (2009).
19. M. Dömök, M. Toth, J. Rasko, A. Erdöhelyi, *Appl. Catal. B: Environ.*, **69**, 262 (2007).

# ИЗУЧАВАНЕ НА НАНЕСЕНИ CoNi КАТАЛИЗАТОРИ ЗА РЕФОРМИРАНЕ НА ЕТАНОЛ С ВОДНА ПАРА С ПОМОЩТА НА РЕНТГЕНОВА АБСОРБЦИОННА СПЕКТРОСКОПИЯ

А. Брага<sup>1</sup>, Х. Б. Сантос<sup>1</sup>, С. Дамянова<sup>2\*</sup>, Х. М. К. Буено<sup>1</sup>

<sup>1</sup> Департамент по инженерна химия, Федерален университет на Сан Карлос, Сан Карлос, Бразилия

<sup>2</sup> Институт по катализ, Българска академия на науките, ул. „Акад. Г. Бончев“, бл. 11, 1113 София, България

Постъпила на 10 октомври 2015 г.; Преработена на 17 ноември 2015 г.

(Резюме)

Синтезирани са монометални никелови и кобалтови и биметални CoNi катализатори, нанесени върху носител MgAl<sub>2</sub>O<sub>4</sub>. Електронната структура на катализаторите е охарактеризирана *in situ* с помощта на рентгенова абсорбционна спектроскопия. Резултатите показват, че редукцията на кобалтово оксидни съединения в кобалт-съдържащи образци протича през два етапа: (а) редукция на Co<sub>3</sub>O<sub>4</sub> до CoO и (б) трансформиране на CoO до Co<sup>0</sup>. Едновременно присъствие на Co<sup>3+</sup>, Co<sup>2+</sup> и Co<sup>0</sup> се наблюдава за биметална CoNi система, като първият етап приключва при по-висока температура на редукция. Присъствието на кобалт в биметален CoNi катализатор не позволява редукцията на никелово оксидни съединения да протича при по-ниска температура. Различни етапи на реакцията протичат едновременно по време на реформинг на етанол с водна пара, изразено чрез разпределението на реакционните продукти като функция от температурата на реакцията. Това се дължи на изменението на концентрациите на металните частици и кислород-съдържащи съединения на кобалта и никела в условията на протичане на реакцията. Биметален CoNi катализатор показва най-висока селективност по водород при ниска температура на реакцията (около 400°C), което се отдава на близкия контакт между кобалта и никела стабилизиращ активните метални каталитични центрове.

## Nanosized cobalt oxides modified with palladium for oxidation of methane and carbon monoxide

S. Todorova<sup>1\*</sup>, A. Ganguly<sup>2</sup>, A. Naydenov<sup>3</sup>, H. Kolev<sup>1</sup>, I. Yordanova<sup>1</sup>, M. Shopska<sup>1</sup>, S. Mondal<sup>2</sup>, G. Kadinov<sup>1</sup>, S. Saha<sup>2</sup>, A. K. Ganguli<sup>2,4,5</sup>

<sup>1</sup> Institute of Catalysis, Bulgarian Academy of Sciences, Acad. G. Bonchev St., Bldg. 11, 1113 Sofia, Bulgaria

<sup>2</sup> Department of Chemistry, Indian Institute of Technology, Hauz Khas, New Delhi 110016, India

<sup>3</sup> Institute of General and Inorganic Chemistry, Bulgarian Academy of Sciences, Acad. G. Bonchev St., Bldg. 11, 1113 Sofia, Bulgaria

<sup>4</sup> Nanoscale Research Facility, Indian Institute of Technology, Hauz Khas, New Delhi 110016, India

<sup>5</sup> Institute of Nano Science & Technology, Habitat Centre, Phase – X, Mohali, Punjab, 160062, India

Received September 29, 2015; Revised October 20, 2015

Nanosized  $\text{Co}_3\text{O}_4$  oxide was prepared and modified with palladium. Catalyst samples were characterized by X-ray diffraction, X-ray photoelectron spectroscopy, transmission electron microscopy, temperature-programmed reduction, and diffuse reflectance infrared spectroscopy. The catalytic performance of the as synthesized materials was examined in the reactions of methane combustion and CO oxidation. Finely divided PdO particles were formed on the surface of the modified cobalt oxides.

Based on diffuse reflectance infrared spectroscopy investigations a Langmuir-Hinshelwood mechanism was proposed for the oxidation of carbon monoxide on the studied samples up to 150°C. A linearly adsorbed CO species was formed and involved in the reaction over Pd/ $\text{Co}_3\text{O}_4$  under these conditions. At a higher temperature, the palladium surface was mainly covered by dissociatively adsorbed oxygen and the reaction proceeded through the Eley-Rideal mechanism: chemisorbed oxygen atoms react with gaseous carbon monoxide. A Mars-van Krevelen mechanism cannot be excluded as well. Carbon dioxide was detected after introduction of a  $\text{CO}+\text{N}_2$  mixture into the cell, which indicates that CO oxidation proceeded most probably due to a reaction between carbon monoxide and lattice oxygen from PdO and/or  $\text{Co}_3\text{O}_4$ .

**Keywords:** Pd-modified nanosized  $\text{Co}_3\text{O}_4$  oxide, mechanism of CO oxidation, methane combustion.

### INTRODUCTION

The design of an effective and less expensive catalytic system for complete oxidation of methane and carbon monoxide is an important problem of modern environmental catalysis. Methane makes the second largest contribution to the global warming after carbon dioxide [1, 2]. Methane catalytic combustion has been extensively studied for emission control and power generation during the last decades. CO oxidation at low temperatures has attracted great attention because of its wide applications in exhaust gas treatment, automotive emission control, and CO preferential oxidation in hydrogen feed for use in proton exchange membrane fuel cells [3].

Supported palladium catalysts are widely accepted as the most active catalysts for both catalytic combustion of methane and low temperature oxidation of CO [3, 4]. Palladium has been used in three-way catalysts because of its superior oxidation properties in comparison with platinum and rhodium. Concern-

ing the methane oxidation reaction, the main drawback of the palladium catalysts is their deactivation at high temperatures. Thus, efforts are directed toward searching novel materials or for improving existing catalysts by better dispersion of Pd on catalytically active supports, such as premodified alumina, hexaaluminates, etc. [5–7].

The activity of palladium in the reaction of CO oxidation is dependent on particle size, morphology, and Pd-support interactions. Highly dispersed species are considered more active than large particles. The interfaces between metal and metal oxide phases probably provide active sites. The support could play a role as an oxygen-storage material and may take part in the reaction [8–10]. Recently, Jin *et al.* [11] reported a preparation technique for very active catalysts by depositing palladium on different mesoporous oxides.

The present work is aimed at developing highly active catalysts for CO oxidation and methane combustion by a suitable combination between Pd and nanosized cobalt oxide of controlled size, shape, and morphology.

\* To whom all correspondence should be sent  
E-mail: todorova@ic.bas.bg

## EXPERIMENTAL

### 2.1 Synthesis of nanosized $\text{Co}_3\text{O}_4$

Cobalt acetate was added to a mixture of double distilled water and ethanol at a 1:10 ratio in a beaker and the new mixture was stirred to get a clear solution. Liquor ammonia was added to this clear solution. It was then treated hydrothermally at 150°C for 3 h. The black colour precipitate was washed twice with ethanol and finally dried at 70°C [12].

### 2.2. Synthesis of Pd/ $\text{Co}_3\text{O}_4$

Cobalt oxide was modified with palladium to improve the catalytic activity. Before Pd deposition, the metal oxide was calcined in air at 450°C for 2 h. Samples were prepared by introduction of the metal oxide to an aqueous solution of  $\text{Pd}(\text{NO}_3)_2 \cdot 2\text{H}_2\text{O}$  to achieve 0.5 wt.% Pd/ $\text{Co}_3\text{O}_4$ . After the impregnation, a quick evaporation of the solvent was applied in order to coat the metal oxide particles by a thin layer of palladium [13]. The samples were finally calcined in air at 450°C for 2 h.

### 2.3. Catalyst characterization

The specific surface area of the supported catalyst samples was determined by low temperature adsorption of nitrogen according to the BET method using a Nova 1200 (Quantachrome) apparatus. Prior to measurements, the samples were degassed for 5 h at temperatures in the interval 70–150°C.

X-ray diffraction (XRD) patterns were obtained on a TUR M62 apparatus, HZG-4 goniometer with Bragg-Brentano geometry,  $\text{CoK}\alpha$  radiation, and Fe filter. XRD data processing was performed using the X'Pert HighScore program.

Temperature-programmed reduction (TPR) was carried out using a flow mixture of 10%  $\text{H}_2$  in argon at a flow rate of 10  $\text{ml}\cdot\text{min}^{-1}$  and a temperature ramp of 10  $\text{deg}\cdot\text{min}^{-1}$  up to 700°C. Prior to the TPR experiments, the samples were treated in argon flow at 150°C for 1 h.

X-ray photoelectron measurements were carried out on an ESCALAB MkII (VG Scientific) electron spectrometer at a base pressure in the analysis chamber of  $5 \times 10^{-10}$  mbar using a twin anode  $\text{MgK}\alpha/\text{AlK}\alpha$  X-ray source with excitation energies of 1253.6 and 1486.6 eV, respectively. The spectra were recorded at a total instrumental resolution (as it was measured by the FWHM of Ag  $3d_{5/2}$  photoelectron line) of 1.06 and 1.18 eV for  $\text{MgK}\alpha$  and  $\text{AlK}\alpha$  excitation sources, respectively. The energy scale has been calibrated by normalizing the C 1s line of adsorbed adventitious hydrocarbons to 285.0 eV. Spectra processing included a subtraction of X-ray satellites and Shirley-type background [14]. Peak

positions and areas were evaluated by a symmetrical Gaussian-Lorentzian curve fitting. The relative concentrations of the different chemical species were determined based on normalization of the peak areas to their photoionization cross-sections, calculated by Scofield [15].

High-resolution transmission electron microscopy (HRTEM) studies were carried out by using a FEI Technai G<sup>2</sup> 20 (200 kV) instrument. The samples were prepared by dispersion in ethanol and loading on a holey copper grid.

Carbon monoxide adsorption on Pd/ $\text{Co}_3\text{O}_4$  catalysts was studied *in situ* by diffuse reflectance infrared spectroscopy (DRIRS) using a Nicolet 6700 spectrometer equipped with a high temperature vacuum chamber installed in the Collector II accessory (Thermo Spectra-Tech). CO was adsorbed from  $\text{CO}+\text{N}_2$  or  $\text{CO}+\text{O}_2+\text{N}_2$  mixture flows at room temperature. Experiments were carried out on oxidized ('as prepared') catalysts pretreated in nitrogen at 350°C for 1 h.

### 2.4. Catalyst characterization

Catalytic activity tests were performed using an integrated quartz micro-reactor and mass spectrometer analysis system (CATLAB, Hiden Analytical, UK). Reactant gases were supplied through electronic mass flow controllers. The catalysts (particle sizes of 0.3–0.6 mm) were held between plugs of quartz wool in a quartz tubular vertical flow reactor ( $\phi = 6$  mm). CO and methane inlet concentrations in air were kept 600 and 900 ppm, respectively. External mass transfer limitations were minimized by working at gas hourly space velocities (GHSV) of 60 000  $\text{h}^{-1}$ .

## RESULTS AND DISCUSSION

Powder X-ray diffraction studies of the metal oxide nanoparticles suggest the formation of a cubic phase for cobalt oxide (PDF 01-080-1539) (Fig. 1).

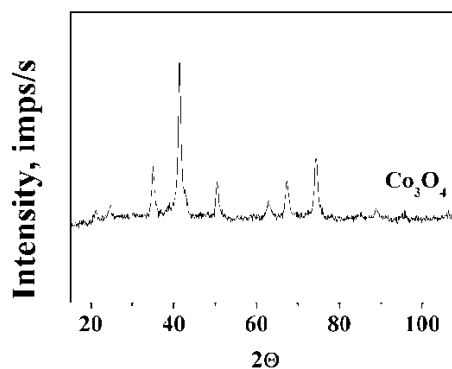
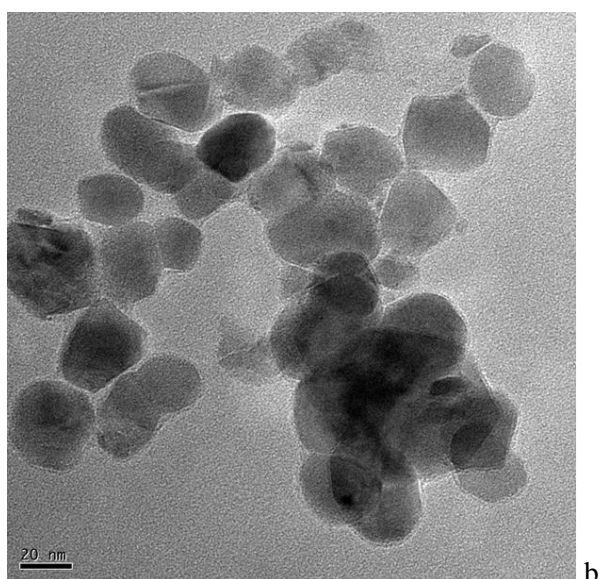
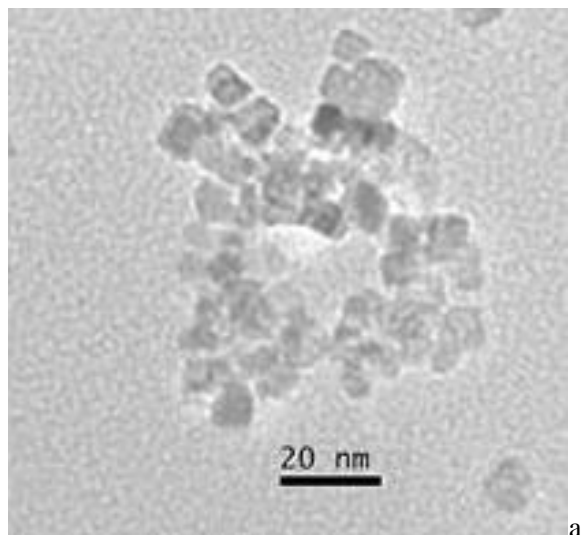


Fig. 1. XRD pattern of as synthesized metal oxide before calcination.

The size and morphology of the metal oxide were studied by TEM and the image shown in figure 2 reveals the formation of cube-shaped particles of cobalt oxide of ~8–10-nm size. These materials are characterised by high surface area of ~125 m<sup>2</sup>.g<sup>-1</sup> value, which makes them ideal for catalytic reactions.



**Fig. 2.** TEM images of cobalt oxide nanosized particles: a. as synthesized, b. after calcination

Palladium or palladium oxide were not detected in the XRD patterns after Pd deposition and following calcination. Co<sub>3</sub>O<sub>4</sub> particle size calculation, according to Scherrer equation and TEM images (Fig. 2B), showed about a two-fold increase in particle mean diameter after calcination. No additional increase in Co<sub>3</sub>O<sub>4</sub> particle sizes was observed after Pd deposition and following calcination (Table 1). A decrease in the specific surface area was found after treatment in air at 450°C for 2 h.

TPR profiles of the pure metal oxide after calcination and after Pd deposition are presented in figure 3.

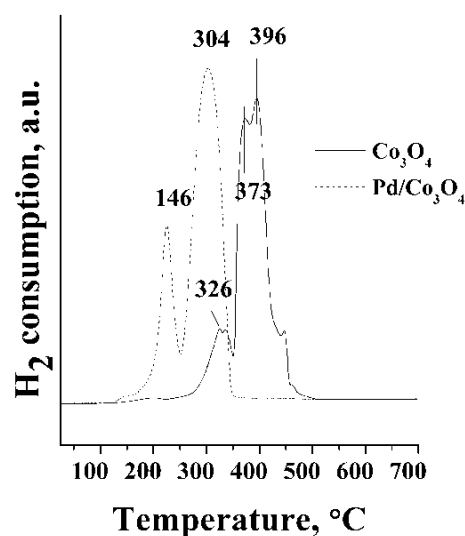


**Fig. 3.** TPR profile of cobalt oxides before and after palladium modification.

The reduction profile of pure cobalt oxide consists of two overlapping peaks at 326 and 336°C and other two peaks with maxima at about 373 and 396°C, accordingly. The reduction profiles of the Co<sub>3</sub>O<sub>4</sub> sample fit well within the stepwise reduction of the metal oxide (Co<sub>3</sub>O<sub>4</sub> → CoO → Co) [16]. Two reduction peaks, registered in both intervals, could be a result of a bimodal distribution of the cobalt oxide particles. A particle size effect on the TPR reduction profile was established: the smaller the particle size the lower the registered reduction temperature is. Okamoto et al. have found the same tendency for reduction of silica-supported Co<sub>3</sub>O<sub>4</sub> of different size [17].

Palladium introduction led to a significant decrease of the reduction temperature of Co<sub>3</sub>O<sub>4</sub>. Two major reduction peaks were detected during the reduction of a Pd/Co<sub>3</sub>O<sub>4</sub> sample. It is well known that a noble metal added to a metal oxide catalyst accelerates the reduction of the latter by supplying hydrogen via spillover from the prerduced noble metal particles to the metal oxide [18, 19]. It should be noted that a separate peak corresponding to the reduction of Pd oxide (if formed as a separate phase during the calcination) was not observed in our TPR experiments. Usually, a TPR peak of noble metal reduction in supported catalysts is registered at a temperature below 50°C and even well below the room temperature. Our results could be due to a low Pd content and a high Co<sub>3</sub>O<sub>4</sub>/Pd ratio resulting in a very small hydrogen consumption by the palladium

oxide compared to that detected with another metal oxide.

The chemical state of palladium and cobalt and the atomic concentrations of the different elements on the catalyst surface were studied by X-ray photoelectron spectroscopy (Figs. 4a and 4b). The XPS spectrum of Pd/Co<sub>3</sub>O<sub>4</sub> in the Co 2p region manifests a binding energy at 780.5 eV and a 2p<sub>3/2</sub>-2p<sub>1/2</sub> splitting of 15.4 eV that are characteristic of octahedral Co<sup>3+</sup> ions [20].

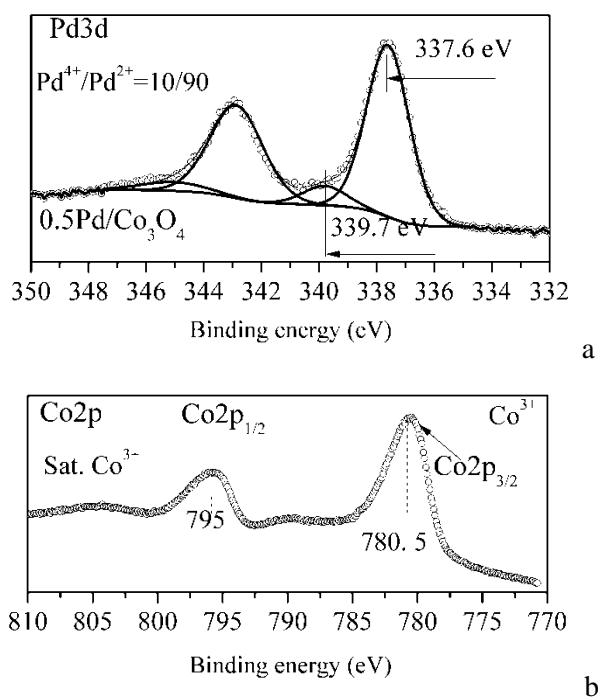


**Fig. 4.** XPS spectra of a sample after deposition of palladium and calcination at 450°C for 2 h:

a. Pd 3d region; b. Co 2p.

The binding energy in the range of 337.2–337.6 eV for a palladium-modified sample indicates the presence of PdO [21, 22]. A third component at 339.6 eV was observed for all samples. It was smaller than other detected components and contributed by 10–12% to the total Pd signal. This peak may be associated with Pd<sup>4+</sup> from PdO<sub>2</sub> [22]. Pd<sup>4+</sup> ions in PdO<sub>2</sub> are highly unstable, but according to Barr [23] the palladium metal particles, exposed long enough to air, form palladium oxide with outermost layers of PdO<sub>2</sub> or Pd(OH)<sub>4</sub> on their surface.

In situ DRIRS was used as one of the most powerful methods to obtain information about the type of the active sites, their stability and reactivity, chemical state of the surface under static and dynamic conditions in a wide temperature interval, and after various pretreatments. The most frequently used probe molecule to study supported catalysts is carbon monoxide due to the sensitivity of the stretching  $\nu(\text{C}-\text{O})$  vibration to the chemical state of

the metal atom(s) to which it is coordinated. The IR spectra provide knowledge of the relative adsorption strength that is closely related to the catalytic activity of the respective sites and allow understanding of the CO oxidation reaction mechanism [24, 25]. DRIRS experiments were carried out to investigate both the CO adsorption on the surface of Pd supported on cobalt oxide and the behaviour of adsorbed CO surface species in flow mixtures of CO+N<sub>2</sub> and CO+N<sub>2</sub>+O<sub>2</sub>. Infrared spectra of CO adsorbed on Pd/Co<sub>3</sub>O<sub>4</sub> samples are displayed in figures 5 and 7 and the assignment of the IR bands is given in Table 2.

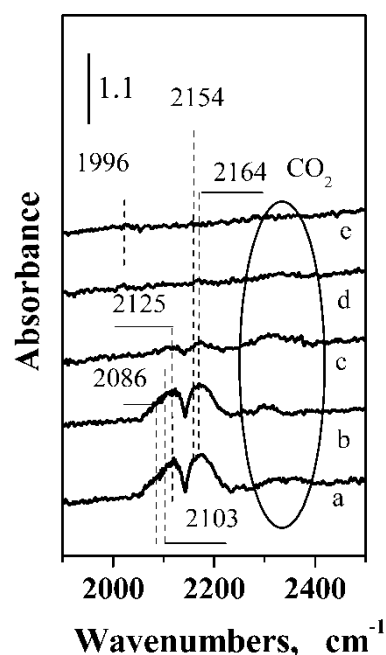


**Fig. 5.** DRIRS spectra of Pd/Co<sub>3</sub>O<sub>4</sub> after: a. 10 min in a flow mixture of 10% CO in nitrogen at room temperature; b. a stay for 2 h in a mixture of 10% CO in nitrogen at room temperature; c. a stay for 18 h in a mixture of 10% CO in nitrogen at room temperature; d. desorption of CO for 1 min in nitrogen flow; e. desorption for 11 min in nitrogen flow.

**Table 2.** Assignment of IR bands ( $\nu\text{C}-\text{O}$ ) of adsorbed CO species [26, 30].

Sample	Infrared band assignment			
	Pd <sup>2+</sup> -CO	Pd <sup>1+</sup> -CO	Pd <sup>0</sup> -CO	(Pd <sup>0</sup> ) <sub>2</sub> -CO
Pd/Co <sub>3</sub> O <sub>4</sub>	2154 cm <sup>-1</sup>	2125 cm <sup>-1</sup>	2086 cm <sup>-1</sup> 2103 cm <sup>-1</sup>	1996 cm <sup>-1</sup>

Bands at 2154, 2125, 2086, 2103, and 1996 cm<sup>-1</sup> were registered in the IR spectra of the calcined Pd/Co<sub>3</sub>O<sub>4</sub> sample after admission of the flow mixture at room temperature. They could be assigned to linearly bonded CO species on Pd<sup>2+</sup>, Pd<sup>+</sup>, and Pd<sup>0</sup> and bridge bonded CO to Pd<sup>0</sup>, respectively [26–29]. According to literature data,

the formation of mono carbonyl CO–Pd<sup>0</sup> species is manifested by a band in the frequency interval of 2100–2050 cm<sup>-1</sup> [26–29]. In our experiments, this band appeared at a slightly higher frequency of 2103 cm<sup>-1</sup>. One possible explanation is that Pd has a partial positive charge (Pd<sup>δ+</sup>) due to a strong interaction between finely divided palladium and the support. CO adsorption on metallic palladium with weak electron-donor properties shifts the band to higher wavenumbers. A band at the same position has been observed for CO adsorption on Pd-ZSM-5 [30]. The bands of linearly bonded CO to Pd<sup>2+</sup> and Pd<sup>+</sup> species at 2154 and 2125 cm<sup>-1</sup>, respectively, are overlapped by those of the gaseous CO (Figs. 5 and 7). In all spectra, the bands in the region 2300–2400 cm<sup>-1</sup> are assigned to gaseous carbon dioxide. XPS data obtained for the catalysts before CO adsorption revealed that the main state of palladium was Pd<sup>2+</sup> and partly that of Pd<sup>4+</sup>. IR bands due to CO adsorbed on Pd<sup>+</sup> and Pd<sup>0</sup> after introduction of a CO+N<sub>2</sub> mixture indicate a partial reduction of the palladium surface even at room temperature. However, under these conditions the reduction of the palladium particles in the outermost layer(s) of their surface was not complete which was confirmed by very low intensity of the bands at about 1996 cm<sup>-1</sup> ascribed to bridge-bonded CO to Pd<sup>0</sup> in the spectra of Pd/Co<sub>3</sub>O<sub>4</sub>. A non-well resolved band at ~2164 cm<sup>-1</sup> in the IR spectrum of Pd/Co<sub>3</sub>O<sub>4</sub> has been assigned to CO adsorbed on Co<sup>2+</sup> ions [31]. Weak bands due to CO<sub>2</sub> in the gas phase registered in the spectra of cobalt oxide in Figs. 5a and 5b suggest some reduction process not only with Pd on the surface of the catalyst but, also, to some extent with Co<sup>3+</sup> to Co<sup>2+</sup>.

Carbon dioxide detected in the cell after introduction of the CO+N<sub>2</sub> mixture indicates that CO oxidation occurred at room temperature most probably due to a reaction between CO and lattice oxygen from PdO and/or cobalt oxide. The increase in intensity of the bands due to gaseous CO<sub>2</sub> accompanied by an intensity decrease and even disappearance of the bands of the various adsorbed CO species is visible in the IR spectra of the catalyst during a 20-h stay of the samples in a mixture of CO+N<sub>2</sub> (Fig. 5c). This experiment was carried out to follow the stability of the CO species adsorbed on the surface metal ions in the Pd/Co<sub>3</sub>O<sub>4</sub> catalyst and proved their low stability. The bands assigned to CO–Pd<sup>1+</sup> and CO–Pd<sup>2+</sup> species (2125 and 2154 cm<sup>-1</sup>, respectively) disappeared completely in nitrogen flow at room temperature.

The catalytic properties of palladium-modified cobalt oxide in the reactions of CO oxidation and complete oxidation of methane are illustrated in

figure 6. The catalytic activity of the pure cobalt oxide in both reactions is given for comparison. H<sub>2</sub>O and CO<sub>2</sub> were the only detectable reaction products of the methane oxidation. In a recent investigation [32] we established that the catalytic performance of Pd/Al<sub>2</sub>O<sub>3</sub> in methane combustion could be improved significantly by addition of metal oxides of Ni, Co and mixed Co-Ce, Co-Mn binary oxides. This effect was attributed to formation of highly dispersed and well-stabilized Pd or PdO clusters on the support. A close contact between the palladium and a metal oxide may increase the concentration of surface oxygen species around the palladium thus stabilizing PdO on the surface. We established that the most promising catalysts were those that contain cobalt and nickel. Results of the present study supplement our previous statement, namely, that a combination between palladium and cobalt oxide could be used to prepare highly active catalysts for methane combustion.

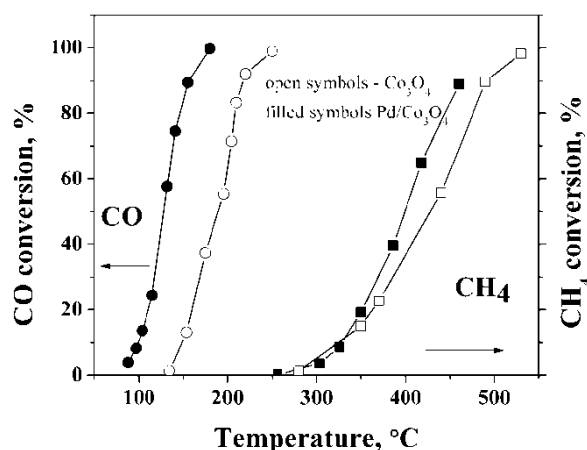
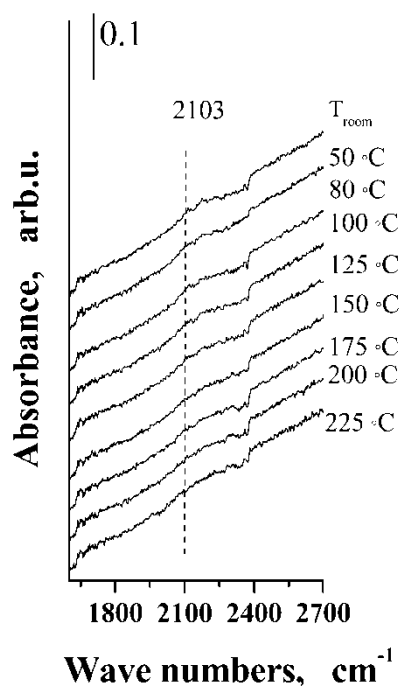


Fig. 6. Carbon monoxide and methane oxidation over Co<sub>3</sub>O<sub>4</sub> and Pd/Co<sub>3</sub>O<sub>4</sub> catalysts.

In order to throw some light on the reaction mechanism, DRIRS was used to examine the oxidation of carbon monoxide in a flow of CO+O<sub>2</sub>+N<sub>2</sub> (1% CO, 10% O<sub>2</sub>) mixture at various temperatures (Fig. 7). During the flow experiments at room temperature, the CO oxidation over Pd/Co<sub>3</sub>O<sub>4</sub> produced only one band due to linear CO–Pd<sup>0</sup> species. The bands of gaseous CO<sub>2</sub> were hardly noticeable under these conditions and their intensity increased above 150°C.

It is known that slow reaction rates of CO oxidation over supported Pd catalysts at a low temperature are a result of strong CO adsorption, which inhibits oxygen dissociative adsorption on the same sites [26, 33]. To enhance the catalytic activity at a lower temperature, supports like CeO<sub>2</sub>, SnO<sub>2</sub>, and MnO<sub>x</sub>, which can supply active oxygen under these conditions, have been used. Thus, noble

metals supported on these supports exhibited a higher activity at low temperatures, which was suggested to be a result of oxygen provided by the support to the metal [33].



**Fig. 7.** DRIRS spectra of CO adsorption on Pd/Co<sub>3</sub>O<sub>4</sub> in a flow mixture of 1% CO + 10% O<sub>2</sub> in nitrogen at various temperatures.

DRIRS data on CO adsorption from a mixture of 10 vol.% CO in nitrogen or 1 vol.% CO + 10 vol.% O<sub>2</sub> in nitrogen indicate the following. Firstly, the CO adsorption on Pd/Co<sub>3</sub>O<sub>4</sub> is not stable at ambient temperature because the bands of different surface carbonyls disappeared shortly after blowing purge in nitrogen flow), and secondly part of the palladium is in reduced (Pd<sup>0</sup>) state under oxidation conditions.

The Langmuir-Hinshelwood (L-H) mechanism has been well established as the dominant reaction pathway when CO is the main surface species [34]. The rate-determining step is reaction between adsorbed CO and oxygen species. As was mentioned above, linear bonded CO species were observed in the IR spectra of a Pd/Co<sub>3</sub>O<sub>4</sub> sample during CO oxidation up to a temperature of 150°C. Based on this it is possible to suggest that the reaction mechanism is of L-H type including these linearly adsorbed CO species and oxygen species. The CO species are not stable at elevated temperatures; hence, a larger part of the Pd surface will be accessible for O<sub>2</sub> adsorption and next dissociation. Thus, the chemisorbed oxygen atoms will react with the gaseous CO through an Eley-Rideal (E-R) type mechanism. A Mars van Krevelen reaction mechanism involving interaction between CO adsorbed on

a noble metal and oxygen from the oxide components is also possible as was demonstrated in our DRIRS experiments with reaction mixtures of different nature: reduction (CO+N<sub>2</sub>) and oxidizing (CO+O<sub>2</sub>+N<sub>2</sub>) combinations that give rise to carbon dioxide in the gas phase.

## CONCLUSION

Finely divided PdO particles have been found to occur on the surface of Co<sub>3</sub>O<sub>4</sub>. A DRIRS investigation revealed three possible reaction mechanisms of CO oxidation over the studied catalysts: a Langmuir-Hinshelwood pathway, an Eley-Rideal mode, and a bifunctional reaction path involving an interaction between CO species adsorbed on the noble metal and oxygen entities from a metal oxide (PdO and/or Co<sub>3</sub>O<sub>4</sub>). The Langmuir-Hinshelwood mechanism was proposed for CO oxidation over the studied samples at temperatures up to 150°C. Linearly adsorbed CO species are formed and involved in the reaction over Pd/Co<sub>3</sub>O<sub>4</sub>.

At a higher temperature, the palladium surface is covered predominantly by dissociatively adsorbed oxygen and the reaction proceeds through the E-R mechanism: chemisorbed oxygen atoms react with gaseous carbon monoxide.

*Acknowledgements:* The authors thank the Bulgarian Science Fund for financial support through Contract DFNI/India 01/8 and Contract TO1/6. A.K.G. thanks Department of Science & Technology (DST), Government of India, for funding the Indian-Bulgarian project and Department of Electronics & Information Technology (DeiT<sub>y</sub>) and IIT Delhi for setting up the nanoscale research facility. A.G. thanks DeiT<sub>y</sub> for financial support.

## REFERENCES

1. Federal Register, Vol. 78, No. 63 / Tuesday, April 2, 2013 / Proposed Rules, Environmental Protection Agency, 40 CFR Part 98, 2013.
2. European Commission Global Methane Reduction Actions, Ref. Ares (2013) 2843722 – 06/08/2013
3. M. Jin, J.-N. Parka, J. Kuk Shona, J. H. Kima, Z. Li, Y.-K. Park, J. M. Kima, *Catal. Today*, **185**, 183 (2012).
4. R. A. Searles, *Stud. Surf. Sci. Catal.*, **116**, 23 (1998).
5. N. E. Machin, E. E. Cakirca, A. Ates, in: Catalytic Combustion of Methane, 6<sup>th</sup> International Advanced Technologies Symposium (IATS'11), 16–18 May 2011, Elazığ, Turkey, p. 253.
6. P. Hurtado, S. Ordóñez, H. Sastre, F. H. Diez, *Appl. Catal. B-Environ.*, **47**, 85 (2004).
7. A. Ersson, Ph.D. Thesis, Kungliga Tekniska Högskolan, Department of Chemical Engineering and Chemical Technology, Stockholm, 2003.

8. S. Bernal, J. J. Calvino, M. A. Cauqui, J. M. Gatica, C. Larese, J. A. Perez Omil, J. M. Pintado, *Catal. Today*, **50**, 175 (1999).
9. C. N. Costa, S. Y. Christou, G. Georgiou, A. M. Efstathiou, *J. Catal.*, **219**, 259 (2003).
10. M. Zhao, M. Shen, J. Wang, W. Wang, *Ind. Eng. Chem. Res.*, **46**, 7883 (2007).
11. M. Jin, J.-N. Park, J. K. Shon, J. H. Kim, Z. Li, Y.-K. Park, J. M. Kim, *Catal. Today*, **185**, 183 (2012).
12. Y. Zhang, J. Rosen, G. S. Hutchings, F. Jiao, *Catal. Today*, **225**, 171 (2014).
13. J. Hagen, *Industrial Catalysis. A Practical Approach*, Wiley-VCH Verlag KGaA, Weinheim, Germany, 2006.
14. D. Shirley, *Phys. Rev. B*, **5**, 4709 (1972).
15. J. H. Scofield, *J. Electron Spectrosc. Relat. Phenom.*, **8**, 129-137 (1976).
16. D. Shanke, S. Vada, E. A. Blekkan, A. M. Hilmen, A. Hoff, *J. Catal.*, **156**, 85 (1995).
17. Y. Okamoto, K. Nagata, T. Adach, T. Imanaka, K. Imamura, T. Takyu, *J. Phys. Chem.*, **95**, 310 (1991).
18. Cl. Bianchi, *Catal. Lett.*, **76**, 155 (2001).
19. H. Duan, D. Xu, W. Li, H. Xu, *Catal. Lett.*, **124**, 318 (2008).
20. D. Shanke, S. Vada, E. A. Hilmen, A. Hoff, *J. Catal.*, **156**, 85 (1995).
21. V. A. de la Peña O'Shea, M. C. Alvarez-Galvan, J. L. G. Fierro, P. L. Arias, *Appl. Catal. B-Environ.*, **57**, 191 (2005).
22. V. A. de la Peña O'Shea, M. C. Alvarez-Galvan, J. Requies, V. L. Barrio, P. L. Arias, J. F. Cambra, M. B. Güemez, J. L. G. Fierro, *Catal. Commun.*, **8**, 1287 (2007).
23. T. L. Barr, *J. Phys. Chem.*, **82**, 1801 (1978).
24. C. D. Zeinalipour-Yazdi, A. L. Cooksy, A. M. Efstathiou, *Surf. Sci.*, **602**, 1858 (2008).
25. S. R. Monteiro, L. C. Dieguez, M. Schmal, *Catal. Today*, **65**, 77 (2001).
26. A. Palazov, G. Kadinov, Ch. Bonev, R. Dimitrova, D. Shopov, *Surf. Sci.*, **225**, 21 (1990).
27. P. Chou, M. A. Vannice, *J. Catal.*, **104**, 17 (1987).
28. K. I. Choi, M. A. Vannice, *J. Catal.*, **127**, 465 (1991).
29. K. I. Choi, M. A. Vannice, *J. Catal.*, **131**, 1 (1991).
30. K. Hadjiivanov, G. Vayssilov, *Adv. Catal.*, **47**, 307 (2002).
31. G. Kadinov, Ch. Bonev, S. Todorova, A. Palazov, *J. Chem. Soc. Faraday Trans.*, **94**, 3027 (1998).
32. S. Todorova, P. Stefanov, A. Naydenov, H. Kolev, *Rev. Roum. Chim.*, **59**, 251 (2014).
33. S. Park, D. S. Doh, K.-Y. Lee, *Top. Catal.*, **10**, 127 (2000).
34. T. Engel, G. Ertl, in: *The Chemical Physics of Solid Surfaces and Heterogeneous Catalysis*, Vol. 4, D. A. King, D. P. Woodruff (Eds.), Elsevier, Amsterdam, 1982, p. 73.

## НАНОРАЗМЕРЕН КОБАЛТОВ ОКСИД МОДИФИЦИРАН С ПАЛАДИЙ ЗА ОКИСЛЕНИЕ НА МЕТАН И ВЪГЛЕРОДЕН ОКСИД

С. Тодорова<sup>1</sup>, А. Гангули<sup>2</sup>, Ант. Найденов<sup>3</sup>, Х. Колев<sup>1</sup>, Ил. Йорданова<sup>1</sup>, М. Шопска<sup>1</sup>, С. Мондал<sup>2</sup>, Г. Кадинов<sup>1</sup>, С. Саха<sup>2</sup>, А. К. Гангули<sup>2,4,5</sup>

<sup>1</sup> Институт по катализ, Българска академия на науките, ул. „Акад. Г. Бончев“, бл. 11, 1113 София, България

<sup>2</sup> Факултет по химия, Индийски технологичен институт, Хаус Кназ, Делхи 110016, Индия

<sup>3</sup> Институт по обща и неорганична химия, Българска академия на науките, ул. „Акад. Г. Бончев“, бл. 11, 1113 София, България

<sup>4</sup> Факултет за разработки и изследвания на нанотехнологии, Индийски технологичен институт, Хаус Кназ, Делхи 110016, Индия

<sup>5</sup> Институт по нанонауки и технологии, Хабитат Център, Мохали, Пенжаб 160062, Индия

Постъпила на 29 септември 2015 г.; Преработена на 20 октомври 2015 г.

(Резюме)

Нано размерен  $\text{Co}_3\text{O}_4$  е получен посредством утаяване на кобалтов ацетат с амониев хидроксид и следваща хидротермална обработка. Така приготвеният оксид е накален и модифициран с паладий. Катализаторните образци са охарактеризирани с рентгенова дифракция, рентгенова фотоелектронна спектроскопия, трансмисионна електронна микроскопия, температурно програмирана редукция и дифузионно отразителна инфрачервена спектроскопия. Каталитичните свойства на синтезираните материали са изследвани в реакциите на пълно окисление на метан и въглероден оксид. Установено е образуване на финодисперсен PdO на повърхността на кобалтовия оксид.

Въз основа на изследвания с инфрачервена спектроскопия е предположено, че реакцията на окисление на CO при температури до 150°C протича по механизъм на Ленгмюир-Хиншелууд, включващ линейно свързани с паладия молекули на въглеродния оксид. При по-висока температура паладиевата повърхност е покрита главно от дисоциативно адсорбиран кислород и реакцията продължава чрез механизма на Или-Ридил: хемисорбирани кислородни атоми реагират с газообразен въглероден оксид. Не е изключен и механизмът на Марс ван Кревелен, поради факта, че се регистрира въглероден диоксид след пропускане на смес от  $\text{CO} + \text{N}_2$  (без кислород), което показва, че най-вероятно въглеродният оксид взаимодейства с решетъчен кислород от PdO и/или  $\text{Co}_3\text{O}_4$ .

## Catalytic decomposition of ozone: from laboratory fixed bed reactor to design of adiabatic monolithic reactor

A. I. Naydenov

*Institute of General and Inorganic Chemistry, Bulgarian Academy of Sciences,  
Acad. G. Bonchev St., Block 11, 1113 Sofia, Bulgaria*

Received September 29, 2015; Revised October 28, 2015

The purpose of the present paper is to demonstrate an approach to establish kinetics parameters of ozone decomposition aimed at being suitable for further application to design monolithic reactors for neutralization of waste gases. A catalytic system of Ag/anodized alumina/aluminium foil was selected for this purpose. To obtain kinetic data close to plug-flow reactor conditions, the catalyst was tested in the form of 2×5 mm sheets loaded randomly in the reactor. The same amount of catalyst has been rolled to create tubes of circular cross-section (diameter of 2.5 mm) to resemble a geometrical configuration of a single monolithic channel. Two kinetic equations of first order and partial order reaction were selected to fit experimental data. Purification of waste gases containing ozone in a monolithic reactor was simulated by a two-dimensional heterogeneous model accounting for concentration and temperature profiles inside both the gas phase in the channel and the catalytic active phase.

**Keywords:** ozone, catalytic decomposition, reaction kinetics, two-dimensional model, monolithic channel.

### INTRODUCTION

The reaction of catalytic decomposition of ozone is of practical interest for several reasons. Exit gases from ozonation of wastewater and drinking water, sterilization, and deodorization contain residual ozone and because ozone itself is very toxic, these gases must be neutralized [1]. The catalytic decomposition of ozone is required for purification of indoor ventilation air including aircrafts, where ozone peak levels without catalytic converters exceeds 100 ppb, with some flights having long periods when these levels are above 75 ppb [2]. The role of aerosol particles in depleting the stratospheric ozone layer is a problem of major importance. There has been long evidence for a negative correlation between ozone and aerosols during desert dust outbreaks [3]. *In situ* measurements show a significant reduction in ozone layer under high dust concentrations [4, 5].

Ag-containing catalysts exhibit highest activity when compared with oxides of Co, Ni, Fe, Mn, Ce, Cu, Pb, Bi, Sn, Mo, V, and Si [6]. It has been reported that a silver-based catalyst demonstrate a remarkable activity and stability even at low temperatures [7–12]. During the catalytic decomposition of ozone, a highly reactive oxygen species is produced that is able to oxidize completely toxic compounds at room temperature [13]. There is an increased interest in the complete oxidation of VOCs (volatile organic compounds) [13–20] and

CO [21, 22] in waste gases by catalytic ozonation. Most of the available data in the literature related to the catalytic decomposition of ozone are based on testing the catalysts in the form of small particles (sizes below 1 mm) of irregular shape and, at the same time, significant results on monolithic (structured) catalysts are missing.

The aim of the present paper was to demonstrate an alternative approach to establish kinetic parameters of ozone decomposition that are suitable for further application to design monolithic reactors. The active phase of the catalyst (Ag) was supported on a thin layer of  $\gamma$ -alumina obtained by anodizing an aluminium foil. The catalyst had well defined geometrical characteristics, which were proper for operation under plug-flow conditions by testing catalytic samples in the form of rectangular-shaped sheets thus ensuring almost perfect mixing around each catalytic element. For tests in a laminar gas flow inside a monolithic element, the same catalyst was examined in the form of a channel of circular cross-section. A possibility to apply the results of fixed bed reactor experiments by simulating the behaviour of a monolithic reactor for ozone-containing waste gas abatement by a two-dimensional heterogeneous model of monolithic channel is also considered.

### EXPERIMENTAL

The catalytic support was prepared by anodizing an aluminium foil (thickness of 0.30 mm, 99%

\* To whom all correspondence should be sent  
E-mail: naydenov@svr.igic.bas.bg

purity) and rolled to create tubes of circular cross-section of a 153-mm length and diameter of 2.5 mm to achieve a geometrical configuration of a single monolithic channel. Anodizing was applied to obtain a thin film layer of  $\gamma$ -Al<sub>2</sub>O<sub>3</sub>, which is suitable for a catalyst supports for Ag. A scanning electron micrograph (SEM) of the catalyst revealed an average thickness of the alumina layer of 15  $\mu$ m, while a BET surface area of 14 m<sup>2</sup>.g<sup>-1</sup> was measured on a Quantachrome Nova 1200 instrument.

A catalytically active phase of 2 wt.% silver, measured by a Perkin-Elmer atomic absorption analyser, was deposited on the support by direct impregnation with an aqueous solution of AgNO<sub>3</sub>, then dried, and calcined at 400°C for 2 h.

The following experimental conditions were applied to obtain kinetic data. A catalyst sample (12 cm<sup>2</sup>) was tested in the form of 2×5 mm sheets, then loaded randomly in the reactor (quartz glass tube, i.d. 5.5 mm), and mixed with  $\alpha$ -alumina spherical particles of 0.6–0.7-mm size. The pressure drop was measured to be below 1 kPa and it was disregarded. Radial concentration profiles and axial dispersion effects were also neglected.

Ozone was synthesized in a flow of oxygen (99.7%) using an ozone generator with silent discharge and coaxial electrodes. The inlet concentration of ozone was varied from 0.04 to 0.17 mol.m<sup>-3</sup>. Ozone concentration was measured by an Ozomat GM ozone analyser (Anseros, Germany). The reaction temperature was varied from -40 to +40°C and was kept with an accuracy of  $\pm 0.5^\circ\text{C}$  by

means of a thermostat with a mixture of acetone and dry ice (carbon dioxide, T = -78°C).

## RESULTS

The decomposition of ozone on an Ag/anodized alumina catalyst loaded in the reactor in the form of 2×5 mm sheets proceeds at a measurable rate at a temperature below -40°C (Fig. 1). Further, analysis of catalyst behaviour was extended by investigation of reaction kinetics. To calculate kinetic parameters both inlet concentration of the ozone and gas hourly space velocity (GHSV) were varied.

Data on conversion-temperature dependencies were used to fit kinetic parameters by applying the method described by Duprat [23] and Harriot [24]. The results are presented in Table 1. Details on the calculation procedure were published elsewhere [25]. In brief, it consists of a direct integration of the reaction rate based on data on temperature-conversion curves by using a one-dimensional pseudo-homogeneous model of plug-flow isothermal reactor. The residual squared sum (RSS) between experimental data and model predictions was minimized (an optimization criterion) and the square of correlation coefficient (R<sup>2</sup>) was calculated and used as a measure of model applicability. Values for the effectiveness factor of first-order kinetics and slab geometry were calculated by Thiele modulus [26, 27]. Calculations showed that at temperatures above -10°C, where resistance due to internal diffusion plays a significant role, the decrease of the effectiveness factor could not be neglected.

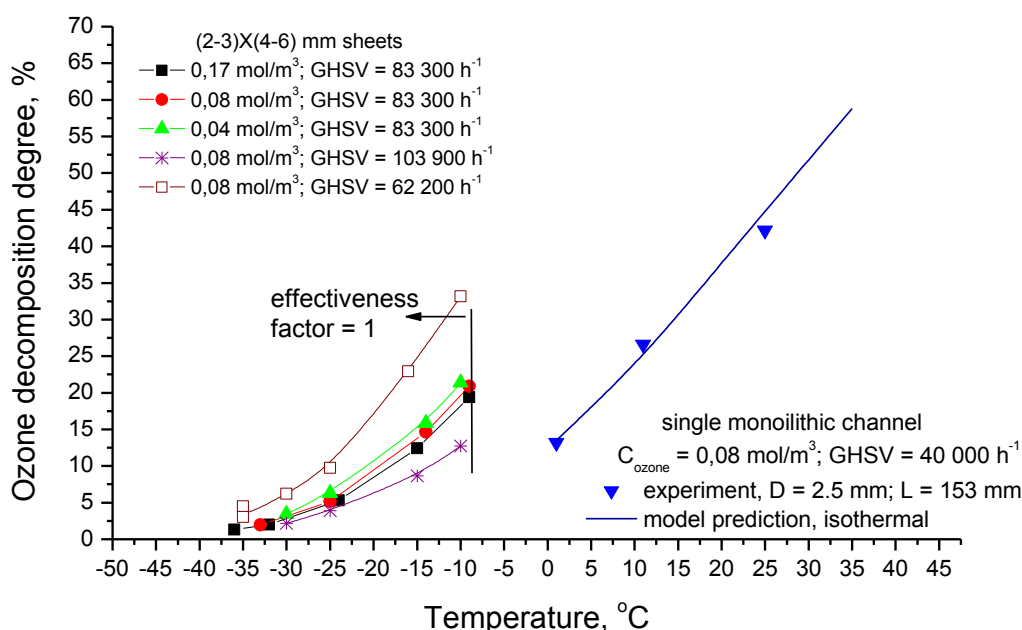
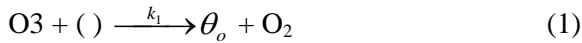


**Fig. 1.** Measured conversions of ozone decomposition over Ag/anodized Al-catalyst tested under conditions of plug-flow reactor and single monolithic channel with circular cross-section: comparison with model prediction.

**Table 1.**

Model	$k_o$	$E_a$	m	RSS	$R^2$
First order kinetics:					
$r_a = kP_{O_3}$	2.25E+12	52.0		1,7	0.988
Power-law kinetics:					
$r_a = kP_{O_3}^m$	2.25E+12	52.7	0.95	1.6	0.989
$k = k_o \cdot \exp(-E_a/RT)$ ; $E_a$ , kJ.mol <sup>-1</sup> ; $k_o$ , mol.s <sup>-1</sup> .m <sup>-3</sup> .atm <sup>-(1-m)</sup> .					

In general the heterogeneous catalytic decomposition of ozone can be presented by the following scheme [28]:



$$r = 2 \frac{k_1 \cdot k_2}{k_1 + k_2} \cdot P_{o_3} \quad (3)$$

Obviously, equation (3) applies for a first-order reaction (stoichiometric equation is  $2O_3 \rightarrow 3O_2$ ). However, the present experimental results show an increased conversion value at a lower inlet concentration of ozone, i.e. the observed reaction order is somewhat lower than unity. A similar observation has been reported by Oyama and Li [29]. These authors proposed a simple rate expression of global kinetics: a power rate law dependence on ozone partial pressure that was linear over several orders of magnitude of ozone partial pressure change,  $r = kP^{0.94}$ .

Results of fixed bed reactor tests were applied to simulate the behaviour of a monolithic reactor for

abatement of waste gases containing ozone. A two-dimensional heterogeneous model of monolithic channel was used to simulate ozone decomposition in a monolithic reactor. The basic principles of the model have been described in detail by Belfiore [28] and Nauman [29]. A single channel model was the subject of mathematical description. A finite difference method was applied and the corresponding computational code was written by using a standard Excel® (Microsoft) program. Verification of the model was performed by a comparative calculation with the corresponding analytical solutions for certain boundary cases.

Figure 2 shows results of experiments with the monolithic element and calculations using the kinetics parameters as given in Table 1. Channel dimensions were selected in a way that channel area be the same as for a tested sample in a fixed bed reactor in the form of rectangular shaped sheets. The results are related to calculated conversion and temperature profiles inside the monolithic channel using data on first-order reactions at different channel dimensions (diameter and channel length), gas-hourly space velocities, inlet ozone concentrations, and data on an isothermal or adiabatic reactor operation. Furthermore, it was of practical interest to calculate the necessary amount of catalyst to achieve a specified degree of waste gas purification (e.g., if 98% of containing ozone is to be decomposed or to simulate the process in monoliths at a different channel/aspect ratio). For the purpose, experimental results acquired by means of an isothermal laboratory reactor (Fig. 2a) were used to simulate the abatement of methane containing gases under adiabatic conditions (Fig. 2b).

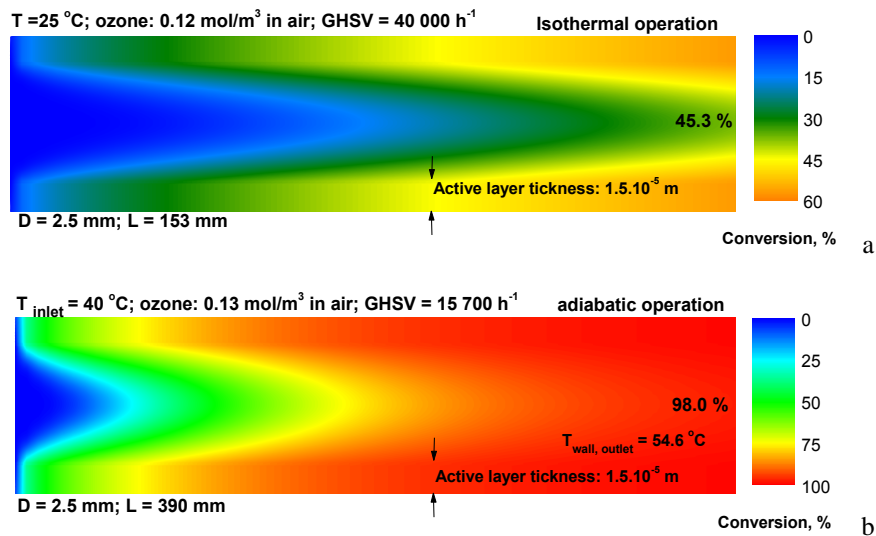


**Fig. 2.** Experimental (a) and calculated (b) conversion profiles inside the monolithic channel at a different channel length using the obtained data on first-order kinetics.

The proposed experimental approach can also be used to collect data on a detailed reaction mechanism by applying the co-called transient response method, first developed by Kobayashi [30]. It is based on analysis of the response of the catalytic system when a fast step-wise change of reaction parameters is applied.

### CONCLUSION

Based on experimental results and performed calculations one may conclude that the reaction of catalytic decomposition of ozone was investigated under proper experimental conditions and data on further application to design structured (monolithic) reactors for abatement of ozone in waste gases could be provided.

*Acknowledgements: Financial support by the European Social Fund through Contract BG051PO001-3.3.06-0050 and by a Collaborative project between the Bulgarian Academy of Sciences and the Macedonian Academy of Sciences and Arts is gratefully acknowledged. The author also thanks the Bulgarian Science Fund for Grant No TO1/6.*

### REFERENCES

1. S. Rakovsky, G. Zaikov, Kinetics and Mechanism of Ozone Reactions with Organic and Polymeric Compounds in Liquid Phase, Nova Science Publishers, Inc., Commack, New York, 1999.
2. C. Weisel, C. J. Weschler, K. Mohan, J. Vallarino, J. D. Spengler, *Environ. Sci. Technol.*, **47**, 4711 (2013).
3. J. Andrey, E. Cuevas, M. C. Parrondo, S. Alonso-Pérez, A. Redondas, M. Gil-Ojeda, *Atmos. Environ.*, **84**, 28 (2014).
4. M. de Reus, F. Dentener, A. Thomas, S. Borrmann, J. Ström, J. Lelieveld, *J. Geophys. Res.*, **105**, 15263 (2000).
5. E. Cuevas, Y. González, S. Rodríguez, J. C. Guerra, A. J. Gómez-Peláez S. Alonso-Pérez, J. Bustos, C. Milford, *Atmos. Chem. Phys.* **13**, 1973 (2013).
6. S. Imamura, M. Ikebata, T. Ito, T. Ogita, *Ind. Eng. Chem. Res.*, **30**, 217 (1991).
7. A. Naydenov, P. Konova, P. Nikolov, F. Klingstedt, N. Kumar, D. Kovacheva, P. Stefanov, R. Stoyanova, D. Mehandjiev, *Catal. Today.*, **137**, 471 (2008).
8. N. Kumar, P. Konova, A. Naydenov, T. Heikillä, T. Salmi, D. Yu. Murzin, *Catal. Lett.*, **98**, 57 (2004).
9. N. Kumar, P. Konova, A. Naydenov, T. Salmi, D. Yu. Murzin, T. Heikillä, V.-P. Lehto, *Catal. Today*, **119**, 342 (2007).
10. P. Nikolov, K. Genov, P. Konova, K. Milenova, T. Batakliiev, V. Georgiev, N. Kumar, D. K. Sarker, D. Pishev, S. Rakovsky, *J. Hazard. Mater.*, **184**, 16 (2010).
11. K. Genov, V. Georgiev, T. Batakliiev, D. K. Sarker, *Int. J. Civ. Environ. Eng.*, **33**, 205 (2011).
12. T. Batakliiev, G. Tyuliev, V. Georgiev, M. Anachkov, A. Eliyas, S. Rakovsky, *Ozone: Sci. Eng.*, **37**, 3, 216 (2015).
13. A. Naydenov, D. Mehandjiev, *Appl. Catal. A: General*, **97**, 17 (1993).
14. H. Einaga, S. Futamura, *J. Catal.*, **227**, 304 (2004).
15. H. Einaga, S. Futamura, *Appl. Catal. B: Environ.*, **60**, 49 (2005).
16. H. Einaga, S. Futamura, *J. Catal.*, **243**, 446 (2006).
17. H. Einaga, M. Harada, A. Ogata, *Catal. Lett.*, **129**, 422 (2009).
18. H. Einaga, A. Ogata, *J. Hazard. Mater.*, **164**, 1236 (2009).
19. H. Einaga, N. Maeda, S. Yamamoto, Y. Teraoka, *Catal. Today*, **245**, 22 (2015).
20. Y. Liu, X. Li, J. Liu, C. Shi, A. Zhu, *Chin. J. Catal.*, **35**, 1465 (2014)
21. A. Naydenov, R. Stoyanova, D. Mehandjiev, *J. Mol. Catal.*, **98**, 9 (1995).
22. K. Soni, S. C. Shekar, B. Singh, A. Agrawal, *Ind. J. Chem.*, **53A**, 484 (2014).
23. F. Duprat, *Chem. Eng. Sci.*, **57**, 901 (2002).
24. P. Harriot, Chemical Reactor Design, Marcel Dekker Inc., 2003.
25. S. Todorova, A. Naydenov, H. Kolev, J. P. Holgado, G. Ivanov, G. Kadinov, A. Caballero, *Appl. Catal. A:General*, **43**, 413 (2012).
26. C. N. Satterfield, Mass Transfer in Heterogeneous Catalysis, MIT Press, Cambridge, Mass., 1970.
27. O. Levenspiel, Chemical Reactor Engineering, 3<sup>rd</sup> edn., John Wiley & Sons Inc., 1999.
28. G. I. Golodetz, Heterogeneous catalytic reactions involving molecular oxygen, Elsevier, 1983, ISBN: 978-0-444-42204-0.
29. S. T. Oyama, W. Li, *Topics in Catalysis.*, **8**, 75 (1999).
30. L. A. Belfiore, Transport Phenomena for Chemical Reactor Design, John Wiley & Sons Inc., 2003.
31. E. B. Nauman, Chemical Reactor Design, Optimization, and Scaleup, McGraw-Hill, 2002.
- H. Kobayashi, M. Kobayashi, *Catal. Rev. Sci. Eng.*, **10**, 1 (1974).

## КАТАЛИТИЧНО РАЗЛАГАНЕ НА ОЗОН – ОТ ЛАБОРАТОРЕН РЕАКТОР С НЕПОДВИЖЕН СЛОЙ КЪМ ОРАЗМЕРЯВАНЕ НА МОНОЛИТЕН АДИАБАТЕН РЕАКТОР

Ант. Ил. Найденов

*Институт по обща и неорганична химия, Българска академия на науките,  
ул. „Акад. Г. Бончев“, бл. 11, 1113 София, България*

Постъпила на 29 септември 2015 г.; Преработена на 28 октомври 2015 г.

(Резюме)

Целта на настоящата работа е да се покаже възможността за определяне на кинетичните параметри на реакцията на каталитично разлагане на озон с оглед последващо им приложение при оразмеряването на монолитни реактори за обезвреждане на отпадъчни газове. Каталитичната система Ag/анодиран алуминий/алуминиево фолио бе избрана за настоящото изследване. За получаване на данни за кинетиката при условия в реактора, близки до режим на идеално изместване, катализаторът бе тестван под формата на ленти с размери 2×5 mm, заредени в неподреден вид в каталитичния реактор. От същото количество катализатор бяха изработени и тръбни елементи с кръгло сечение с диаметър 2.5 mm с цел доближаване до геометричните характеристики на единичен канал от монолитен каталитичен елемент. За изчисляване на кинетичните параметри бяха подбрани две уравнения: от първи и от дробен порядък спрямо озона. Очистването на отпадъчни газове, съдържащи озон, бе симулирано чрез двумерен хетерогенен модел на реактор, предвиждащ концентрационния и температурния профил както в газова фаза, така също и в активната фаза на катализатора.

## Complete oxidation of methane on Pd-substituted perovskite $\text{LaCu}_{0.5}\text{Mn}_{0.5}\text{O}_3$

Ts. Lazarova, P. Tzvetkov, V. Tumbalev, S. Atanassova-Vladimirova<sup>1</sup>, G. Ivanov, A. Naydenov, D. Kovacheva\*

*Institute of General and Inorganic Chemistry, Bulgarian Academy of Sciences, Acad. G. Bonchev St., Bldg. 11, 1113, Sofia, Bulgaria*

<sup>1</sup> *Institute of Physical Chemistry, Bulgarian Academy of Sciences, Acad. G. Bonchev St, Bldg. 11, 1113, Sofia, Bulgaria*

Received September 25, 2015; Revised December 4, 2015

B-site substituted perovskite compounds  $\text{LaCu}_{0.5}\text{Mn}_{0.5}\text{O}_3$  and  $\text{LaCu}_{0.45}\text{Pd}_{0.05}\text{Mn}_{0.5}\text{O}_3$  were synthesized by urea-assisted combustion method and considered for further application as catalysts for methane combustion. Palladium substitution for copper in terms of effect on catalyst structural and physicochemical properties has been investigated by using X-ray diffraction (XRD), low-temperature adsorption of nitrogen (BET), and scanning electron microscopy (SEM). Results showed that incorporation of palladium into perovskite crystal structure brings about a material of high thermal stability and improved catalytic properties compared with non-substituted  $\text{LaCu}_{0.5}\text{Mn}_{0.5}\text{O}_3$ .

**Keywords:** perovskite, Pd-substituted perovskite, methane catalytic oxidation, XRD, SEM, BET.

### INTRODUCTION

Methane accounts for 14% of the total amount of greenhouse gas (GHG) emissions originating from mines, agriculture, and gas facilities [1]. There are some considerations for assessing a new value for methane global warming potential (GWP). The Environmental Protection Agency (EPA) recently proposed raising methane's GWP value from 21 to 25 [2]. The European Union (EU) tackles methane emissions together with other GHG emissions, planning a reduction in the EU's greenhouse gas emissions by 20% in 2020 compared to 1990 [2]. The emission of methane can be used as a fuel in combustion processes as well as in thermal and catalytic reverse flow reactors, catalytic monolith combustors, catalytic lean burn gas turbines, recuperative gas turbines, or concentrators [3]. Neutralization of gases containing methane can be realized by variety of methods, one of them being the complete catalytic oxidation [4,5]. In the case of complete oxidation of methane, palladium and platinum are the most widely used metals because of their high activity [6–9]. It was found that Pd is more active than Pt for methane oxidation, and most of the research works have concentrated on Pd as the active component in recent years. Most studies have primarily focused on the use of alumina as the supporting material for Pd-based catalysts [7–10], and these studies have shown that the activity of each catalyst is influenced by many factors, e.g.

precursor, support, Pd loading, calcination temperature, morphology of the Pd crystallites, catalyst pretreatment procedure, and reaction conditions. The main disadvantage of Pd catalysts is their instability and high price. In recent years, a lot of research effort has been focused on the synthesis of perovskite-type oxides as possible catalysts in the process of catalytic combustion [11]. Perovskites are characterized by a general  $\text{ABO}_3$  structure and remarkable heat resistance [11,12]. The perovskites can be modified in terms of non-stoichiometry and partial substitution by varying the types of atoms at the A and B sites thus providing an opportunity to prepare different perovskites with possible application as catalysts in the reaction of complete oxidation of methane. Since the type of B-site cations determines the catalytic properties of perovskite-type oxides, the B-site substitution of perovskites was considered an effective way to modify their catalytic properties due to generation of new lattice defects, mixed valence states, and nonstoichiometric oxygen.

The aim of the present study was to investigate the effect of introducing a noble metal into the perovskite structure as a low-level substituting element. B-site substituted perovskites,  $\text{LaCu}_{0.5}\text{Mn}_{0.5}\text{O}_3$  and  $\text{LaCu}_{0.45}\text{Pd}_{0.05}\text{Mn}_{0.5}\text{O}_3$ , obtained by urea-assisted combustion synthesis, were selected and investigated for further application as catalysts in methane combustion.

### EXPERIMENTAL

$\text{LaCu}_{0.5}\text{Mn}_{0.5}\text{O}_3$  and  $\text{LaCu}_{0.45}\text{Pd}_{0.05}\text{Mn}_{0.5}\text{O}_3$  samples were synthesized by solution-combustion

\* To whom all correspondence should be sent  
E-mail: didka@svr.igic.bas.bg

© 2015 Bulgarian Academy of Sciences, Union of Chemists in Bulgaria

method using a stoichiometric mixture of the corresponding metal nitrates as oxidizers and urea as fuel. Initial compounds were dissolved in appropriate amount of distilled water. The clear solution was evaporated on a laboratory heater. After evaporation a self-initialized ignition process occurred. Combustion resulted in a fine powder residue. The sample  $\text{LaCu}_{0.5}\text{Mn}_{0.5}\text{O}_3$  was thermally treated at  $550^\circ\text{C}$  for 30 min., after that at  $750^\circ\text{C}$  for 1 h, and finally treated at  $1100^\circ\text{C}$  for 5 h. The  $\text{LaCu}_{0.45}\text{Pd}_{0.05}\text{Mn}_{0.5}\text{O}_3$  sample was thermally treated at  $550^\circ\text{C}$  for 30 min, then at  $750^\circ\text{C}$  for 1 h, and finally at  $1100^\circ\text{C}$  for 2 h. Palladium substitution for Cu with reference to influence on structure and morphology was studied using X-ray diffraction of Bruker D8 Advance with Cu  $K\alpha$  radiation and LynxEye detector. Powder diffraction patterns were collected between 10 and 120 degrees  $2\theta$  with a step of 0.02 degree  $2\theta$  and counting time 175 s/step. Phase identification was performed by Diffracplus EVA using ICDD-PDF2 database. The mean crystallite size was determined based on all peaks within recorded powder patterns using whole powder pattern fitting with Topas-4.2 software package and fundamental parameters of the peak shape description including appropriate corrections for instrumental broadening and diffractometer geometry. Rietveld refinement of the structural parameters was performed with Topas 4.2.

Specific surface area of the catalyst samples ( $S_{\text{BET}}$ ) was determined by low-temperature adsorption of nitrogen according to the BET method using a Quantachrome NOVA 1200 apparatus.  $S_{\text{BET}}$  was calculated applying the Brunauer, Emmet and Teller (BET) equation for  $\text{N}_2$  relative pressure within the range of  $0.05 < P/P_0 < 0.30$ .

Elemental composition as well as morphology and microstructure of the catalysts were studied by a JEOL-JSM-6390 scanning electron microscope equipped with energy dispersion spectroscopy (EDS) with (Li, Si) detector.

Catalytic activity tests were carried out by means of a CATLAB Hiden Analytical apparatus equipped with a mass-spectrometer in a continuous-flow type quartz-glass reactor at atmospheric pressure. The following testing conditions were applied: catalyst bed volume of  $0.5 \text{ cm}^3$ , irregular shaped particles of 0.7-mm average diameter, and inner reactor diameter of 7.0 mm ( $D_{\text{reactor}}/D_{\text{particles}} \approx 10$ ). The gaseous hourly space velocity (GHSV) was fixed at  $12000 \text{ h}^{-1}$ . Water vapour effect on the methane combustion was also investigated.

## RESULTS AND DISCUSSION

Figure 1 shows XRD patterns of the  $\text{LaCu}_{0.5}\text{Mn}_{0.5}\text{O}_3$  and  $\text{LaCu}_{0.45}\text{Pd}_{0.05}\text{Mn}_{0.5}\text{O}_3$  samples heated at  $1100^\circ\text{C}$ . Both patterns show diffraction peaks corresponding to the perovskite structure displayed by both samples. For both samples heated at  $500^\circ\text{C}$ , XRD analysis indicates formation of a  $\text{La}_2\text{CuO}_4$  impurity phase. After thermal treatment of the  $\text{LaCu}_{0.5}\text{Mn}_{0.5}\text{O}_3$  sample at  $750^\circ\text{C}$  the amount of  $\text{La}_2\text{CuO}_4$  phase is decreased. Upon further heating at  $1100^\circ\text{C}$ , the  $\text{La}_2\text{CuO}_4$  phase disappears completely. In  $\text{LaCu}_{0.45}\text{Pd}_{0.05}\text{Mn}_{0.5}\text{O}_3$ , the amount of  $\text{La}_2\text{CuO}_4$  phase was very small even after heating at a temperature of  $750^\circ\text{C}$ . This fact indicates that the presence of Pd suppresses the formation of  $\text{La}_2\text{CuO}_4$  phase in favour of the perovskite phase.

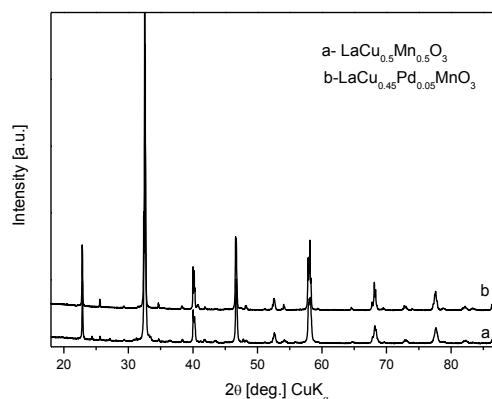


**Fig. 1.** XRD patterns of  $\text{LaCu}_{0.5}\text{Mn}_{0.5}\text{O}_3$  and  $\text{LaCu}_{0.45}\text{Pd}_{0.05}\text{Mn}_{0.5}\text{O}_3$  heated at  $1100^\circ\text{C}$

Powder diffraction patterns of both samples heated at  $1100^\circ\text{C}$  can be indexed in orthorhombic space group Pbnm with very close unit cell parameters. A Rietveld structure refinement was performed. Refined parameters were unit cell parameters, line profile parameters, zero shifts, background parameters, positional parameters, occupancy, and thermal displacement parameters of ions in the structure. Preferred orientation effects were not included. Results of the structure refinement are shown in tables 1 and 2. The present results show systematic changes in unit cell parameters after doping with Pd. The polyhedral crystal structure of orthorhombic perovskite is presented in figure 2.

A calculation of cell deformation index was performed by using the following equation:  $ap = (a/\sqrt{2} + b/\sqrt{2} + c/2)/3$  [13]. An estimate of polyhedron deformation parameter was carried out through the equation:  $\Delta = \sum[(r_i - r)/r]/n \times 10^3$ , where  $r$  is the individual bond length (A–O or B–O), and  $n$

is the number of bonds [14]. The results are presented in Table 3. It is seen that palladium introduction to the perovskite structure decreases the deformation level, thus stabilizing the structure.

Elemental analysis results for a sample of nominal composition  $\text{LaCu}_{0.5}\text{Mn}_{0.5}\text{O}_3$  are presented in table 4, while table 5 gives data on a sample of nominal composition  $\text{LaCu}_{0.45}\text{Pd}_{0.05}\text{Mn}_{0.5}\text{O}_3$ . Obviously, the experimental elemental composition

of both samples is close to the corresponding nominal composition.

Fig. 3 shows SEM images of the samples at different magnifications. It is seen that the  $\text{LaCu}_{0.5}\text{Mn}_{0.5}\text{O}_3$  sample is a ceramic material with smooth surface, while  $\text{LaCu}_{0.45}\text{Pd}_{0.05}\text{Mn}_{0.5}\text{O}_3$  is a material containing particles with well-developed porous surface.

**Table 1.** Crystal structure data on  $\text{LaCu}_{0.5}\text{Mn}_{0.5}\text{O}_3$  SG. Pbnm a = 5.5225(1) (Å), b = 5.4800(1) (Å), c = 7.7680(2) (Å)

Site	N	x	y	z	Occ	Bizo
A	4	0.0002(7)	0.5192(2)	1/4	(La+3) 1	0.94(2)
B	4	0	0	0	(Mn+4) 0.5 (Cu+2) 0.5	0.51(3) 0.51(3)
O1	4	-0.078(2)	0.003(2)	1/4	(O-2) 1	1.3(1)
O2	8	0.220(2)	0.289(2)	0.022(1)	(O-2) 1	1.3(1)

**Table 2.** Crystal structure data on  $\text{LaCu}_{0.45}\text{Pd}_{0.05}\text{Mn}_{0.5}\text{O}_3$  SG. Pbnm a = 5.52702(5) (Å), b = 5.48809(6) (Å), c = 7.77305(8) (Å)

Site	N	x	y	z	Occ	Bizo
A	4	0.0029(4)	0.5224(1)	1/4	(La+3) 1	0.68(2)
B	4	0	0	0	(Mn+4) 0.5 (Cu+2) 0.45 (Pd+2) 0.05	0.67(3) 0.67(3) 0.67(3)
O1	4	0.084(2)	0.002(2)	1/4	(O-2) 1	1.1(1)
O2	8	0.226(2)	0.271(2)	0.030(1)	(O-2) 1	1.1(1)

**Table 3.** Structure deformation indicators

	$\text{LaCu}_{0.5}\text{Mn}_{0.5}\text{O}_3$	$\text{LaCu}_{0.45}\text{Pd}_{0.05}\text{Mn}_{0.5}\text{O}_3$
cell deformation index	4.75	4.13
deformation of octahedron	0.2158	0.0799

**Table 4.** Theoretical and experimental atomic percentage of  $\text{LaCu}_{0.5}\text{Mn}_{0.5}\text{O}_3$

Atomic %	La	Cu	Mn	O
teoretical	20	10	10	60
experimental	20.35	10.61	9.25	61.13

**Table 5.** Theoretical and experimental atomic percentage of  $\text{LaCu}_{0.45}\text{Pd}_{0.05}\text{Mn}_{0.5}\text{O}_3$

Atomic %	La	Cu	Pd	Mn	O
teoretical	20	9	1	10	60
experimental	24.65	9.91	0.99	10.93	55.52

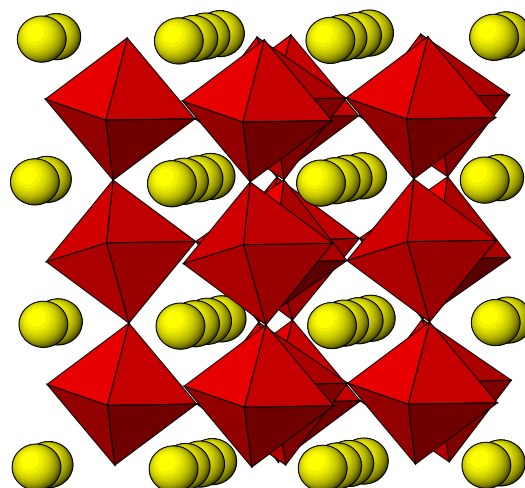


**Fig. 2.** Polyhedral presentation of the crystal structure of  $\text{LaCu}_{0.5}\text{Mn}_{0.5}\text{O}_3$ : octahedra –  $\text{MO}_6$ , bals –  $\text{La}^{3+}$  ions

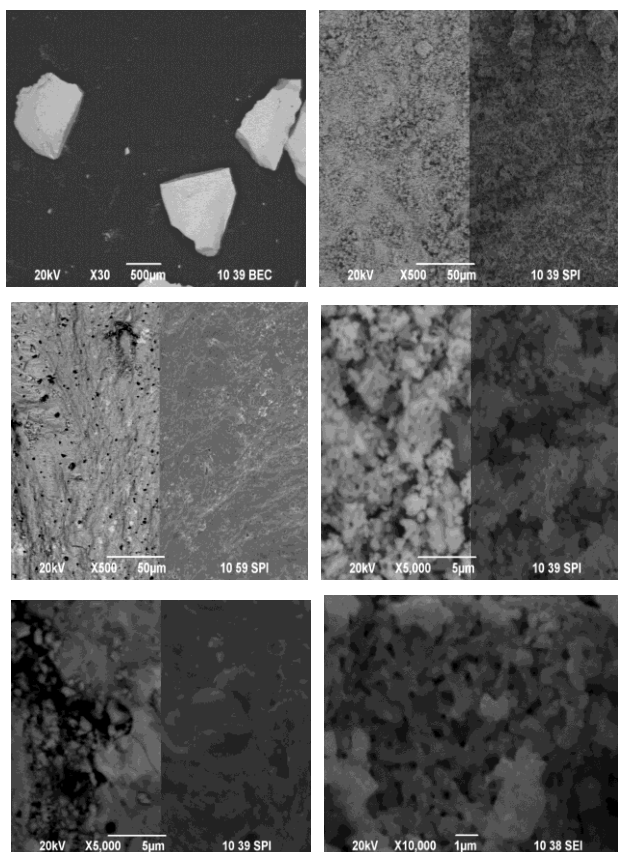


**Fig. 3.** SEM photograph images of  $\text{LaCu}_{0.5}\text{Mn}_{0.5}\text{O}_3$  (left column) and  $\text{LaCu}_{0.45}\text{Pd}_{0.05}\text{Mn}_{0.5}\text{O}_3$  (right column) at different magnifications.

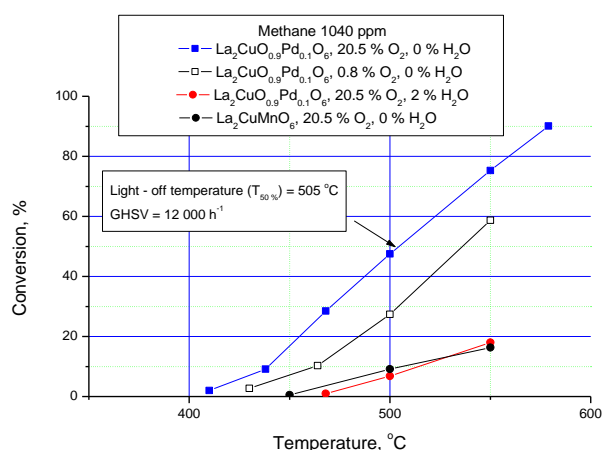


**Fig. 4.** Catalytic activities of  $\text{LaCu}_{0.5}\text{Mn}_{0.5}\text{O}_3$  and  $\text{LaCu}_{0.45}\text{Pd}_{0.05}\text{Mn}_{0.5}\text{O}_3$  in reaction of complete oxidation of methane.

Figure 4 displays comparative results of the catalytic activities of  $\text{LaCu}_{0.5}\text{Mn}_{0.5}\text{O}_3$  and  $\text{LaCu}_{0.45}\text{Pd}_{0.05}\text{Mn}_{0.5}\text{O}_3$  samples in the reaction of complete methane oxidation. Evidently, the catalytic activity of  $\text{LaCu}_{0.45}\text{Pd}_{0.05}\text{Mn}_{0.5}\text{O}_3$  is higher than that of  $\text{LaCu}_{0.5}\text{Mn}_{0.5}\text{O}_3$ . This fact cannot only be explained by a difference in specific surface area ( $0.6 \text{ m}^2 \cdot \text{g}^{-1}$  and  $0.2 \text{ m}^2 \cdot \text{g}^{-1}$ , respectively). Calculated

values for the rate constants at  $500^\circ\text{C}$  show a ratio of 6.8:1 in favour of the palladium containing catalyst. As the observed activation energies (assuming first-order kinetics) for both samples have almost the same values ( $\sim 105 \text{ kJ} \cdot \text{mol}^{-1}$ ), this fact gives an opportunity to compare the pre-exponential factors (10.2:1). It is seen that water vapour has an inhibition effect on the Pd-containing sample. The reaction rate is also dependent on oxygen content in the gas phase thus revealing a more complicated reaction mechanism than that described by simple first-order kinetics.

## CONCLUSIONS

Urea-assisted combustion synthesis was proved an appropriate method for synthesis of B-site substituted perovskite compounds. Palladium substitution for copper has influence on the structural and physicochemical properties of the catalysts demonstrating that Pd incorporation into perovskite crystal structure gives rise to a material of high thermal stability and bettered catalytic properties compared with non-substituted  $\text{LaCu}_{0.5}\text{Mn}_{0.5}\text{O}_3$ .

*Acknowledgements:* Financial support by European Social Fund through contract BG051PO001-3.3.06-0050 and by a collaborative project between Bulgarian Academy of Sciences and Macedonian Academy of Sciences and Arts is gratefully acknowledged.

## REFERENCES

1. Federal Register No. 63/Proposed Rules, Environmental Protection Agency, 40 CFR Part 98, 2013 Revisions to the Greenhouse Gas Reporting Rule and Proposed Confidentiality Determinations for New or Substantially Revised Data Elements, **78** (2013)
2. European Commission Global Methane Reduction Actions, Ref. Ares 2843722 (2013).
3. B. Kucharczyk, *Pol. J. Chem. Technol.*, **13**, 57 (2011).
4. M. Berg, S. Jaras, *Appl. Catal. A*, **114**, 227 (1994).
5. V. I. Vedenev, V. S. Arutyunov, V. Y. Basevich, M. Ya. Goldenberg, M. A. Teitelboim, N. Yu. Krymov, *Catal. Today*, **21**, 527 (1994).
6. E. Long, X. Zhang, Li. Yile, Z. Liu, Y. Wang, M. Gong, Y. Chen, *J. Nat. Gas Chem.*, **19**, 134 (2010).
7. J. G. McCarthy, Y.-F. Chang, V. L. Wong, M. E. Johansson, *Div. Petrol. Chem.*, **42**, 158 (1997).
8. K. Sekizawa, K. Eguchi, H. Widjaja, M. Machida, H. Arai, *Catal. Today*, **28**, 245 (1996). H. Widjaja, K. Sekizawa, K. Eguchi, H. Arai, *Catal. Today*, **47**, 95 (1999).
9. H. Widjaja, K. Sekizawa, K. Eguchi, H. Arai, *Catal. Today*, **47**, 95 (1999).

10. Y. Liu, S. Wang, D. Gao, T. Sun, C. Zhang, S. Wang, *Fuel Process. Technol.*, **111**, 55 (2013).
11. D. König, W. H. Weber, B. D. Poindexter, J. R. McBride, G. W. Graham, K. Otto, *Catal. Lett.*, **29**, 329 (1994).
12. G. B. Hound, Zh. H. Li, W. S. Epling, T. Gobel, P. Schneider, H. Hahn, *React. Kinet. Catal. Lett.*, **70**, 97 (2000).
13. K. Knizek, Z. Jirak, J. Hejtmanek, M. Veverka, M. Maryško, G. Maris, T. T. M. Palstra, *Eur. Phys. J. B*, **47**, 213 (2005).
14. R. D. Shannon, *Acta Crystallogr.*, **A32**, 751 (1976).

ПЪЛНО ОКИСЛЕНИЕ НА МЕТАН ВЪРХУ ЗАМЕСТЕН С ПАЛАДИЙ ПЕРОВСКИТ  
 $\text{LaCu}_{0.5}\text{Mn}_{0.5}\text{O}_3$

Цв. Лазарова, П. Цветков, В. Тумбалева, С. Атанасова-Владимирова<sup>1</sup>, Г. Иванов, Ант. Найденов,  
Д. Ковачева\*

*Институт по обща и неогранична химия, Българска академия на науките, ул. „Акад. Г. Бончев” бл. 11,  
1113, София, България*

<sup>1</sup>*Институт по физикохимия, Българска академия на науките, ул. „Акад. Г. Бончев” бл. 11,  
1113, София, България*

Постъпила на 25 септември 2015 г.; Преработена на 3 декември 2015 г.

(Резюме)

За получаване на Б-катионно заместени перовскитови състави  $\text{LaCu}_{0.5}\text{Mn}_{0.5}\text{O}_3$  и  $\text{LaCu}_{0.45}\text{Pd}_{0.05}\text{Mn}_{0.5}\text{O}_3$  бе използван метода синтез чрез изгаряне от разтвор с използване на гориво урея с оглед възможното им приложение като катализатори за изгаряне на метан. Влиянието на заместването на Cu с Pd върху физико-химичните свойства на катализаторите беше изследвано с помощта на прахова рентгенова дифракция (РД), нискотемпературна адсорбция на азот (БЕТ) и сканираща електронна микроскопия (SEM). Резултатите за влиянието на паладия при заместването на Cu показват, че включването на Pd в кристалната структура води до получаване на материал с по-висока термична стабилност и с подобрени каталитични свойства в сравнение с  $\text{LaCu}_{0.5}\text{Mn}_{0.5}\text{O}_3$ .

## Effect of carbon in cobalt-silica-carbon composite catalysts for NO reduction by CO

N. Stoeva, I. Spassova\*, R. Nickolov<sup>1</sup>, G. Atanasova, M. Khristova

*Institute of General and Inorganic Chemistry, Bulgarian Academy of Sciences, 1113 Sofia, Bulgaria*

<sup>1</sup> *University of Chemical Technology and Metallurgy, 8 Kliment Ohridski Blvd., 1756 Sofia, Bulgaria*

Received: September 29, 2015; Revised December 7, 2015

Cobalt-silica-carbon composites were prepared by sol-gel method and tested as catalysts for NO reduction by CO. Active carbons of different texture parameters were used for synthesis of these composites. A cobalt-silica composite was also prepared for comparison purposes. The catalysts were characterized by low-temperature nitrogen adsorption, X-ray diffraction (XRD), and X-ray photoelectron spectroscopy (XPS) and tested in NO reduction by CO up to 300°C. Carbon-containing composites were found to exhibit a considerably higher activity in NO reduction by CO than a cobalt-silica catalyst even at low temperatures. A significant difference in transient responses between carbon-containing and carbon-free composition samples was observed revealing different rate controlling steps of the reaction. Carbon presence in cobalt-silica-carbon composites greatly influenced their microstructure including Co<sub>3</sub>O<sub>4</sub> crystalline domain size, surface area, surface composition, and oxidation state, which strongly affected catalyst performance. An increased activity could be due to cobalt sites of different oxidation state with silicon and carbon atoms in their vicinity.

**Keywords:** silica-carbon composites, sol-gel method, cobalt catalyst, NO reduction by CO.

### INTRODUCTION

NO<sub>x</sub> gases from stationary and mobile combustion sources induce a negative impact on the environment. Various methods for removing these emissions have recently been developed. Selective catalytic reduction (SCR) has been found to be an effective means for NO<sub>x</sub> removal by catalytic reduction to nitrogen in presence of reducing agents. Many active metals (Pd, Rh, Pt, Cu, Ni, Fe, Co, V, Mn, and Zn [1–4]), and catalyst preparation techniques (impregnation, sol-gel method, and coprecipitation [5–7]) have been studied. It is known that plenty of industrially applied catalysts consist of metals or metal compounds supported on a suitable support, the main role of which is to maintain the active phase in a highly divided state. However, it is proved that the role of the support is not only that of a carrier but it may contribute to the catalytic activity and can also react to some extent with other catalyst ingredients during preparation. Further, the interaction between active phase and support can affect the catalytic activity. Among many possible supports, practically only three combine an optimal chemical composition, surface area, stability, and mechanical properties, and they account for the most widely used industrial supported catalysts: alumina, silica, and carbon [8]. One of the most active catalysts for NO<sub>x</sub> elimination, that was expected to replace noble metal

catalysts, has been found to be a cobalt-based material [9–12]. In order to achieve high cobalt dispersion and reduce costs, various supports have been used, including silica, alumina, titania, and carbon. The structure of these supports and their properties, such as pore diameter, pore volume, and surface area can significantly influence cobalt dispersion and catalyst reducibility and activity/selectivity. Song and Li [13] have studied Co/SiO<sub>2</sub> catalysts with silica pore sizes of 2.4–15.8 nm and have found that larger SiO<sub>2</sub> pore sizes caused the formation of larger Co<sub>3</sub>O<sub>4</sub> crystallites, but the larger sizes also resulted in lower Co dispersion. Mesoporous silicas, MCM-41 and SBA-15, of different pore diameters [14–15] have also been selected to evaluate the effect of support porosity on cobalt dispersion. Compared with conventional metal oxide supports, active carbons (AC) display special properties, such as high purity, high mechanical strength, good electrical conductivity, and large surface area [16–19], and they are increasingly attracting considerable attention as potential supports. Fu *et al.* have found that carbon structure and cobalt dispersion determine CO conversion [20]. A high catalytic activity has been achieved by an active finely dispersed copper phase on an AC support [21]. Acidic pretreatment of the support was found to be favourable in SCR of NO<sub>x</sub> [22]. Silica is able to adsorb various gaseous and liquid compounds *via* both isolated and H-bonded surface OH groups. Wide applications of carbons are associated with surface hydrophobicity, good thermal stability, high

\* To whom all correspondence should be sent  
E-mail: ispasova@svr.igic.bas.bg

surface area, and large pore volume. It was of interest to combine a few properties of two types of material, i.e. hydrophilic silica and hydrophobic carbon, and to use the resulting material as a support for cobalt catalysts in NO reduction. A better understanding of the relationship between support features and catalytic performance of the cobalt catalyst is important for designing a better cobalt catalyst.

The objective of this study was to investigate composite catalysts based on cobalt, silica, and different ACs in the reduction of NO by CO and to find a relationship between composite porous characteristics and catalytic performance.

## EXPERIMENTAL

Sol-gel prepared cobalt-silica-carbon composites were prepared by adding  $\text{Co}(\text{NO}_3)_2$ , tetraethyl orthosilicate (TEOS), and carbon during the sol-gel process using an alkaline catalyst ( $\text{NH}_4\text{OH}$ ). TEOS,  $\text{HNO}_3$ , ethanol, and water were placed in a glass tube at room temperature and heated upon stirring to a temperature of 80–85°C under reflux conditions. The solution was kept at this temperature for 2 h. After that, the necessary amounts of metal nitrate and carbon were added into the mixture and stirred for 1 h. To obtain gel,  $\text{NH}_4\text{OH}$  was introduced to the solution. After aging for a day, the composites were dried at 120°C to obtain homogeneous solid catalysts, which were calcined at 300°C for 4 h. Inserted carbon and cobalt were 8 wt.%. Three hydrophobic active carbons (AC1, AC2, and AC3) of different texture parameters were used to prepare the catalysts, where AC1 was made of apricot shells, whereas AC2 and AC3 originated from coal and coconut shells, respectively. The samples were denoted as Co/Si-AC1, Co/Si-AC2, and Co/Si-AC3. A carbon-free catalyst, Co/Si, of the same cobalt content was prepared for comparison purposes.

Texture characteristics were determined by low-temperature (77.4 K) nitrogen adsorption on a NOVA 1200e apparatus (Quantachrome Instruments, USA). Nitrogen adsorption-desorption isotherms were analysed to evaluate specific surface areas ( $S_{\text{BET}}$ ),

based on the BET equation, and total pore volumes ( $V_t$ ), estimated in accordance with Gurvich rule. Values of micropore volume ( $V_{\text{MI}}$ ), specific surface area related to micropores ( $S_{\text{MI}}$ ), and external specific surface area ( $S_{\text{ext}}$ ) were assessed according to the V-t method [23]. Additionally, pore size distributions were calculated applying the NLDFT method using equilibrium models with cylindrical pores (for silica), a slit shape (for carbon), and slit-shaped/cylindrical pores in carbons (for silica-carbon) [24].

Powder XRD patterns were collected within the range of 10 to 80° 2 $\theta$  on a Bruker D8 Advance diffractometer with Cu  $K_\alpha$  radiation and a LynxEye detector. Average crystallite sizes were evaluated by using Scherrer equation.

XPS measurements were performed in the UHV chamber of an ESCALAB-Mk II (VG Scientific) electron spectrometer with Al  $K_{\alpha 1,2}$  radiation ( $h\nu = 1486.6$  eV). The surface composition was obtained from the ratio of the corresponding intensities of C 1s, O 1s, Si 2p, Co 2p photoelectron peaks corrected by the Scofield's [25] photoionization cross-sections. The spectra were calibrated according to the Si 2p peak at 103.4 eV.

The catalytic experiments were carried out in a flow apparatus with an isothermal flow reactor in the temperature range of 20–300°C. After each catalytic measurement a temperature-programmed desorption (TPD) run at 25°C was carried out. The transient response method was used to study the interaction between gas phase and catalyst surface.

## RESULTS AND DISCUSSION

Table 1 presents adsorption properties of initial carbon materials and prepared composites.

Texture parameters of the initial ACs as specific surface area, pore volume, and micro-meso porosity are quite different. The resulting composites have specific surface areas more close to the cobalt-silica composite than to AC ingredients. However, addition of carbon led to increased  $S_{\text{BET}}$  and decreased  $V_t$  compared to the pure cobalt-silica. Carbon microporosity reflected strongly micropore availability of

**Table 1.** Texture parameters of active carbons, cobalt-silica, and cobalt-silica-carbon composites

Sample	$S_{\text{BET}}$ $\text{m}^2\text{g}^{-1}$	$S_{\text{ext}}$ $\text{m}^2\text{g}^{-1}$	$V_t$ $\text{cm}^3\text{g}^{-1}$	$V_{\text{mi}}$ $\text{cm}^3\text{g}^{-1}$	$V_{\text{mes}}$ $\text{cm}^3\text{g}^{-1}$	$V_{\text{mi}}/V_{\text{mes}}$	$D_{\text{av}}$ nm
AC1	700	158	0.38	0.22	0.16	1.38	2.2
AC2	804	183	0.50	0.25	0.25	1.00	2.5
AC3	1108	232	0.55	0.38	0.17	2.24	1.9
Co/Si-AC1	553	222	0.34	0.14	0.20	0.70	2.5
Co/Si-AC2	579	418	0.39	0.07	0.32	0.22	2.7
Co/Si-AC3	565	199	0.30	0.16	0.14	1.14	2.1
Co/Si	533	349	0.30	0.08	0.22	0.35	2.4

the composites. For the Co/Si-AC2 composite, the main part of the pore volume belonged to the mesoporous space with a minor contribution of micropores. Additionally, this sample had the highest specific surface area and pore volume.

Figure 1 displays adsorption-desorption isotherms (a) and pore size distribution (PSD) curves (b) of the composites (shifted). One can see differences in porous texture.

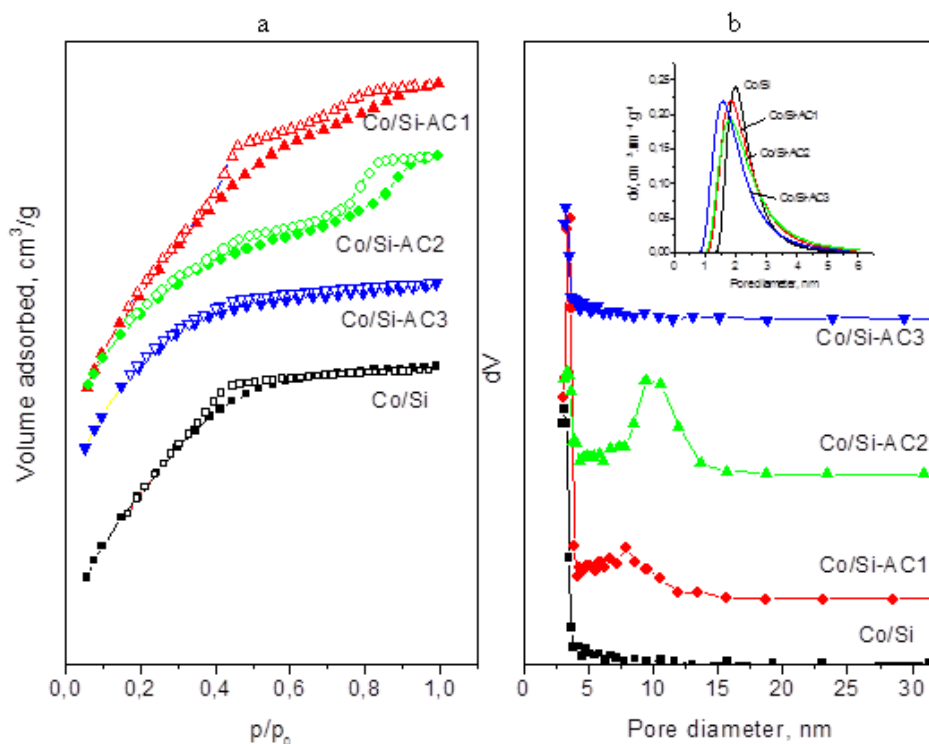
The adsorption-desorption isotherms are of the I/IV type according to IUPAC classification. They reveal influence of texture parameters of the ACs modifiers on the sol-gel process in presence of cobalt. The role of the cobalt salt in the process is most clearly evident with the Co/Si sample, which is a fine mesopore material, so Co is related primarily to reducing mesopore size (Fig. 1b), as also reported in Ref. [26]. AC3 is a micro-mesoporous material having the highest specific surface and external area whereas Co/Si-AC3 was a composite of the most developed microporosity due to AC3 contribution. The slope in the isotherm is a result of adsorption along with capillary condensation on the external surface. The hysteresis loops observed with Co/Si-AC2 and Co/Si-AC1 indicate at least a bidisperse mesoporous texture due to conflicting contribution of the two modifiers: cobalt and active carbon. One could suggest that if cobalt contributed to a fine pore formation, AC might have led to larger pores including formation of globules on the external

surface. As used ACs could sorb cobalt ions, they counteracted the effect of Co and caused the occurrence of areas of different thickness.

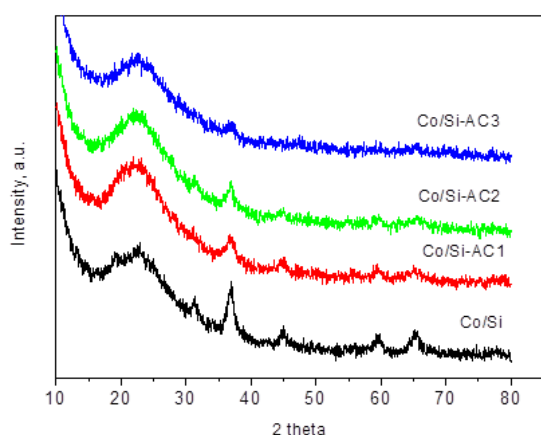
XRD data are shown in figure 2. The diffraction pattern at around  $22.5^\circ$  with a broad peak could be attributed to amorphous silica with a contribution of broad diffraction features due to a turbostratic structure of disordered carbon (expected at  $26.5^\circ$ ).

A Co/Si sample (PDF 71-4921) with crystallite sizes of  $\sim 10$  nm demonstrates well-defined reflections, which are typical of  $\text{Co}_3\text{O}_4$ :  $2\theta$   $19.1^\circ$ ,  $31.45^\circ$ ,  $37.06^\circ$ ,  $45.07^\circ$ ,  $59.71^\circ$ ,  $65.64^\circ$ . No shift of diffraction peaks was observed with respect to a conventional  $\text{Co}_3\text{O}_4$  spinel indicating that no Si-containing solid solution has been formed. At the same time, small reflections, typical of  $\text{Co}_3\text{O}_4$ , were registered for the AC-containing samples, probably due to higher Co dispersion (Fig. 2) and smaller particle sizes. The average diameter of the crystallites in these cases, based on calculations by Scherrer equation, was about 6–7 nm, thus indicating higher dispersion of the cobalt particles in the carbon-containing composites.

XPS measurements were carried out to investigate the presence, content, and chemical state of silicon, carbon, cobalt, and oxygen in the samples. Surface compositions derived from respective peak areas are given in Table 2. XPS spectra of Si 2p and O 1s (not presented) indicate that these elements are mainly in the  $\text{SiO}_2$  oxide form.



**Fig. 1.** Adsorption-desorption isotherms (a) and pore size distribution (b) of synthesized composites.



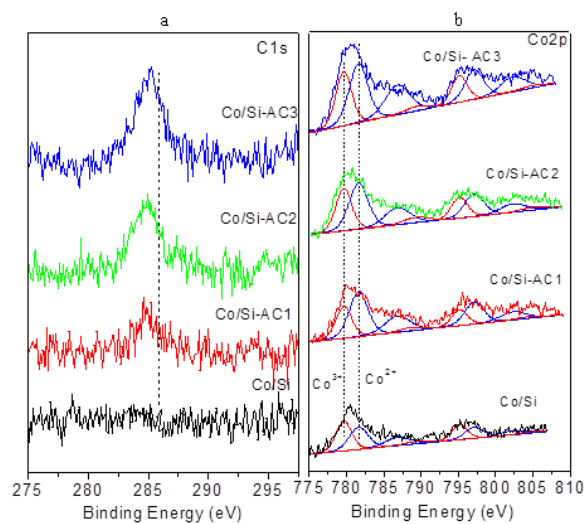
**Fig. 2.** XRD patterns of cobalt-silica-carbon and cobalt-silica composites.

Figure 3 discloses XPS spectra of C 1s (a) and Co 2p (b) of the investigated catalysts. For the cobalt-silica-carbon composites, one peak at 284.8 eV was registered in the C 1s spectra. Binding energies (BEs) of about 284.8–285.2 eV could be attributed to overlapping peaks of  $sp^2$ - and  $sp^3$ -hybridized as well as adventitious carbon phases [27]. Evaluation of Co 2p narrow scans allows assigning cobalt oxidation state.  $Co^{2+}$  and  $Co^{3+}$  ions could be distinguished by the binding energies and intensities of shakeup peaks. Whereas  $Co^{3+}$  ions show only very weak shakeup peaks with a main signal at  $\sim 791$  eV,  $Co^{2+}$  has pronounced shakeup peaks at about 785 and 801 eV [28]. The binding energies of the Co  $2p_{3/2}$  and Co  $2p_{1/2}$  peaks are at 780.4 and 795.9 eV, respectively, with splitting energies at 15.5 eV indicating that  $Co_3O_4$  has been mainly in the form of a spinel phase [29, 30]. The Co 2p spectra were further deconvoluted into  $Co^{2+}$  and  $Co^{3+}$ , respectively. Co 2p peaks at  $\sim 779.6$ , 789.3, 795.1, and 804.8 eV are characteristic of  $Co^{3+}$ , while the peaks at 781.6, 786.8, 797.1, and 802.3 eV correspond to  $Co^{2+}$ .

Shakeup satellites at about 787.1 eV, the latter being an intermediate value compared with that for CoO (785 eV) and  $Co_3O_4$  (789 eV) [28], indicate a higher presence of  $Co^{2+}$  species on the surface compared to stoichiometric  $Co_3O_4$  (Fig. 3 and Table 2). Such a surface enrichment in  $Co^{2+}$  has been registered for cobalt-silica catalysts [31]. However, the AC containing composites have more  $Co^{2+}$  species evidencing a reductive role of the carbon along with supporting higher dispersion of the cobalt particles (Fig. 3 and Table 2).

XPS studies indicate that cobalt ion distribution over the surface and into the bulk is dependent on carbon ingredient type used and micro-mesoporous space formed. Cobalt particles penetrate into the bulk if the mesopore volume is higher (Co/Si-AC2)

and stay on the surface if the micropore space is significant (Co/Si-AC1 and Co/Si-AC3). The highest cobalt-rich surface was that of Co/Si which is logical bearing in mind its fine porous structure hindering cobalt penetration. Hence, carbon presence has influence on cobalt distribution between surface and the bulk. These results confirm data on adsorption measurements. Quantitative XPS results showed that the molar Si/Co ratio at the surface was much higher than that of the bulk. The same tendency was observed for carbon confirming that most of the silica was on the surface of the catalysts.



**Fig. 3.** XPS spectra of C 1s (a) and Co 2p (b) of cobalt-silica-carbon and cobalt-silica composites.

**Table 2.** Surface compositions derived from XPS

Sample	C, at. %	O, at. %	Si, at. %	Co, at. %	$Co^{3+}/Co^{2+}$
Co/Si-AC1	3.5	60.2	35.7	0.6	0.61
Co/Si-AC2	4.1	59.3	35.7	0.9	0.48
Co/Si-AC3	2.4	62.4	34.2	1.0	0.55
Co/Si	–	63.7	34.8	1.5	0.89

Figure 4 illustrates a temperature dependence of NO conversion degree and the respective TPD profiles. The investigation showed that the reduction of NO by CO proceeded to nitrogen, i.e. no  $N_2O$  was registered in the whole temperature interval. The cobalt-silica catalyst was slightly active whereas carbon addition led to a significant increase in catalytic activity: all cobalt-silica-carbon catalysts manifested a high activity by CO toward NO even at 100°C. Co/Si-AC2 demonstrated a 70% conversion of NO to nitrogen at 200°C and almost 100% activity at 300°C. TPD spectra of NO indicated no desorption from Co/Si. The carbon-containing samples desorbed NO in the temperature range of 100–250°C. It is evident that they desorbed different amounts of NO. One broad NO desorption peak for

Co/Si-AC1 and Co/Si-AC2 is available in the upper interval considering a variety of NO adsorbed species, while for Co/Si-AC3 two distinct desorption peaks are observed. The amount of desorbed NO from Co/Si-AC1 and Co/Si-AC2 was more than that with Co/Si-AC3, which coincides with the order of activity of the investigated samples. The role of composite texture was decisive. It can be seen in figure 1b and table 1 that enhanced  $V_{mes}$  enables better mass transfer of reagents and products.

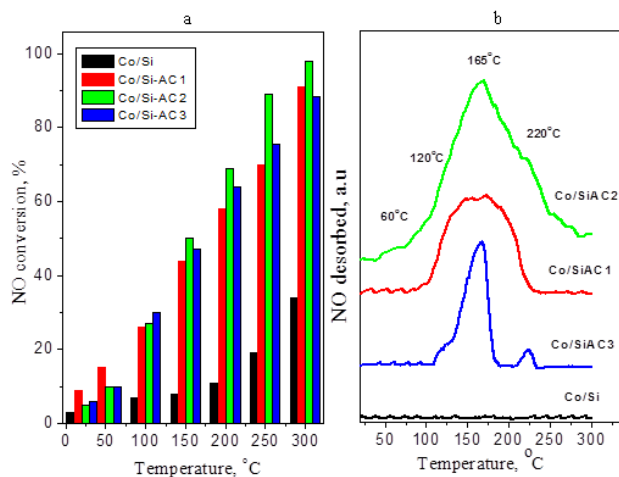


Fig. 4. Temperature dependence of NO conversion degree (a) and TPD spectra of NO (b).

Figure 5 displays response curves of the NO and CO reagents and  $N_2$  and  $CO_2$  products at a temperature of 50, 100, 200, and 300°C. Differences in the curves reveal different rate-controlling steps of the reaction over the catalysts and a change in the rate-controlling step is associated with a change of reaction mechanism. A significant difference in the response curves was observed for samples with and without AC in the composition. The response curves for NO and CO at 50°C on Co/SiAC1 and Co/SiAC2 are of an overshoot type, while responses of Co/Si and Co/SiAC3 are of a momentous and monotonically growing type. The overshoot response indicates that the rate-limiting step is concurrent adsorption of the reagent or regeneration of the active centres. With the less active cobalt-silica-carbon catalyst, an overshoot response appeared only at 200°C. The momentous response shows that the rate-limiting step is associated with surface reaction or adsorption of the reagents. The monotonically growing type response reveals that a combination between surface reaction and product slow desorption is the rate-limiting step. NO and CO desorption curves of Co/SiAC3 at temperatures up to 200°C at stop-stages show that the rate-limiting step is related to adsorption of the reagents and their slow desorption. The results of transient responses support the TPD studies presented above.

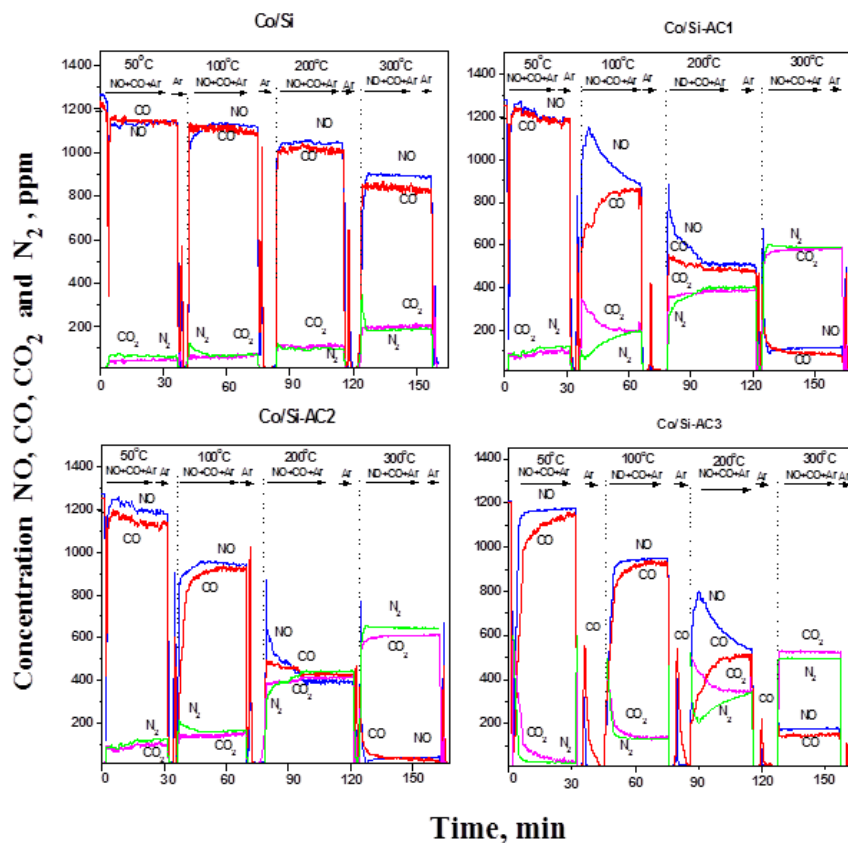


Fig. 5. Transient response curves of NO, CO,  $CO_2$ , and  $N_2$ .

Catalytic measurements of abiotic hematite and a thermally treated biomass sample in the flow-type glass reactor showed that at temperatures below 240°C the abiotic sample is a little bit more active. Both materials demonstrate the same CO conversion level in the reaction of CO oxidation at temperatures higher than 240°C (Fig. 6). Spectra of spent samples after the catalytic tests did not show any changes under reaction conditions (cf. spectra 'a' and 'b' in Fig. 4 and spectra 'b' and 'c' in Fig. 5). Despite the different methods of sample synthesis that result in different original iron oxide phases, the catalytic performance in the reaction of CO oxidation is very close.

### CONCLUSION

Cobalt-silica-carbon composites exhibit a considerably higher activity in NO reduction by CO than cobalt-silica catalyst even at low temperatures. The presence of carbon greatly influences the microstructure (including crystalline size of Co<sub>3</sub>O<sub>4</sub>, surface area, surface composition, and oxidation state) of the cobalt-silica-carbon composites, which may strongly affect catalyst performance. An increased activity could be due to cobalt sites of different oxidation state with Si and C atoms in their vicinity.

*Acknowledgements:* This work was financially supported by the European Social Fund through Grant BG051PO001-3.3.06-0050 and by the Bulgarian Science Fund (Grant E02/2- 2014).

### REFERENCES

- G. M. Tonetto, M. L. Ferreira, D. E. Damiani, *J. Mol. Catal. A-Chem.*, **193**, 121 (2003).
- P. S. Dimick, J. L. Kross, E. G. Roberts, R. G. Herman, H. G. Stenger, C. E. Lyman, *Appl. Catal. B-Environ.*, **89**, 1 (2009).
- H. H. Tseng, H. Y. Lin, Y. F. Kuo, Y. T. Su, *Chem. Eng. J.*, **160**, 13 (2010).
- J. Zhu, F. Gao, L. Dong, W. Yu, L. Qi, Z. Wang, L. Dong, Y. Chen, *Appl. Catal. B-Environ.*, **95**, 144 (2010).
- C. Y. Lu, M. C. Wei, S. H. Chang, M. Y. Wey, *Appl. Catal. A-Gen.*, **354**, 57 (2009).
- X. Gao, Y. Jiang, Y. Zhong, Z. Luo, K. Cen, *J. Hazard. Mater.*, **174**, 734 (2010).
- F. Zhang, S. Zhang, N. Guan, E. Schreier, M. Richter, R. Eckelt, R. Fricke, *Appl. Catal. B-Environ.*, **73**, 209 (2007).
- F. Rodriguez-Reinoso, *Carbon*, **36** (3), 159 (1998).
- B. Meng, Z. Zhao, X. Wang, J. Liang, J. Qiu, *Appl. Catal. B-Environ.*, **129**, 491 (2013).
- X. Chen, J. Zhang, Y. Huang, Z. Tong, M. Huang, *J. Environ. Sci.*, **21**, 1296 (2009).
- A. E. Palomares, A. Uzcátegui, A. Corma, *Catal. Today*, **137** (2–4), 261 (2008).
- F. Lónyi, J. Valyon, L. Gutierrez, M. A. Ulla, E. A. Lombardo, *Appl. Catal. B-Environ.*, **73** (1–2), 1 (2007).
- D. Song, J. Li, *J. Mol. Catal. A-Chem.*, **247**, 206 (2006).
- A. Y. Khodakov, A. Griboval-Constant, R. Bechara, F. Villain, *J. Phys. Chem. B*, **105**, 9805 (2001).
- H. F. Xiong, Y. H. Zhang, K. Y. Liew, J. L. Li, *J. Mol. Catal. A-Chem.*, **295**, 68 (2008).
- R. Q. Long, R. T. Yang, *Ind. Eng. Chem. Res.*, **40**, 4288 (2001).
- M. Hussain, J. S. Yun, S. K. Ihm, N. Russo, F. Geobaldo, *Ind. Eng. Chem. Res.*, **50**, 2530 (2011).
- Y. H. Hu, E. Ruckenstein, *Ind. Eng. Chem. Res.*, **43**, 708 (2004).
- C. H. See, A. T. Harris, *Ind. Eng. Chem. Res.*, **46**, 997 (2007).
- T. Fu, J. Lv, Z. Li, *Ind. Eng. Chem. Res.*, **53**, 1342 (2014).
- C. Y. Lu, M. Y. Wey, Y. H. Fu, *Appl. Catal. A-Gen.*, **344**, 36 (2008).
- K.-H. Chuang, C.-Y. Lu, M.-Y. Wey, Y.-N. Huang, *Appl. Catal. A-Gen.*, **397**, 234 (2011).
- B. C. Lippens, J. H. de Boer, *J. Catal.*, **4**, 319 (1965).
- A. V. Neimark, P. I. Ravikovitch, *Micropor. Mesopor. Mater.*, **44/45**, 697 (2001).
- J. Scofield, *J. Electron. Spectrosc. Relat. Phenom.*, **8**, 129 (1976).
- G. A. Santos, C. M. B. Santos, S. W. da Silva, E. A. Urquieta-González, P. P. Confessori Sartoratto, *Colloids Surf. A-Physicochem. Eng. Aspects*, **395**, 217 (2012).
- M. V. Sopinsky, V. S. Khomchenko, V. V. Strelchuk, A. S. Nikolenko, G. P. Olchovyk, V. V. Vishnyak, V. V. Stonis, *Nanoscale Res. Lett.*, **9**, 182 (2014).
- A. D. Pandey, C. Jia, W. Schmidt, M. Leoni, M. Schwickardi, F. Schüth, C. Weidenthaler, *J. Phys. Chem. C*, **116**, 19405 (2012).
- S. W. Ho, M. Houalla, D. M. Hercules, *J. Phys. Chem.*, **94**, 6396 (1990).
- H. A. E. Hagelin-Weaver, G. B. Hoflund, D. M. Minahan, G. N. Salaita, *Appl. Surf. Sci.*, **235**, 420 (2004).
- C.-J. Jia, M. Schwickardi, C. Weidenthaler, W. Schmidt, S. Korhonen, B. M. Weckhuysen, F. Schüth, *J. Am. Chem. Soc.*, **133**, 11279 (2011).
- S. Zhang, J. Shan, Y. Zhu, L. Nguyen, W. Huang, H. Yoshida, S. Takeda, F. Tao, *Nano Lett.*, **13**, 3310 (2013).
- X. Chen, A. Zhu, C. Shi, *Catal. Lett.*, **133**, 134 (2009).
- J. Li, G. Lu, G. Wu, D. Mao, Y. Guo, Y. Wang, Y. Guo, *RSC Adv.*, **3**, 12409 (2013).
- L. Xue, C. Zhang, H. He, Y. Teraoka, *Appl. Catal. B-Environ.*, **75**, 167 (2007).

## ВЛИЯНИЕ НА ВЪГЛЕРОДА В КОБАЛТ-СИЛИКАТНО-ВЪГЛЕРОДНИ КОМПОЗИТНИ КАТАЛИЗАТОРИ ЗА РЕДУКЦИЯ НА NO С CO

Н. Стоева, Ив. Спасова\*, Р. Николов<sup>1</sup>, Г. Атанасова, М. Христова

*Институт по обща и неорганична химия, Българска академия на науките, 1113 София, България*

<sup>1</sup> *Химико-технологичен и металургичен университет, Бул. „Климент Охридски“ 8, 1756 София, България*

Постъпила на 29 септември 2015 г.; Преработена на 7 декември 2015 г.

(Резюме)

Кобалт-силикатно-въглеродни композити са получени по зол-гел метод и са тествани като катализатори за редукция на азотен оксид с въглероден оксид. Активни въглени с различни текстурни параметри са използвани за синтез на композитите. За сравнение е получен кобалт-силикатен композит. Катализаторите са охарактеризирани посредством нискотемпературна адсорбция на азот, рентгенова дифракция (XRD), рентгенова фотоелектронна спектроскопия (XPS) и тествани за редукция на NO с CO при температури до 300°C. Намерено е, че въглерод-съдържащите композити показват значително по-добра активност от кобалт-силициево оксиден катализатор при редукция на NO с CO дори при ниски температури. Наблюдава се значителна разлика във вида на кривите на отклик на образците с и без въглерод, разкриваща различни определящи скоростта етапи при тях. Наличието на въглерод влияе значително на микроструктурата (включително размер на  $\text{Co}_3\text{O}_4$  кристали, специфична повърхност, повърхностен състав и окислително състояние) на кобалт-силикатно-въглеродните композити, което се отразява върху каталитичната им активност. Повишената активност вероятно се дължи на кобалтови йони в различни окислителни състояния в близост до силициеви и въглеродни атоми.

## Purification of hydrogen-rich streams from CO<sub>2</sub> by methanation

M. V. Gabrovska<sup>1\*</sup>, R. M. Edreva-Kardjieva<sup>1</sup>, M. G. Shopska<sup>1</sup>, D. A. Nikolova<sup>1</sup>,  
L. P. Bilyarska<sup>1</sup>, D. Crişan<sup>2</sup>, M. Crişan<sup>2</sup>

<sup>1</sup>*Institute of Catalysis, Bulgarian Academy of Sciences, Acad. G. Bonchev St. Bldg. 11, 1113 Sofia, Bulgaria*  
<sup>2</sup>*Ilie Murgulescu Institute of Physical Chemistry, Romanian Academy, 202 Splaiul Independentei St.,  
060021 Bucharest-12, Romania*

Received: September 12, 2015; Revised December 14, 2015

Magnesium effect on structure and activity of coprecipitated Ni-Al layered double hydroxides as catalyst precursors for purification of hydrogen-rich streams from CO<sub>2</sub> by methanation was examined. Various M<sup>2+</sup>/Al<sup>3+</sup> (M<sup>2+</sup> = Ni<sup>2+</sup>, Ni<sup>2+</sup>+Mg<sup>2+</sup>) molar ratios (1.5 and 3.0), reduction and reaction temperatures as well as gas hourly space velocities (GHSV) were applied. Magnesium content was identical, at the expense of nickel, in both modified samples.

All catalysts prepared by reduction at 400, 450, 530, or 600°C hydrogenated carbon dioxide successfully to 0–10 ppm levels at reaction temperatures in the range of 400–320°C and GHSV from 3000 to 22000 h<sup>-1</sup>. Highly loaded nickel catalysts (3.0NiAl and 3.0NiMgAl) manifested a tendency to be more active than low loaded materials (1.5NiAl and 1.5NiMgAl).

At lower reaction temperatures (280 and 260°C) after reduction at 400 and 450°C, non-modified 3.0NiAl and 1.5NiAl catalysts' activity was attributed to larger specific surface areas and smaller particle sizes of metal nickel (higher Ni dispersion). Further treatment of the catalysts at 530 and 600°C induced sintering of the nickel metal particles, thus leading to a decrease of methanation activity.

The Mg-containing catalysts had the advantage of preserving nickel metal dispersion after reduction above 500°C due to a retarding effect on Ni sintering.

The Mg-modified highly loaded Ni catalyst (3.0NiMgAl) can be recommended as a suitable material for deep CO<sub>2</sub> removal from hydrogen-rich gas streams through the methanation reaction at low temperatures, such as 240 and 220°C.

**Keywords:** Ni-Al layered double hydroxides, Mg modifier, CO<sub>2</sub> removal by methanation

### INTRODUCTION

Coal conversion and utilization technologies are gaining considerable attention because of increasing prices and demand of oil. Synthetic natural gas (SNG) production from coal is considered promising for obtaining valuable gaseous fuel with high combustion efficiency and environment friendliness [1–5]. The methanation reaction represents a key step in coal-to-SNG production, where the catalytic hydrogenation of carbon oxides (CO and CO<sub>2</sub>) provides an efficient alternative to conventional natural gas [6].

The hydrogenation of carbon dioxide to methane, also called the Sabatier reaction or methanation, can be used as a particularly promising technique for purification of H<sub>2</sub>-rich streams from traces of CO<sub>2</sub> to prevent catalyst poisoning especially in the fuel cell anode technology and ammonia synthesis industry [7–11]. The methanation reaction is commonly applied in ammonia plants at the final stage of purification of the synthesis gas in which low-

concentration carbon monoxide and carbon dioxide (0.1–0.5%) are catalytically removed. The reaction is of crucial importance due to the poisonous effect of carbon oxides on ammonia synthesis [8].

Although many metals such as Ni, Co, Fe, Ru, Rh, etc., supported on various oxide carriers (e.g., SiO<sub>2</sub>, TiO<sub>2</sub>, Al<sub>2</sub>O<sub>3</sub>, ZrO<sub>2</sub>, and CeO<sub>2</sub>) have been used to catalyse the reaction, nickel and ruthenium are the most effective [11]. Nickel catalysts have been extensively investigated because of the metal availability and economic considerations. With regard to this, industrial methanation catalysts are essentially based on metal nickel demonstrating high activity, selectivity toward methane formation in preference to other hydrocarbons, high thermal stability, and relatively low cost [7, 12, 13].

Methanation catalysts are exposed to extreme conditions owing to the highly exothermic nature of the CO<sub>2</sub> methanation reaction and the fact that steam is one of the reaction products: CO<sub>2</sub> + 4H<sub>2</sub> → CH<sub>4</sub> + 2H<sub>2</sub>O, ΔH<sub>300°C</sub> = -175.4 kJ.mol<sup>-1</sup> [7]. Overheating, sintering, and deactivation of the catalysts occur due to nickel crystallite growth with resultant reduction of the active nickel surface area. These phenomena require usage of mechanically and

\* To whom all correspondence should be sent  
E-mail: margo@ic.bas.bg

© 2015 Bulgarian Academy of Sciences, Union of Chemists in Bulgaria

thermally stable supports such as stable to sintering alumina.

A major requirement in manufacturing Ni/Al<sub>2</sub>O<sub>3</sub> catalysts is the catalyst to be sufficiently active to ignite the reaction at low temperatures, i.e. to contain a relatively large portion of nickel metal, usually over 60 wt.%. Ni-Al layered double hydroxides (LDHs) with takovite-like (TKI) structure can be obtained from Ni and Al salts at Ni<sup>2+</sup>/Al<sup>3+</sup> molar ratios between 1.0 and 5.6 in the fresh precipitates corresponding to 59.5–88.0 and 40.5–12.0 wt.% of NiO and Al<sub>2</sub>O<sub>3</sub>, respectively, as it has been documented in Ref. 14. In our recent study [15], we specified that Ni-Al LDHs with TKI structure are effective catalyst precursors for complete CO<sub>2</sub> removal from hydrogen-rich gas stream by methanation reaction.

Ni-Al LDHs belong to a great group of natural and synthetic inorganic lamellar compounds with a chemical composition of general formula [Ni<sup>2+</sup><sub>1-x</sub>Al<sup>3+</sup><sub>x</sub>(OH)<sub>2</sub>]<sup>x+</sup>[A<sup>n-</sup><sub>x/n</sub>]<sup>x-</sup>·mH<sub>2</sub>O, where Ni<sup>2+</sup> and Al<sup>3+</sup> ions are located in the brucite-like hydroxide layers. Charge compensating exchangeable anions (A<sup>n-</sup>) such as CO<sub>3</sub><sup>2-</sup>, NO<sub>3</sub><sup>-</sup>, SO<sub>4</sub><sup>2-</sup>, Cl<sup>-</sup>, etc. as well as water molecules are situated in the interlayer space of the layered structure. Here, *x* represents the fraction of Al<sup>3+</sup> cations, and *m* is the number of water molecules. Ni-Al layered systems represent promising catalysts due to their high specific surface area, good distribution of both Ni<sup>2+</sup> and Al<sup>3+</sup> ions despite the high content of Ni<sup>2+</sup> ions, high metal dispersion after reduction, and small crystallite size. A wide variety of M<sup>2+</sup> or M<sup>3+</sup> cations may be incorporated or replaced at the octahedral sites of the brucite-type sheets by other entities having similar ionic radius, thus forming different layered compounds [16–19].

An inspection of the literature suggests that MgO is an effective promoter to minimize the sintering of nickel metal particles [20].

The purpose of the present investigation was to elucidate magnesium dopant effect on the properties and catalytic activity of Ni-Al LDHs with TKI structure in the model reaction of CO<sub>2</sub> methanation.

## EXPERIMENTAL

### Sample preparation

Carbonate forms of TKI precursors with M<sup>2+</sup>/Al<sup>3+</sup> molar ratios of 1.5 and 3.0, where M<sup>2+</sup> = Ni<sup>2+</sup> or M<sup>2+</sup> = Ni<sup>2+</sup> + Mg<sup>2+</sup> were prepared. All precursors were synthesized by coprecipitation of mixed Ni(Mg)-Al nitrate solution with Na<sub>2</sub>CO<sub>3</sub> at constant pH = 8.0 and temperature of 80°C. ‘Pro analyze’ purity grade nitrate salts of the corresponding metals, Ni(NO<sub>3</sub>)<sub>2</sub>·6H<sub>2</sub>O, Mg(NO<sub>3</sub>)<sub>2</sub>·6H<sub>2</sub>O, and

Al(NO<sub>3</sub>)<sub>3</sub>·9H<sub>2</sub>O were used. A more detailed description of the preparation procedure is reported in Ref. 15. A modification of the brucite-like hydroxide layer by partial isomorphous Mg<sup>2+</sup> substitution for the Ni<sup>2+</sup> ions was applied. Magnesium content was identical, at the expense of nickel, in both modified samples. The obtained precipitate was further dried at 80°C for 20 h and named ‘as-synthesized’ precursor, designated as *x*NiAl, where *x* represents the M<sup>2+</sup>/Al<sup>3+</sup> molar ratio, for example 3.0NiAl (Table 1).

### Sample characterization

The chemical composition of the ‘as-synthesized’ materials was determined by inductively coupled plasma atomic emission spectroscopy (ICP-AES) using a JY 38 (Jobin-Yvon) spectrometer.

Powder X-ray diffraction (PXRD) data were collected on a TUR-M 62 conventional HZG-4 powder diffractometer employing CoK<sub>α</sub> radiation (λ = 0.15418 nm). The crystalline phases were identified using Joint Committee on Powder Diffraction Standards (JCPDS) files.

Specific surface area (SSA) of the ‘as-synthesized’ samples was measured employing the single point BET method using a FlowSorb II 2300 Micromeritics apparatus with a N<sub>2</sub>-He mixture (15% N<sub>2</sub>) at the boiling temperature of liquid nitrogen.

Gas-phase hydrogenation of CO<sub>2</sub> to CH<sub>4</sub> was carried out in a fixed-bed flow reactor set-up under ambient pressure. The amount (about 0.8 g) and particle size (0.4–0.8 mm) of the loaded ‘as-synthesized’ precursors were determined based on preliminary accomplished experiments aimed at eliminating mass transfer effects. Catalyst activation was performed by *in situ* reduction in the equipment at two stages.

The first stage consisted of heating the precursors in a flowing mixture of 5 vol.% hydrogen in argon to 150°C and keeping this temperature for 60 min, then heating to 240°C and holding for 60 min. The second stage involved further reduction of the precursors in a pure hydrogen flow consecutively at steps of 400, 450, 530, and 600°C for 3 h. Both reduction procedures were realized at a constant gas hourly space velocity (GHSV) of 2000 h<sup>-1</sup> and a heating rate of 1.7 deg.min<sup>-1</sup>. Catalytic activity measurements were accomplished after each reduction step at atmospheric pressure with a CO<sub>2</sub>/H<sub>2</sub>/Ar mixture of 0.65/34.35/65.0 vol.% in the temperature interval of 220–400°C and GHSV from 3000 to 22000 h<sup>-1</sup>. The catalysts were kept in a steady state for 30 min at each reaction temperature. The GHSV was varied at each reaction temperature until 0–50-ppm CO<sub>2</sub> levels were attained. Residual CO<sub>2</sub>

amount was determined using an online-connected Uras 3G gas analyser (Hartmann-Braun AG). A cooling trap (−40°C) between the reactor and the gas analyser removed the water obtained as a co-product during the reaction. The catalyst bed temperature was measured by a shielded chromel-alumel thermocouple. Gas-mass analysis of the outlet gas mixture was performed on a MS-10 spectrometer.

Hydrogen chemisorption measurements were carried out using a volumetric laboratory set-up at room temperature and hydrogen pressure range of 0–13.33 kPa. The samples were submitted beforehand to *in situ* reduction in the equipment at 400, 450, 530, and 600°C for 3 h with a gaseous mixture of H<sub>2</sub>/Ar (1/2, v/v) at a flow rate of 6.5 l.h<sup>−1</sup> and a heating rate of 2 deg.min<sup>−1</sup>. Monolayer coverage (capacity for hydrogen adsorption) was determined by extrapolating the linear part of the isotherm to zero pressure. The total amount of adsorbed hydrogen was used to determine nickel metal specific surface area and to calculate nickel particles size in the reduced precursors at the above-mentioned temperatures. Particle size calculations were carried out presuming complete reduction of the Ni<sup>2+</sup> ions to Ni<sup>0</sup> as well as a cubic form of the reduced nickel metal particles. Adsorption stoichiometry of one hydrogen atom bonded to one surface nickel metal atom was assumed, the surface density of Ni atoms being taken as 1.54×10<sup>19</sup> atoms.m<sup>−2</sup> Ni [21].

## RESULTS AND DISCUSSION

Chemical analysis data listed in Table 1 reveal that the M<sup>2+</sup>/Al<sup>3+</sup> molar ratio of the dried ‘as-synthesized’ samples is consistent with that of the mixed nitrate solutions used in the preparation procedure.

### Powder X-ray diffraction

Diffraction patterns of the ‘as-synthesized’ samples are displayed in Figs. 1a-d. A well-crystallized TK1 structure containing carbonate anions in the interlayer space was registered only in the 3.0NiAl precursor (Fig. 1a): sharp and symmetrical reflections for the (003), (006), (110), and (113) planes and broad and asymmetric reflections for (012), (015), and (018) (JCPDF file 00-015-0087). Because of lower nickel loading (Fig. 1b), 1.5NiAl causes sample crystallinity to diminish due to decreased crystallite sizes accompanied by increased specific surface area (Table 1). No aluminium hydroxide/oxyhydroxide phase was detected despite that the Ni<sup>2+</sup>/Al<sup>3+</sup> ratio in the sample is lower than 2.0, a typical value of stoichiometric TK1 structure.

**Table 1.** Sample notation, chemical composition, and specific surface area of the ‘as-synthesized’ samples

Sample	Chemical composition						SSA m <sup>2</sup> g <sup>−1</sup>
	wt.%			molar ratio			
	Ni	Mg	Al	Ni <sup>2+</sup> /Al <sup>3+</sup>	Ni <sup>2+</sup> /Mg <sup>2+</sup>	M <sup>2+</sup> /Al <sup>3+</sup>	
1.5NiAl	32.9	–	10.1	1.5	–	1.5	91
3.0NiAl	42.6	–	6.5	3.0	–	3.0	71
1.5NiMgAl	20.2	5.4	10.1	0.9	1.5	1.5	102
3.0NiMgAl	31.4	5.4	6.8	2.1	2.4	3.0	86

PXRD patterns of Mg-containing samples (Figs. 1c,d) are similar to the corresponding Ni-Al entities. However, they are broader and of lower intensity, which is more appreciable for 3.0NiMgAl. This result is evidence for partial replacement of the smaller Ni<sup>2+</sup> ions having an octahedral ionic radius *r* of 0.069 nm by the larger Mg<sup>2+</sup> ions (*r* = 0.072 nm) [22]. Consequently, the modification of the Ni-Al system with Mg<sup>2+</sup> ions causes partial amorphization of the TK1 structure associated with specific surface area development (Table 1).

### CO<sub>2</sub> removal by methanation reaction

The catalytic tests showed successful CO<sub>2</sub> hydrogenation to 0–10-ppm levels at reaction temperatures in the range of 400–320°C and GHSV from 3000 to 22000 h<sup>−1</sup> on all catalysts after their reduction at 400, 450, 530, and 600°C. Differences in activity became evident at lower reaction temperatures such as 300°C (Fig. 2).

Highly loaded Ni catalysts demonstrated a higher methanation activity at a reaction temperature of 300°C than catalysts of low Ni content (Figs. 2a-d). The 3.0NiMgAl catalyst showed the highest activity (0-ppm level) after reduction at all studied temperatures. The 3.0NiAl catalyst hydrogenated CO<sub>2</sub> below a 4-ppm level even on raising the GHSV to 22000 h<sup>−1</sup> irrespective of reduction temperature. A decrease of the Ni loading in the catalysts led to a decrease in activity, particularly with the 1.5NiMgAl catalyst after reduction at 400°C (Fig. 2a) where a CO<sub>2</sub> residual content of 22-ppm level at GHSV = 22000 h<sup>−1</sup> was registered. However, increasing the reduction temperature up to 450°C (Fig. 2b), 530°C (Fig. 2c), and markedly to 600°C (Fig. 2d) has brought about a successful purification of the stream by all the catalysts at high GHSV levels keeping the residual CO<sub>2</sub> in the range of 0–6 ppm.

Taking into account that the lower temperatures are thermodynamically and economically favourable to carry on the reaction, catalyst activities were examined in an extended reaction temperature range within 280–220°C (Fig. 3).

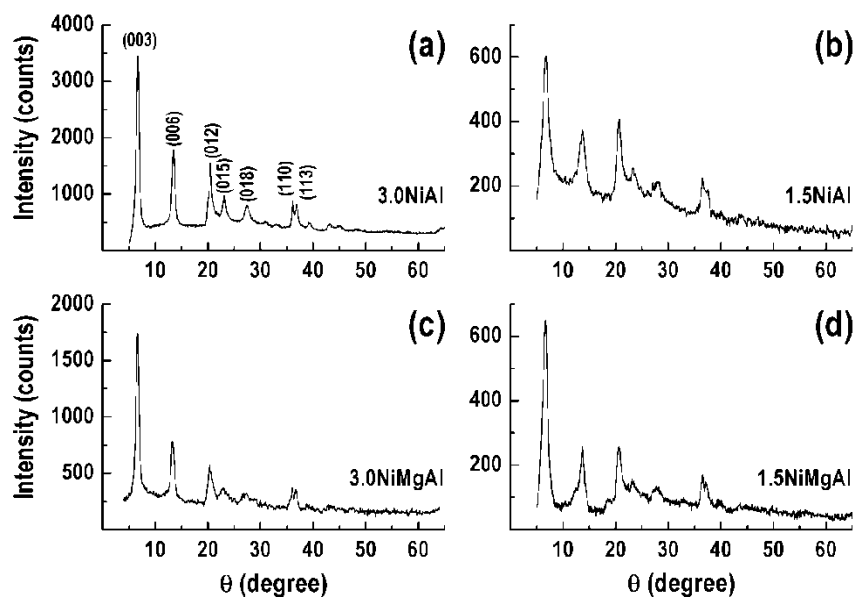


Fig. 1. PXRD patterns of the ‘as-synthesized’ samples: (a) 3.0NiAl, (b) 1.5NiAl, (c) 3.0NiMgAl, (d) 1.5NiMgAl.

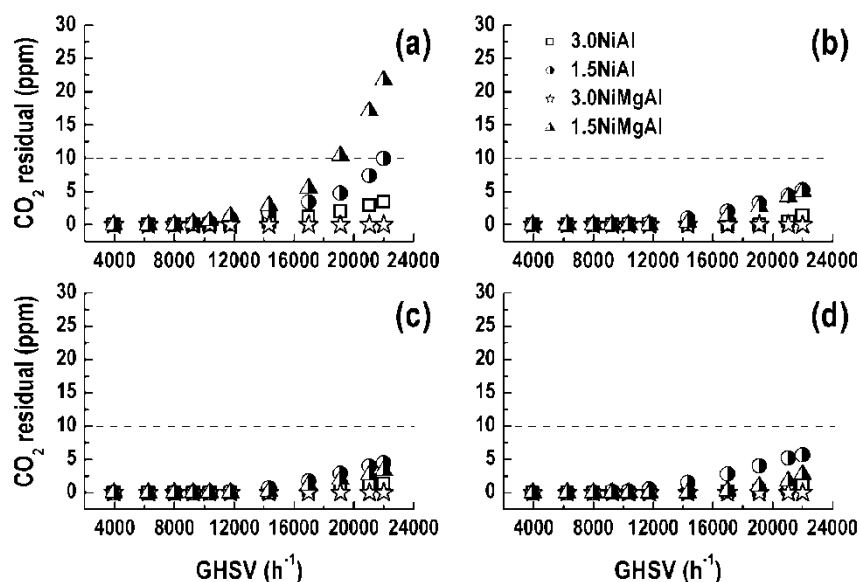
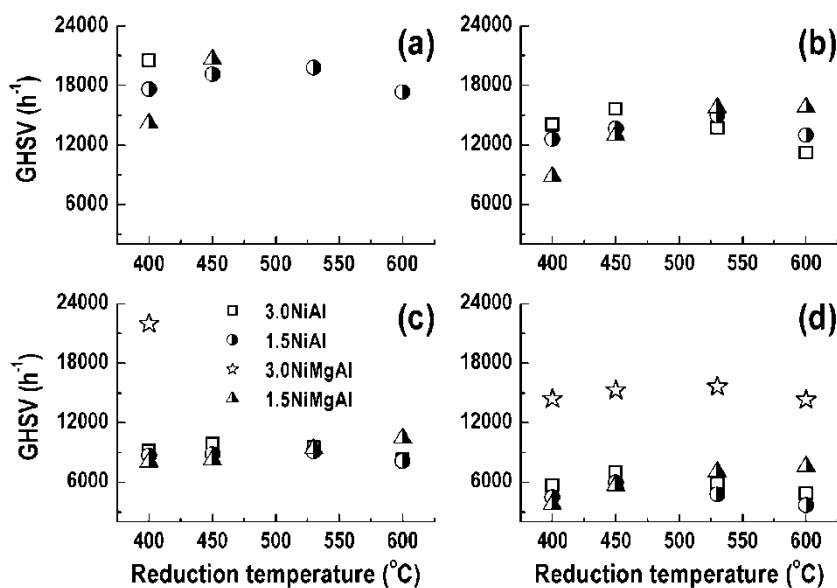


Fig. 2. Dependence of the methanation activity at 300°C on GHSV of the catalysts reduced at 400°C (a), 450°C (b), 530°C (c), and 600°C (d).

Similar relations of activity were observed at lower reaction temperatures (280–240°C) after catalyst reduction in the range of 400–600°C (Fig. 3a, b) if the activity is evaluated by the highest GHSV at which a residual 10-ppm level of CO<sub>2</sub> concentration at the reactor outlet is attained. The latter is an admissible limit in the feedstock of industrial ammonia production. It satisfies the requirements for safety work of fuel cell anodes as well. The 3.0NiMgAl catalyst showed again the highest methanation activity of 0-ppm level at T ≥ 260°C and GHSV of 22000 h<sup>-1</sup> after treatment at all reduction temperatures. An exception was observed

at a reaction temperature of 240°C if the catalyst was reduced at 400°C where a 10-ppm residual CO<sub>2</sub> level was registered (Fig. 3c). The non-modified 3.0NiAl catalyst remained also active at 280°C since raising the reduction temperature above 400°C gave rise to CO<sub>2</sub> levels below 10-ppm. In the region of 280–260°C, the Mg-containing low-loaded catalyst 1.5NiMgAl exhibited an increased activity after reduction at 450°C. CO<sub>2</sub> removal demonstrated by the 1.5NiAl catalyst was generally the lowest at reaction temperatures below 300°C; the latter has shown a slight variation in activity yet after reduction at 530°C.



**Fig. 3.** Comparison of the methanation activity of the catalysts at various reaction temperatures: (a) 280°C, (b) 260°C, (c) 240°C, and (d) 220°C represented as dependence of necessary GHSV to keep a 10-ppm CO<sub>2</sub> level in H<sub>2</sub> on reduction temperature.

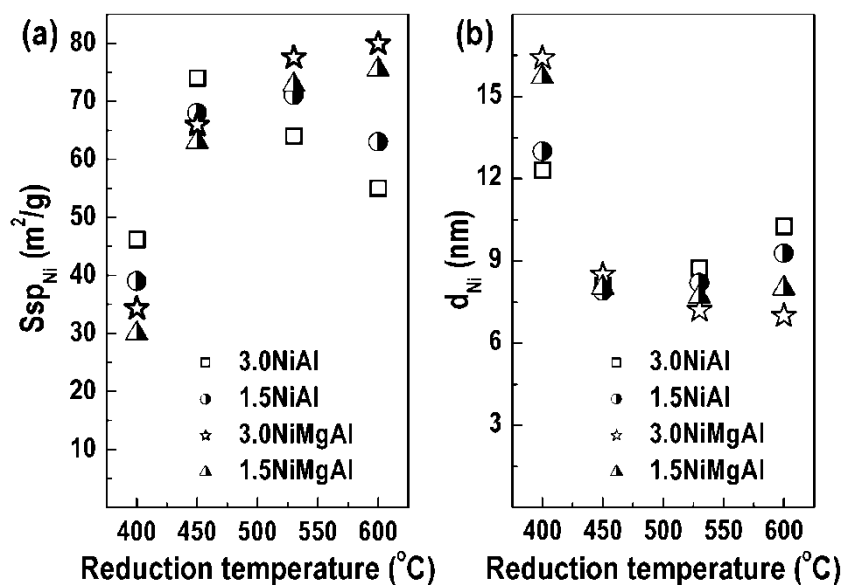


**Fig. 4.** Dependence of nickel metal specific surface area (a) and nickel metal particle size (b) on reduction temperature.

Lowering the reaction temperature to 220°C (Fig. 3d) caused a fall in activity with all the catalysts regardless of applied low space velocities. Nevertheless, the 3.0NiMgAl catalyst was still sufficiently active since the GHSV giving rise to 10-ppm CO<sub>2</sub> is quite high (about 15000 h<sup>-1</sup>). The rest of catalysts manifested a similar activity after reduction at all studied temperatures.

#### *H<sub>2</sub> chemisorption measurements*

An explanation of the observed dependences of methanation activity could be found using results of

H<sub>2</sub> chemisorption measurements. Considering that the model reaction takes place on the metal surface, nickel metal specific surface area (SSA<sub>Ni</sub>) and, accordingly, nickel metal particle size (d<sub>Ni</sub>) have predominant importance on hydrogenation activity.

According to the H<sub>2</sub> chemisorption data a larger SSA<sub>Ni</sub> (Fig. 4a) and, therefore, a smaller d<sub>Ni</sub> (higher Ni<sup>0</sup> dispersion) (Fig. 4b) of the 3.0NiAl and 1.5NiAl samples after reduction at 400 and 450°C presume a larger number of active centres on which the reaction takes place. Further treatment of these samples at 530 and 600°C induces sintering of the nickel

metal particles by a particle-migration mechanism [23, 24]. This phenomenon provokes a decrease of the SSA<sub>Ni</sub> and, accordingly, of the number of nickel metal atoms on the catalyst surface, thus leading to a decrease in methanation activity. In contrast, a gradual increase in SSA<sub>Ni</sub> and a decrease of d<sub>Ni</sub> were observed with the Mg-containing samples on raising the reduction temperature above 500°C. These results may be related to minimized migration of Ni<sup>0</sup> due to the presence of magnesium as a barrier/spacer to sintering of Ni<sup>0</sup> particles [25]. As nickel particle size becomes smaller, a greater number of nickel atoms will be exposed to the surface thus provoking a higher catalytic activity. This finding is predetermined by the structure sensitivity of the reaction as stated for methanation of 1% CO in hydrogen over nickel catalyst (MCR-2X, Haldor Topsøe A/S) at 250°C and a total pressure of 1 bar [26].

#### Mass-gas analysis

Carbon dioxide high-level removal invokes some doubt that measured activities include some partial hydrogenation of CO<sub>2</sub> to CO. For this purpose, the outlet gas mixture after the catalytic tests was collected and analysed. The data indicated methane as the only product. This result confirmed that CO<sub>2</sub> hydrogenation on the studied catalysts was complete.

#### CONCLUSIONS

A powder X-ray diffraction study revealed formation of Ni-Al takovite-like layered double hydroxides of different degree of crystallization depending on the Ni<sup>2+</sup>/Al<sup>3+</sup> ratio and the presence of magnesium additive. Modification of Ni-Al layered double hydroxides with magnesium caused partial amorphization of the layered structure. No aluminium hydroxide/oxyhydroxide phase was registered.

Variations of CO<sub>2</sub> methanation activity with changes of space velocity depended on nickel content, magnesium presence, and reduction and reaction temperatures.

Comparison of the catalytic activities showed that after reduction at 530 and 600°C the Mg-modified highly loaded Ni catalyst (3.0NiMgAl) dominated in CO<sub>2</sub> purification at reaction temperatures from 260 to 220°C due to (i) an increase of nickel metal specific surface area and (ii) retarding the effect of magnesium on metal nickel sintering.

The main effect of the magnesium dopant in Ni-Al layered double hydroxides is expressed in preserving nickel metal dispersion after reduction above 500°C.

Bearing in mind that lower temperatures are thermodynamically and economically favourable for

the studied reaction, the Mg-modified highly loaded Ni catalyst 3.0NiMgAl can be recommend as a suitable candidate for deep CO<sub>2</sub> removal from hydrogen-rich gas streams through the methanation reaction at low temperatures, such as 240 and 220°C.

**Acknowledgements:** This article has been realized in the frame of interacademic collaboration between Institute of Catalysis, Bulgarian Academy of Sciences, and Ilie Murgulescu Institute of Physical Chemistry, Romanian Academy.

#### REFERENCES

1. J. Kopyscinski, T. Schildhauer, S. Biollaz, *Fuel*, **89**, 1763 (2010).
2. Z. Liu, B. Chu, X. Zhai, Y. Jin, Y. Cheng, *Fuel*, **95**, 599 (2012).
3. M. Gassner, F. Marechal, *Energy Environ. Sci.*, **5**, 5768 (2012).
4. T. Kienberger, C. Zuber, K. Novosel, C. Baumhagl, J. Karl, *Fuel*, **107**, 102 (2013).
5. D. Hu, J. Gao, Y. Ping, L. Jia, P. Gunawan, Z. Zhong, G. Xu, F. Gu, F. Su, *Ind. Eng. Chem. Res.*, **51**, 4875 (2012).
6. C. Krier, M. Hackel, C. Hägele, H. Urtel, C. Querner, A. Haas, *Chem. Ing. Tech.*, **85**, 523 (2013).
7. F. Mills, F. Steffgen, *Catal. Rev.-Sci. Eng.*, **8**, 159 (1974).
8. K. Xavier, R. Sreekala, K. Rashid, K. Yusuff, B. Sen, *Catal. Today*, **49**, 17 (1999).
9. G. Xu, X. Chen, Z-G. Zhang, *Chem. Eng. J.*, **121**, 97 (2006).
10. W. Wang, J. Gong, *Front. Chem. Sci. Eng.*, **5**, 2 (2011).
11. W. Wang, Sh. Wang, X. Ma, J. Gong, *Chem. Soc. Rev.*, **40**, 3703 (2011).
12. M. Vannice, *Catal. Rev.-Sci. Eng.*, **14**, 153 (1976).
13. G. Bridger, C. Woodward, Production of methanation catalysts, *Stud. Surf. Sci. Catal.*, Vol. 1, p. 331, Elsevier, Amsterdam, 1976.
14. P. de Korte, E. Doesburg, C. de Winter, L. van Reijen, *Solid State Ionics*, **16**, 73 (1985).
15. M. Gabrovska, R. Edreva-Kardjieva, D. Crişan, P. Tzvetkov, M. Shopska, I. Shtereva, *React. Kinet. Mech. Catal.*, **105**, 79 (2012).
16. F. Cavani, F. Trifirò, A. Vaccari, *Catal. Today*, **11**, 173 (1991).
17. A. Vaccari, *Catal. Today*, **41**, 53 (1998).
18. A. Vaccari, *Appl. Clay Sci.*, **14**, 161 (1999).
19. B. Zümreoglu-Karan, A. Ay, *Chem. Pap.*, **66**, 1 (2012).
20. T. Qing, X. Guo, X. Han, *CN Patent* 101 391 218 (2009).
21. J. Anderson, Structure of metallic catalysts, Academic Press, New York, 1975.
22. R. Shannon, *Acta Crystallogr. A*, **32**, 751 (1976).
23. H. Tamagawa, K. Oyama, T. Yamaguchi, H. Tanaka, H. Tsuiki, A. Ueno, *J. Chem. Soc. Faraday Trans. I*, **83**, 3189 (1987).
24. C. Bartholomev, R. Pannel, *J. Catal.*, **65**, 390 (1980).

25. P. Babu, K. Ghuge, S. Rammohan, V. Krishnan, A. Bhat, *Catal. Lett.*, **15**, 95 (1992). 26. J. Rostrup-Nielsen, K. Pedersen, J. Sehested, *Appl. Catal. A-Gen.*, **330**, 134 (2007).

## ОЧИСТВАНЕ НА БОГАТИ НА ВОДОРОД ГАЗОВЕ ОТ CO<sub>2</sub> ЧРЕЗ МЕТАНИРАНЕ

М. В. Габровска<sup>1\*</sup>, Р. М. Едрева-Кърджиева<sup>1</sup>, М. Г. Шопска<sup>1</sup>, Д. А. Николова<sup>1</sup>,  
Л. П. Билярска<sup>1</sup>, Д. Кришан<sup>2</sup>, М. Кришан<sup>2</sup>

<sup>1</sup> *Институт по катализ, Българска академия на науките, ул. „Акад. Г. Бончев“, бл. 11, 1113 София, България*

<sup>2</sup> *Институт по физикохимия „Илие Мъргулеску“, Румънска академия, бул. „Индепенденцей“ 202, 060021 Букурещ-12, Румъния*

Постъпила на 12 септември 2015 г.; Преработена на 14 декември 2015 г.

(Резюме)

Изследван е ефектът на магнезия върху структурата и активността на сътаени Ni-Al слоеви двойни хидроксиди като прекурсори на катализатори за очистване на богати на водород газове от въглероден диоксид чрез реакцията на метаниране. Изследванията са провеждани чрез промяна на молното съотношение M<sup>2+</sup>/Al<sup>3+</sup> в прекурсорите (M<sup>2+</sup>/Al<sup>3+</sup> = 1.5 и 3.0, където M<sup>2+</sup> = Ni<sup>2+</sup> или M<sup>2+</sup> = Ni<sup>2+</sup> + Mg<sup>2+</sup>), температурата на редукция, реакционната температура и обемната скорост. Съдържанието на магнезий е идентично (за сметка на никела) и в двата модифицирани образца.

Всички катализатори успешно хидрогенират CO<sub>2</sub> до стойности 0–10 ppm при реакционни температури в интервала 400–320°C и обемни скорости от 3000 до 22000 ч<sup>-1</sup>, след редукция при 400, 450, 530 и 600°C. Катализаторите с високо съдържание на никел (3.0NiAl и 3.0NiMgAl) проявяват тенденция да са по-активни.

След редукция при 400 и 450°C, активността на немодифицираните 3.0NiAl и 1.5NiAl катализатори при пониски реакционни температури (280 и 260°C) се приписва на по-голяма специфична повърхност на металния никел и по-малки размери на металните никелови частици (висока никелова дисперсност). По-нататъшната обработка на катализатори при 530 и 600°C предизвиква синтеруване на металните никелови частици, което води до намаляване на метаниращата активност.

Предимството на Mg-съдържащите катализатори се проявява в запазване дисперсността на металния никел при редукция над 500°C, дължащо се на забавящия ефект на магнезия върху синтеруването на металния никел.

Модифицираният с Mg катализатор с високо съдържание на никел (3.0NiMgAl) може да се препоръча като подходящ кандидат за дълбоко очистване от CO<sub>2</sub> на богати на водород газове смеси чрез реакцията на метаниране при ниски реакционни температури като 240 и 220°C.

## Comparative analysis of the catalytic behaviour in CO oxidation of iron containing materials obtained by abiotic and biotic methods and after thermal treatment

M. Shopska\*, S. Todorova, I. Yordanova, S. Mondal<sup>1</sup>, G. Kadinov

*Institute of Catalysis, Bulgarian Academy of Sciences, Acad. G. Bonchev St., Bldg. 11, 1113 Sofia, Bulgaria*

<sup>1</sup>*Department of Chemistry, Indian Institute of Technology, Delhi Hauz Khas, New Delhi 110016, India*

Received: September 12, 2015; Revised November 6, 2015

This work concerns synthesis of iron oxide containing materials by biotic and abiotic methods and comparison of their properties aimed at finding a common point of intersection that may determine a possible replacement of abiotic materials. Biosynthesis comprised *Leptothrix* genus of bacteria cultivation in growth medium of Adler. Thermal treatment of biomass samples was used in order to approximate synthesis conditions of the biogenic iron oxide material to those of abiotically obtained hematite. The catalytic activity of the samples was measured in the reaction of CO oxidation by two ways: *in situ* infrared spectroscopy using a diffuse-reflectance measuring chamber of Nicolet 6700 spectrometer high-temperature vacuum accessory and a flow-type glass reactor. Biomass showed low CO conversions up to 200°C but an increase at 250°C was registered by both used methods. This increase was accompanied by phase transformation. Initial catalytic activity was a result of predominant work of lepidocrocite, whereas a higher activity at 250°C was due to formed maghemite. Abiotic hematite was a bit more active below 240°C than a thermally treated biomass sample in flow-type glass reactor experiments. At higher temperatures, both materials demonstrated the same CO conversion. Spent samples did not show any changes of composition. Although the studied samples were synthesized by different methods, which resulted in different original iron oxide phases, their catalytic performance was very close. Thermally treated biomass samples (obtained by cultivation in Adler's medium) could replace chemically obtained iron oxide as a catalyst in the studied reaction.

**Keywords:** biogenic iron-containing material, *Leptothrix* genus of bacteria, CO oxidation, *in situ* diffuse-reflectance infrared spectroscopy, chemically synthesized iron oxide.

### INTRODUCTION

Iron oxide compounds are widely used in catalysis as active components or as ingredients that improve performance of other catalytically active materials. Various methods are used for their synthesis. Chemical methods use toxic substances, consume much energy, and produce hazardous waste solutions. [1–5]. Despite these drawbacks the obtained products are of good purity and, usually, have well-defined properties. In nature, iron oxide and iron hydroxide compounds are obtained owing to iron biomineralization. Bio-inspired technologies are aimed at imitating these processes by inclusion of different mediators like microorganisms and phytochemicals. These methods are realized at ambient pressure and temperature and manifest ecology friendly features [3,4,6–15]. However, the obtained products exhibit a multicomponent character.

This work is aimed at comparing the properties of iron oxide containing materials, synthesized by biotic and abiotic methods, in order to find a common point of intersection that will determine a possible substitution of the abiotic materials.

### EXPERIMENTAL

Magnetite, Fe<sub>3</sub>O<sub>4</sub>, was synthesized by a chemical route in which FeSO<sub>4</sub> and Fe(NO<sub>3</sub>)<sub>3</sub> solutions were mixed, purged for 30 min with N<sub>2</sub> and then precipitated by addition of NaOH solution at pH = 13.5. The obtained precipitate was washed with distilled water and ethanol and dried at 70°C. The synthesized Fe<sub>3</sub>O<sub>4</sub> was calcined at 450°C for 2 h to be converted into a stable form of iron oxide.

Biogenic iron-containing material was supplied by Prof. V. Groudeva and coworkers from the Faculty of Biology at St. Kliment Ohridski University of Sofia. Biosynthesis has been performed by a six-month cultivation of bacteria from *Leptothrix* genus in growth medium of Adler. In the literature, it is referred to a medium that is suitable for cultivation of *Sphaerotilus-Leptothrix* group of bacteria [16]. Obtained biomass has been separated by decantation of the liquid, washed by distilled water, and dried at 40°C.

The catalytic activity of the samples was studied in a test reaction of CO oxidation. Experiments with the biogenic material were performed in two different ways. One of them involved reaction in a high-temperature vacuum chamber (HTVC) accessory of

\* To whom all correspondence should be sent  
E-mail: shopska@ic.bas.bg

Nicolet 6700 spectrometer and was monitored *in situ* by diffuse-reflectance (DR) infrared spectroscopy. Before catalytic measurement the sample was subjected to a surface cleaning procedure in a flow mixture ( $40 \text{ ml}\cdot\text{min}^{-1}$ ) of  $\text{N}_2+\text{O}_2$  (25 vol.%  $\text{O}_2$ ) at temperatures up to  $200^\circ\text{C}$ . Further, the measurements were performed using a gas flow mixture of  $88 \text{ ml}\cdot\text{min}^{-1}$  (9 vol.% CO, 11.4 vol.%  $\text{O}_2$ ,  $\text{N}_2$ ) at various reaction temperatures (100, 150, 200,  $250^\circ\text{C}$ ) at a heating rate of  $10 \text{ deg}\cdot\text{min}^{-1}$  and a 30-min soak at each attained level. This procedure was used in order to achieve constant parameters of the studied system (constant infrared spectra for selected conditions). The second mode considered the CO oxidation reaction in a flow-type glass reactor (FTGR) with  $0.3\text{-cm}^3$  samples (mesh of  $0.63\text{--}0.8 \text{ mm}$ ). CO conversion was followed by a Hewlett Packard 5890 Series II gas chromatograph. Elapsed time to attain steady state working conditions was different depending on the reaction temperature (50, 100, 200, and  $250^\circ\text{C}$ ). To approximate synthesis conditions of the biogenic iron oxide material to the chemically obtained counterpart, the biomass sample was pretreated in the glass reactor using a flow mixture of 1760 ppm CO, 0.92 vol.%  $\text{O}_2$ , and  $\text{N}_2$  at a GHSV of  $40000 \text{ h}^{-1}$  from ambient temperature to  $300^\circ\text{C}$ . The latter composition of the flow mixture was further used for catalytic tests of both samples. Such a preconditioning was assumed applicable to compare the catalytic properties of both the biogenic and synthetic materials.

All 'as synthesized' biomass samples, thermally treated and spent after catalytic tests, were studied by transmission infrared spectroscopy in the far and middle regions using KBr pellets containing 0.5 or 1% of studied substance. Spectra were recorded on the same spectrometer.

## RESULTS AND DISCUSSION

Spectra of biomass obtained after cultivation of *Leptothrix* genus of bacteria (Fig. 1a) show bands characteristic of  $\gamma\text{-FeOOH}$  at 277, 371, 398, 474/480, 560, 748, 882, 1022, and  $1152 \text{ cm}^{-1}$  [17–21]. However, the spectral features direct also to the presence of some  $\gamma\text{-Fe}_2\text{O}_3$  (broad bands at about 398 and  $560 \text{ cm}^{-1}$  and a shoulder at about  $330 \text{ cm}^{-1}$ ) and  $\alpha\text{-FeOOH}$  (bands positioned at about 277, 398, 882, and  $\sim 3152 \text{ cm}^{-1}$ ) [17–21]. The analysis allows claiming that the biomass contains lepidocrocite ( $\gamma\text{-FeOOH}$ ) as a predominant phase with some amounts of hematite ( $\alpha\text{-Fe}_2\text{O}_3$ ) and maghemite ( $\gamma\text{-Fe}_2\text{O}_3$ ). In a previous study of biomass obtained by cultivation of *Leptothrix* bacteria in various cultivation media [22,23]  $\gamma\text{-FeOOH}$  has been found

as an essential component in an iron-containing material formed in Adler's medium by Mössbauer spectroscopy and XRD.

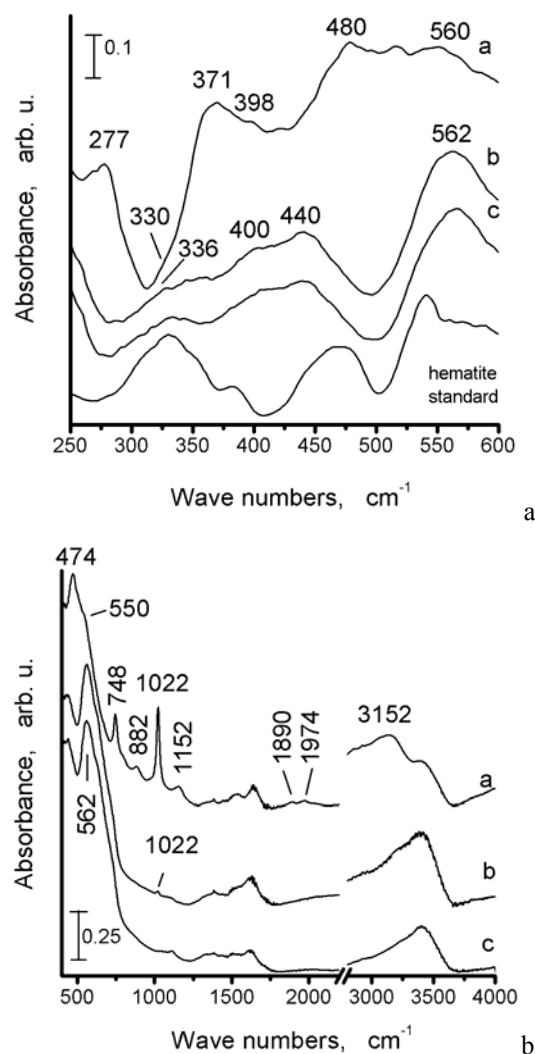


**Fig. 1.** Transmission infrared spectra of a biomass sample in the far (a) and middle (b) regions: a – fresh biomass sample; b – spent sample after catalytic measurements in the high-temperature vacuum chamber; c – spent sample after a catalytic test in a flow type reactor.

*In situ* DR spectra recorded during the reaction of CO oxidation over a biomass sample (Fig. 2) disclose bands at 1890, 1974, and  $3209 \text{ cm}^{-1}$  characteristic of iron oxide/oxyhydroxide structures and the characteristic doublet of CO in the reaction system with a minimum centred at  $2142 \text{ cm}^{-1}$  [23]. Integrated intensity of the CO bands was accepted as a measure of catalytic activity of the studied samples in this set of experiments. It decreased on increasing the reaction temperature (Fig. 3, HTVC). The decrease in integrated band intensity of the gas phase CO amount was about 40% at  $250^\circ\text{C}$ . The changes were accompanied by a decrease and disappearance of the bands at 1890 and  $1974 \text{ cm}^{-1}$ ,

as it is seen in figure 2 in the spectrum taken at 250°C. Changes during the course of the catalytic reaction at 250°C are in accordance with a phase transition process  $\text{FeOOH} \rightarrow \text{Fe}_2\text{O}_3$  [21].

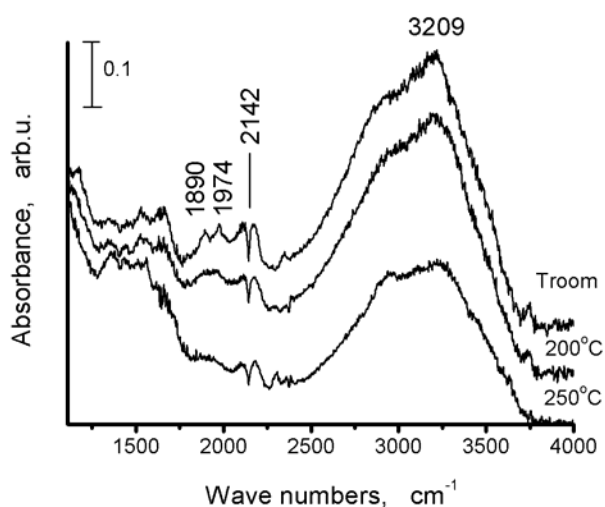


**Fig. 2.** *In situ* diffuse-reflectance infrared spectra of a biomass sample recorded at different reaction temperatures.

Spectra of the spent sample (Fig. 1b) confirm the phase transformation. The bands at 336, 400, and 562  $\text{cm}^{-1}$  are characteristic of maghemite  $\gamma\text{-Fe}_2\text{O}_3$  [17]. Bands at 336 and 562  $\text{cm}^{-1}$  propose also presence of hematite  $\alpha\text{-Fe}_2\text{O}_3$ . Formation of these modifications of the iron oxide is expected as the initial sample contains  $\alpha,\gamma\text{-FeOOH}$  that is converted into the respective oxides under such conditions [21]. The presence of some unconverted lepidocrocite should not be excluded because of the wide band at 440  $\text{cm}^{-1}$  and that of very low intensity at 1022  $\text{cm}^{-1}$ .

Catalytic measurements of biomass samples obtained by the both used technical methods showed a low CO conversion up to 200°C and an increase at 250°C (Fig. 3). This increase was accompanied by phase transformation that started at 200°C and continued at higher temperatures, as evidenced by the infrared spectra displayed in figure 2. Bearing in mind the different reaction conditions of applied experimental setup for examination of the catalytic properties of the biomass, the conversion of carbon monoxide registered at 250°C should be related to sample composition by the end of the process of phase transformations. Analysis of the spectra of biomass tested in the HTVC shows the presence mainly of maghemite and small amounts of hematite and lepidocrocite. After reaction for 150 min in the flow-type glass reactor (FTGR, Fig. 3) the biomass contained mainly maghemite and some amount of hematite (larger than that of HTVC experiment) and lepidocrocite. The far IR spectrum of a spent sample after catalysis in the flow-type reactor (Figs. 1a,c)

resembles that of a spent biomass sample after a catalytic test conducted in the diffuse-reflectance accessory (Figs. 1a,b). However, the former suggests the presence of a bit higher amount of hematite taking into account the increased intensity of the band at about 336  $\text{cm}^{-1}$  and broadening of the band at 562  $\text{cm}^{-1}$ . These results allowed us to accept that the chemical composition of the studied biomass samples was the same or nearly coincided with that resulted at 250°C under the reaction conditions used in both types of experiments.

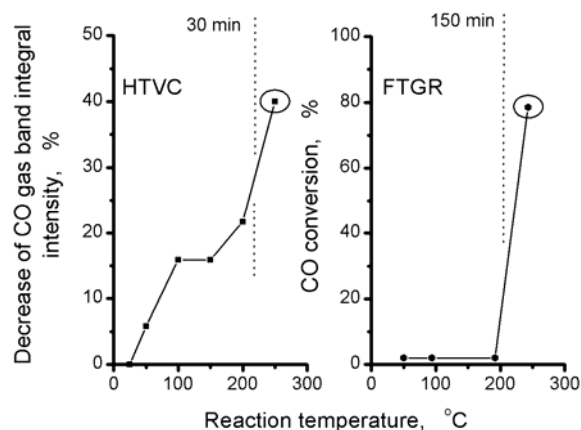


**Fig. 3.** Change of catalytic activity in dependence of reaction temperature: HTVC – evaluated by a decrease of integral CO gas band intensity; FTGR – CO conversion.

Abiotic magnetite and biomass samples were thermally treated before examination in the flow-type glass reactor. The aim of this pretreatment was to obtain a relatively stable sample composition and to approximate to some extent the conditions of material preparation, which is a prerequisite for their comparative study. Infrared spectra of ‘as synthesized’ and calcined abiotic iron oxide are displayed in figure 5. Spectrum ‘a’ confirms that the obtained iron oxide is magnetite (bands at 398, 455, and 576  $\text{cm}^{-1}$ ). Spectrum ‘b’ shows bands at about 310, 385, 462, and 540  $\text{cm}^{-1}$ , all characteristic of hematite [10, 21]. The result indicates that calcination of the magnetite at 450°C for 2 h is sufficient to convert this compound in a most stable form. Thermally treated biomass produced an infrared spectrum with bands located at about 333, 408, 440, and 565  $\text{cm}^{-1}$  (Fig. 4a). Their intensity and position correspond to those of the spent biomass samples after HTVC and FTGR catalytic tests (Figs. 1a,b) and (Figs. 1a,c), respectively. These features correspond to a complex composition of the thermally treated biomass containing maghemite, hematite, and lepidocrocite. Maghemite is still the predominant phase, while hematite and traces of unconverted lepidocrocite exist together with the main phase as it is shown for mentioned spent samples.

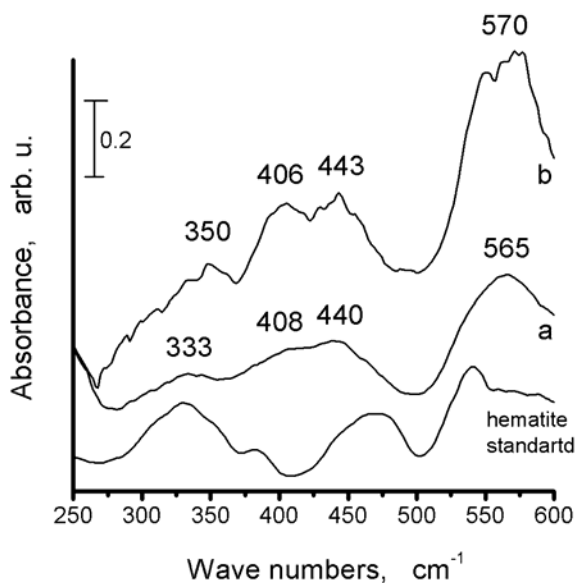


**Fig. 4.** Far-IR transmission spectra of biomass samples: a – thermally treated biomass sample; b – thermally treated biomass sample after catalytic test.

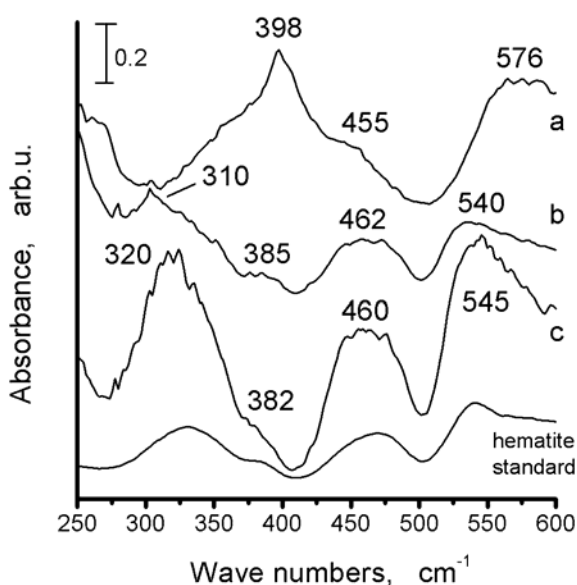


**Fig. 5.** Far-IR transmission spectra of abiotically synthesized iron oxide: a – ‘as synthesized’ sample ( $\text{Fe}_3\text{O}_4$ ); b – after calcination of abiotic sample at  $450^\circ\text{C}$  for 2 h ( $\alpha\text{-Fe}_2\text{O}_3$ ); c – calcined abiotic sample after catalytic test in a flow-type reactor.

Catalytic measurements of abiotic hematite and a thermally treated biomass sample in the flow-type glass reactor showed that at temperatures below  $240^\circ\text{C}$  the abiotic sample is a little bit more active. Both materials demonstrate the same CO conversion level in the reaction of CO oxidation at temperatures higher than  $240^\circ\text{C}$  (Fig. 6). Spectra of spent samples after the catalytic tests did not show any changes under reaction conditions (cf. spectra ‘a’ and ‘b’ in Fig. 4 and spectra ‘b’ and ‘c’ in Fig. 5). Despite the different methods of sample synthesis that result in

different original iron oxide phases, the catalytic performance in the reaction of CO oxidation is very close.

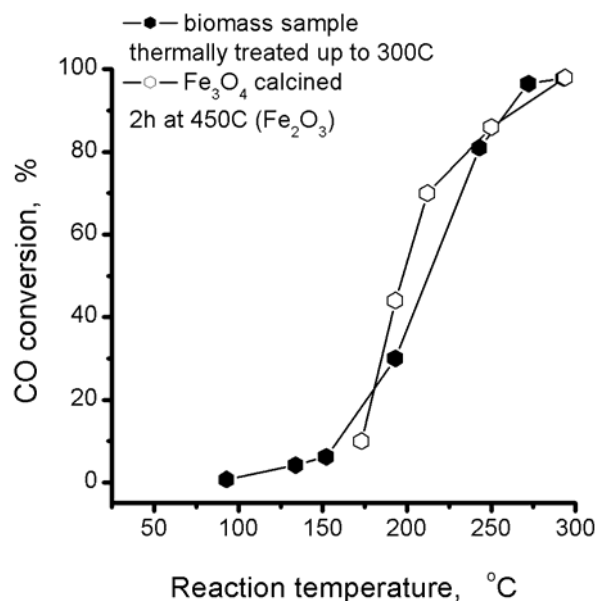


**Fig. 6.** Catalytic performance of biogenic iron-containing sample and abiotic hematite in the CO oxidation reaction registered using a flow-type glass reactor.

In conclusion, it should be noted that: (i) the catalytic activity up to  $200^\circ\text{C}$  of biotically obtained iron-containing material in the reaction of CO oxidation is a result of predominant work of lepidocrocite, but the increase in activity at  $250^\circ\text{C}$  is due to formed maghemite; (ii) a biogenic material thermally treated at  $300^\circ\text{C}$  is composed of maghemite, hematite, and lepidocrocite and showed almost the same catalytic activity in the reaction of CO oxidation like abiotically obtained hematite; (iii) both biogenic and abiotic thermally treated samples preserved their composition during the catalytic tests; (iv) thermally treated biomass, prepared by *Leptothrix* genus of bacteria cultivation in Adler’s growth medium, could replace chemically obtained iron oxide as a catalyst in the studied reaction.

*Acknowledgements: The authors are grateful to the Bulgarian Science Fund for financial support by projects T02-17/2014, DID 02/38/2009, and DNTS India 01/8. Preparation of the biogenic material by Prof. V. Groudeva and Dr. R. Angelova from St. Kliment Ohridski University of Sofia is greatly acknowledged. This work was also supported by the Bulgarian Academy of Sciences and the Slovak Academy of Sciences through the bilateral project ‘Mechanochemical synthesis – an ecologically friendly process in the production of materials for photocatalytic purification of air and water’.*

REFERENCES

1. K. B. Narayanan, N. Sakthivel, *Adv. Colloid Interface Sci.*, **156**, 1 (2010).
2. H. Jung, J.-W. Kim, H. Choi, J.-H. Lee, H.-G. Hur, *Appl. Catal. B-Environ.*, **83**, 208 (2008).
3. B. Kazprzyk-Hordern, M. Ziolk, J. Nawrocik, *Appl. Catal. B-Environ.*, **46**, 639 (2003).
4. A. B. Seabra, P. Haddad, N. Duran, *IET Nanobiotechnol.*, **7**, 90 (2013).
5. T. Shahwan, S. Abu Sirriah, M. Nairat, E. Boyaci, A. E. Eroglu, T. B. Scott, K. R. Hallam, *Chem. Eng. J.*, **172**, 258 (2011).
6. H. Hashimoto, S. Yokoyama, H. Asaoka, Y. Kusano, Y. Ikeda, M. Seno, J. Takada, T. Fujii, M. Nakanishi, R. Murakami., *J. Magnet. Magnet. Mater.*, **310**, 2405 (2007).
7. T. Sakai, Y. Miyazaki, A. Murakami, N. Sakamoto, T. Ema, H. Hashimoto, M. Furutani, M. Nakanishi, T. Fujii, J. Takada, *Org. Biomol. Chem.*, **8**, 336 (2010).
8. B. Xin, D. Zhang, X. Zhang, Y. Xia, F. Wu, S. Chen, L. Li, *Bioresour. Technol.*, **100**, 6163 (2009).
9. J. A. Rentz, I. P. Turner, J. L. Ullman, *Water Res.*, **43**, 2029 (2009).
10. R. Cornell, U. Schwertmann, *Iron Oxides*, Wiley-VCH Verlag, Weinheim, Germany, 2003.
11. R. W. Fitzpatrick, R. Naidu, P. G. Self, in: *Bio-mineralization Processes of Iron and Manganese - Modern and Ancient Environments*, Catena Supplement 21, (H. C. W. Skinner, R. W. Fitzpatrick, Eds.), Catena Verlag, Reiskirchen, Germany, 1992, p. 263.
12. D. A. Ankrah, E. G. Sogaard, in *13<sup>th</sup> Int. Water Technol. Conf., IWTC 13, 2009*, Hurghada, Egypt, p. 999.
13. T. Ema, Y. Miyazaki, I. Kozuki, T. Sakai, H. Hashimoto, J. Takada, *Green Chem.*, **13**, 3187 (2011).
14. A. Alharthi, R. A. Blackley, T. H. Flowers, J. S. J. Hergreaves, I. D. Pulford, J. Wigzell, W. Zhou, *J. Chem. Technol. Biotechnol.*, (2014), doi:10.1002/jctb.4434.
15. G. E. Hoag, J. B. Collins, J. L. Holcomb, J. R. Hoag, M. N. Nadagouda, R. S. Varma, *J. Mater. Chem.*, **19**, 8671 (2009).
16. D. Ellis, *Microbiology of the Iron-depositing Bacteria*, Wexford College Press, Palm Springs, CA, 2003.
17. A. U. Gehring, A. M. Hofmeister, *Clays and Clay Minerals*, **42**, 409 (1994).
18. N. Lazaroff, W. Sigal, A. Wasserman, *Appl. Environ. Microbiol.*, **43**, 924 (1982).
19. S. Music, A. Saric, S. Popovic, K. Nomura, T. Sawada, *Croat. Chem. Acta*, **73**, 541 (2000).
20. B. Weckler, H. D. Lutz, *Eur. J. Solid State Inorg. Chem.*, **35**, 531 (1998).
21. R. M. Cornell, U. Schwertmann, *The Iron Oxides. Structure, Properties, Reactions, Occurrences and Uses*, Wiley-VCH Verlag, Weinheim, 2003.
22. M. Shopska, Z. Cherkezova-Zheleva, D. Paneva, M. Iliev, G. Kadinov, I. Mitov, V. Grudeva, *Nanoscience & Nanotechnology*, Vol. 13, (Proc. 14<sup>th</sup> Workshop on Nanostructured Materials Application and Innovation Transfer, 2013, Sofia), Eds. E. Balabanova, E. Mileva, Bulgarian Academy of Sciences, Sofia, 2013, p. 31.
23. L. H. Little, *Infrared spectra of adsorbed species*, Academic Press, London, 1966.

# СРАВНИТЕЛЕН АНАЛИЗ НА КАТАЛИТИЧНОТО ПОВЕДЕНИЕ В ОКИСЛЕНИЕ НА СО НА ЖЕЛЯЗО-СЪДЪРЖАЩИ МАТЕРИАЛИ ПОЛУЧЕНИ С АБИОТИЧНИ И БИОТИЧНИ МЕТОДИ И СЛЕД ТЕРМИЧНА ОБРАБОТКА

М. Шопска\*, С. Тодорова, Ил. Йорданова, С. Мондал<sup>1</sup>, Г. Кадинов

*Институт по катализ, Българска академия на науките, ул. „Акад. Г. Бончев“, бл. 11, 1113 София, България*

*<sup>1</sup> Департамент по химия, Индийски технологичен институт, Делхи Хауз Кас, Ню Делхи 110016, Индия*

Постъпила на 12 септември 2015 г.; Преработена на 6 ноември 2015 г.

(Резюме)

Изследването е свързано с получаване чрез биологичен или небιологичен метод на материали съдържащи железен оксид и сравняване на техните свойства за да се намери пресечна точка определяща възможност за заместване на абиотичните материали. Биологичният синтез включва култивиране на бактерия от рода *Leptothrix* в среда на Адлер. Използвана е термична обработка на образец от биомаса за наподобяване на условията на синтез на биогенния железен оксид на тези на получаване на небιогенен хематит. Каталитичната активност на образците е измерена в реакцията на окисление на СО по два начина – чрез „ин ситу“ дифузно-отражателна инфрачервена спектроскопия в кювета за изследване при висока температура и в стъклен реактор от проточен тип. И при двата метода на изследване биомасата показва ниска конверсия на СО при температури до 200°C, но се регистрира повишение при 250°C. Нарастването на активността е съпроводено от промяна във фазовия състав. Началната каталитична активност е резултат от преобладаващ принос на лепидокрокита, докато по-високата активност при 250°C се дължи на образуването на магхемит. Експериментите проведени в проточен реактор показаха, че при температура под 240°C абиотичният хематит е малко по-активен от термично обработения образец от биомаса. Двата вида материали показаха една и съща конверсия на СО при по-високи температури. Съставът на отработените образци не се различава. Въпреки, че изследваните образци са синтезирани по различен начин, водещ до различни начални фази от железни оксиди, каталитичните им свойства са много близки. Термично обработени биогенни образци, получени чрез култивиране на бактериите в среда на Адлер, биха могли да заместят като катализатор за изследваната реакция железен оксид получен чрез химичен синтез.

## Preparation of Fe-Pd/Al-Si-O catalyst using biogenic iron of cultivated *Leptothrix* genus bacteria

M. G. Shopska<sup>1\*</sup>, G. B. Kadinov<sup>1</sup>, J. Briančin<sup>2</sup>, I. D. Yordanova<sup>1</sup>, H. G. Kolev<sup>1</sup>, M. Fabián<sup>2</sup>

<sup>1</sup> Institute of Catalysis, Bulgarian Academy of Sciences, Acad. G. Bonchev St., Bldg. 11, 1113 Sofia, Bulgaria

<sup>2</sup> Institute of Geotechnics, Slovak Academy of Sciences, 45 Watsonova St., 040 01 Košice, Slovakia

Received: September 15, 2015; Revised November 4, 2015

A composite has been prepared by modification of 0.3%Pd/Al-Si-O fibrous catalyst, synthesized by a sol-gel method, with a biogenic material upon applying cultivation of *Leptothrix* genus of bacteria in a silicon-iron-glucose-peptone elective medium. Samples were characterized by infrared spectroscopy, scanning electron microscopy with energy dispersive X-ray analysis, low temperature adsorption of nitrogen, and X-ray photoelectron spectroscopy. The hybrid material contained biogenic iron  $\gamma$ -FeOOH. Catalytic activity in the CO oxidation reaction was monitored by *in situ* diffuse-reflectance infrared spectroscopy. Catalytic activity tests were aimed at evaluating the catalytic performance and examining a possibility to prepare iron-containing catalysts with biogenic material. Our study showed similarities between catalytic performances of the studied systems, which are assigned to uniform and stable distribution of the palladium and iron on the surface. The catalytic activity of synthesized composite was essentially due to Pd.

**Keywords:** biogenic iron-containing material; *Leptothrix* genus of bacteria; X-ray photoelectron spectroscopy; CO oxidation; *in situ* diffuse-reflectance infrared spectroscopy; scanning electron microscopy with electron dispersive analysis.

### INTRODUCTION

Biogenic iron-containing materials are applicable in the heterogeneous catalysis in gaseous or liquid medium playing different roles as a catalyst precursor, active component, catalyst support, and immobilizing carrier. Investigations are concentrated on reactions of oxidation, degradation of dyes, transformation of secondary alcohols, formation of intermediates for pharmacy and organic synthesis, CH<sub>4</sub> cracking, mediation in dechlorination of Cl-containing hydrocarbons [1–11].

Studies of natural biogenic material, a product of *Sphaerotilus-Leptothrix* group bacteria metabolism collected from small water streams at Vitosha Mountain (Bulgaria), showed that an iron-containing ingredient is goethite [3]. Biogenic iron-containing materials obtained by laboratory cultivation of *Leptothrix* genus of bacteria in different growth media contained mixtures of  $\alpha$ -FeOOH,  $\gamma$ -FeOOH, and  $\gamma$ -Fe<sub>2</sub>O<sub>3</sub> [12]. Both the natural and laboratory obtained biogenic materials exhibited some catalytic activity in the reaction of carbon monoxide oxidation [3, 12]. Thus, the biogenic materials were regarded potentially suitable as a catalyst support or as active components in catalysts after modification.

Chemical methods for production of iron oxides use toxic substances, consume much energy, and

produce dangerous waste solutions [2, 7, 13–15]. Iron oxide/hydroxide compounds are obtained in nature because of iron biomineralization. Bio-inspired technologies imitate these processes including mediators like microorganisms and phytochemicals. Such methods are realized under ambient conditions and have an ecology friendly character [2, 5, 6, 11, 15–22]. Such a production does not require big investments and additional energy supply because iron bacteria are normal cell metabolites.

The present investigation is concerned with characterization of a hybrid material prepared by deposition of biogenic iron on a fibrous Pd catalyst by cultivation of iron bacteria in selected medium. The following methods were used in the study: X-ray photoelectron spectroscopy (XPS), scanning electron microscopy with electron dispersive analysis (SEM-EDX), infrared spectroscopy (IRS), and low temperature adsorption of nitrogen (Brunauer-Emmett-Teller method). *In situ* diffuse-reflectance infrared spectroscopy (DRIRS) was applied to monitor catalytic tests of the composite in the reaction of CO oxidation.

### EXPERIMENTAL

A 0.3%Pd/Al-Si-O fibrous catalyst, synthesized by a sol-gel method [23], reduced at 400°C for 2 h, and then kept in air was used. A Fe-Pd/Al-Si-O sample was obtained by deposition of biogenic iron on a previously prepared 0.3%Pd/Al-Si-O by culti-

\* To whom all correspondence should be sent.  
E-mail: shopska@ic.bas.bg

vation in laboratory conditions of the *Leptothrix* genus of bacteria in a silicon-iron-glucose-peptone elective medium (SIGP [24]) under static conditions at 20°C. The fibrous material was sterilized by autoclaving for 15 min at 1 atm and 120°C and then added to the medium before its infection with the bacteria. After a 36-day period of cultivation, the product was collected through decantation, washed with distilled water, and dried at 40°C for 24 h.

Specific surface area of the studied basic materials was measured according to the BET method (adsorption of N<sub>2</sub> at -196°C) by a NOVA-1200e high-speed gas sorption analyser (Quantachrome Instruments, USA). Prior to measurement, the samples were evacuated at 100°C for 12 h. Pore size distribution was estimated using the BJH method.

XPS measurements were carried out in the UHV chamber of an ESCALAB-MkII (VG Scientific) electron spectrometer with a base pressure of about  $1 \times 10^{-10}$  mbar ( $1 \times 10^{-9}$  mbar during measurements) at room temperature. The photoelectron spectra were obtained using unmonochromatized AlK $\alpha$  ( $h\nu = 1486.6$  eV) radiation. Passing through a 6-mm slit (entrance/exit) of a hemispherical analyser enabled detection of electrons of 20-eV energy by a channeltron. Because of a small signal for Pd 3d, 50-eV pass energy was used. The instrumental resolution, measured as the full width at half maximum (FWHM) of the Ag 3d<sub>5/2</sub> photoelectron peak, was about 1 eV. The energy scale was corrected to the C 1s peak maximum at 285.0 eV for electrostatic sample charging. Processing of the measured spectra included a subtraction of X-ray satellites and Shirley-type background [25]. Peak positions and areas were evaluated by a symmetrical Gaussian-Lorentzian curve fitting. The relative concentrations of the different chemical species were determined based on normalization of the peak areas to their photoionization cross-sections calculated by Scofield [26].

Scanning electron micrographs were recorded on a MIRA3 FE-SEM microscope (TESCAN, Czech Republic) working at accelerating voltage up to 30 kV and magnification up to 1000000x. Energy dispersive X-ray analysis (EDX) (Oxford Instruments, UK) of selected parts of the samples was applied to determine chemical composition and analyse Pd and Fe distribution in the catalysts.

Infrared spectra (IR) of the samples were recorded on a Nicolet 6700 FTIR spectrometer (Thermo Electron Corporation, USA) using the method of dilution of studied material in KBr pellets (0.5% of studied substance). The spectra were collected in the middle region using 50 scans. Catalytic activity in the CO oxidation reaction was studied using a high-temperature vacuum chamber

diffuse-reflectance accessory of the spectrometer (Collector II, Thermo Spectra-Tech). Prior to catalytic measurements, the samples were treated in oxidative flow of 25% O<sub>2</sub> in N<sub>2</sub> in T<sub>room</sub>-200°C's interval in order to clean their surfaces. *In situ* measurements were performed using a reaction flow mixture of 9 vol.% CO, 11.4 vol.% O<sub>2</sub> in nitrogen at 88 ml.min<sup>-1</sup>. The used interval of reaction temperatures was T<sub>room</sub>-250°C as well as T<sub>room</sub>-300°C only for 0.3%Pd/Al-Si-O. The temperature was raised consecutively to the necessary reaction temperature at a rate of 10 deg.min<sup>-1</sup> and held for 30 min at each attained level. This procedure was aimed at achieving constant parameters of the studied system (constant infrared spectra in selected conditions).

## RESULTS AND DISCUSSION

BET measurements of the initial 0.3%Pd/Al-Si-O catalyst determined a specific surface area of 29 m<sup>2</sup>.g<sup>-1</sup>. Registered pore size distribution revealed a mesoporous material (2–50 nm) displaying a predominant pore size of about 6.5 nm (Fig. 1). Deposition of biogenic iron-containing material slightly changes composite surface properties: the specific surface area of the Fe-Pd/Al-Si-O sample is 37 m<sup>2</sup>.g<sup>-1</sup>, while predominant pore sizes are 3.8 and 5.3 nm.

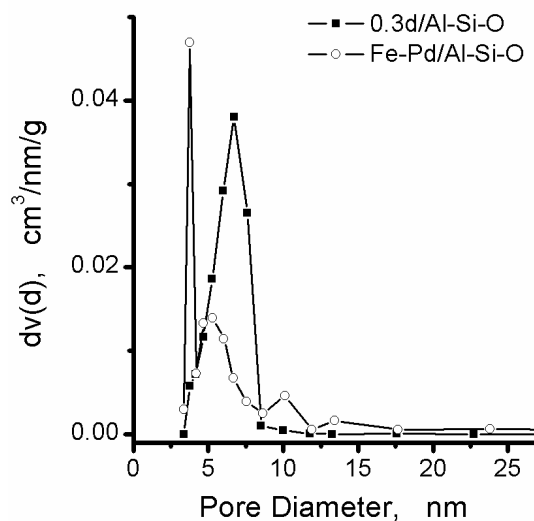


Fig. 1. Pore size distribution in the studied materials.

IR spectra of the samples were characterized by a spectrum drop in the region under 1200 cm<sup>-1</sup> (Figs. 2 and 3). This feature is attributable to fibre sample morphology and different refractive indices of fibrous material and used matrix. Sets of bands characteristic of alumina and silica supports were registered at 570, 665 cm<sup>-1</sup> (Al-O), and 570, 798 (Si-O) for the 0.3%Pd/Al-Si-O system and at 550, 583, and 664 cm<sup>-1</sup> (Al-O), and 380, 583, 790, and 1080 cm<sup>-1</sup> (Si-O) for the Fe-Pd/Al-Si-O system [27]. The IR spectrum of biogenic material cultivated in

the absence of fibrous material proves the formation of  $\gamma$ -FeOOH in SIGP medium. This is shown as inset in figure 3. Characteristic bands of lepidocrocite were registered at 480, 575, 950, 1040, and 1150  $\text{cm}^{-1}$  [28–31].

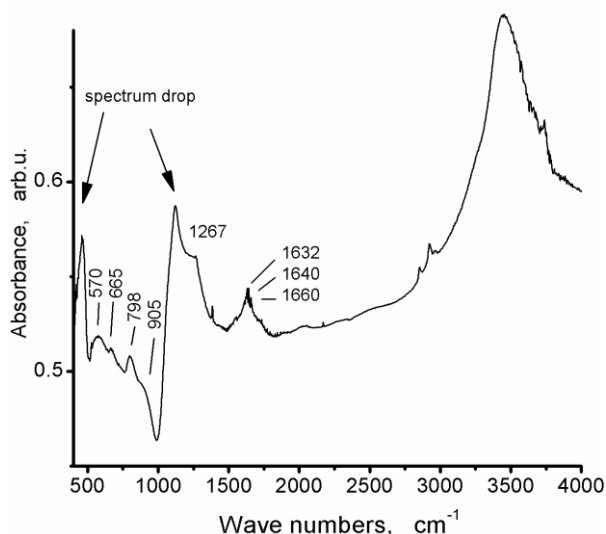


Fig. 2. IR spectrum of 0.3%Pd/Al-Si-O fibrous catalyst.

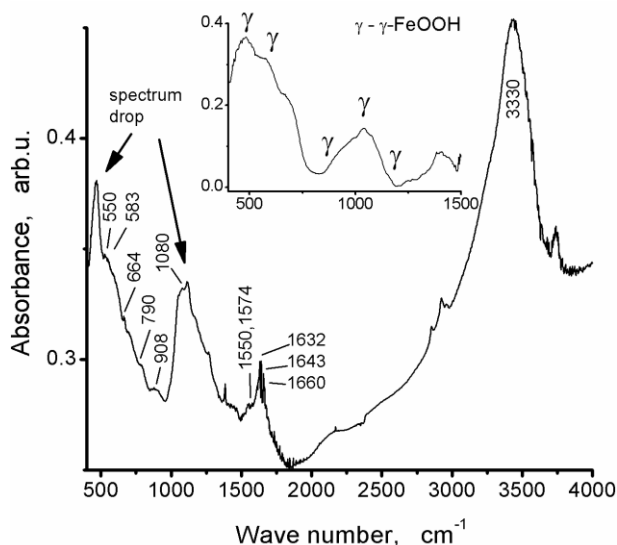


Fig. 3. IR spectrum of Fe-Pd/Al-Si-O sample. Inset – IR spectrum of biogenic iron-containing material obtained in SIGP medium in absence of 0.3%Pd/Al-Si-O fibrous catalyst.

XPS measurements were performed to monitor elements present on the surface and their oxidation states. XP spectra of the substrate revealed occurrence of Al–O (probably  $\text{Al}_2\text{O}_3$ ), Si=O (characteristic of  $\text{SiO}_2$ ), and Si–O species. Our XPS analysis was focused on the Pd and Fe catalytic materials. It was observed that palladium was present in two different oxidation states on the surface of an as-received Pd/Al-Si-O sample (prereduced and kept in air), namely,  $\text{Pd}^{2+}$  and  $\text{Pd}^0$  at a  $\text{Pd}^{2+}/\text{Pd}^0$  ratio of 0.4 (Fig. 4). Comparison with data acquired after calcina-

tion at 300°C for 30 min disclosed Pd redistribution giving rise to about a 20%-increase in surface concentration of the palladium (from  $2.5 \times 10^{-3}$  to  $3 \times 10^{-3}$  at.%). Both forms of Pd were present but the  $\text{Pd}^{2+}/\text{Pd}^0$  ratio was changed to two.

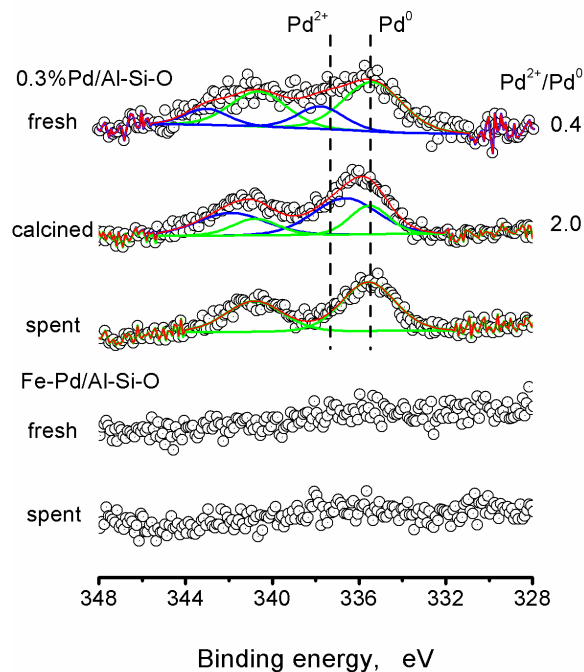


Fig. 4. High resolution XP spectra of Pd and respective  $\text{Pd}^{2+}/\text{Pd}^0$  ratios.

High resolution XP spectra of as received fresh and used Fe-Pd/Al-Si-O samples demonstrated the presence of iron in two forms,  $\text{Fe}^{3+} \approx \text{Fe}^{2+}$  at a Fe/(Al+Si) ratio of about  $10.5 \times 10^{-2}$  (Fig. 5).

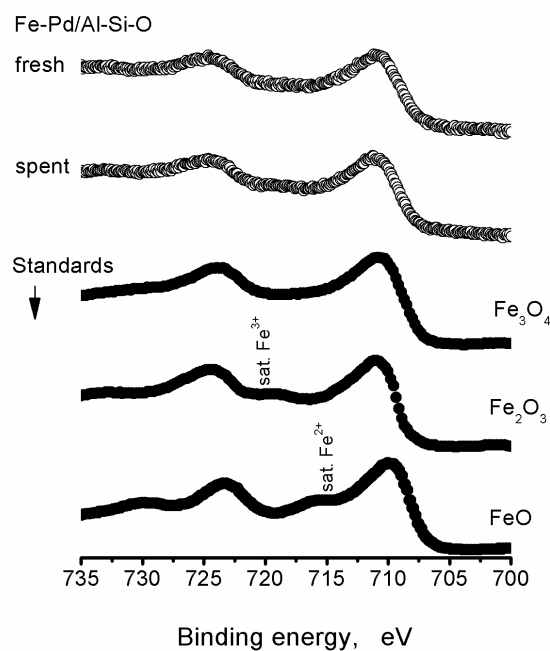
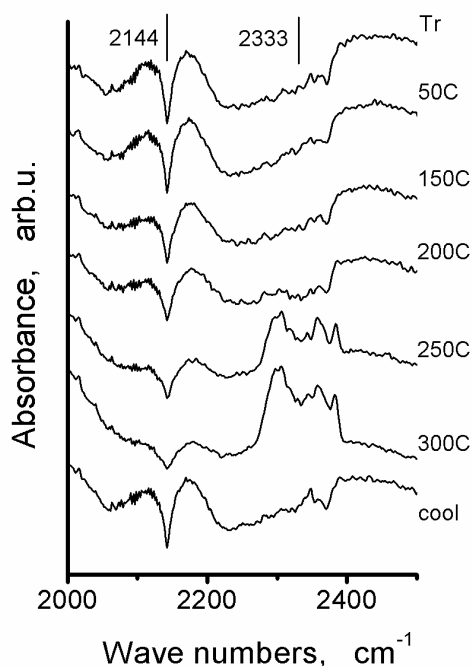


Fig. 5. High resolution XP spectra of Fe in Fe-Pd/Al-Si-O sample and standards used.

Iron occurrence in both forms was concluded after comparison of the measured XP spectra with standard spectra of  $\text{Fe}^{2+}$  and  $\text{Fe}^{3+}$  and a mixture of equal amounts of  $\text{Fe}^{2+}$  and  $\text{Fe}^{3+}$  [32]. A very low amount of palladium, within the limits of instrument error, was observed (two bottom lines in figure 4). Additionally, we observed contaminations of C, Cl, and F from preparation procedures, which are not discussed.

The studied samples were tested in the reaction of CO oxidation. The process was monitored *in situ* by diffuse-reflectance infrared spectroscopy. Collected spectra are shown in figures 6 and 7. CO appears in all spectra as a doublet centred at  $2144/2142\text{ cm}^{-1}$  [27]. The two wings are not symmetrical, which directs to availability of adsorbed form of CO on the surface of both samples.  $\text{CO}_2$  is a reaction product and it was registered by a band at about  $2333/2335\text{ cm}^{-1}$  [27]. On increasing the reaction temperature, the CO characteristic doublet was decreased in intensity whereas the  $\text{CO}_2$  band intensity was increased. The observed changes were more pronounced in the case of the 0.3%Pd/Al-Si-O system. A general observation in both studied systems was a gradual loss of OH surface coverage, which was well visible above  $150^\circ\text{C}$  through an intensity decrease of the band at about  $3400\text{ cm}^{-1}$  [27].



**Fig. 6.** In situ DRIR spectra collected during CO oxidation in the presence of 0.3% Pd/Al-Si-O fibrous catalyst.

Catalytic activity of the used materials was evaluated through changes in CO gas-phase band integral intensity on increasing the temperature. A

2.5-fold decrease of the carbon monoxide in the reaction mixture was measured over the Pd/Al-Si-O catalyst at  $250^\circ\text{C}$ . Fe-Pd/Al-Si-O manifested nearly a 2-fold decrease at this temperature. An additional 2-fold decrease was determined for 0.3%Pd/Al-Si-O after a temperature rise from  $250$  to  $300^\circ\text{C}$ .

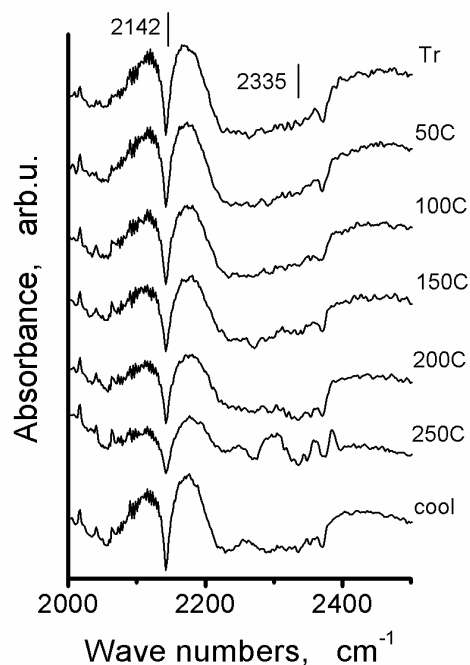


**Fig. 7.** In situ DRIR spectra collected during CO oxidation in presence of biogenic iron-containing Fe-Pd/Al-Si-O sample.

Figure 8 shows calculated CO conversions in conducted experiments. 0.3%Pd/Al-Si-O demonstrates an almost constant increase in activity with reaction temperature rise. Biogenic iron-containing material demonstrates a slightly lower activity despite that it contains two potentially active components in oxidation reaction, namely Pd and the redox couple of  $\text{Fe}^{3+}$ - $\text{Fe}^{2+}$ . Actually, the Fe-Pd/Al-Si-O system manifests a CO conversion at  $50^\circ\text{C}$  showing that the biogenic iron-containing material has intrinsic activity. The 0.3%Pd/Al-Si-O sample has very low activity at  $50^\circ\text{C}$  and becomes more active at higher temperatures. The obtained results correspond to a necessity of Pd to be converted in active form. Thus, the experiment indicates that the initial material changes with time on stream. Formation of more or a less active iron-containing phase in the Fe-Pd/Al-Si-O sample can be supposed to occur in the interval  $150$ – $200^\circ\text{C}$  giving rise to a shift of the curve but keeping the slope at higher temperatures. Our previous investigations on the catalytic activity of biogenic iron-containing materials showed that FeOOH modifications were converted to respective  $\text{Fe}_2\text{O}_3$  under these conditions [12].

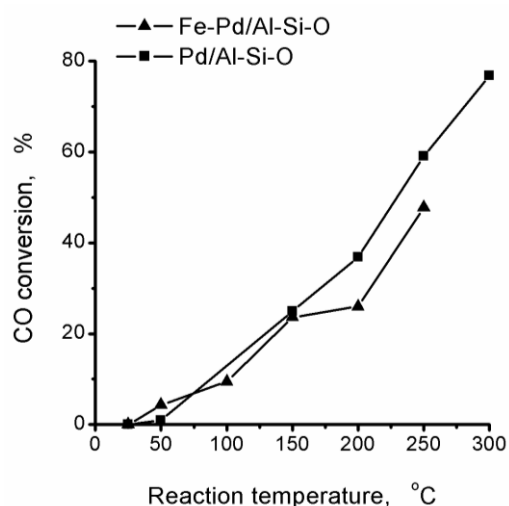


Fig. 8. CO conversion on studied samples.

Spent samples (after catalytic measurements) were studied by SEM and XPS. SEM images (Figures 9 and 10) show broken fibres (visible as dark area) with deposited phases of Pd/PdO and biogenic iron (visible as light area). EDX study showed uniform distribution of Pd on the surface in both tested catalyst samples. However, iron was unevenly distributed, sometimes as being predominantly concentrated on fibre edges. The latter observation corresponds to very small changes of specific

surface area after deposition of biogenic iron as determined by BET measurements of the hybrid material. As it is shown on both sample map sum spectra, Pd concentration is 0.7(1) wt.% and that of Fe is 18.8%. These results show that the expected composition of the hybrid sample has been achieved. SEM-EDX analyses revealed a Pd concentration value, which is not in contradiction of XPS data. A registered very low amount of Pd, within the error limits of the ESCALAB instrument, is due to method constraints. Both methods derive information on sample surface from different depth. Sampling depth of XPS analysis is up to 10 nm (depending on the kinetic energy of detected electron), however, for SEM-EDX it is up to 5  $\mu\text{m}$ . Thus, XPS results show that Pd is ‘buried’ in the alumina-silica matrices of the fibrous material [23] and additionally by deposited biogenic iron as the depth is more than 10 nm. Therefore, Pd is detectable by the SEM-EDX method but not completely by the XPS.

In this context, a lower catalytic activity of the hybrid material can be explained by partial pore and Pd surface blocking, as seen by iron surface concentration in the composite material, which is more than one order of magnitude higher than that of palladium.

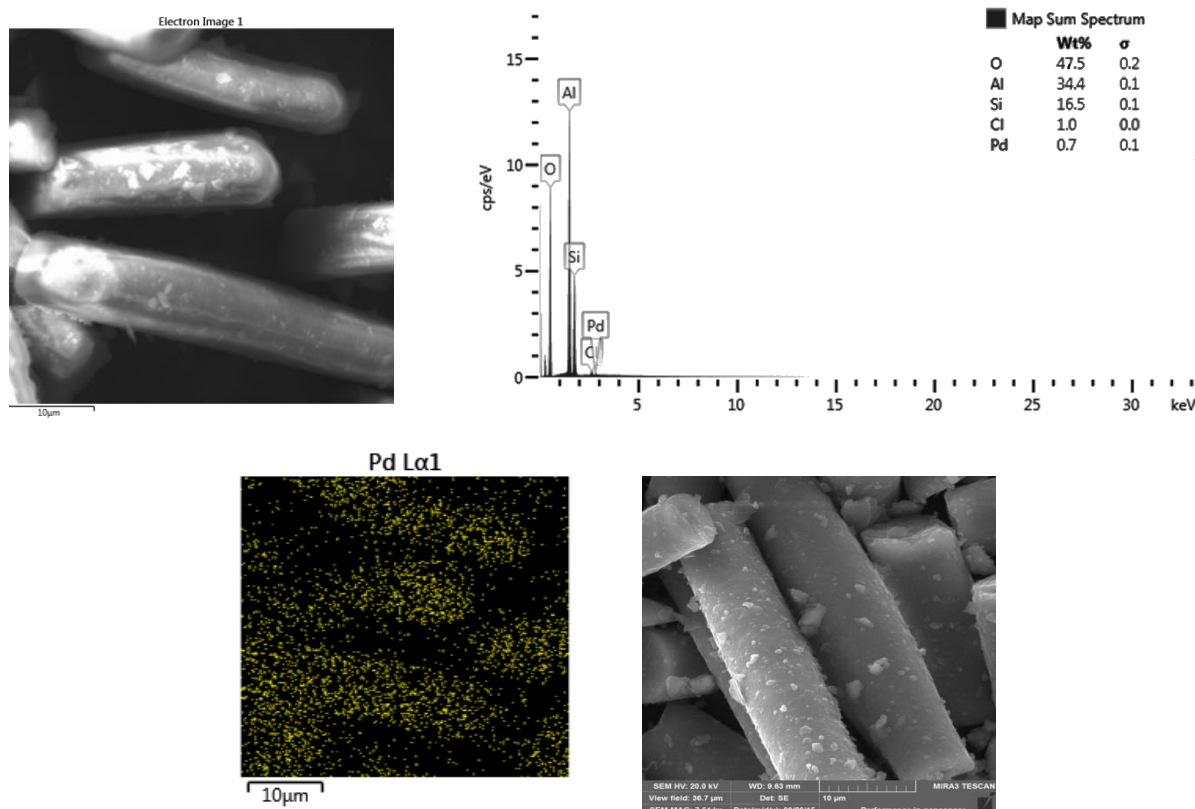
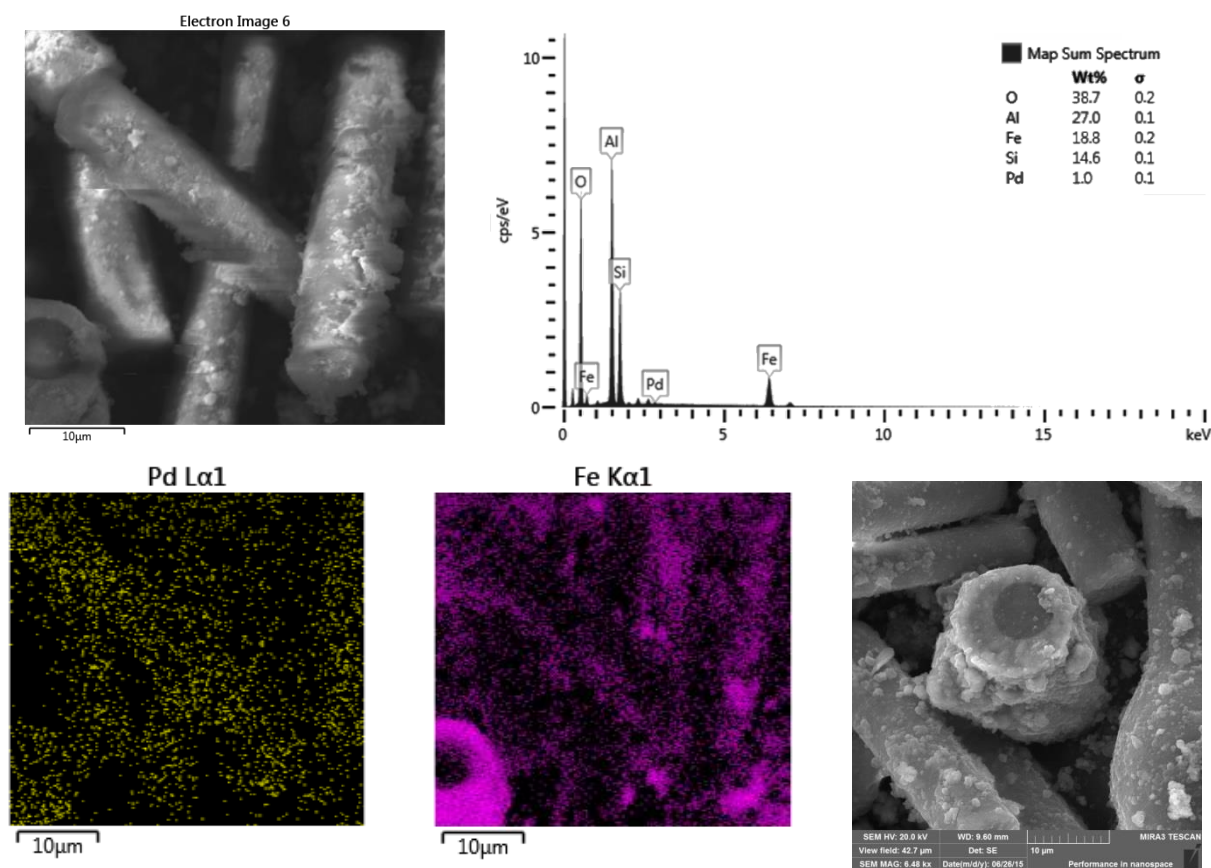


Fig. 9. Electron images of spent 0.3% Pd/Al-Si-O fibrous material, EDX map sum spectrum and EDX map of Pd(L $\alpha$ 1) distribution.



**Fig. 10.** Electron images of spent biogenic iron-containing Fe-Pd/Al-Si-O sample, EDX map sum spectrum and EDX maps of Pd(L $\alpha$ 1) and Fe(K $\alpha$ 1) distribution.

High resolution XPS analysis of the tested samples revealed existence of Pd<sup>0</sup> only on the surface of the 0.3%Pd/Al-Si-O sample at a Pd/(Al+Si) ratio of  $2.3 \times 10^{-3}$ , which was similar to that in the fresh sample (Fig. 4). Comparative XPS investigation of the fresh and spent 0.3%Pd/Al-Si-O system proved transition of Pd<sup>2+</sup> to Pd<sup>0</sup>. This supports a process of Pd transformation into an active form with time on stream at elevated temperatures due to reduction of Pd by CO in the mixture. The fibrous Fe-Pd/Al-Si-O catalyst with deposited biogenic iron was almost unchanged after the catalytic test. Palladium amount was preserved (within the error limits of the XP spectrometer) at a Pd/(Al+Si) ratio of  $1.7 \times 10^{-3}$ . Iron was present in two forms on the surface, Fe<sup>3+</sup>  $\approx$  Fe<sup>2+</sup>, at a Fe/(Al+Si) ratio of  $11.4 \times 10^{-2}$  (Fig. 5).

The results obtained on studying spent samples by SEM and XPS allow concluding that a close catalytic behaviour of both the studied systems is due to stable dispersion of Pd and iron on the catalyst surface that is preserved during/after reaction.

## CONCLUSIONS

This study indicated that the catalytic activity of both 0.3%Pd/Al-Si-O and Fe-Pd/Al-Si-O systems was essentially due to palladium. Despite the presence of

a Fe<sup>3+</sup>-Fe<sup>2+</sup> couple, which is active in oxidation reactions, no synergism was observed. Similarities between the catalytic performances of the studied systems could be explained by uniform and stable distribution of palladium and iron on the surface, which is preserved under reaction conditions.

*Acknowledgements:* The authors are grateful to the Bulgarian Science Fund for financial support by project T02-17/2014 as well as to the Bulgarian Academy of Sciences and the Slovak Academy of Sciences for support through the bilateral project 'Mechanochemical synthesis – an ecological friendly process in the production of materials for photocatalytic air and water purification'. The supply of Pd catalyst by Dr. L. Spasov and Dr. Ch. Bonev (Institute of Catalysis), and the deposition of biogenic material by Prof. V. Groudeva and Dr. M. Iliev (Sofia University) is greatly acknowledged. M.F. and J.B. also thank VEGA (2/0097/13) and APVV (14-0103) for support of their work.

## REFERENCES

1. H. Jung, H. Park, J. Kim, J.-H. Lee, H.-G. Hur, N. V. Myung, H. Choi, *Environ. Sci. Technol.*, **41**, 4741 (2007).

2. B. Kazprzyk-Hordern, M. Ziolek, J. Nawrocik, *Appl. Catal. B: Environ.*, **46**, 639 (2003).
3. K. Mandai, T. Korenaga, T. Ema, T. Sakai, M. Furutani, H. Hashimoto, J. Takada, *Tetrahedron Lett.*, **53**, 329 (2012).
4. T. Ema, Y. Miyazaki, I. Kozuki, T. Sakai, H. Hashimoto, J. Takada, *Green Chem.*, **13**, 3187 (2011).
5. G. E. Hoag, J. B. Collins, J. L. Holcomb, J. R. Hoag, M. N. Nadagouda, R. S. Varma, *J. Mater. Chem.*, **19**, 8671 (2009).
6. T. Shahwan, S. Abu Sirriah, M. Nairat, E. Boyaci, A. E. Eroglu, T. B. Scott, K. R. Hallam, *Chem. Eng. J.*, **172**, 258 (2011).
7. R. A. Maithreepala, R.-A. Doong, *Chemosphere*, **70**, 1405 (2008).
8. B. Kumar, K. Smita, L. Cumbal, A. Debut, *J. Saudi Chem. Soc.*, (2014), <http://dx.doi.org/10.1016/j.jscs.2014.01.003>
9. A. Alharthi, R. A. Blackley, T. H. Flowers, J. S. J. Hergreaves, I. D. Pulford, J. Wigzell, W. Zhou, *J. Chem. Technol. Biotechnol.*, (2014), doi:10.1002/jctb.4434
10. T. Sakai, Y. Miyazaki, A. Murakami, N. Sakamoto, T. Ema, H. Hashimoto, M. Furutani, M. Nakanishi, T. Fujii, J. Takada, *Org. Biomol. Chem.*, **8**, 336 (2010).
11. M. Shopska, Z. Cherkezova-Zheleva, D. Paneva, M. Iliev, G. Kadinov, I. Mitov, V. Groudeva, *Cent. Eur. J. Chem.*, **11**, 215 (2013).
12. M. Shopska, D. Paneva, G. Kadinov, S. Todorova, M. Fabian, I. Yordanova, Z. Cherkezova-Zheleva, I. Mitov, *Reac. Kinet. Mechan. Catal.* (submitted).
13. K. B. Narayanan, N. Sakthivel, *Adv. Colloid Interface Sci.*, **156**, 1 (2010).
14. H. Jung, J.-W. Kim, H. Choi, J.-H. Lee, H.-G. Hur, *Appl. Catal. B: Environ.*, **83**, 208 (2008).
15. A. B. Seabra, P. Haddad, N. Duran, *IET Nanobiotechnol.*, **7**, 90 (2013).
16. H. Hashimoto, S. Yokoyama, H. Asaoka, Y. Kusano, Y. Ikeda, M. Seno, J. Takada, T. Fujii, M. Nakanishi, R. Murakami., *J. Magnet. Magnet. Mater.*, **310**, 2405 (2007).
17. B. Xin, D. Zhang, X. Zhang, Y. Xia, F. Wu, S. Chen, L. Li, *Bioresour. Technol.*, **100**, 6163 (2009).
18. J. A. Rentz, I. P. Turner, J. L. Ullman, *Water Res.*, **43**, 2029 (2009).
19. R. Cornell, U. Schwertmann, *Iron Oxides*, Wiley-VCH Verlag, Weinheim, Germany, 2003.
20. R. W. Fitzpatrick, R. Naidu, P. G. Self, in: *Biomineralization Processes of Iron and Manganese - Modern and Ancient Environments*, Catena Suppl. 21, H. C. W. Skinner, R. W. Fitzpatrick Eds., Catena Verlag, Reiskirchen, Germany, 1992, p. 263.
21. D. A. Ankrah, E. G. Sogaard, 13th Int. Water Technol. Conf., IWTC 13, 2009, Hurghada, Egypt, p. 999.
22. A. Alharthi, R. A. Blackley, T. H. Flowers, J. S. J. Hergreaves, I. D. Pulford, J. Wigzell, W. Zhou, *J. Chem. Technol. Biotechnol.*, **89**, 1317 (2014).
23. L. Spasov, P. Dimitrov, Ch. Vladov, V. Zhelyazkov, Ch. Bonev, L. Petrov, in: *Heterogeneous Catalysis (Proc. 8th Int. Symp. Heterogen. Catal., Varna, 5–9 October 1996)*, Institute of Catalysis, Bulgarian Academy of Sciences, Sofia, 1996, p. 751.
24. M. Sawayama, T. Suzuki, H. Hashimoto, T. Kasai, M. Furutani, N. Miyata, H. Kunoh, J. Takada, *Curr. Microbiol.*, **63**, 173 (2011).
25. D. Shirley, *Phys. Rev. B*, **5**, 4709 (1972).
26. J. H. Scofield, *J. Electron Spectrosc. Relat. Phenom.*, **8**, 129 (1976).
27. L. H. Little, *Infrared Spectra of Adsorbed Species*, Academic Press Inc., London, New York, 1966.
28. A. U. Gehring, A. M. Hofmeister, *Clays Clay Miner.*, **42**, 409 (1994).
29. N. Lazaroff, W. Sigal, A. Wasserman, *Appl. Environ. Microbiol.*, **43**, 924 (1982).
30. S. Music, A. Saric, S. Popovic, K. Nomura, T. Sawada, *Croat. Chem. Acta*, **73**, 541 (2000).
31. B. Weckler, H. D. Lutz, *Eur. J. Solid State Inorg. Chem.*, **35**, 531 (1998).
32. S. Gota, E. Guiot, M. Henriot, M. Gautier-Soyer, *Phys. Rev. B*, **60**, 14387 (1999).

## СИНТЕЗ НА КАТАЛИЗАТОР Fe-Pd/Al-Si-O СЪДЪРЖАЩ БИОГЕННО ЖЕЛЯЗО ЧРЕЗ КУЛТИВИРАНЕ НА БАКТЕРИИ ОТ РОДА *LEPTOTHRIX*

М. Г. Шопска<sup>1\*</sup>, Г. Б. Кадинов<sup>1</sup>, Я. Бриянчин<sup>2</sup>, Ил. Д. Йорданова<sup>1</sup>, Хр. Г. Колев<sup>1</sup>, М. Фабиан<sup>2</sup>

<sup>1</sup> *Институт по катализ, Българска академия на науките, ул. „Акад. Г. Бончев”, Бл. 11, 1113 София, България*

<sup>2</sup> *Институт по геотехника, Словацка академия на науките, ул. „Ватсонова” № 45, 040 01 Кошице, Словакия*

Постъпила на 15 септември 2015 г.; Преработена на 4 ноември 2015 г.

(Резюме)

Чрез култивиране на бактерии от рода *Leptothrix* в среда силиций-желязо-глюкоза-пептон е отложено биогенно желязо върху влакнест катализатор 0.3%Pd/Al-Si-O. Така е получен композитен материал Fe-Pd/Al-Si-O. Методите инфрачервена спектроскопия, сканираща електронна микроскопия (с енергийно дисперсивен рентгенов анализ), нискотемпературна адсорбция на азот и рентгенова фотоелектронна спектроскопия бяха използвани при охарактеризиране на изследваните образци. Установено бе, че хибридният материал съдържа биогенен лепидокрокит,  $\gamma$ -FeOОН. Каталитичната активност на образците бе изследвана в реакцията на окисление на СО. Поведението на системите бе регистрирано *in situ* чрез дифузно-отражателна инфрачервена спектроскопия. Каталитичните изпитания целяха оценка на качествата на системи, получени при модифициране на биогенно желязо. Влакнестият катализатор 0.3%Pd/Al-Si-O и хибридният материал Fe-Pd/Al-Si-O показаха подобни каталитични отнасяния. Това се дължи на еднородното и стабилно разпределение на паладия и желязото по повърхността на образците. Въпреки, че на синтезирания композит е присъща каталитичната активност при ниски температури, регистрираната активност в изследвания интервал от реакционни температури до голяма степен се дължи на паладия.

## Mechanochemical synthesis, characterization, and photocatalytic activity of CdS/TiO<sub>2</sub> composites in air purification

N. G. Kostova<sup>1</sup>, E. Dutkova<sup>2</sup>, A. Eliyas<sup>1</sup>, E. Stoyanova-Eliyas<sup>3</sup>, M. Fabián<sup>2</sup>, P. Balaž<sup>2</sup>

<sup>1</sup>*Institute of Catalysis, Bulgarian Academy of Sciences, 1113 Sofia, Bulgaria*

<sup>2</sup>*Institute of Geotechnics, Slovak Academy of Sciences, 04001 Košice, Slovakia*

<sup>3</sup>*Institute of Physical Chemistry, Bulgarian Academy of Sciences, 1113 Sofia, Bulgaria*

Received September 29, 2015; Revised October 27, 2015

Two samples of CdS/TiO<sub>2</sub> composites have been prepared by single-step solid-state mechanochemical route. Sample 1 was prepared in a ball mill by mixing commercial TiO<sub>2</sub> Degussa P25 with CdS mechanochemically synthesized in advance (cubic hawleyite phase). Sample 2 has been obtained by the mechanochemical synthesis from cadmium acetate and sodium sulphide in the presence of TiO<sub>2</sub> Degussa P25. Characterization of the synthesized composite materials by means of XRD, DRS, PL, SEM, and EDX showed that the CdS particles were attached to titania. XRD analysis proved that the rutile TiO<sub>2</sub> phase is prevailing in Sample 1, unlike the case of Sample 2, which contained mainly anatase TiO<sub>2</sub> phase. UV-vis diffuse reflectance spectroscopy was applied in order to evaluate the band gaps of the synthesized samples. Obtained values of the band gap for the composite CdS/TiO<sub>2</sub> samples are lying below the band gap value interval of pure anatase TiO<sub>2</sub> phase (3.2 eV) and that of pure CdS (2.42 eV) enabling visible light illumination. The photocatalytic oxidation of ethylene (model air contaminant) was studied both under the effect of UV- and under visible light irradiation. It was established that the mechanochemically synthesized CdS/TiO<sub>2</sub> shows a higher photocatalytic activity in the oxidation of ethylene under visible light irradiation in comparison with pure titania due to the effect of the CdS component.

**Key words:** mechanochemistry, photocatalysis, titania, CdS, ethylene, air pollution.

### INTRODUCTION

Contaminated air exerts harmful effects on human health [1]. Volatile organic compounds are the basic pollutants in contaminated air [2]. A number of technologies have been elaborated to purify air, for instance passing it through a filter of activated carbon [3]. Processes of thermal oxidation or catalytic oxidation have also been applied [4]. However, these processes occur at high temperatures and pressures [5]. Heterogeneous photocatalytic oxidation is an alternative approach, which happens at room temperature and atmospheric pressure [6]. A great variety of photocatalytic materials enable efficient purification of polluted air [7]. Titania is the most widely applied photocatalyst to degrade organic contaminants in air and water [8]. But anatase TiO<sub>2</sub> absorbs only photons of the UV region, which comprises only 5% of the solar spectrum. Titania modifying with other semiconductors of narrow band gap and absorbing visible light is a popular approach to improving its light absorbance properties [9]. The present work is focused on TiO<sub>2</sub> modification with cadmium sulphide. Composite samples were prepared by the

mechanochemical route. Mechanochemical synthesis produces surface clean semiconductor nanoparticles without any influence of organic ligands, applied in chemical process, and such nanoparticles can be tested as a photocatalyst [10].

Ethylene was selected as a model air contaminant [11]. Ethylene is causing air pollution due to its large-scale production in the petrochemical plants. The photocatalytic oxidation of ethylene is therefore a hot topic of the day [12, 13]. In the present work mechanochemically synthesized CdS/TiO<sub>2</sub> composites were tested and their photocatalytic activities were compared with data obtained beforehand by the traditionally used reference photocatalyst TiO<sub>2</sub> Degussa P25. The investigation of ethylene photocatalytic oxidation was carried out in a recently designed and constructed gas-phase flat-plate continuous flow photocatalytic reactor over a thin film coating of semiconductor material. The aim of the present paper was to investigate the influence of the synthesis conditions for preparing CdS/TiO<sub>2</sub> composites by monitoring their physicochemical properties and testing their efficiency as photocatalysts for complete oxidation of ethylene.

\* To whom all correspondence should be sent:  
E-mail: nkostova@ic.bas.bg

## EXPERIMENTAL

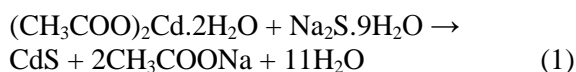
### 2.1 Materials

CdS/TiO<sub>2</sub> composites were synthesized from cadmium acetate (CH<sub>3</sub>COO)<sub>2</sub>Cd.2H<sub>2</sub>O (98%, ITES, Slovakia), sodium sulphide Na<sub>2</sub>S.9H<sub>2</sub>O (98%, Aldrich, Germany), and TiO<sub>2</sub> Degussa P25.

### 2.2. Mechanochemical synthesis

The mechanochemical synthesis of the samples was carried out in a Pulverisette 6 planetary ball mill (Fritsch, Germany). The ball mill was charged with 50 balls made of tungsten carbide having a diameter of 10 mm and weighing 360 grams. The rate of rotation of the planetary carrier was 500 rpm. Experimental runs were conducted in argon at room temperature.

Pure cadmium sulphide was mechanochemically prepared by following equation (1). Further details are published elsewhere [14].



One of the composite samples, denoted as CdS/TiO<sub>2</sub>-1, was synthesized by milling in a planetary ball mill using pure cadmium sulphide prepared beforehand [14] and the commercially available TiO<sub>2</sub> at a ratio of 1:4. The milling time interval was 30 min.

For a second mechanochemically synthesized composite sample, CdS/TiO<sub>2</sub>-2, a mixture of cadmium acetate, sodium sulphide, and TiO<sub>2</sub> P25 Degussa was used. The synthesis was carried out in the planetary ball mill in inert atmosphere under the same conditions as described above.

### 2.3. Characterization techniques

X-ray diffraction (XRD) patterns were recorded on a D8 Advance diffractometer (Bruker, Germany) using CuK $\alpha$  radiation.

Specific surface area ( $S_A$ ) values were obtained by the low-temperature nitrogen adsorption method using a Gemini 2360 sorption apparatus (Micromeritics, USA).

Diffuse reflectance UV-vis spectra were measured on a Thermo Evolution 300 UV-Vis Spectrophotometer equipped with a Praying Mantis device with Spectralon as the reference. Spectralon is a fluoropolymer, which has the highest diffuse reflectance among all the known materials or coatings over the ultraviolet, visible, and near-infrared regions of the spectrum. Kubelka-Munk relationships were used to transform the reflectance data into absorption spectra.

Photoluminescence (PL) spectra at room temperature were acquired at right angle on a photon counting spectrofluorometer PC1 (ISS) with a photoexcitation wavelength of 325 nm. A 300-W xenon lamp was used as the excitation source. The emission was collected in a 25-cm monochromator with resolution of 0.1 nm equipped with a photomultiplier. The photoexcitation and photo-emission slit widths were 1 and 2 mm, respectively. For measuring the PL intensity, the powders were suspended in absolute ethanol.

The photocatalytic activity of the samples in the reaction of ethylene complete oxidation was measured under UV-A polychromatic light illumination (the so called Black Light Blue BLB lamp with  $\lambda_{\text{max}} = 365$  nm), UV-C monochromatic illumination (TUV lamp  $\lambda = 254$  nm), and under visible light illumination. The standard reference experimental conditions and the reactor configuration have been described elsewhere [15], while the operational parameters are listed in Table 1.

**Table 1.** Comparison between CdS/TiO<sub>2</sub> composites and commercial TiO<sub>2</sub> Degussa P 25 in the photocatalytic conversion of ethylene (30% and O<sub>2</sub> excess) under illumination with different types of light

Photocatalyst	Ethylene conversion, %	Type of illumination	Intensity of illumination, W.cm <sup>-2</sup>
CdS/TiO <sub>2</sub> -1	0.7	UV-A	0.014
CdS/TiO <sub>2</sub> -1	4.5	UV-C	0.014
CdS/TiO <sub>2</sub> -1	11.5	visible	8.9
CdS/TiO <sub>2</sub> -2	3.7	UV-A	0.014
CdS/TiO <sub>2</sub> -2	5.1	UV-C	0.014
CdS/TiO <sub>2</sub> -2	14.4	visible	8.9
TiO <sub>2</sub> Degussa P25	12.8	UV-A	0.014
TiO <sub>2</sub> Degussa P25	27.3	UV-C	0.014
TiO <sub>2</sub> Degussa P25	0	visible	8.9

The support bearing the photocatalytic layer of CdS/TiO<sub>2</sub> composites and TiO<sub>2</sub> was a commercially available Al foil, covered with silica gel (0.2 mm), manufactured by Merck for the purposes of thin layer chromatography (TLC Merck Art. 5554 Kieselgel 60 F<sub>254</sub>). A suspension (56 mg CdS/TiO<sub>2</sub> in 5 ml H<sub>2</sub>O) was ultrasonically treated as in Ref. [16].

## RESULTS AND DISCUSSION

The XRD measurements were carried out to study the phase composition of the obtained samples. Figure 1 represents XRD patterns of the two mechanochemically synthesized CdS/TiO<sub>2</sub> composite materials. The X-ray patterns of the cadmium sulphide and of the commercial product

TiO<sub>2</sub> P25 Degussa are also given for comparison. The profile of TiO<sub>2</sub> P 25 Degussa shows that it is composed of crystallites of anatase and rutile at a ratio of 75:25. Some diffraction lines are observable in the XRD pattern of the CdS, which indicate the cubic structure of hawleyite CdS (JCPDS 00-010-044). All the diffraction lines are wide, which give evidence for the formation of fine-sized crystallites [17] as well as for structural disorder, which appears in the cadmium sulphide during the milling process [10].

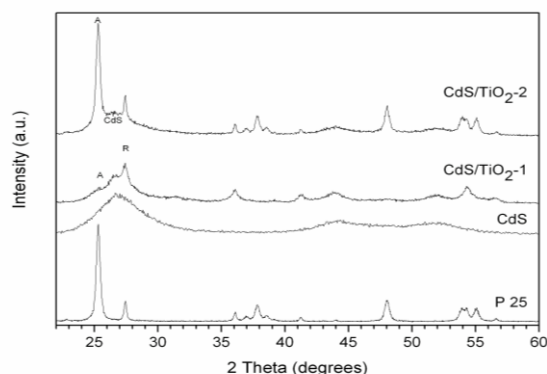


**Fig. 1.** XRD patterns of TiO<sub>2</sub> P25 Degussa and of mechanochemically synthesized CdS, CdS/TiO<sub>2</sub>-1, and CdS/TiO<sub>2</sub>-2 samples.

Substantial changes were registered in the XRD pattern of the CdS/TiO<sub>2</sub>-1 sample. This sample, obtained by means of mechanochemical synthesis starting from a mixture of cadmium sulphide and TiO<sub>2</sub> P 25 in the ball mill, gives rise to a substantial decrease in intensity of the peak at  $2\theta = 25.2^\circ$  related to the plane (101) of the anatase. A significant widening was observed for all the registered diffraction lines. A considerable decrease of the crystallite size was registered with this sample. Some lines characteristic of CdS are also present. Rutile is the prevailing phase in this sample. Wide diffraction lines of the mechanochemically synthesized CdS clearly prove the nanosized nature of the sample [18]. The impact of energy during the milling process is manifested in the form of phase transformation [19].

Regarding the diffraction pattern of sample CdS/TiO<sub>2</sub>-2, which was prepared by direct mechanochemical synthesis of CdS from cadmium acetate and sodium sulphide on the surface of TiO<sub>2</sub> P 25, all the lines characteristic of TiO<sub>2</sub> P 25 are present as well as some others, which are characteristic of CdS having a cubic structure of hawleyite. No phase transformation of anatase into rutile was registered in this case. Here, the high-energy milling was accompanied by generation of fresh surface, which is displayed in a considerable

growing up of the specific surface area of the CdS/TiO<sub>2</sub>-2 sample ( $72 \text{ m}^2 \text{ g}^{-1}$ ) in comparison to that of P 25 ( $50 \text{ m}^2 \text{ g}^{-1}$ ). The specific surface area of sample CdS/TiO<sub>2</sub>-1 was measured to be  $19 \text{ m}^2 \text{ g}^{-1}$ . Specific surface area values of the samples are one of the most important features of the milled samples [10]. High values of the specific surface area of mechanochemically synthesized samples suppose an effective application of the latter to surface-area dependent processes, such as sorption, heterogeneous catalysis (both dependent on the number of surface active sites) and others. The CdS/TiO<sub>2</sub>-1 sample represents a less crystalline material, while sample CdS/TiO<sub>2</sub>-2 is a more crystalline material (Fig. 1).

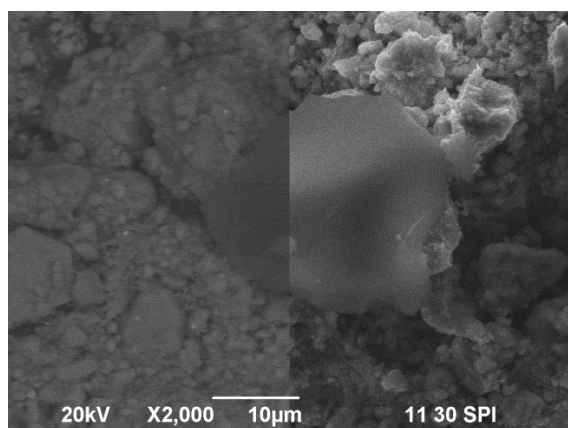
A SEM micrograph of the CdS/TiO<sub>2</sub>-2 sample is shown in figure 2. It represents juxtaposition of back-scattered (left side) and secondary electron images (right side) of CdS deposited on TiO<sub>2</sub>. There is better sharpness of secondary electron image (SEI), but the chemical contrast in the back scattered image (BEC) gives more information: bright area is CdS and dark area is TiO<sub>2</sub> as the atomic mass of Cd is higher than that of Ti; therefore, the electron yield (brightness) from Cd is also higher. Elemental composition of CdS/TiO<sub>2</sub>-2 was determined by EDS (energy dispersive spectroscopy) and it is shown in Table 2.

**Table 2.** Composition of the CdS/TiO<sub>2</sub>-2 sample supported on a commercially available Al foil covered by silica gel (0.2 mm)

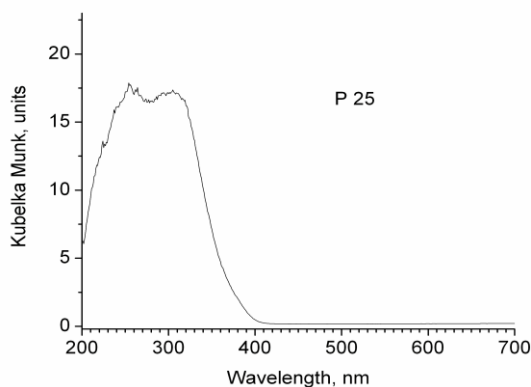
Element	Weight, %	Content, at. %
O	41.91	71.09
Si	2.29	2.21
S	5.15	4.36
Ti	31.11	17.62
Cd	19.54	4.72
total	100.00	100.00

Figure 2 represents DRS spectra of the initial TiO<sub>2</sub> P25 Degussa sample and the mechanochemically synthesized sample CdS/TiO<sub>2</sub>-2. The absorbance spectrum of TiO<sub>2</sub> P25 consists of intensive absorbance only in the ultraviolet region. The absorbance edge of the pure titania is about 390 nm. In contrast, the absorbance edge in the spectrum of the synthesized samples of CdS/TiO<sub>2</sub>-2 was registered at 530 nm, i.e. already in the visible region (Fig. 3b). A red shift towards longer wavelengths is observed in the range of visible light. The band gaps  $E_g$  of the samples were calculated on the basis of Tauc equation [21]. Evaluated band gap values of the samples were 3.3, 2.46, 2.2, and 2.35 eV for TiO<sub>2</sub> P 25, CdS, CdS/TiO<sub>2</sub>-1, and CdS/TiO<sub>2</sub>-2,

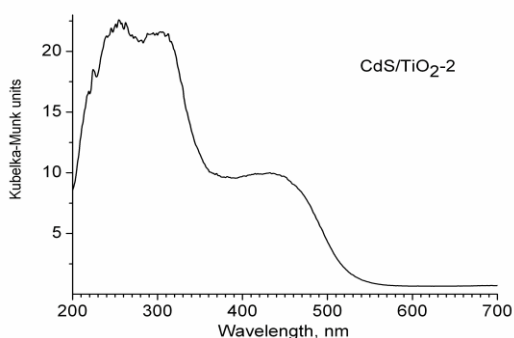
respectively. The band gap of the mechanochemically synthesized CdS/TiO<sub>2</sub> composites lies below that of CdS and thus allows visible light illumination.



**Fig. 2.** SEM image of sample CdS/TiO<sub>2</sub>-2 particles on the surface of SiO<sub>2</sub> coated by a TLC plate.



A



B

**Fig. 3.** A. UV-vis drs spectrum of TiO<sub>2</sub> P25 sample. B. UV-vis DR spectrum of mechanochemically synthesized CdS/TiO<sub>2</sub>-2 sample.

The photoluminescence (PL) spectra of the initial TiO<sub>2</sub> P 25 Degussa and mechanochemically synthesized CdS, CdS/TiO<sub>2</sub>-1, and CdS/TiO<sub>2</sub>-2 samples, photoexcited at 325 nm at room temperature, are displayed in figures 4 and 5. The photoexcitation wavelength of 325 nm, corresponding to photon energy of 3.81 eV, is greater than

the band gap energy of titania. This energy was an absorbed exciting transition of valence band electrons to the conduction band.

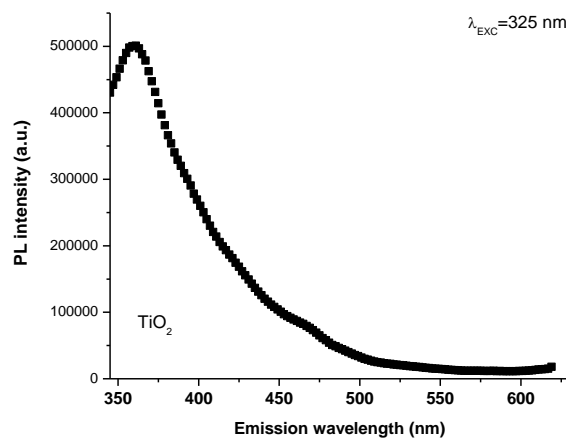


**Fig. 4.** Photoluminescence spectrum of TiO<sub>2</sub> P25 Degussa.

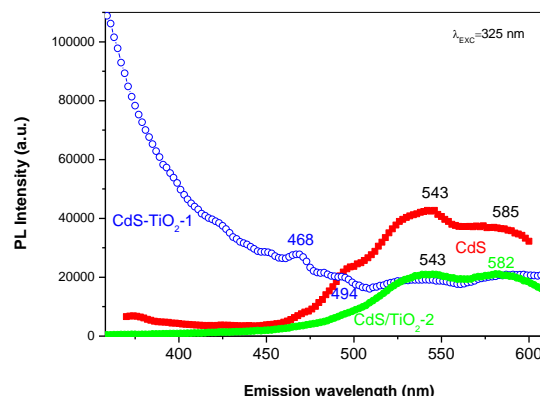


**Fig. 5.** Photoluminescence spectra of mechanochemically synthesized CdS, CdS/TiO<sub>2</sub>-1, and CdS/TiO<sub>2</sub>-2 samples.

The emission intensive peak in the spectrum of TiO<sub>2</sub> P 25 Degussa with a maximum in the near ultraviolet region at about 361 nm (3.43 eV) can be ascribed to emission of a photon having energy equal or slightly higher than the band gap width of the anatase phase of TiO<sub>2</sub> and it provides evidence for a direct recombination of a photoexcited electron and a positively charged hole [22, 23]. The photoluminescence emission is the result of two effects: part of the illuminating photons energy goes for a non-radiative transition (a transition between two vibrational energy levels of the crystal lattice nodes). Another part is emitted as a result of recombination of photoexcited electrons and holes (lower energy photons).

It is known that CdS nanoparticles manifest a light-emitting behaviour at a specific wavelength corresponding to the band gap width, which can be determined in this way. Thus, the formation of CdS nanoparticles can also be confirmed by photo-

luminescence spectroscopy [24]. The photoluminescence spectrum of the mechanochemically synthesized CdS shows a broad emission band with a maximum of the emission at 543 nm (2.3 eV) accompanied by a very slight emission peak at 585 nm (2.1 eV). The emission peak at 543 nm can be assigned to the surface-trap-induced photoluminescence, which involves the recombination of electrons with a trapped hole-sulphur vacancy inside the valence band of CdS nanoparticles [25]. A similar result has also been obtained [26].

The photoluminescence spectrum of the mechanochemically synthesized CdS/TiO<sub>2</sub>-2 sample is similar to that of the pure cadmium sulphide, but having a substantially lower intensity. The lower PL intensity of the CdS/TiO<sub>2</sub>-2 sample indicates a lower recombination rate of photoexcited electrons and holes [27]. No emission was observed in the case of TiO<sub>2</sub> P25 within the region of 475 up to 650 nm (Fig. 4). The presence of CdS in the composite CdS/TiO<sub>2</sub>-1 sample is leading to substantial changes in their PL spectra (Fig. 5) indicating an efficient transfer of electrons from the CdS particles to the titania. This results in suppression of the recombination of charge carriers in CdS/TiO<sub>2</sub> compared to titania. A PL spectrum of this sample is complicated because there are many factors that can influence the fluorescence signals such as surface states and bulk defects. In the spectrum of mechanochemically synthesized CdS/TiO<sub>2</sub>-1 sample, the minor emission peaks at 468 and 494 nm correspond to titania and only slightly pronounced wider emission peaks at 540 and 585 nm belong to CdS, accordingly. The emission at 468 nm (2.6 eV) proves the presence of oxygen vacancies, while that at about 494 nm (2.6 eV) could be ascribed to indirect recombination of defects involving interaction of phonons in the lattice oxygen vacancies in titania [20]. It is known that the electronic properties of CdS depend on the particle size [28]. Since the PL emission is the result of recombination of photoexcited electrons and holes, the lower photoluminescence intensity of synthesized composite CdS/TiO<sub>2</sub> samples proves a lower recombination rate of the photoexcited electrons and holes [29], which was aimed intentionally in this study by adding CdS.

It has been reported earlier that there is no PL peak emitted by the pure anatase phase, but a weak PL peak in the rutile phase of titania [30]. However, in our case we have observed fine PL peaks for rutile phase and enhanced PL entities for the anatase phase of the corresponding CdS/TiO<sub>2</sub> samples, which is in contrast with earlier reports.

The degree of ethylene conversion was taken as a measure of the photocatalytic activity. As it can be

seen from the data presented in Table 1, the best photocatalytic efficiency in ethylene photocatalytic oxidation under both kinds of UV-light illumination is exhibited by the TiO<sub>2</sub> Degussa P25, where the UV-C light is more effective due to the higher energy of the photons with all the three studied samples.

However, anatase TiO<sub>2</sub> was inactive under visible light illumination, where both CdS/TiO<sub>2</sub> samples exhibited some activity (Fig. 6). The CdS/TiO<sub>2</sub>-2 sample was superior to the CdS/TiO<sub>2</sub>-1 sample under visible light owing to the higher specific surface area and higher quantum yield.

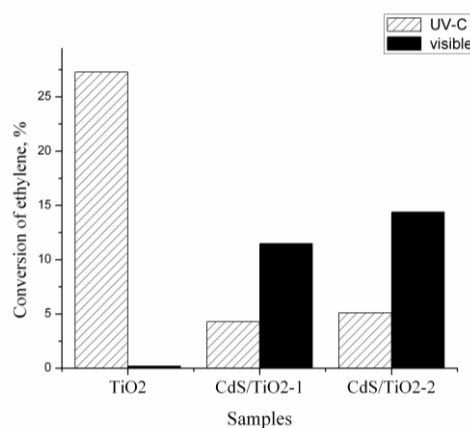


**Fig. 6.** Photocatalytic conversion of ethylene under illumination with different types of light over CdS/TiO<sub>2</sub> composites and commercial TiO<sub>2</sub> Degussa P25.

Composite CdS/TiO<sub>2</sub> materials could be a promising photocatalyst to utilize a wide share of solar light irradiation. Upon irradiation of the samples with visible light the electrons in the valence band of CdS are photoexcited and they are transferred to the conduction band and further to the TiO<sub>2</sub> conduction band as the two conduction bands are merging at the interphase boundary between the two attached particles. This is due to the fact that the oxidation potential of TiO<sub>2</sub> is superior to that of CdS, so the local electric field at the interphase boundary enables this transition of the photoexcited electrons from the conduction band of CdS to the conduction band of TiO<sub>2</sub> through the interphase boundary layer between the attached two particles. In this way the photoinduced charge carriers (e<sup>-</sup> and h<sup>+</sup>) in CdS appear to be effectively separated, which hinders their recombination prolonging the lifetime of the holes that are, in fact, the oxidation active sites of the catalyst in an oxidation reaction. Therefore, the result is that the mechanochemically synthesized CdS/TiO<sub>2</sub> samples manifest a higher photocatalytic activity in the oxidation of ethylene under visible light irradiation in comparison with pure titania.

## CONCLUSION

The present paper represents a detailed study of the structural, optical, and photocatalytic properties of mechanochemically synthesized CdS/TiO<sub>2</sub> composite materials. The XRD pattern analysis of the CdS/TiO<sub>2</sub>-1 sample, prepared by mechanochemical synthesis in a planetary ball mill of a mechanical mixture of CdS and TiO<sub>2</sub> P25, showed that a phase transition into rutile occurred in a larger fraction of anatase of the initial TiO<sub>2</sub> P 25 material. The phase composition of TiO<sub>2</sub> P 25 was preserved during the mechanochemical synthesis of the crystalline CdS/TiO<sub>2</sub>-2 sample. The specific surface area of this sample was higher by 50% than that of the initial TiO<sub>2</sub> P 25. A DRS study revealed that all the mechanochemically synthesized samples demonstrated a strong absorbance in the visible light region. Evaluated band gap values of the samples were 3.3, 2.46, 2.2, and 2.35 eV for TiO<sub>2</sub> P 25, CdS, CdS/TiO<sub>2</sub>-1, and CdS/TiO<sub>2</sub>-2, respectively. An enhanced photocatalytic activity of the synthesized composite materials in the visible range of the spectrum for ethylene oxidation in polluted air is owing to an efficient separation of photoexcited electrons and holes, i.e. the charge carriers between attached CdS and TiO<sub>2</sub> phases.

*Acknowledgement:* This work was supported by a bilateral cooperation project between the Bulgarian Academy of Sciences and Slovak Academy of Sciences, Slovak projects VEGA 2/0097/13 and 2/0027/14, project APVV-14-0103, and by the Bulgarian Science Fund through project T02-17/2014.

## REFERENCES

1. T. N. Obee, R. T. Brown, *Environ. Sci. Technol.*, **29**, 1223 (1995).
2. X. Chen, S. A. C. Carabineiro, S. S. T. Basts, P. B. Tavares, J. J. M. Orfao, M. F. R. Pereira, J. L. Figueiredo, *Appl. Catal. A-Gen.*, **472**, 101 (2014).
3. S. Sircar, T. C. Golden, M. B. Rao, *Carbon*, **34**, 1 (1999).
4. S. Ojala, S. Pitkäaho, T. Laitinen, N. Niskala-Koivikko, R. Brahmī, J. Gaállová, L. Matejova, R. L. Keiski, *Topics Catal.*, **54**, 1224 (2011).
5. K. Evaræet, J. Baeyens, *J. Hazard. Mater. Rev.*, **14**, 29 (2013).
6. N. Keller, M. N. Ducamp, D. Robert, V. Keller, *Chem. Rev.*, **113**, 5029 (2013).
7. J. Lasek, Y. H. Yu, J. C. S. Wu, *J. Photochem. Photobiol.-Rev.*, **14**, 29 (2013).
8. A. Fujishima, X. Zhang, D. A. Tryk, *Surf. Sci. Rep.*, **63**, 515 (2008).
9. B. Sun, P. G. Smirniotis, P. Boolchand, *Langmuir*, **21**, 11397 (2005).
10. P. Balaz, *Mechanochemistry in Nanoscience and Materials Engineering*, Springer, Berlin, 2008.
11. M. Hussain, R. Ceccarelli, D. L. Marchisio, D. Fino, N. Russo, F. Ceobaldo, *Chem. Eng. J.*, **157**, 45 (2010).
12. P. Long, Y. Zhang, X. Chen, Z. Yi, *J. Mater. Chem. A* **3**, 4163 (2015).
13. X. Chen, X. Huang, Z. Yi, *Chemistry - A Europ. J.*, **20**, 17590 (2015).
14. P. Balaz, M. Balaz, E. Dutkova, A. Zorkovska, J. Kovac, P. Hronec, J. Kovac, Jr., M. Caplovicova, J. Mojzis, G. Mojzisova, A. Eliyas, N. G. Kostova, *Mater. Sci. Eng. C*, in press, DOI:10.1016/j.msec.2015.09.040.
15. A. Eliyas, K. Kumbilieva, V. Iliev, S. Rakovsky, *React. Kinet., Mech. Catal.*, **102**, 251 (2011).
16. A. Eliyas, V. Iliev, I. Mitov, S. Rakovsky, *Nanoscience and Nanotechnology*, Issue 10, Eds. E. Balabanova, I. Dragieva, BPS Publ. Co, 2010, p. 38.
17. J. Z. Niu, W. W. Xu, H. B. Shen, S. Li, H. Z. Wag, L. S. Li, *Bull. Korean Chem. Soc.*, **33**, 393 (2012).
18. V. Sepelak, A. Duvel, M. Wilkening, K.-D. Becker, P. Heitjans, *Chem. Soc. Rev.*, **42**, 7507 (2013).
19. I. J. Lin, S. Nadiv, *Mater. Sci. Eng.*, **39**, 93 (1979).
20. B. Choudhury, A. Choudhury, *Mater. Chem. Phys.*, **132**, 1112 (2012).
21. M. Bagheri-Mohagheghi, N. Shahtahmasebi, M. Alinejad, *Phys. B-Condensed Matter*, **403**, 2431 (2008).
22. B. S. Liu, X.-J. Zhao, Q. Zhao, X. He, J. Feng, *J. Electron Spectrosc. Relat. Phenom.*, **148**, 158 (2005).
23. D. Dastan, P. U. Loundhe, N. B. Chaure, *J. Mater. Sci.-Mater. Electr.*, **25**, 3473 (2014).
24. D. C. Onwudiwe, T. P. J. Kruger, O. S. Oluwatobi, Ch. A. Strydom, *Appl. Surf. Sci.*, **290**, 18 (2014).
25. Y. Wang, N. Herron, *J. Phys. Chem.*, **92**, 4988 (1988).
26. Q. Wang, G. Chen, C. Zhou, R. C. Jin, L. Wang, *J. Alloy Comp.*, **503**, 485 (2010).
27. S. Jostar, *Mater. Sci. Semiconductor Proc.*, **34**, 65 (2015).
28. P. A. Sant, P. V. Kamat, *Phys. Chem. Chem. Phys.*, **4**, 198 (2002).
29. J. Xu, L. Li, Y. Yan, H. Wang, X. Wang, X. Fu, G. Li, *J. Colloid. Inter. Sci.*, **318**, 29 (2008).
30. L. G. J. de Haart, G. Blasse, *J. Solid State Chem.*, **61**, 135 (1986).

## МЕХАНОХИМИЧЕН СИНТЕЗ, ОХАРАКТЕРИЗИРАНЕ И ФОТОКАТАЛИТИЧНА АКТИВНОСТ НА CdS/TiO<sub>2</sub> КОМПОЗИТИ ЗА ОЧИСТВАНЕ НА ЗАМЪРСЕН ВЪЗДУХ

Н. Г. Костова<sup>1</sup>, Ер. Дуткова<sup>2</sup>, Ал. Елияс<sup>1</sup>, Ем. Стоянова-Елияс<sup>3</sup>, М. Фабиан<sup>2</sup>, П. Балаж<sup>2</sup>

<sup>1</sup> *Институт по катализ, Българска академия на науките, 1113 София, България*

<sup>2</sup> *Институт по геотехника, Словацка академия на науките, 04001 Кошице, Словакия*

<sup>3</sup> *Институт по физикохимия, Българска академия на науките, 1113 София, България*

Постъпила на 29 септември 2015 г.; Преработена на 27 октомври 2015 г.

(Резюме)

CdS/TiO<sub>2</sub> композитни образци са получени чрез едноетапен твърдотелен механохимичен синтез. Образец CdS/TiO<sub>2</sub>-1 е получен в топкова мелница чрез смесване на TiO<sub>2</sub> P25 Degussa с предварително получен CdS (кубична фаза hawleyite). Образец CdS/TiO<sub>2</sub>-2 е получен чрез механохимичен синтез от кадмиев ацетат и натриев сулфид в присъствие на TiO<sub>2</sub> P25 Degussa. Охарактеризирането на синтезираните композитни материали с рентгенофазов анализ, дифузионно-отражателна спектроскопия, фотолуминесцентна спектроскопия, сканираща електронна микроскопия и енергийно дисперсионен анализ показва, че частици от CdS са закрепени в титановия диоксид. Рентгенофазов анализ показва, че в образец CdS/TiO<sub>2</sub>-1 преобладава фазата рутил за разлика от образец CdS/TiO<sub>2</sub>-2, който съдържа основно анатаз. Дифузионно-отражателна спектроскопия беше използвана за определяне на забранената зона на механохимично синтезираните образци. Получените стойности за забранените зони на композитните образци са между забранената зона на чистия TiO<sub>2</sub> (3.2 eV) и CdS (2.42 eV). Фотокаталитичното окисление на етилен (моделен замърсител на въздух) е изследвано при облъчване както с ултравиолетова, така също и с видима светлина. Установено е, че механохимично синтезираните CdS/TiO<sub>2</sub> композитни образци показват по-висока фотокаталитична активност в окислението на етилен при облъчване с видима светлина в сравнение с чист титанов диоксид.

## Preparation of ZnO photocatalysts by copolymer Pluronic-assisted hydrothermal process

A. E. Eliyas<sup>1\*</sup>, I. D. Stambolova<sup>2</sup>, V. N. Blaskov<sup>2</sup>, D. Stoyanova<sup>2</sup>, K. I. Milenova<sup>1</sup>, L. D. Dimitrov<sup>3</sup>, M. G. Shipochka<sup>2</sup>, O. S. Dimitrov<sup>4</sup>

<sup>1</sup> Institute of Catalysis, Bulgarian Academy of Sciences, Acad. G. Bonchev St., Bldg. 11, 1113 Sofia, Bulgaria

<sup>2</sup> Institute of General and Inorganic Chemistry, Bulgarian Academy of Sciences, Acad. G. Bonchev St., Bldg. 11, 1113 Sofia, Bulgaria

<sup>3</sup> Acad. I. Kostov Institute of Mineralogy and Crystallography, Bulgarian Academy of Sciences, Acad. G. Bonchev St., Bldg. 107, 1113 Sofia, Bulgaria

<sup>4</sup> Institute of Electrochemistry and Energy Systems, Bulgarian Academy of Sciences, Acad. G. Bonchev St., Bldg. 10, 1113 Sofia, Bulgaria

Received: September 12, 2015; Revised November 6, 2015

Mesoporous ZnO powders were prepared by hydrothermal treatment (HT) of a three-block copolymer (P123) containing precipitate. Well-crystallized wurtzite ZnO phase powders were obtained. The particles consisted of oval nest-like units, which contained both non-uniformly distributed nanosheets and nanorods. Increasing the Pluronic (P123) content up to a certain value led to a larger share of the mesopores at the expense of micropore part. The ZnO samples, obtained from polymer-modified HT precipitate, exhibited a higher photocatalytic activity in oxidative discoloration of Reactive Black (RB5) dye than that of the reference sample. A larger surface area and a larger pore volume provided a larger number of surface active sites for the photocatalytic reaction increasing the adsorption capacity and facilitating the transportation of the dye.

**Keywords:** zinc oxide, photocatalyst, porosity, wastewaters, polymer modification.

### INTRODUCTION

Zinc oxide is known to be an excellent material for photocatalytic decontamination of wastewaters due to its high UV-light photosensitivity, nontoxic nature, and large band gap [1]. It has been demonstrated that the photocatalytic activity of ZnO is strongly dependent on its crystallite size, specific surface area, surface morphology, and texture. Various routes such as chemical bath deposition [2], thermal decomposition [3], vapour phase deposition [4], and hydrothermal process [5] have been applied to synthesize ZnO powders. The conventional hydrothermal method and its modifications such as electrochemically assisted, microwave-assisted, and surfactant-assisted versions have been developed as suitable methods for preparation of multifunctional ceramics materials. The surfactant-assisted hydrothermal synthesis of ZnO is an important phase method, which is used to prepare porous ZnO materials. Aimable *et al.* [6] have revealed that the size and morphology of precipitated ZnO can be tuned by addition of various anionic polymers, which cause reduction of the final particle size and lower the degree of agglomeration. Nanocrystalline meso-

porous assembled TiO<sub>2</sub> photocatalyst has been synthesized using laurylamine hydrochloride, CH<sub>3</sub>(CH<sub>2</sub>)<sub>11</sub>NH<sub>2</sub>.HCl, as a structure-directing surfactant behaving as a mesopore-forming agent and tested in the photocatalytic degradation of monoazo dye [7].

Recent investigations have indicated that polymers could also be used as templates to direct the formation of mesoporous oxides having high specific area, large pore volume, and small pore size. Therefore, mesoporous oxide should be a more effective photocatalyst because it offers a greater number of active sites for carrying out catalytic reactions. The mesoporous structures allow rapid diffusion of various reactants and products and enhance the rate of photocatalytic reaction [8]. In view of this, mesoporous ZnO powders can be prepared *via* addition of definite quantity of triblock copolymer as structure-directing agent for organizing the network-forming ZnO species and for controlling the pore size.

The aim of this work was to prepare mesoporous ZnO powders using three-block copolymer named Pluronic (P123) to assist the hydrothermal method and to study the effect of polymer concentration on the structure and on the photocatalytic efficiency.

\* To whom all correspondence should be sent  
E-mail: alel@ic.bas.bg

## EXPERIMENTAL

ZnO was synthesized by mixing zinc nitrate and P123 aqueous solutions.  $Zn^{2+}$  reactant solution was prepared by dissolving 2 g of Zn acetate in 200 ml deionized water. To prepare the P123-modified solutions, different quantities of tri-block copolymer Pluronic (P123,  $EO_{20}PO_{70}EO_{20}$ , Sigma-Aldrich) were diluted in small quantity of water and then added to the zinc acetate solution. Samples containing 2, 4, and 8 g of P123 were denoted as P1, P2, and P3, respectively. A sodium hydroxide aqueous solution was used to induce precipitation. For the sake of comparison, a reference sample was also obtained without any addition of polymer solution under the same preparation conditions (sample P0). The resulting mixture was transferred into an autoclave for thermal treatment at  $140^{\circ}C$  for 12 h. Then the autoclave was cooled down naturally to room temperature. The precipitates were washed several times with water and ethanol and dried in an oven at  $60^{\circ}C$ .

X-ray diffraction (XRD) patterns were recorded on a Bruker D2 Phaser diffractometer varying  $2\theta$  values between  $25$  and  $75^{\circ}$  and using  $Cu K_{\alpha}$  radiation ( $\lambda = 0.154056$  nm) at 40 kV. The single-point BET method has been applied to measure the specific surface area based on low-temperature adsorption of nitrogen. Method relative error amounts to about 8%. Specific surface area and pore-size distribution measurements were accomplished on an automated NOVA Win-CFR Quantachrom gas sorption system. The average pore diameter was evaluated by DFT assuming a cylindrical model of the pores. The total pore volume was estimated in accordance with the rule of Gurvich at a relative pressure of 0.96. For morphological characterization of the surface, a JEOL JEM-200CX scanning electron microscope (SEM) was used. The images were recorded at 80 keV accelerating voltage in secondary electrons image (SEI) mode. The samples were coated with a thin layer of carbon and gold for better conductivity prior to the investigation.

The photocatalytic discoloration of Reactive Black 5 azo dye was evaluated using aqueous solution of initial concentration of 20 ppm under polychromatic UV-A lamp illumination (18 W) with maximum emission at wavelength 365 nm. A semi-batch photocatalytic reactor was used feeding continuously  $O_2$  and creating large dissolved oxygen excess with respect to the stoichiometrically required amount for oxidation reaction. This allowed us to assume practically constant dissolved oxygen concentration and to include its value in the apparent rate constant,  $k_{app}$ . Therefore, the bimolecular reaction of Langmuir-Hinshelwood type of mecha-

nism is reduced to a pseudo-first order kinetic equation following only the azo dye concentration decrease with time of illumination. The course of the oxidative discoloration reaction was monitored by a CamSpec M501 UV-Vis spectrophotometer within the wavelength range from 200 to 800 nm in absorbance mode. The samples were equilibrated in the dark (reaching adsorption-desorption equilibrium) for about 30 min before switching on the irradiation. The photocatalytic activity tests were carried out by taking sample aliquots of the suspension from the reaction vessel at regular time intervals and filtering them. After measuring the absorbance, the amount was placed back into the reactor to have constant volume operation.

## RESULTS AND DISCUSSION

The X-ray diffraction patterns (Fig. 1) of both types of samples revealed narrow and sharp diffraction peaks, which proved a well crystallized phase identified as a hexagonal wurtzite type structure of ZnO (JCPDS 36-1451).

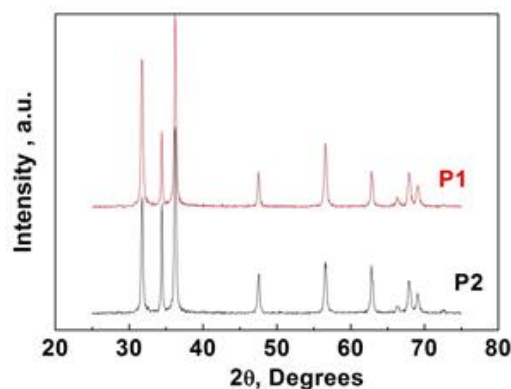


Fig. 1. XRD patterns of polymer modified samples.

The adsorption-desorption isotherms of the samples can be ascribed to type IV of the IUPAC classification, which shows the dominating presence of mesopores. The hysteresis loop could be interpreted as an H3 type. An almost horizontal section is observed, whereupon the hysteresis loop is shifted towards higher relative pressure ( $P/P_0$  approximately 1), which implies the presence of cylindrical pores. A similar behaviour was observed with the dry pressed ZnO nanoparticles with elongated shape [9]. The pore size distribution of the P0 sample is shown in figure 2. Polymer modification of the zinc precursor solution increases the relative share of the mesopores at the expense of the share of micropores (Fig. 3). Increasing the Pluronic concentration up to a certain value leads to a larger share of the mesopores lowering the share of micropores. The ZnO powders P3 contain predominantly micropores, while the mesopore volume drops down abruptly.

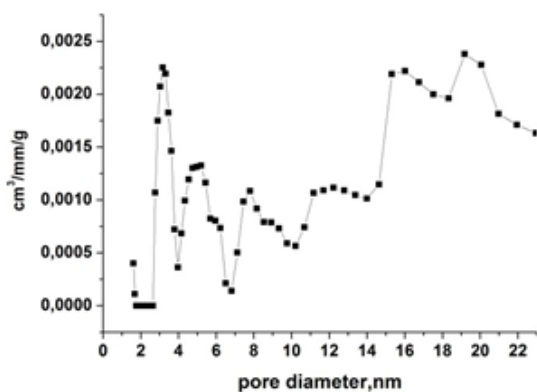


Fig. 2. Pore size distribution of P0 sample.

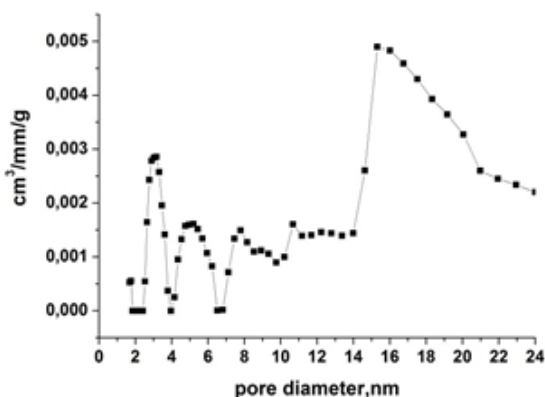


Fig. 3. Pore size distribution of P2 sample.

The BET surface area ( $S$ ) and average pore diameters of the samples are shown in table 1. BET measurements have revealed an enhancement of both specific surface area and average pore diameter of the Pluronic-modified powders (Table 1).

Table 1. BET surface area ( $S$ ) and average pore size ( $d$ ) of the samples

Sample	$S$ [ $\text{m}^2/\text{g}$ ]	$d$ [nm]
P0	10	8.4
P1	13	9.2
P2	14	9.3
P3	14	8.4

XPS analyses of  $\text{Zn}2p_{3/2}$  and  $\text{ZnO}1s$  spectra of the hydrothermally obtained samples disclosed similar features. The  $\text{Zn}2p_{3/2}$  peak has a maximum at  $\sim 1021.7$  eV that is typical of  $\text{Zn}^{2+}$  oxidation state. The  $\text{O}1s$  spectrum shows a mean peak at  $\sim 530.5$  eV and a shoulder at  $\sim 532.0$  eV, respectively. The former is assigned to lattice oxygen in zinc oxide while the latter is attributed to adsorbed hydroxyl groups. The  $\text{Zn}/\text{O}_T$  atomic ratio was evaluated from the values of  $\text{Zn}2p_{3/2}$  and  $\text{O}1s$  peak areas, normalized by corresponding photoionization cross-sections.

It has to be noted that all samples were non-stoichiometric. The values of  $\text{Zn}/\text{O}_T$  atomic ratio are lower for samples P2 and P3 (Table 2).

Table 2. XPS chemical compositions of the samples

Sample	O [at.%]	Zn [at.%]	$\text{Zn}/\text{O}_T$
P0	54.7	45.3	0.83
P2	56.5	43.5	0.77
P3	57.6	42.4	0.74

The surface morphologies of the prepared ZnO samples were investigated by SEM (Figs. 4 and 5). As can be seen in the figures, in all cases oval nest-like units appear which consist of some non-uniform in size nanosheets and nanorods (Fig. 4). When Pluronic was added into the solution, the surface morphology of the product was slightly changed (Fig. 5). The number of nanorods decreases, but their length slightly increases. They have lengths in the range of 250–500 nm and diameters in the range of 30–60 nm. A further increase in the Pluronic concentration did not lead to any obvious changes in size and shape of the nanosheets and nanorods. A similar morphology of ZnO powders, obtained from PEG-modified solution of zinc acetate precipitated with NaOH, has been shown in the work of Adhyapak and co-workers [10].

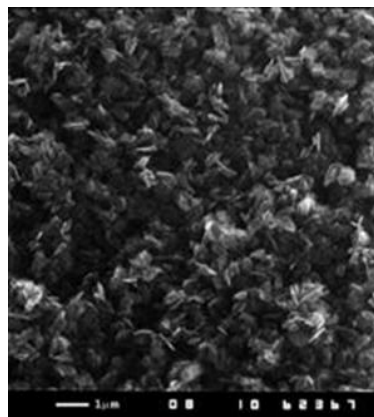


Fig. 4. SEM photograph of P0 sample.

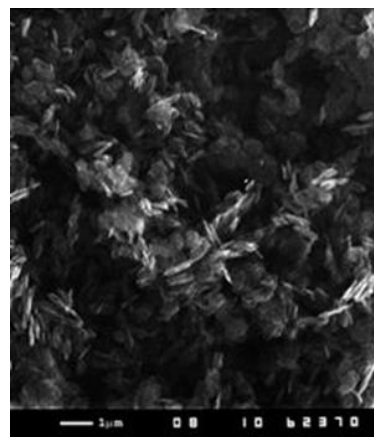


Fig. 5. SEM photograph of P2 sample.

The photocatalytic efficiencies of the samples were evaluated in the reaction of RB5 oxidative discoloration and the results are displayed in figure 6.

The reaction kinetics is represented by plotting the natural logarithm of the pollutant concentration ratio  $-\ln(C/C_0)$  as a function of the illumination time interval  $t$ . The experimental results showed that the photocatalytic oxidative discoloration of the dye solution under UV-light irradiation follows a pseudo-first order reaction kinetics due to great excess of oxygen in the solution, and it is expressed by the equation:

$$\ln(C/C_0) = -kt, \quad (2)$$

where  $C_0$  is the initial concentration of the dye,  $C$  is the concentration of the dye after irradiation for a certain time interval  $t$ , and  $k$  is the apparent rate constant. The latter was evaluated based on the slope of the straight linear dependence  $-\ln(C/C_0)$  vs time.

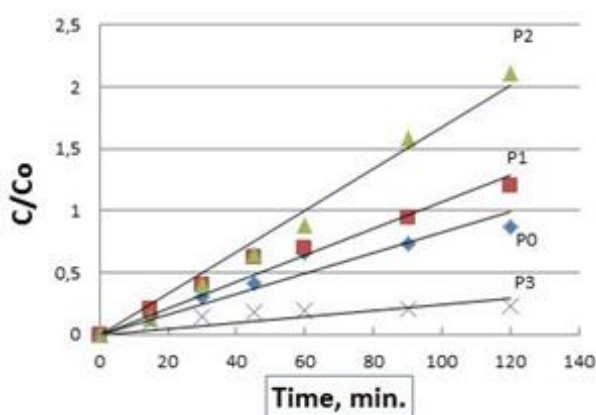


**Fig. 6.** Kinetic curves of dye discoloration on the samples, obtained by Pluronic modified hydrothermal method.

It can be seen in the figure that the reference sample and sample P3 exhibit lower activities for dye discoloration than those of samples P1 and P2. The best photocatalytic activity is displayed by sample P2 (when 4 g of P123 were added into solution). Thus, this is the optimal Pluronic concentration in the zinc solution to obtain a highly active mesoporous photocatalyst. The apparent rate constants ( $k$ ) are  $1.5 \times 10^{-3} \cdot \text{min}^{-1}$ ,  $10.3 \times 10^{-3} \cdot \text{min}^{-1}$ ,  $15.8 \times 10^{-3} \cdot \text{min}^{-1}$ , and  $2.5 \times 10^{-3} \cdot \text{min}^{-1}$  for the P0, P1, P2, and P3 samples, respectively. We have also estimated the ratio of rate constant to specific surface area ( $k/S$ ) for polymer-modified samples in order to determine the photocatalytic activity related to unit of surface area. The  $k/S$  ratios are 0.0008, 0.014, and 0.00017 for samples P1, P2, and P3, respectively. As it was proved by BET measurements, the ZnO samples, produced by hydrothermal treatment of three-block copolymer containing precipitate, have slightly higher surface areas and possess more mesopores than the reference sample. It is well known that the photocatalytic activities are strongly dependent on the surface area of the photocatalysts, as the reacting

molecules have to be first adsorbed on their surfaces. The presence of numerous nanosheets and nanorods ensures large surface, leading to the enhancement of dye adsorption and easier transportation. Higher values of surface area and pore volume for the polymer-modified samples provide a larger number of surface active sites for the photocatalytic reactions. In addition to this, the mesoporous channels also facilitated the diffusion of reactant molecules thereby increasing the reaction rate [11]. According to Barauch *et al.* [12], the mesoporous structure of ZnO can provide more active sites available for adsorption of reactive species due to the larger pore volume, which causes improvement in the photocatalytic activity. It is also possible that the Zn/O ratio influences the photocatalytic behaviour besides the surface area and particle size. The powders obtained from HT polymer-modified precipitate have a lower value of  $\text{Zn}/\text{O}_T$  ratio and a higher discoloration rate than those of the reference samples. It is worth mentioning that introducing P123 in the samples leads to creation of more oxygen vacancies on the surface of ZnO photocatalysts in comparison with those of the reference samples. These oxygen defects are adsorption sites, which result in an enhanced photocatalytic activity.

The results obtained indicate that the Pluronic-modified hydrothermal method can be used successfully to prepare highly effective photocatalysts representing well-crystallized mesoporous powders for oxidative dye discoloration.

## CONCLUSIONS

Applied polymer-assisted precipitation, in combination with hydrothermal treatment, is beneficial in view of the effectiveness of the mesoporous ZnO photocatalytic material. The phase composition of all the samples represents a well-crystallized wurtzite phase. Typical of the ZnO samples are particles consisting of oval nest-like units, which contain some non-uniform nanosheets and nanorods. The polymer modification of zinc precursor solution with Pluronic (P123) results in an increased share of mesopores, which is accompanied by a decrease in the share of micropores. The superior photocatalytic performance in discoloration of azo dye by comparing modified samples with reference ZnO can be explained based on a larger share of mesopores enabling faster molecular diffusion and enhanced adsorption capacity as well as formation of a larger number of oxygen vacancies in the ZnO lattice.

*Acknowledgements:* The authors are grateful for sponsorship of Projects BG051PO001-3.3.06-0050 and DFNI T-02/16, and contract 'Development of

advanced catalytic systems applicable to chemical and photochemical processes for neutralization of environmental pollutions' (EBR SANI).

#### REFERENCES

1. Y. Jang, C. Simer, T. Ohm, *Mater. Res. Bull.*, **41**, 67 (2006).
2. R. Zhang, L. L. Kerr, *J. Solid State Chem.*, **180**, 988 (2007).
3. C. W. Yao, H. P. Wu, M. Y. Ge, L. Yang, Y. W. Zeng, Y. W. Wang, J. Z. Jiang, *Mater. Lett.*, **61**, 3416 (2007).
4. W. Jin, I. Lee, K. Kompch, U. Dorfler, M. Winterer, *J. Eur. Ceram. Soc.*, **27**, 4333 (2007).
5. C. H. Lu, C. H. Yen, *Ceram. Int.*, **26**, 351 (2000).
6. A. Aimable, M. T. Buscaglia, V. Buscaglia, P. Bowen, *J. Eur. Ceram. Soc.*, **30**, 591 (2010).
7. P. Jantawasu, T. Sreethawong, S. Chavadej, *Chem. Eng. J.*, **155**, 223 (2009).
8. D. Zhao, J. Feng, Q. Huo, B. F. Chmelka, G. D. Stucky, *Science*, **249**, 458 (1998).
9. I.-H. Liu, P. Chen, *Ceram. Int.*, **36**, 1289 (2010).
10. P. V. Adhyapak, S. P. Meshram, D. P. Amalnerkar, I. S. Mulla, *Ceram. Int.*, **40**, 1951 (2014).
11. R. Lamba, A. Umar, S. K. Mehta, S. K. Kansal, *Talanta*, **131**, 490 (2015).
12. S. Barauh, M. A. Mahmood, M. I. Z. Myint, T. Bora, J. Dutta, *Beilstein J. Nanotechnol.*, **1**, 14 (2010).

### ХИДРОТЕРМАЛНО ПОЛУЧАВАНЕ НА ФОТОКАЛИЗАТОРИ ОТ ZnO С ПОМОЩТА НА КОПОЛИМЕР ПЛУРОНИК

Ал. Ел. Елияс<sup>1\*</sup>, Ир. Д. Стамболова<sup>2</sup>, Вл. Н. Блъсков<sup>2</sup>, Д. Стоянова<sup>2</sup>, К. И. Миленова<sup>1</sup>,  
Л. Д. Димитров<sup>3</sup>, М. Г. Шипочка<sup>2</sup>, Ог. С. Димитров<sup>4</sup>

<sup>1</sup> Институт по катализ, Българска академия на науките, ул. „Акад. Г. Бончев“, бл. 11, 1113 София, България

<sup>2</sup> Институт по обща и неорганична химия, Българска академия на науките, ул. „Акад. Г. Бончев“, бл. 11, 1113 София, България

<sup>3</sup> Институт по минералогия и кристалография „Акад. И. Костов“, Българска академия на науките, ул. „Акад. Г. Бончев“, бл. 107, 1113 София, България

<sup>4</sup> Институт по електрохимия и енергийни системи, Българска академия на науките, ул. „Акад. Г. Бончев“, бл. 10, 1113 София, България

Постъпила на 12 септември 2015 г.; Преработена на 6 ноември 2015 г.

(Резюме)

Мезопорести прахове от ZnO бяха получени чрез хидротермална обработка на утайки, съдържащи триблоков съполимер. Получени са прахове от добре кристализирала вюрцитна фаза. Частиците са съставени от овални гнездовидни структури, съдържащи нееднакви нанолити и нанопръчки. Увеличаването на концентрацията на Плуроник (P123) до определена стойност води до по-голям дял на мезопорите за сметка на микропорите. Образците от ZnO, получени от полимерно модифицирани хидротермално обработени утайки, проявяват по-висока фотокаталитична активност в реакцията на окислително обезцветяване на багрилото Реактивно Черно в сравнение с образеца за сравнение. По-високата специфична повърхност и по-големия обем на порите предоставят по-голям брой повърхностни активни центрове за фотокаталитичната реакция като повишават адсорбционния капацитет и улесняват транспорта на молекулите на багрилото.

## Photocatalytic properties of ferrite/activated carbon composites for degradation of Malachite Green in aqueous medium

K. L. Zaharieva\*, K. I. Milenova, Z. P. Cherkezova-Zheleva, A. E. Eliyas, B. N. Kunev, I. G. Mitov

*Institute of Catalysis, Bulgarian Academy of Sciences, Acad. G. Bonchev St., Bldg. 11, 1113 Sofia, Bulgaria*

Received: October 12, 2015; Revised: November 11, 2015

Ferrite/activated carbon (AC) composites of different formulation:  $\text{Co}_{0.5}\text{Fe}_{2.5}\text{O}_4/\text{AC}$ ,  $\text{Cu}_{0.5}\text{Fe}_{2.5}\text{O}_4/\text{AC}$ , and  $\text{Mn}_{0.5}\text{Fe}_{2.5}\text{O}_4/\text{AC}$  were prepared by coprecipitation and thermal treatment in nitrogen and studied as photocatalysts for oxidative degradation of Malachite Green dye in aqueous solution under UV-A light irradiation. The phase composition and magnetic behaviour of the prepared materials were established by powder X-ray diffraction analysis and Mössbauer spectroscopy. Synthesized ferrite/AC composites exhibit a superparamagnetic and collective magnetic excitation behaviour. A degradation degree of Malachite Green dye, used as model pollutant, reached 93% for  $\text{Mn}_{0.5}\text{Fe}_{2.5}\text{O}_4/\text{AC}$  and 99% for  $\text{Co}_{0.5}\text{Fe}_{2.5}\text{O}_4/\text{AC}$  and  $\text{Cu}_{0.5}\text{Fe}_{2.5}\text{O}_4/\text{AC}$  composites, which shows that these materials are applicable as photocatalysts for purification of waters containing above-mentioned dye. Photocatalytic results indicate that  $\text{Co}_{0.5}\text{Fe}_{2.5}\text{O}_4/\text{AC}$  manifested the highest photocatalytic activity. Comparison of the photocatalytic properties of the synthesized ferrite/activated carbon materials proved that the rate constants over the tested materials are increasing in the following order:  $7.1 \times 10^{-3} \text{ min}^{-1}$  ( $\text{Mn}_{0.5}\text{Fe}_{2.5}\text{O}_4/\text{AC}$ ) <  $24.1 \times 10^{-3} \text{ min}^{-1}$  ( $\text{Cu}_{0.5}\text{Fe}_{2.5}\text{O}_4/\text{AC}$ ) <  $28.4 \times 10^{-3} \text{ min}^{-1}$  ( $\text{Co}_{0.5}\text{Fe}_{2.5}\text{O}_4/\text{AC}$ ).

**Keywords:** photocatalytic properties, Malachite Green dye, ferrite/activated carbon composites.

### INTRODUCTION

Nanodimensional spinel ferrites with general formula  $\text{MFe}_2\text{O}_4$  (M = Mn, Co, Ni, Cu, or Zn) are magnetic materials of certain chemical and thermal stability. The electromagnetic properties of ferrites are related to their microstructure and composition depending on the preparation conditions [1]. Activated carbons (ACs), also known as active charcoal, are very promising and versatile materials used for example as catalysts, catalyst supports, and effective adsorbents exhibiting highly developed porosity, large surface area, high degree of surface reactivity, and variable characteristics of surface chemistry. There are several possible approaches aimed at improving the application potential of activated carbons. One of them is formation of composite materials obtained by incorporation of appropriate inorganic (nano) particles in the structure of activated carbons [2]. Dye contaminants originating from the textile industries are among the major sources of environmental pollution. Semiconductor photocatalytic reactions have attracted considerable interest of the researchers in recent decades [3]. Activated carbon/cobalt ferrite/alginate composite beads, being a magnetically separable adsorbent prepared using a simple ionic polymerization route, have been used for effective removal of Methylene Blue dye from aqueous solution [4]. An  $\text{AC}/\text{CoFe}_2\text{O}_4$

composite has been prepared by a simple single-step refluxing route and used as adsorbent for removal of Malachite Green dye from water [5]. The catalytic activity of cobalt ferrite nanoparticles hosted in activated carbon [6] and nanostructured iron and mixed iron-cobalt oxides supported on activated carbon [7] has been studied for methanol decomposition [6,7].  $\text{CuFe}_2\text{O}_4/\text{AC}$  magnetic adsorbents prepared by a chemical coprecipitation method showed a high adsorption capacity for Acid Orange II (AO7) in water and later it could be separated from the medium by a magnetic technique [8].  $\text{MnFe}_2\text{O}_4/\text{AC}$  magnetic composites, prepared by a simple chemical coprecipitation procedure, have demonstrated high adsorption efficiency for tetracycline in water [9]. Wan *et al.* [10] have studied the removal efficiency of sulphamethoxazole in aqueous solution by using magnetic manganese ferrite nanoparticles on activated carbon synthesized by chemical coprecipitation at various temperatures ranging from 25 to 150°C [10]. Co, Cu, Li, Zn, Ni, and Mg ferrites have been synthesized by impregnation of iron and metal salt aqueous solutions onto activated carbon followed by calcination at low temperatures of 300–500°C [11]. They have been tested for hydrogen sulphide adsorption [11].  $\text{NiFe}_2\text{O}_4/\text{AC}$  composites were obtained by coprecipitation method [12] or facile hydrothermal synthesis [13] and used for removal of Alizarin Yellow R [12] and Methyl Orange [12,13] in water [12,13].  $\text{NiFe}_2\text{O}_4$  supported on activated carbon from petroleum coke (petcoke) was prepared

\* To whom all correspondence should be sent  
E-mail: zaharieva@ic.bas.bg

and the magnetic properties of the nanoparticles indicated a strong dependence on particle size [14]. Zinc ferrites were obtained in the presence of activated carbon, activated carbon fibre, and Yallourn coal and their adsorption properties for H<sub>2</sub>S were examined [15]. ZnFe<sub>2</sub>O<sub>4</sub> supported on porous carbon was synthesized by pyrogenation of a mixture of ZnCl<sub>2</sub>, Fe(NO<sub>3</sub>)<sub>3</sub>, and novolac resin and it was used for catalytic degradation of mercaptan under alkaline-free conditions [16]. Manganese-zinc ferrites/AC nanocomposites (Mn<sub>0.5</sub>Zn<sub>0.5</sub>Fe<sub>2</sub>O<sub>4</sub>) obtained by using the hydrothermal method demonstrated some fine adsorptive efficiency for Methylene Blue and a magnetic response [17].

Malachite Green (MG) is an N-methylated diaminotriphenylmethane basic dye [18]. Its chemical structure is shown in figure 1. The crystalline powder of this dye dissolved in water gives a bluish-green coloured solution [19]. MG is widely used as a colouring agent on wool, silk, jute, cotton, leather, paper, and acrylic. This dye is known to be carcinogenic, mutagenic, and teratogenic to mammalian cell. It has potentially harmful effects on the liver, kidneys, gills, gonads, and intestines in organisms [20]. The release of coloured wastewater containing dyes and their by-products has led to great damage to plants and aquatic animals [21]. Consequently, the elimination of Malachite Green from polluted water before its entrance into the food chain and environment is a very important and necessary action [22].

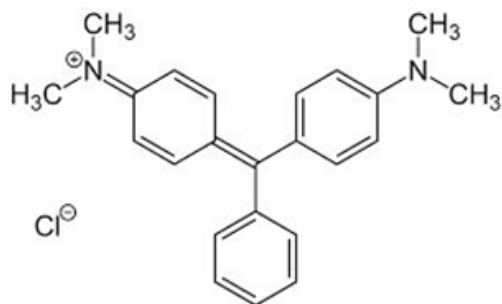


Fig. 1. Chemical structure of Malachite Green dye.

The present article deals with a study and comparison of photocatalytic activities of ferrite/activated carbon materials, such as Co<sub>0.5</sub>Fe<sub>2.5</sub>O<sub>4</sub>/AC, Cu<sub>0.5</sub>Fe<sub>2.5</sub>O<sub>4</sub>/AC, and Mn<sub>0.5</sub>Fe<sub>2.5</sub>O<sub>4</sub>/AC, prepared by coprecipitation technique and thermal treatment in nitrogen. Physicochemical methods including powder X-ray diffraction analysis and Mössbauer spectroscopy were applied to investigate the phase composition and magnetic behaviour of composite samples. In order to establish changes in photocatalytic efficiency of the ferrite/activated carbon composites, they were tested in the reaction of oxidative degradation of Malachite Green dye under UV irradiation.

## EXPERIMENTAL

Ferrite/activated carbon composites having different compositions: Co<sub>0.5</sub>Fe<sub>2.5</sub>O<sub>4</sub>/AC (sample 1), Cu<sub>0.5</sub>Fe<sub>2.5</sub>O<sub>4</sub>/AC (sample 2), and Mn<sub>0.5</sub>Fe<sub>2.5</sub>O<sub>4</sub>/AC (sample 3) were synthesized by the coprecipitation technique. Initial 0.03 M aqueous solutions of Fe(NO<sub>3</sub>)<sub>3</sub>·9H<sub>2</sub>O (Alfa Aesar) and Co(NO<sub>3</sub>)<sub>2</sub>·6H<sub>2</sub>O (GPR Rectapur/VWR Prolabo Chemicals), Cu(NO<sub>3</sub>)<sub>2</sub>·3H<sub>2</sub>O (Merck) or Mn(NO<sub>3</sub>)<sub>2</sub>·4H<sub>2</sub>O (Alfa Aesar) were mixed at a preset ratio. Activated carbon (2 g), obtained from peach stones (provided by Laboratory of Chemistry of Solid Fuels, Institute of Organic Chemistry with Centre of Phytochemistry, Sofia), was then added to the mixture. A precipitating agent, 0.3 M NaOH (Valerus Co.), was slowly added dropwise into the mixture under continuous stirring. Upon reaching pH = 12.5 for samples 1 and 3 and pH = 13 for sample 2, NaOH addition was discontinued and the mixture was aged under continuous stirring for one hour. Obtained samples were centrifuged and washed with distilled water until a neutral reaction (pH = 7) was attained. The so-prepared precipitates were dried at 110°C for 1 h in air. Afterwards all the samples were calcined at 400°C for 3 h in inert nitrogen.

The prepared ferrite/activated carbon materials were investigated by powder X-ray diffraction analysis (PXRD) and Mössbauer spectroscopy in order to determine their phase composition and magnetic behaviour.

The PXRD analysis was carried out using a TUR M62 apparatus with PC control and data acquisition applying an HZG-4 goniometer and CoK $\alpha$  radiation. Phases were identified by means of JCPDS database (Powder Diffraction Files, Joint Committee on Powder Diffraction Standards, Philadelphia PA, USA, 1997).

Mössbauer spectra were registered on a Wissenschaftliche Elektronik GmbH apparatus, working at a constant acceleration mode, and using a <sup>57</sup>Co/Rh source (activity  $\approx$ 50 mCi) and  $\alpha$ -Fe standard. The parameters of hyperfine interactions of Mössbauer spectral components: isomeric shift (IS), quadrupole splitting (QS), effective hyperfine magnetic field at iron nuclei (H<sub>eff</sub>), line widths (FWHM), and component relative weights (G) were estimated by computer fitting.

The photocatalytic properties of thermally treated ferrite/AC composites were tested for oxidative degradation of Malachite Green dye in aqueous solution under UV-A light illumination applying polychromatic (320–400 nm) radiation with maximal emission at 365 nm and a black light blue BLB lamp of 18 W. The reaction course was followed spectrophotometrically using a CamSpec M501 UV-vis

spectrophotometer based on the absorbance of dye solution in the UV-vis wavelength range from 200 to 800 nm. A semi-batch suspension photocatalytic reactor was used applying a fixed amount of photocatalyst and polluted water and continuous airflow through two frits to saturate the solution in oxygen. Thus, oxygen was in large stoichiometric excess, its concentration was practically constant, and it could be included in the value of the apparent rate constant. Therefore, the Langmuir-Hinshelwood mechanism of a bimolecular reaction is reduced to a pseudo-first order rate equation. The photocatalytic measurements were performed at a constant stirring rate (400 rpm) under ambient conditions. MG dye solutions had an initial concentration of 5 ppm. The investigated systems reached an equilibrium state after about 30 min in the dark before switching on the lamp. Sample aliquots of the suspension were taken out of the reaction vessel after regular time intervals in order to measure the photocatalytic activities of ferrite/activated carbon materials. The powder was then separated from the aliquot solution by centrifugation before UV-Vis spectrophotometric measurement of dye concentration. After that the aliquot solution together with the photocatalyst sample were placed back into the reaction vessel (constant volume operation). Apparent rate constants,  $k$ , were estimated by neglecting the dissolved oxygen con-

centration based on the straight-line slope of plotted  $-\ln(C/C_0) = k_{app} \cdot t$  logarithmic dependence.

## RESULTS AND DISCUSSION

Figure 2 illustrates powder X-ray diffraction patterns of the synthesized ferrite/activated carbon materials and activated carbon. As it can be seen, the presence of non-stoichiometric spinel cobalt ferrite  $\text{Co}_x\text{Fe}_{3-x}\text{O}_4$  (PDF-22-1086; PDF-75-0449), copper ferrite  $\text{Cu}_x\text{Fe}_{3-x}\text{O}_4$  (PDF-34-0425; PDF-75-0449), or manganese ferrite  $\text{Mn}_x\text{Fe}_{3-x}\text{O}_4$  (PDF-73-1964; PDF-75-0449), and also activated carbon phases were registered in presented PXRD patterns. A hematite phase (PDF-89-0599) was also observed in the case of thermally treated cobalt and copper ferrite-type/AC materials.

The registered Mössbauer spectra of the obtained samples at room temperature (RT) are displayed in figure 3. The spectra of  $\text{Co}_{0.5}\text{Fe}_{2.5}\text{O}_4/\text{AC}$  (sample 1) and  $\text{Cu}_{0.5}\text{Fe}_{2.5}\text{O}_4/\text{AC}$  (sample 2) are a superposition of sextet and doublet components. Doublet lines were only recorded in the spectrum of  $\text{Mn}_{0.5}\text{Fe}_{2.5}\text{O}_4/\text{AC}$  (sample 3). A spinel phase, registered in the spectrum of sample 1, is presented by three sextet components: Sxt2 due to octahedrally coordinated  $\text{Fe}^{3+}$  ions, Sxt3 belonging to tetrahedrally coordinated  $\text{Fe}^{3+}$  ions, and Sxt4 – related to iron ions in a spinel phase with an average size below 20 nm. This phase

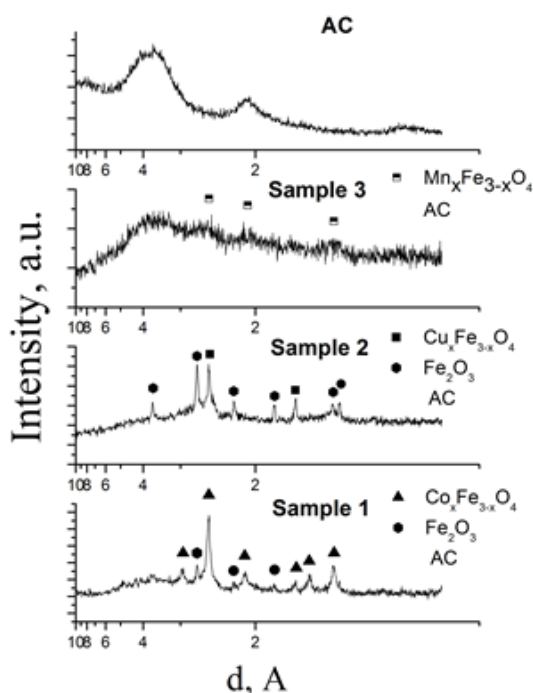


Fig. 2. PXRD patterns of thermally treated ferrite/AC composites and activated carbon.

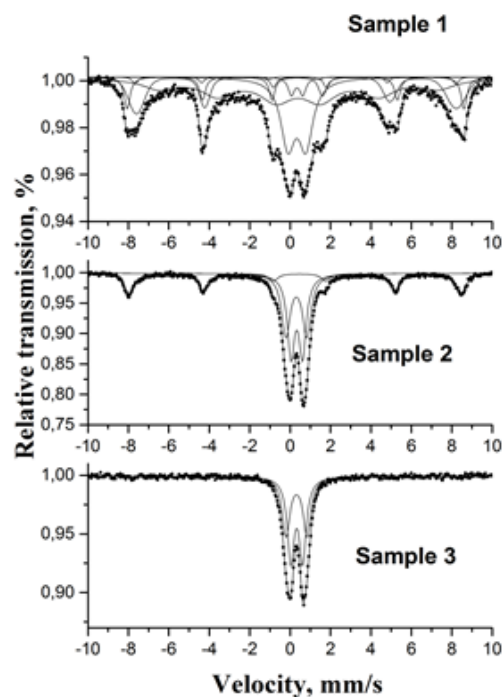


Fig. 3. Mössbauer spectra of ferrite/AC composites at room temperature.

exhibits a high dispersion degree and collective magnetic excitation (CME) behaviour. In the spectra of sample 1 and sample 2, the sextet component, Sxt1, is attributed to ferric ions ( $\text{Fe}^{3+}$ ) in a hematite phase. Calculated hyperfine parameters of doublet components could be assigned to the presence of ferrite particles of superparamagnetic (SPM) behaviour and an average size below 10 nm [23] (Table 1). Mössbauer measurements confirmed the powder X-ray diffraction studies.

The degree of degradation of the Malachite Green dye as a function of time interval under UV-A light irradiation during photocatalytic tests over prepared ferrite/AC composites is given in figure 4. The results indicate that samples 1 and 2 manifested the highest photocatalytic activity (99%) in the oxidative degradation of Malachite Green dye after 120 min.

The apparent rate constants of ferrite/AC photocatalysts determined by the slopes of the curves

using pseudo-first order kinetics [3],  $-\ln(C/C_0) = k_{\text{app}}.t$ , are shown in figure 5. Differences in photocatalytic activity of tested materials proved that a maximum in the rate constant was observed with sample 1 ( $\text{Co}_{0.5}\text{Fe}_{2.5}\text{O}_4/\text{AC}$ ). The photocatalytic activity of the ferrite/AC samples is decreasing in the order:  $28.4 \times 10^{-3} \text{ min}^{-1}$  ( $\text{Co}_{0.5}\text{Fe}_{2.5}\text{O}_4/\text{AC}$ ) >  $24.1 \times 10^{-3} \text{ min}^{-1}$  ( $\text{Cu}_{0.5}\text{Fe}_{2.5}\text{O}_4/\text{AC}$ ) >  $7.1 \times 10^{-3} \text{ min}^{-1}$  ( $\text{Mn}_{0.5}\text{Fe}_{2.5}\text{O}_4/\text{AC}$ ).

## CONCLUSIONS

A coprecipitation procedure followed by thermal treatment in inert nitrogen at  $400^\circ\text{C}$  for 3 h was successfully used to prepare ferrite/activated carbon photocatalysts of different composition:  $\text{M}_x\text{Fe}_{3-x}\text{O}_4/\text{AC}$  ( $\text{M} = \text{Co}^{2+}, \text{Cu}^{2+}, \text{Mn}^{2+}; x = 0.5$ ). A powder X-ray diffraction study showed that spinel ferrite and activated carbon phases were registered

**Table 1.** Mössbauer parameters of prepared ferrite/AC materials.

Sample	Component	IS $\text{mm.s}^{-1}$	QS $\text{mm.s}^{-1}$	$H_{\text{eff}}$ T	FWHM $\text{mm.s}^{-1}$	G %
sample 1	Sxt 1 – $\text{Fe}^{3+}$ hematite	0.37	-0.21	51.8	0.35	10
	Sxt 2 – $\text{Fe}^{3+}$ octa	0.24	0.05	49.3	0.31	2
	Sxt 3 – $\text{Fe}^{3+}$ tetra	0.34	-0.05	49.2	0.33	22
	Sxt 4 – Fe - spinel, CME	0.41	0.02	42.8	1.94	40
	Dbl 1 – SPM	0.35	0.57	–	0.39	3
sample 2	Dbl 2 – SPM	0.34	0.90	–	0.85	23
	Sxt 1 – $\text{Fe}^{3+}$ hematite	0.36	-0.21	51	0.54	28
	Dbl 1 – SPM	0.33	0.58	–	0.43	37
sample 3	Dbl 2 – SPM	0.31	1.04	–	0.51	35
	Dbl 1 – SPM	0.33	0.59	–	0.41	55
	Dbl 2 – SPM	0.32	1.04	–	0.45	45

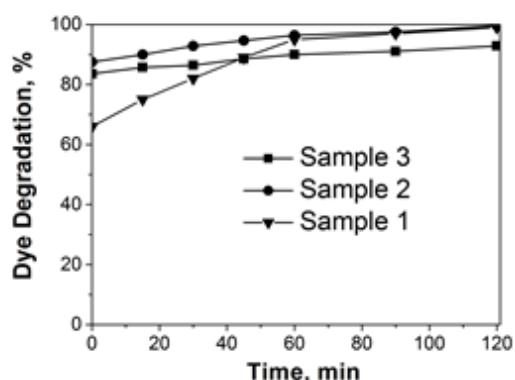


**Fig. 4.** Degree of degradation of MG dye calculated as  $[(C_0 - C)/C_0] \times 100\%$ , where  $C_0$  is the initial concentration before switching on illumination and  $C$  is current concentration of the solution based on changes in peak intensity having maximal absorbance at 615 nm with time under UV-A irradiation using synthesized ferrite/AC samples in a semi-batch reactor.

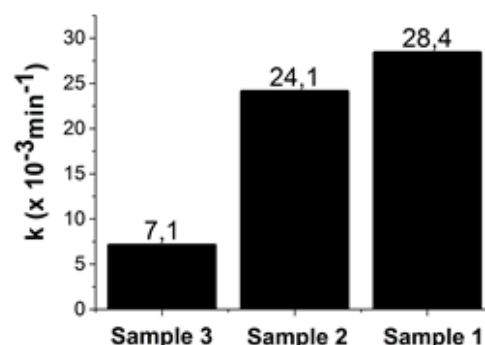


**Fig. 5.** Comparison data of calculated apparent rate constants,  $k$  (disregarding dissolved oxygen concentration) under UV-A illumination using ferrite/AC photocatalysts in photodegradation of Malachite Green dye.

in all the samples. A hematite phase was also observed in the case of calcined cobalt and copper ferrite-type/AC materials. Mössbauer measurements at room temperature verified that the synthesized ferrite/AC composites exhibited a superparamagnetic and collective magnetic excitation behaviour and indicated a highly dispersed ferrite phase of an average particle size below 20 nm. Photocatalytic activity tests demonstrated a high degree of degradation of the Malachite Green dye, used as model pollutant, being within 93–99% for obtained ferrite/AC composites. The present results give evidence that the prepared ferrite/activated composites could be successfully applied to purify polluted waters containing MG dye as contaminant. A certain effect of the different metal ions on the photocatalytic activity was established. The photocatalytic apparent rate constants (a pseudo-first order rate equation) of the investigated samples are increasing as follows:  $7.1 \times 10^{-3} \text{ min}^{-1}$  ( $\text{Mn}_{0.5}\text{Fe}_{2.5}\text{O}_4/\text{AC}$ ) <  $24.1 \times 10^{-3} \text{ min}^{-1}$  ( $\text{Cu}_{0.5}\text{Fe}_{2.5}\text{O}_4/\text{AC}$ ) <  $28.4 \times 10^{-3} \text{ min}^{-1}$  ( $\text{Co}_{0.5}\text{Fe}_{2.5}\text{O}_4/\text{AC}$ ). Among the three materials, the  $\text{Co}_{0.5}\text{Fe}_{2.5}\text{O}_4/\text{AC}$  composite manifested the highest photocatalytic activity.

**Acknowledgements:** The authors thank the Bulgarian Science Fund for financial support by Contract DFNI E02/2/2014.

#### REFERENCES

- M. A. Khan, M. M. Alam, M. Naushad, Z. A. Alothman, M. Kumar, T. Ahamad, *Chem. Eng. J.*, **279**, 416 (2015).
- I. Safarik, K. Horska, K. Pospiskova, M. Safarikova, *Int. Rev. Chem. Eng., Special Section on Open Door Initiative, 2nd Edn.*, **4** (3), 346 (2012).
- R.-C. Wang, K.-S. Fan, J.-S. Chang, *J. Taiwan Inst. Chem. Eng.*, **40**, 533 (2009).
- L. Ai, M. Li, L. Li, *J. Chem. Eng. Data*, **56**, 3475 (2011).
- L. Ai, H. Huang, Z. Chen, X. Wei, J. Jiang, *Chem. Eng. J.*, **156**, 243 (2010).
- I. Genova, T. Tsoncheva, M. Dimitrov, D. Paneva, B. Tsyntsarski, R. Ivanova, Z. Cherkezova-Zheleva, T. Budinova, D. Kovacheva, I. Mitov, N. Petrov, *Catal. Commun.*, **55**, 43 (2014).
- E. Manova, T. Tsoncheva, C. Estournès, D. Paneva, K. Tenchev, I. Mitov, L. Petrov, *Appl. Catal. A-Gen.*, **300**, 170 (2006).
- G. Zhang, J. Qu, H. Liu, A. T. Cooper, R. Wu, *Chemosphere*, **68**, 1058 (2007).
- L. Shao, Z. Ren, G. Zhang, L. Chen, *Mater. Chem. Phys.*, **135**, 16 (2012).
- J. Wan, H. Deng, J. Shi, L. Zhou, T. Su, *Clean Soil, Air, Water*, **42** (9999), 1 (2014).
- N.-O. Ikenaga, N. Chiyoda, H. Matsushima, T. Suzuki, *Fuel*, **81**, 1569 (2002).
- G. Ranjeh, M. Radmanesh, A. Kiafar, *Sci. J. Chem.*, **3** (2), 28 (2015).
- T. Jiang, Y.-D. Liang, Y.-J. He, Q. Wang, *J. Environ. Chem. Eng.*, **3**, 1740 (2015).
- S. Briceño, W. Brämer-Escamilla, P. Silva, J. García, H. Del Castillo, M. Villarroel, J. P. Rodriguez, M. A. Ramos, R. Morales, Y. Diaz, *J. Magn. Magn. Mater.*, **360**, 67 (2014).
- N.-O. Ikenaga, Y. Ohgaito, H. Matsushima, T. Suzuki, *Fuel*, **83**, 661 (2004).
- Q. Li, L. Zhuang, S. Chen, J. Xu, H. Li, *Energy Fuels*, **26**, 7092 (2012).
- B. B. Zhang, J. C. Xu, P. H. Xin, Y. B. Han, B. Hong, H. X. Jin, D. F. Jin, X. L. Peng, J. Li, J. Gong, H. L. Ge, Z. W. Zhu, X. Q. Wang, *J. Solid State Chem.*, **221**, 302 (2015).
- R. Gopinathan, J. Kanhere, J. Banerjee, *Chemosphere*, **120**, 637 (2015).
- Y. Wang, L. Chen, *J. Chromatogr. B*, **1002**, 98 (2015).
- M. Ghasemi, S. Mashhadi, M. Asif, I. Tyagi, S. Agarwal, V. K. Gupta, *J. Mol. Liquids*, **213**, 317 (2016).
- R. K. Gautam, V. Rawat, S. Banerjee, M. A. Sanroman, S. Soni, S. K. Singh, M. C. Chattopadhyaya, *J. Mol. Liquids*, **212**, 227 (2015).
- M. Dastkhooon, M. Ghaedi, A. Asfaram, A. Goudarzi, S. M. Langroodi, I. Tyagi, S. Agarwal, V. K. Gupta, *Separation Purification Technol.*, **156**, 780 (2015).
- U. Schwertmann, R. Cornell, *Iron Oxides in the Laboratory*, Weinheim, New York, 1991.

## ФОТОКАТАЛИТИЧНИ СВОЙСТВА НА КОМПОЗИТИ ФЕРИТ/АКТИВЕН ВЪГЛЕН ЗА РАЗГРАЖДАНЕ НА МАЛАХИТОВО ЗЕЛЕНО ВЪВ ВОДНА СРЕДА

К. Л. Захариева\*, К. И. Миленова, З. П. Черкезова-Желева, Ал. Ел. Елияс, Б. Н. Кунев, Ив. Г. Митов

*Институт по катализ, Българска академия на науките, ул. „Акад. Г. Бончев“, бл. 11, 1113 София, България*

Постъпила на 12 октомври 2015 г.; Преработена на 11 ноември 2015 г.

(Резюме)

Композити ферит/активен въглен с различен състав,  $\text{Co}_{0.5}\text{Fe}_{2.5}\text{O}_4/\text{AC}$ ,  $\text{Cu}_{0.5}\text{Fe}_{2.5}\text{O}_4/\text{AC}$  и  $\text{Mn}_{0.5}\text{Fe}_{2.5}\text{O}_4/\text{AC}$ , бяха получени чрез съутаяване и термична обработка в азотна среда и изследвани като фотокатализатори в окислителното разграждане на Малахитово Зелено (МЗ) багрило във воден разтвор под УВ-А облъчване. Фазовият състав и магнитното поведение на получените материали бяха установени чрез рентгенофазов анализ и Мьосбауерова спектроскопия. Синтезираните композити ферит/активен въглен притежават суперпарамагнитно поведение и колективно магнитно възбуждане. Високите степени на разграждане на багрилото, използвано като моделен замърсител, възлизат на 93% за образеца  $\text{Mn}_{0.5}\text{Fe}_{2.5}\text{O}_4/\text{AC}$  и 99% за  $\text{Co}_{0.5}\text{Fe}_{2.5}\text{O}_4/\text{AC}$  и  $\text{Cu}_{0.5}\text{Fe}_{2.5}\text{O}_4/\text{AC}$  композити, което показва, че тези материали са приложими като фотокатализатори за пречистване на води съдържащи Малахитово Зелено. Получените фотокаталитични резултати показаха, че образецът  $\text{Co}_{0.5}\text{Fe}_{2.5}\text{O}_4/\text{AC}$  има най-висока фотокаталитична активност. Сравнение на фотокаталитичните свойства на синтезираните материали ферит/активен въглен установи, че скоростните константи на изследваните образци нарастват в реда:  $7.1 \times 10^{-3} \text{ min}^{-1}$  ( $\text{Mn}_{0.5}\text{Fe}_{2.5}\text{O}_4/\text{AC}$ ) <  $24.1 \times 10^{-3} \text{ min}^{-1}$  ( $\text{Cu}_{0.5}\text{Fe}_{2.5}\text{O}_4/\text{AC}$ ) <  $28.4 \times 10^{-3} \text{ min}^{-1}$  ( $\text{Co}_{0.5}\text{Fe}_{2.5}\text{O}_4/\text{AC}$ ).

## Mixed cobalt-copper ferrite-type materials: synthesis and photocatalytic efficiency in degradation of Reactive Black 5 dye under UV-light irradiation

K. L. Zaharieva<sup>1\*</sup>, K. I. Milenova<sup>1</sup>, V. Rives<sup>2</sup>, R. Trujillano<sup>2</sup>, Z. P. Cherkezova-Zheleva<sup>1</sup>,  
A. E. Elias<sup>1</sup>, M. P. Tsvetkov<sup>3</sup>, B. N. Kunev<sup>1</sup>, I. G. Mitov<sup>1</sup>

<sup>1</sup> Institute of Catalysis, Bulgarian Academy of Sciences, Acad. G. Bonchev St., Bldg. 11, 1113 Sofia, Bulgaria

<sup>2</sup> GIR-QUESCAT, Dpto. Química Inorgánica, Universidad de Salamanca, 37008-Salamanca, Spain

Received: October 5, 2015; Revised October 20, 2015

Mixed cobalt-copper ferrite-type materials having different compositions were prepared using a coprecipitation technique and mechanochemical or microwave treatment. Various physicochemical methods, such as powder X-ray diffraction, Mössbauer and FTIR spectroscopy, single point BET method, porosity investigations, and temperature-programmed reduction, were used for characterization of the obtained ferrite-type samples. The photocatalytic activities of the so synthesized cobalt-copper ferrite-type materials were examined in oxidative degradation of Reactive Black 5 (RB5) dye as model contaminant in aqueous solution under UV-A light illumination. Photocatalytic activity tests established that microwave treatment of coprecipitated  $\text{Co}_{0.25}\text{Cu}_{0.25}\text{Fe}_{2.5}\text{O}_4$  sample leads to a higher degree of degradation of RB5 dye (98%) compared to that of coprecipitated (96%) and mechanochemically treated (73%) materials. Mechanochemical treatment enhanced the conversion degree of RB5 dye after 120 min of illumination: 77 and 78% for  $\text{Co}_{0.5}\text{Cu}_{0.5}\text{Fe}_2\text{O}_4$  and  $\text{Co}_{0.4}\text{Cu}_{0.1}\text{Fe}_{2.5}\text{O}_4$ , respectively, compared with matching coprecipitated samples (48% and 52%), accordingly. An enhancement of photocatalytic efficiency of prepared cobalt-copper ferrites upon decreasing the cobalt content was established. The photocatalytic properties of obtained mixed cobalt-copper ferrite-type samples were affected by the degree of incorporation of metal ions in the magnetite-type structure and by applied preparation methods.

**Keywords:** mixed cobalt-copper ferrite-type materials, mechanochemical and microwave treatment, Reactive Black 5 dye.

### INTRODUCTION

Studies of nanodimensional ferrites properties have attracted attention in last years because of their significance in the fundamental understanding of physical processes as well as due to their various technological applications [1]. Spinel ferrites possess very interesting catalytic properties compared with single component metal oxides. The catalytic activities of spinel ferrites depend on various factors such as particle size, redox properties of metal ions and their distribution between the tetrahedral (A) and octahedral (B) coordination sites [2]. Investigations of the preparation and properties of cobalt-copper (copper-cobalt) ferrites [1,3–5] and substituted cobalt nanoferrites  $\text{CoM}_x\text{Fe}_{2-x}\text{O}_4$  ( $\text{M}=\text{Cr}^{3+}$ ,  $\text{Ni}^{2+}$ ,  $\text{Cu}^{2+}$ ,  $\text{Zn}^{2+}$ ;  $0.2 \leq x \leq 1.0$ ) [2] of different compositions have been carried out by many researchers [1–5].

The goals of the present work were synthesis, physicochemical characterization, and comparison of photocatalytic activities of mixed cobalt-copper ferrite-type materials of different compositions in degradation of Reactive Black 5 dye as model pollutant in aqueous solution under UV-A light irradiation.

### EXPERIMENTAL

Mixed Co-Cu ferrite-type samples having different stoichiometric compositions:  $\text{Co}_{0.25}\text{Cu}_{0.25}\text{Fe}_{2.5}\text{O}_4$  (A),  $\text{Co}_{0.4}\text{Cu}_{0.1}\text{Fe}_{2.5}\text{O}_4$  (B), and  $\text{Co}_{0.5}\text{Cu}_{0.5}\text{Fe}_2\text{O}_4$  (C) were synthesized by a coprecipitation procedure using 0.03 M aqueous solutions of  $\text{CoCl}_2 \cdot 6\text{H}_2\text{O}$  (Alfa Aesar),  $\text{CuCl}_2 \cdot 2\text{H}_2\text{O}$  (Valerus, p.a.),  $\text{FeCl}_2 \cdot 4\text{H}_2\text{O}$  (Sigma Aldrich, p.a.), and/or  $\text{FeCl}_3 \cdot 6\text{H}_2\text{O}$  (P.P.H. STANLAB s.j) mixed at appropriate ratios. A pH value of 12.5 of the mixture was reached by adding dropwise 0.3 M NaOH under continuous stirring. After coprecipitation, the mixture was stirred for another hour. The obtained precipitates were centrifuged and washed with distilled water until neutral reaction ( $\text{pH} = 7$ ) was achieved. The prepared samples were then sonicated for 5 min. The products were dried in air at room temperature. Coprecipitated ferrite-type samples were mechanochemically treated in a high-energy planetary ball mill (model PM 100, Retsch, Germany). The mechanochemical process was carried out in tungsten carbide vessels of 250-ml volume at a milling speed of 400 rpm for 210 min under argon. The mass ratio of powder amount to applied balls was 1:46. The mechanochemically treated materials were denoted as follows:  $\text{Co}_{0.25}\text{Cu}_{0.25}\text{Fe}_{2.5}\text{O}_4$  as D,

\* To whom all correspondence should be sent  
E-mail: zaharieva@ic.bas.bg

$\text{Co}_{0.4}\text{Cu}_{0.1}\text{Fe}_{2.5}\text{O}_4$  like E, and  $\text{Co}_{0.5}\text{Cu}_{0.5}\text{Fe}_2\text{O}_4$  as F. The coprecipitated sample A was also microwave-treated at  $120^\circ\text{C}$  for 2 h using a microwave apparatus (Milestone Ethos Plus High Performance Microwave Labstation). Afterwards the  $\text{Co}_{0.25}\text{Cu}_{0.25}\text{Fe}_{2.5}\text{O}_4$  material, labelled as G, was centrifuged and dried at  $100^\circ\text{C}$  for 4 h and 30 min.

The structure, phase composition, and magnetic behaviour of the prepared cobalt-copper ferrite-type samples were investigated by several physico-chemical methods.

Powder X-ray diffraction (PXRD) analysis was carried out on a Siemens D-500 diffractometer at 40 kV and 30 mA, using  $\text{CuK}\alpha$  filtered radiation ( $\lambda = 1.5418 \text{ \AA}$ ).

Mössbauer spectroscopy measurements of the synthesized materials were carried out on a Wissenschaftliche Elektronik GmbH apparatus by working at a constant acceleration mode and applying a  $^{57}\text{Co}/\text{Rh}$  source (activity  $\approx 50 \text{ mCi}$ ) and  $\alpha\text{-Fe}$  standard. Hyperfine interaction parameters of Mössbauer spectral components: isomeric shift (IS), quadrupole splitting (QS), hyperfine effective magnetic field at the sites of iron nuclei ( $H_{\text{eff}}$ ), line widths (FWHM), and component relative weights (G) were determined by computer fitting.

A FTIR spectroscopic study was performed using the KBr pellet technique on a Perkin Elmer Spectrum One apparatus by averaging 50 spectra with a nominal resolution of  $4 \text{ cm}^{-1}$ .

A Micromeritics Gemini VII 2390t surface area analyser was used to record nitrogen adsorption-desorption isotherms for specific surface area and porosity assessment. The investigated materials were degassed beforehand in a Micromeritics Gemini Flow Prep 060 degassing unit for 2 h at  $110^\circ\text{C}$  under continuous nitrogen flow.

Temperature-programmed reduction (TPR) experiments were conducted in a Micromeritics TPR-TPD 2900 apparatus by applying a 5-vol.%  $\text{H}_2/\text{Ar}$  mixture (from L'Air Liquide, Spain) at a heating rate of  $10 \text{ grad.min}^{-1}$ . The amount of tested material was selected to satisfy resolution conditions reported by Malet and Caballero [6].

Synthesized materials were tested for photocatalytic activity in oxidative degradation of Reactive Black 5 (RB5) dye under UV-A polychromatic illumination (18-W lamp with maximal emission at 365 nm). The reaction course was followed using a CamSpec M501 UV-Vis spectrophotometer in the wavelength range from 200 to 800 nm. The initial concentration of the used RB5 dye

solution was 20 ppm. The investigated systems reached an equilibrium state in the dark for about 30 min before switching on the UV illumination. The photocatalytic tests were carried out in a semi-batch suspension photocatalytic reactor upon feeding air through two frits to create a large stoichiometric excess of oxygen.

## RESULTS AND DISCUSSION

PXRD patterns of coprecipitated, mechano-chemically and microwave-treated mixed cobalt-copper ferrite-type materials are shown in figure 1. The spinel non-stoichiometric ferrite (PDF-22-1086; PDF-34-0425; PDF-75-0449) and additional iron oxyhydroxide (PDF-75-1594) phases are identified in the PXRD diagrams of coprecipitated samples A, B, and C. Formation of single spinel non-stoichiometric ferrite phases (PDF-22-1086; PDF-34-0425; PDF-75-0449) is observed in the investigated samples both after mechanochemical (D, E, F) and microwave (G) treatment.

Mössbauer data are presented in figure 2. Doublet or doublet and sextet components are observed in the spectra at room temperature (RT) with the so prepared cobalt-copper ferrite-type materials A, B, C, D, E, F, and G. Mössbauer spectra at liquid nitrogen temperature (LNT) were recorded to establish the nature of doublet and sextet lines. A superposition of sextet and doublet components is derived from the LNT spectra of all studied samples. Estimation of the spectra pointed to existence of iron ions in a ultradispersed ferrite phase of superparamagnetic (SPM) behaviour and sizes below 10 nm, and/or ferrite particles of sizes below 20 nm showing a collective magnetic excitation (CME) behaviour for the A, B, C, D, E, F, and G samples and iron ions belonging to an intermediate phase of iron oxyhydroxide with the A, B, and C materials [7].

FTIR spectra of the obtained mixed cobalt-copper ferrite-type samples are displayed in figure 3. The bands positioned below  $700 \text{ cm}^{-1}$  are assigned to vibrations of ions in the crystal lattice [8]. The vibrations recorded around  $3400 \text{ cm}^{-1}$  and  $1625\text{--}1633 \text{ cm}^{-1}$  are due to the O-H stretching and H-O-H bending modes of free or absorbed water molecules [1]. The bands at about  $1352\text{--}1368 \text{ cm}^{-1}$  and  $1464\text{--}1475 \text{ cm}^{-1}$  are ascribed to vibrations of carbonate ( $\text{CO}_3^{2-}$ ) and hydroxycarbonate ( $\text{HCO}_3^-$ ) species [9] adsorbed on the surface. Adsorption of atmospheric  $\text{CO}_2$  could explain the presence of these species.

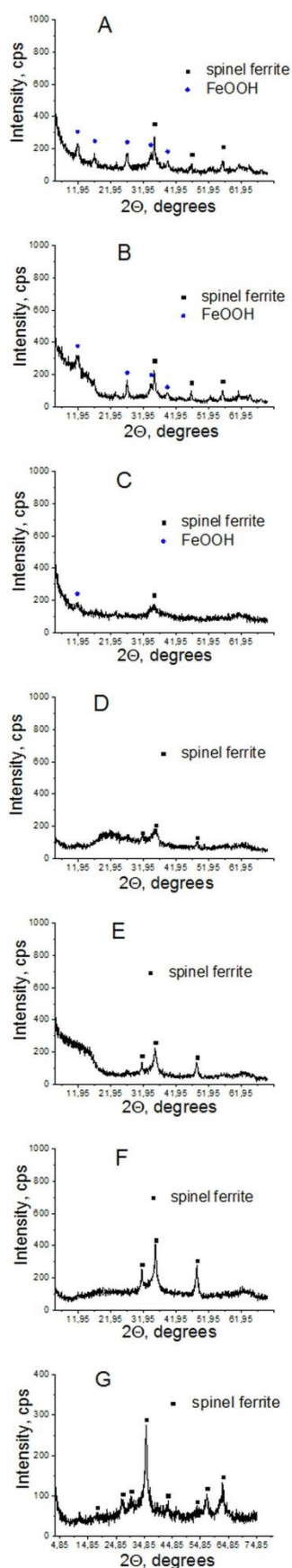


Fig. 1. PXR patterns of synthesized mixed cobalt-copper ferrite-type materials.

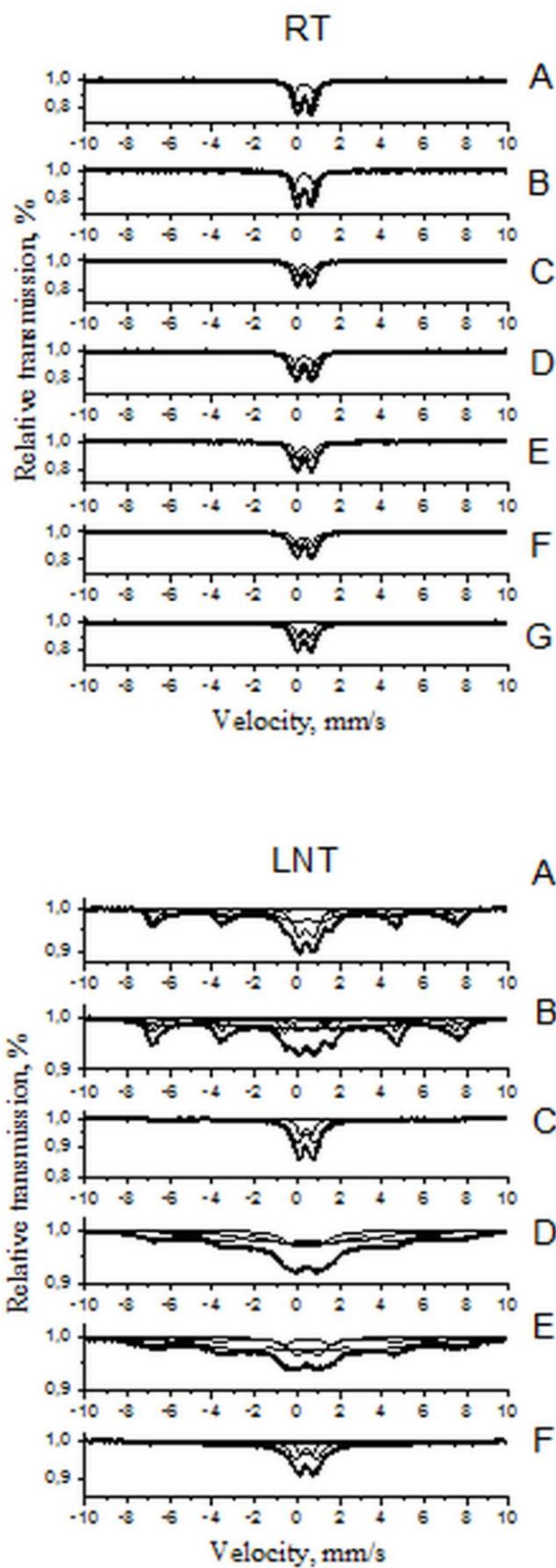
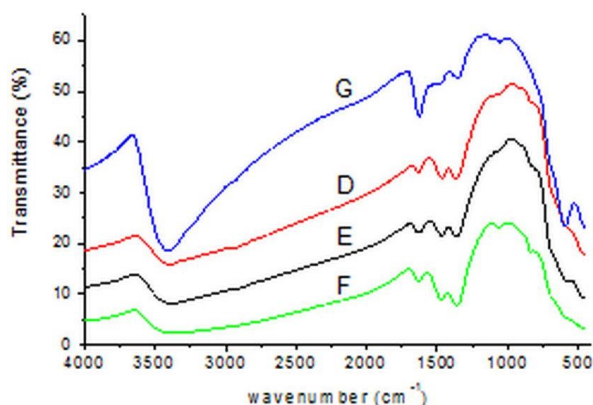
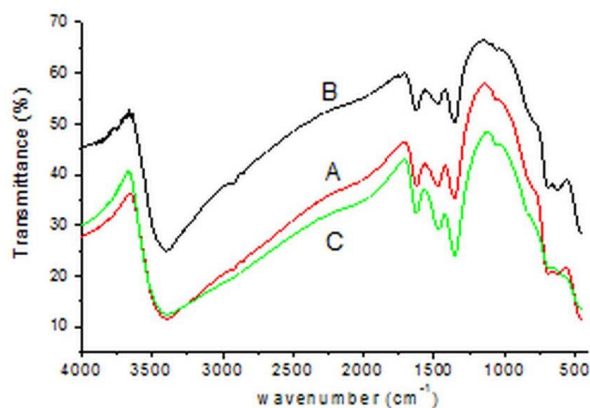


Fig. 2. Mössbauer spectra of prepared mixed Co-Cu ferrite-type samples at room (RT) and liquid nitrogen (LN) temperature.



**Fig. 3.** FTIR spectra of obtained mixed cobalt-copper ferrite-type samples.

Figure 4 shows  $N_2$  adsorption-desorption isotherms at  $-196^\circ\text{C}$  for the synthesized cobalt-copper ferrite-type samples. The adsorption branch in the three isotherms of mechanochemically treated materials D, E, and F belongs to Type II of the IUPAC classification [10]. They display hysteresis loops of type H3 that is typical of non-rigid aggregates of plate-like particles giving rise to slit-shaped pores [11]. Sample F has a notably higher specific surface area value ( $92\text{ m}^2\cdot\text{g}^{-1}$ ) compared to the mechanochemically treated samples D and E,  $37$  and  $51\text{ m}^2\cdot\text{g}^{-1}$ , respectively. The shape of the isotherm of coprecipitated sample C shows a hysteresis loop similar to the H2 type. This hysteresis type has been found for disordered materials of indefinite pore size distribution and shape. On the other hand, the isotherms of samples A, B, and G are similar to those of type IV in the IUPAC classification that is typical of mesoporous materials. Data in table 1 show that the surface area values of the coprecipitated materials are much higher than those of mechanochemically treated series are. Table 1 summarizes values of total specific surface area ( $S_{\text{BET}}$ ), external surface area ( $S_t$ ), micropore volume ( $V_{\text{MP}}$ ), and average pore diameter ( $D_p$ ) calculated from the  $N_2$  adsorption-desorption isotherms at  $-196^\circ\text{C}$ .

**Table 1.** Values of total specific surface area ( $S_{\text{BET}}$ ), external surface area ( $S_t$ ), micropore volume ( $V_{\text{MP}}$ ), and pore diameter ( $D_p$ ) calculated from isotherms of  $N_2$  adsorption-desorption at  $-196^\circ\text{C}$ .

Sample	$S_{\text{BET}}$ $\text{m}^2\cdot\text{g}^{-1}$	$S_t$ $\text{m}^2\cdot\text{g}^{-1}$	$V_{\text{MP}}$ $\text{cm}^3\cdot\text{g}^{-1}$	$D_p$ nm
D	37	27	0.005	4.2
E	51	44	0.004	4.2
F	92	84	0.005	4.2
B	192	192	0.000	5.5
G	204	204	0.000	4.0
A	224	224	0.000	4.7
C	286	286	0.000	3.0

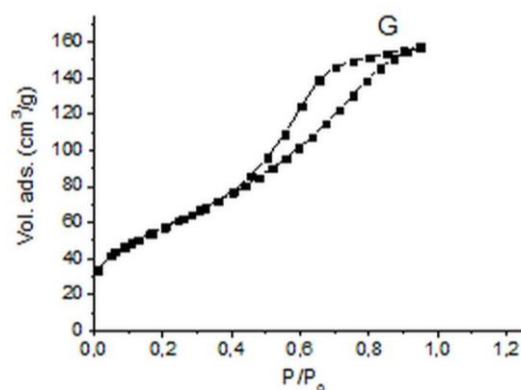
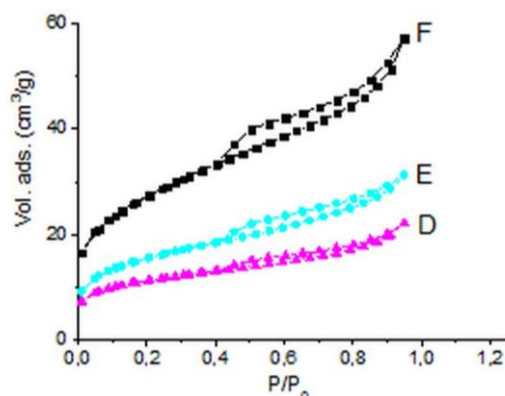
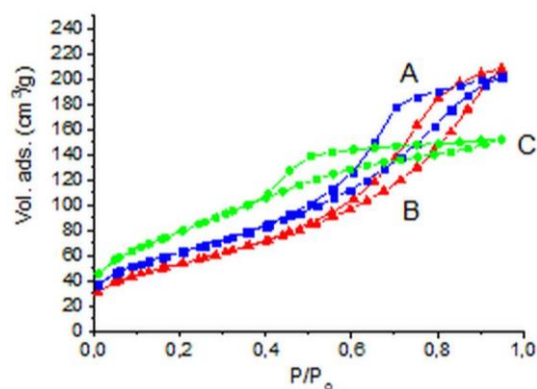


**Fig. 4.** Nitrogen adsorption-desorption isotherms of prepared mixed cobalt-copper ferrite-type materials measured at  $-196^\circ\text{C}$ .

Figure 5 discloses TPR curves of the obtained ferrite-type samples and reduction temperature ranges from 200 to 800°C. All curves have two reduction peaks between 200 and 350°C that could be attributed to reduction of  $\text{Co}^{2+}$  and  $\text{Cu}^{2+}$  species to metallic cobalt and copper phases, respectively. At temperatures between *ca.* 350°C and end of reduction, the curve has several overlapping effects due to the reduction of  $\text{Fe}_2\text{O}_3$ . The TPR curves of samples C and F indicate a lower  $\text{H}_2$  consumption in this interval, as it could be expected in advance due to a lower iron content in these samples. TPR curves belonging to samples of similar compositions show similar shapes, the shifts in temperature of the effects found for the reduction steps being due to differences in dispersion of the species formed depending on synthesis method used.

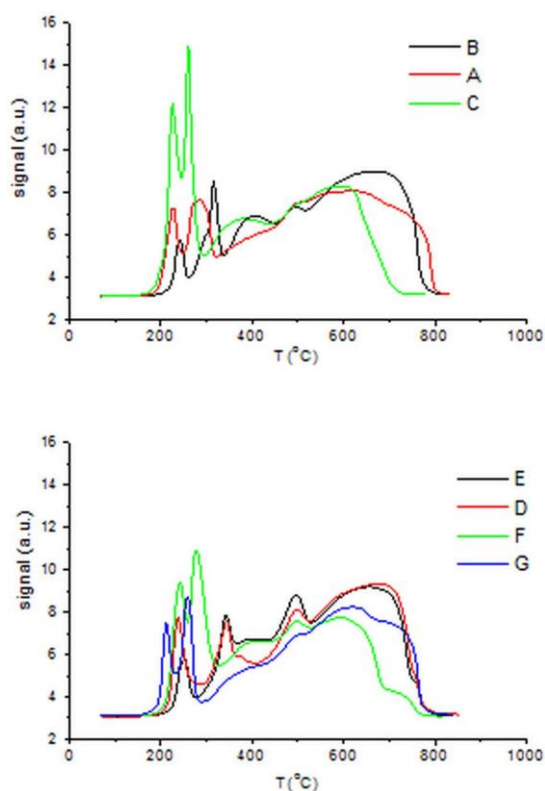


**Fig. 5.** TPR profiles of synthesized mixed cobalt-copper ferrite-type materials.

Table 2 summarizes ratios of hydrogen amount experimentally consumed during TPR analysis to theoretically needed amount for complete reduction of the cations, calculated from the content of each metal cation obtained by element chemical analysis of the samples. Experimental  $\text{H}_2$  consumption values agree well with the calculated ones and a slight deviation is within the experimental error inherent to this technique [12].

The results obtained by PXRD, Mössbauer and FTIR spectroscopy, specific surface area, porosity

measurements, and temperature-programmed reduction are in complete agreement.

**Table 2.** Ratio of experimental to calculated  $\text{H}_2$  consumption based on TPR analysis.

Sample	Exp./calc. amount of consumed $\text{H}_2$
A	1.1
B	1.0
C	0.8
D	1.0
E	1.1
F	1.0
G	1.1

Prior to testing the photocatalytic activities of the samples, the adsorption capacities of the samples (mg dye/mg catalyst) were juxtaposed after 30 min of adsorption time interval in the dark (sufficient to reach adsorption-desorption): 0.02 (A), 0.04 (B), 0.04 (C), 0.06 (D), 0.07 (E), 0.07 (F), and 0.12 (G). Different starting points in figure 6 are due to different adsorption capacities of the samples, however, experimental runs were carried out at one and the same initial concentration,  $C_0 = 20$  ppm. Figure 6 represents comparatively the course of the photocatalytic reaction with time interval of illumination of the RB5 aqueous solution. Photocatalytic testing results established that the conversion degrees of RB5 dye after 120 min over the mechanochemically treated photocatalysts E (78%) and F (77%) are higher than those over samples B (52%) and C (48%) prepared by coprecipitation. An enhancement of the degree of degradation of RB5 dye using the microwave-treated sample G (98%) as photocatalyst is also observed if compared with the coprecipitated sample A (96%) and the mechanochemically treated one D (73%).

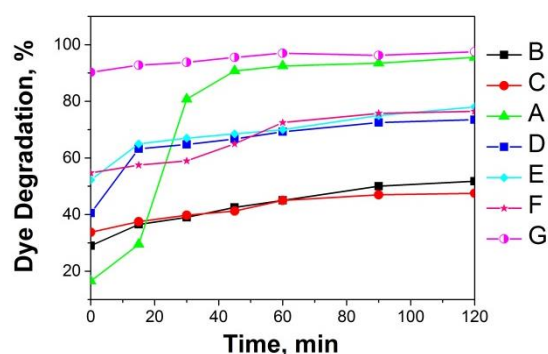


**Fig. 6.** Conversion degrees of RB5 dye solution determined as  $[(C_0 - C)/C_0] \times 100\%$ , where  $C_0$  is the initial concentration (20 ppm) of RB5 dye before switching on the illumination and  $C$  is the current concentration with course of time (maximum absorbance at 599 nm azo bond ( $-\text{N}=\text{N}-$ )) under UV-A illumination over mixed cobalt-copper ferrite-type photocatalysts.

An improvement of photocatalytic efficiency of the mixed cobalt-copper ferrite-type materials is achieved upon lowering the content of cobalt in the magnetite-type host structure. In the general case, the photocatalytic activities are correlating with adsorption capacity: the higher the capacity, the higher the activity with the exception of sample A. In spite of its lowest adsorption capacity, the latter sample is being activated in the course of the photocatalytic test reaching almost the same activity as that of sample G. The mechanism of this activation is not clear yet and it has to be elucidated in a future study. This effect is due to some adsorbed admixture that has remained on the surface after synthesis. In the course of the photocatalytic activity testing, under the effect of the illumination energy the adsorbed amount is being desorbed during the irradiation. Thus, the activation is probably enhancing liberation of adsorption sites, which is evident by a sharp increase in conversion degree with time.

## CONCLUSIONS

Mixed cobalt-copper ferrite-type materials were successfully synthesized using coprecipitation and mechanochemical or microwave treatment. Powder X-ray diffraction data established the presence of spinel ferrite and an iron oxyhydroxide phase in the coprecipitated samples. The single ferrite phase was obtained after mechanochemical or microwave treatment of the mixed cobalt-copper ferrite-type materials. Superparamagnetic and collective magnetic excitation properties of the prepared ferrite powders were estimated by Mössbauer spectroscopy at both room and liquid nitrogen temperature. A coprecipitated  $\text{Co}_{0.5}\text{Cu}_{0.5}\text{Fe}_2\text{O}_4$  sample exhibited the highest specific surface area of  $286 \text{ m}^2 \cdot \text{g}^{-1}$ , which was larger than that of other cobalt-copper ferrite-type materials. A microwave-treated  $\text{Co}_{0.25}\text{Cu}_{0.25}\text{Fe}_{2.5}\text{O}_4$  sample exposed a specific surface area of  $204 \text{ m}^2 \cdot \text{g}^{-1}$ , being higher than that of a mechanochemically treated counterpart ( $S_{\text{BET}} = 37 \text{ m}^2 \cdot \text{g}^{-1}$ ). Photocatalytic studies proved that the mechanochemical treatment leads to an improved degradation conversion degree of RB5 dye after 120 min, 77 and 78% for the  $\text{Co}_{0.5}\text{Cu}_{0.5}\text{Fe}_2\text{O}_4$  and  $\text{Co}_{0.4}\text{Cu}_{0.1}\text{Fe}_{2.5}\text{O}_4$  samples, respectively, compared with coprecipitated

$\text{Co}_{0.5}\text{Cu}_{0.5}\text{Fe}_2\text{O}_4$  (48%) and  $\text{Co}_{0.4}\text{Cu}_{0.1}\text{Fe}_{2.5}\text{O}_4$  (52%) materials. In the case of microwave-treated  $\text{Co}_{0.25}\text{Cu}_{0.25}\text{Fe}_{2.5}\text{O}_4$  sample the degree of discoloration (98%) was higher than that of coprecipitated  $\text{Co}_{0.25}\text{Cu}_{0.25}\text{Fe}_{2.5}\text{O}_4$  (96%) and mechanochemically treated  $\text{Co}_{0.25}\text{Cu}_{0.25}\text{Fe}_{2.5}\text{O}_4$  (73%) samples. The results indicate that the photocatalytic efficiency of synthesized cobalt-copper ferrites is dependent on the degree of incorporation of metal ions in the magnetite type structure and on the preparation conditions. Decreasing the cobalt content in the ferrite-type materials leads to an increase in photocatalytic activity. The present study shows that mixed cobalt-copper ferrite-type materials can find potential application to purification of polluted waters containing azo dyes.

*Acknowledgements:* Financial support by Bulgarian Science Fund through contract DFNI-T02-17/2014 is gratefully acknowledged.

## REFERENCES

1. J. Balavijayalakshmi, N. Suriyanarayanan, R. Jayaprakash, V. Gopalakrishnan, *Phys. Procedia*, **49**, 49 (2013).
2. S. Jauhar, S. Singhal, *Ceram. Int.*, **40**, 11845 (2014).
3. Y. Pu, X. Tao, J. Zhai, J.-F. Chen, *Mater. Res. Bull.*, **45**, 616 (2010).
4. I. Ahmad, T. Abbas, M. U. Islam, A. Maqsood, *Ceram. Int.*, **39**, 6735 (2013).
5. N. Velinov, K. Koleva, T. Tsoncheva, D. Paneva, E. Manova, K. Tenchev, B. Kunev, I. Genova, I. Mitov, *Cent. Eur. J. Chem.*, **12**, 250 (2014).
6. P. Malet, A. Caballero, *J. Chem. Soc. Faraday Trans.*, **84**, 2369 (1988).
7. U. Schwertmann, R. Cornell, *Iron Oxides in the Laboratory*, Weinheim, New York, 1991.
8. H. Emadi, A. Nemati Kharat, *J. Ind. Eng. Chem.*, **21**, 951 (2015).
9. F. A. Miller, C. H. Wilkins, *Anal. Chem.*, **24**, 1253 (1952).
10. K. S. W. Sing, D. H. Everett, R. A. W. Haul, L. Moscou, R. A. Pierotti, J. Rouquerol, T. Siemieniewska, *Pure Appl. Chem.*, **57**, 603 (1985).
11. S. Lowell, J. Shields, M. A. Thomas, M. Thommes, *Characterization of Porous Solids and Powders: Surface Area, Pore Size and Density*, Springer Netherlands, 2010.
12. S. P. Newman, W. Jones, *New J. Chem.*, **22**, 105 (1998).

СМЕСЕНИ КОБАЛТ-МЕДНИ МАТЕРИАЛИ ОТ ФЕРИТЕН ТИП – СИНТЕЗ И  
ФОТОКАТАЛИТИЧНА АКТИВНОСТ В РАЗГРАЖДАНЕТО НА РЕАКТИВНО ЧЕРНО 5 БАГРИЛО  
ПРИ УВ ОБЛЪЧВАНЕ

К. Л. Захаријева<sup>1\*</sup>, К. И. Миленова<sup>1</sup>, В. Ривес<sup>2</sup>, Р. Трухилияно<sup>2</sup>, З. П. Черкезова-Желева<sup>1</sup>,  
Ал. Ел. Елияс<sup>1</sup>, М. П. Цветков<sup>3</sup>, Б. Н. Кунев<sup>1</sup>, Ив. Г. Митов<sup>1</sup>

<sup>1</sup> *Институт по катализ, Българска академия на науките, ул. „Акад. Г. Бончев“, бл. 11, 1113 София, България*

<sup>2</sup> *ПИГ-ХТТМХК, Департамент по неорганична химия, Университет на Саламанка, 37008-Саламанка, Испания*

<sup>3</sup> *Институт по физикохимия, Българска академия на науките, ул. „Акад. Г. Бончев“, бл. 11,  
1113 София, България*

Постъпила на 5 октомври 2015 г.; Преработена на 20 октомври 2015 г.

(Резюме)

Смесени кобалт-медни материали от феритен тип с различен състав бяха получени използвайки техника на съутаяване и механохимична или микровълнова обработка. Различни физикохимични методи като рентгенова дифракция и Мьосбауерова спектроскопия, инфрачервена спектроскопия с Фурие трансформация, БЕТ метод за специфичната повърхност, порьозността и температурно-програмирана редукция бяха използвани за охарактеризиране на получените проби от феритен тип. Фотокаталитичните активности на синтезираните кобалт-медни материали от феритен тип бяха изследвани в окислителното разграждане на Реактивно Черно 5 (PЧ5) багрило като моделен замърсител във воден разтвор при облъчване с UV-A светлина. Фотокаталитични опити установиха, че микровълновата обработка на утаена проба  $\text{Co}_{0.25}\text{Cu}_{0.25}\text{Fe}_{2.5}\text{O}_4$  води до по-висока степен на разграждане на PЧ5 багрилото (98%) в сравнение с тази при използване на утаения (96%) и механохимично обработения (73%) материал. Механохимичната обработка повишава степента на разграждане на PЧ5 багрилото след 120 мин осветяване: 77% и 78% за  $\text{Co}_{0.5}\text{Cu}_{0.5}\text{Fe}_2\text{O}_4$  и  $\text{Co}_{0.4}\text{Cu}_{0.1}\text{Fe}_{2.5}\text{O}_4$ , в сравнение със съответните утаени проби (48% и 52%). Установено е подобрене на фотокаталитичната способност на получените кобалт-медни ферити с намаляване съдържанието на кобалт в материала. Фотокаталитичните свойства на получените смесени кобалт-медни проби от феритен тип зависят от степента на внедряване на металните йони в магнетитовия тип структура и от използваните методи за получаване.

## Influence of mechanochemical activation of metal-doped ZnO on its photocatalytic activity in degradation of Malachite Green dye

K. I. Milenova<sup>1\*</sup>, K. L. Zaharieva<sup>1</sup>, A. E. Eliyas<sup>1</sup>, I. A. Avramova<sup>2</sup>, I. D. Stambolova<sup>2</sup>, V. N. Blaskov<sup>2</sup>, O. S. Dimitrov<sup>3</sup>, S. V. Vassilev<sup>3</sup>, Z. P. Cherkezova-Zheleva<sup>1</sup>, S. K. Rakovsky<sup>1</sup>

<sup>1</sup> Institute of Catalysis, Bulgarian Academy of Sciences, Acad. G. Bonchev St., Bldg. 11, 1113 Sofia, Bulgaria

<sup>2</sup> Institute of General and Inorganic Chemistry, Bulgarian Academy of Sciences, Acad. G. Bonchev St., Bldg. 11, 1113 Sofia, Bulgaria

<sup>3</sup> Institute of Electrochemistry and Energy Systems, Bulgarian Academy of Sciences, Acad. G. Bonchev St., Bldg. 10, 1113 Sofia, Bulgaria

Received: September 28, 2015; Revised December 15, 2015

Mechanochemical activation (MCA) of ZnO samples doped with Ag, Ni, or Co was studied with regard to effect on their photocatalytic activities in degradation of Malachite Green dye. The samples were characterized by XRD and XPS methods. XRD spectra of ZnO photocatalysts showed presence of wurtzite ZnO phase. After MCA, the degree of crystallization was increased and crystallite sizes were smaller. Ratios of defect oxygen species to total oxygen were calculated for mechanochemically treated doped ZnO catalysts and compared with those of matching non-activated ZnO catalysts using X-ray photoelectron spectra.

The rate of Malachite Green oxidative discoloration reaction on cobalt- and silver-doped ZnO increases with duration of post-synthesis mechanochemical treatment. Mechanochemical activation effect is strongest for silver-doped samples due to the smallest size of the crystallites and increased degree of crystallization.

**Keywords:** doping, mechanochemical activation, ZnO, photocatalysts, ultraviolet light.

### INTRODUCTION

Applying mechanochemical treatment procedures for tuning of the activity and physicochemical properties of materials has a significant evolution in recent years. Mechanochemical activation could be an effective route for improvement of the structural and catalytic properties of metal oxide nanoparticles and nanocomposites. Mechanically introduced energy can also create crystal defects such as Schottky or Frenkel defects or crystallographic shear planes which can lead to enhanced catalytic or photocatalytic activities [1]. This technique can improve the surface areas and porous structures. In many cases, mechanochemical nanomaterials and nanocatalysts exhibit comparable or improved catalytic activities as compared to conventionally synthesized materials.

Air and water pollution with persistent organic pollutants can cause significant health and environmental problems. In many cases, conventional purification techniques are not effective. Photocatalysis using inorganic semiconductors is considered to have significant potential to destroy organic pollutants in wastewaters [2]. Recently, ZnO photocatalyst is attracting increased attention due to its

similarity with TiO<sub>2</sub> in band gap, high quantum efficiency, and high photocatalytic activity [3]. Doping is a widely applied procedure to diminish the wide band gap of ZnO and reduce the electron-hole recombination rate of ZnO during the photocatalytic process by using various transition or noble metals such as Cu, Ni, Co, Mn, Ag, *etc.* [4]. Saharan *et al.* [5] have obtained nickel-doped ZnO by chemical precipitation method applying CTAB surfactant at a low temperature. They found that substitutional doping of Ni in ZnO lattice at low temperatures has a positive influence on ZnO electronic structure and improved photocatalytic activity for degradation of anionic (Fast Green) and cationic (Victoria Blue) dyes.

Nickel-ZnO hybrid nanostructures, prepared by reduction of nickel chloride hexahydrate through a solvothermal process followed by surface modification, act as an efficient photocatalyst for decomposition of Methylene Blue (MB) dye [6].

Nanorods of cobalt-doped ZnO, synthesized by hydrothermal method, exhibit a high photocatalytic activity in degradation of methylene blue dye and phenol [4].

Silver-doped ZnO nanorods were synthesized through the precipitation method and their photocatalytic activities at different doping levels were evaluated in the degradation of methylene blue [7].

\* To whom all correspondence should be sent  
E-mail: kmilenova@ic.bas.bg

It has been found that Ag doping leads to optical band gap narrowing. Silver-deposited ZnO nanoparticles (NPs) have been synthesized by sol-gel method designed for visible light excited photocatalytic degradation of methylene blue [8]. Ag/ZnO NPs exhibit a five-fold higher activity than the pristine ZnO and four times greater than that of reference Degussa P-25. A high visible-light activity of Ag/ZnO could be attributed to effective charge separation. Dimitriev *et al.* [9] have performed soft mechanochemical synthesis of ZnO powders to avoid formation of intermediate ZnCO<sub>3</sub> and additional heat treatment. The mechanochemically synthesized ZnO powders possess good photocatalytic properties for degradation of Malachite Green dye.

The purpose of the present study was to perform mechanochemical activation (MCA) of doped ZnO powders and test their photocatalytic activities toward degradation of Malachite Green dye.

## EXPERIMENTAL

Activated ZnO powder samples, doped with 1.5 wt.% Co, Ni or Ag, were prepared using zinc carbonate precursor [10]. The procedure comprised thermal decomposition at 400°C followed by impregnation with the corresponding metal nitrate. Doped samples were finally calcined in air at 500°C for 2 h. The so obtained Co-, Ni- and Ag-doped ZnO samples were mechanochemically treated in a high-energy planetary ball mill (model PM 100, Retsch, Germany). The mechanochemical activation was carried out in an agate-milling container of 80-ml volume for milling time interval of 15 minutes at a milling speed of 400 rpm using air medium. The mass ratio of sample amount to applied balls was 1:9.

Sample morphology was examined on a JEOL model JEM-200CX scanning electron microscope equipped with an EM-ASID3D scanning adaptor.

An X-ray diffraction (XRD) investigation of the samples was performed using a Philips PW 1050 instrument with CuK $\alpha$  radiation. Crystallite sizes were determined by Scherrer formula.

X-ray photoelectron spectroscopy (XPS) studies were carried out in a VG Escalab II electron spectrometer using AlK $\alpha$  radiation with energy of 1486.6 eV under base pressure of 10<sup>-7</sup> Pa and a total instrumental resolution of 1 eV. Binding energies (BE) were determined using the C1s line (from adventitious carbon) as a reference with energy of 285.0 eV. The accuracy of measuring the BE values was 0.2 eV. C1s, Zn2p, and O1s photoelectron lines were recorded and corrected by subtracting Shirley's type of background and quantified using the peak area and Scofield's photoionization cross-sections.

The photocatalytic activities of the prepared samples were measured in the oxidative degradation of Malachite Green dye under UV light irradiation (power of 18 W, maximum emission at 365 nm) in a semi-batch photocatalytic reactor. Feeding large stoichiometric excess of oxygen allows modelling the kinetics of bimolecular reaction reducing it to a pseudo-first order rate equation, disregarding the dissolved oxygen concentration. Being practically constant, C<sub>O<sub>2</sub></sub> is included in the value of the apparent rate constant. The course of the photocatalytic reaction was followed using a UV-Vis absorbance spectrophotometer in the wavelength range from 200 to 800 nm. The initial concentration of the used MG dye solution was 5 ppm ( $\lambda_{\text{max}} = 615$  nm) and the catalyst loading was 1 g.L<sup>-1</sup>. Before UV illumination, the investigated systems were equilibrated in the dark for about 30 min. The rate constants *k* were evaluated as a slope of linear logarithmic dependence  $-\ln(C/C_0) = k_{\text{app}}t$ .

## RESULTS AND DISCUSSION

X-ray diffraction spectra have proved that all doped ZnO samples without mechanochemical treatment represent a wurtzite crystallographic phase (PDF 36-1451) with three main peaks corresponding to (100), (002), and (101) planes orientation [10]. Figure 1 displays XRD patterns of the samples after mechanochemical activation. The Ag/ZnO-MCA sample shows traces of silver oxide phase. The intensity of the crystallographic peaks of MCA samples is twice higher than that of the initial samples.

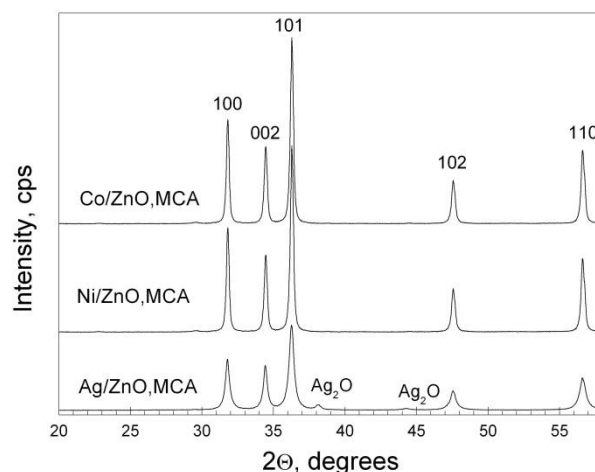


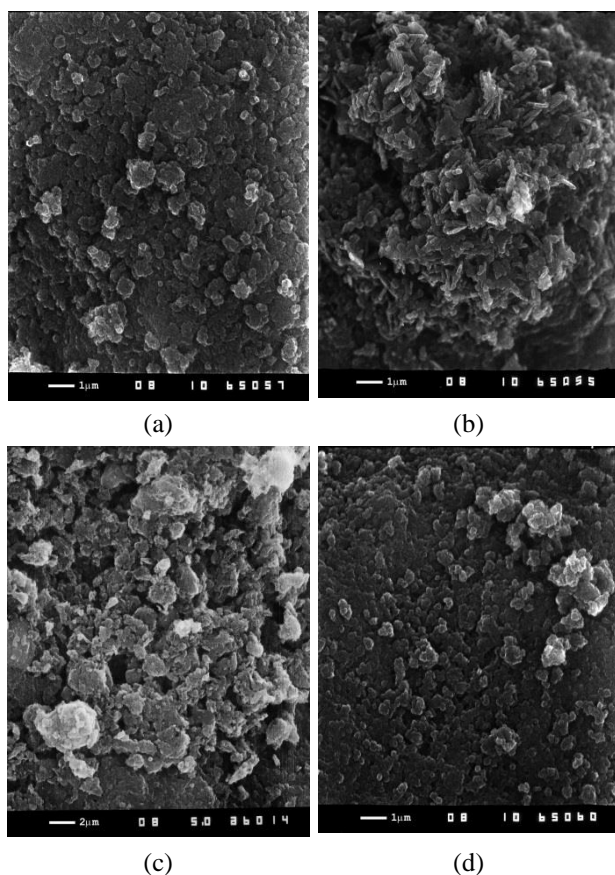
**Fig. 1.** X-ray diffraction patterns of mechanochemically activated samples

Mean crystallite sizes of fresh and mechanochemically activated samples are shown in table 1. The MCA leads to a strong decrease in crystallite sizes.

**Table 1.** Mean crystallites sizes (nm).

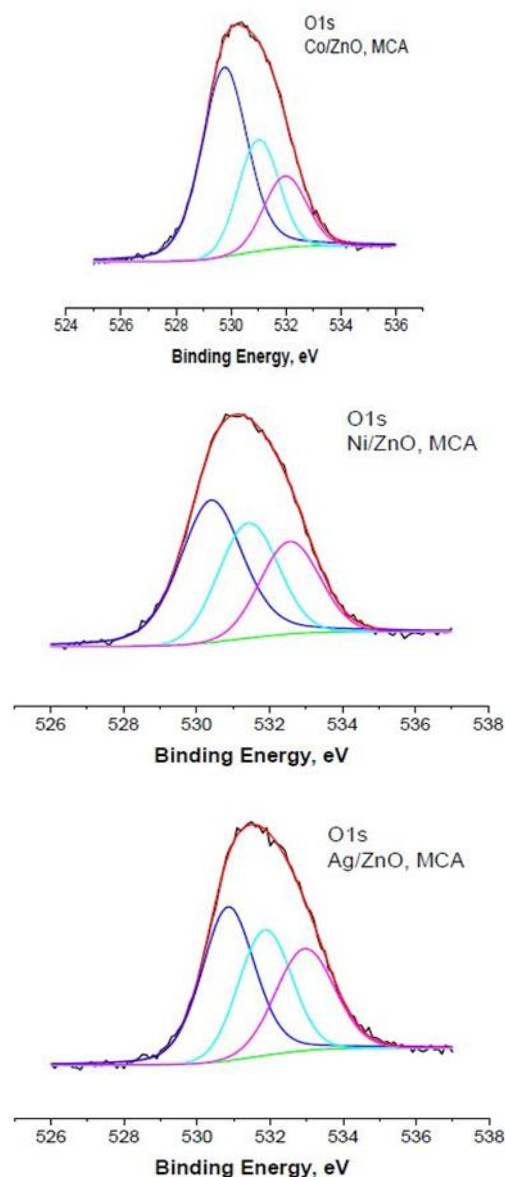
Sample	Before MCA	After MCA
Ni/ZnO	54	24
Co/ ZnO	52	24
Ag/ZnO	50	22

Figure 2 shows SEM pictures of Ni/ZnO, Ni/ZnO-MCA, Ag/ZnO, and Ag/ZnO-MCA samples. Figures 2a,b represent surface morphology species of the Ni/ZnO and Ni/ZnO-MCA samples. It is seen that after mechanochemical activation the spheroidal species is transformed into needle-like crystals. In the case of Ag/ZnO (Figs. 2c,d) the effect of MCA is more strongly expressed. Particles size is being considerably reduced revealing internal surface and the rate of dye molecule diffusion is being increased, whereupon the inner pores become easily accessible. This brings about a higher rate of the photocatalytic reaction. The smaller particle size also causes a reduced degree of scattering of the light beam because of which the reaction is accelerated due to a greater number of active sites.

**Fig. 2.** SEM pictures of: (a) Ni/ZnO, (b) Ni/ZnO, MCA, (c) Ag/ZnO and (d) Ag/ZnO, MCA.

Surface chemical states of the elements in the mechanochemically activated ZnO photocatalysts doped with Ag, Co, and Ni were investigated by using an X-ray photoelectron spectroscopy method.

The most intensive photoelectron lines of zinc, oxygen as well as those of silver, cobalt, and nickel were studied. Recorded Ag3d, Co2p, and Ni2p photoelectron spectra (not shown here) were used to estimate dopant oxidation states as follows: Ag<sup>+</sup>, Co<sup>2+</sup>, and Ni<sup>2+</sup> [10]. O1s photoelectron lines obtained for the ZnO powders were complex and to understand their nature they were subjected additionally to a fitting procedure. The fitted O1s spectra presented in figure 3 manifest three peaks.

**Fig. 3.** XPS spectra of O1s for mechanochemically activated samples.

The peak at around 530.5 eV belongs to oxygen in stoichiometric ZnO, the second one at around 531.5 eV is attributed to oxygen in a non-stoichiometric ZnO matrix and the third peak (around 532.5 eV) is ascribed to chemisorbed oxygen: an OH group or dissociated oxygen on the surface of the

mechanochemically treated doped ZnO catalysts. Ratios of defect oxygen species to total oxygen were calculated for mechanochemically treated doped ZnO catalysts and compared with those of matching non-activated ZnO catalysts. Oxygen species associated with defects related to the total oxygen is increasing in the order: Ag/ZnO-MCA (30.5%) > Ni/ZnO-MCA (30.26%) > Co/ZnO-MCA (26%) > Ag/ZnO (25.3%) > Co/ZnO (23.9%) > Ni/ZnO (20.8%). It is worth mentioning that the mechanochemical activation procedure obviously leads to creation of more oxygen vacancies on the surface of silver-, cobalt-, and nickel-doped ZnO catalysts.

A previous study of mechanochemically activated ZnO powders doped with nickel, cobalt, and silver reports a positive effect on photocatalytic performance for degradation of azo dye RB5 over doped samples, as compared with undoped ZnO in all cases [10]. Degradation rate constants were calculated and increased in the following order: ZnO < Co-ZnO < Ag-ZnO < Ni-ZnO. This confirms the most positive effect of nickel dopant on the photocatalytic properties of activated ZnO. Figures 4 and 5 illustrate the reaction course of Malachite Green dye solution under UV-A illumination over Ni/ZnO, Co/ZnO, Ag/ZnO, Ni/ZnO-MCA, Co/ZnO-MCA, and Ag/ZnO-MCA catalysts. Malachite Green dye was used as a model pollutant due to its carcinogenic and teratogenic effect [11, 12].

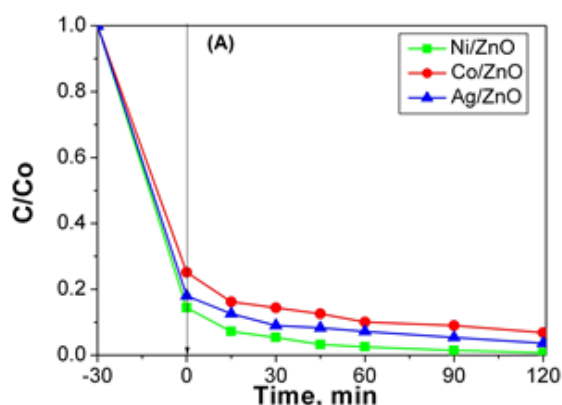


**Fig. 4.** Reaction course of the Malachite Green dye solution under UV-A illumination of (A) Ni/ZnO; Co/ZnO; Ag/ZnO.

The photocatalytic activities of the samples depended both on dopant type and applied activation treatment. Among all the investigated dopants, the nickel doping of ZnO powders affected most favourably the rate of oxidative discoloration reaction of the Malachite Green dye solution. It can be supposed that nickel doping in a semiconductor shifts the Fermi level towards more negative potential and improves the efficiency of the interfacial charge transfer process [13]. Therefore, the transfer

of an electron that takes place from the conduction band of ZnO to the new Fermi level is facilitated in the Ni-doped ZnO, as shown in Ref. 6. Such an electron transfer between the photoexcited semi-conducting ZnO and the dopant prevents electron-hole recombination [14]. As a result, enhanced photodegradation of the dye is observed.

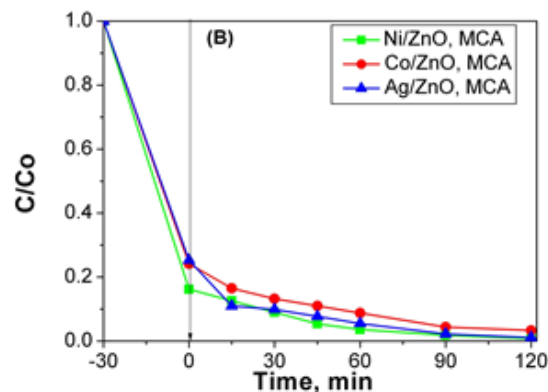


**Fig. 5.** Reaction course of the Malachite Green dye solution under UV-A illumination of (B) Ni/ZnO, MCA; Co/ZnO, MCA; Ag/ZnO, MCA.

Mechanochemically treated Ag- or Co-doped powders increase the photocatalytic efficiency of the samples. This effect was more pronounced in the case of Ag/ZnO-MCA powders. After 120 min of illumination, the conversion degree of dye degradation was 99%, while for the non-treated samples it was 96%. The higher efficiency of mechanically activated Ag/ZnO samples is attributed to enhanced crystallization and a decrease in crystallite size [15].

Figure 6 compares rate constants of the photocatalytic process in presence of the investigated catalysts under UV-A illumination. The photocatalytic activity of ZnO nanomaterials is strongly dependent on porous structure, presence of defects, crystallite size, degree of crystallinity, etc., which are affected by the preparation procedure [15]. The best photocatalytic properties of Ag/ZnO-MCA samples can be ascribed to smaller crystallite sizes and enhanced crystallization in comparison with non-activated Ag/ZnO.

SEM pictures displayed in figure 2d reveal that the Ag/ZnO-MCA sample exposes sphere-like particles that enhanced photocatalytic performance [16, 17] without being aggregates as Ag/ZnO. Aggregation leads to suppression of photocatalytic activity because it can lead to fewer electron-hole pairs, which result in suppressed OH• generation, as in the case of Ni/ZnO-MCA [18]. Another possible reason is associated with aggregate particle size distribution, which may influence both light absorption and light scattering mechanisms that determine the degree of photon interaction with photocatalyst

particles. Scattered light intensity is probably stronger on samples with aggregates.

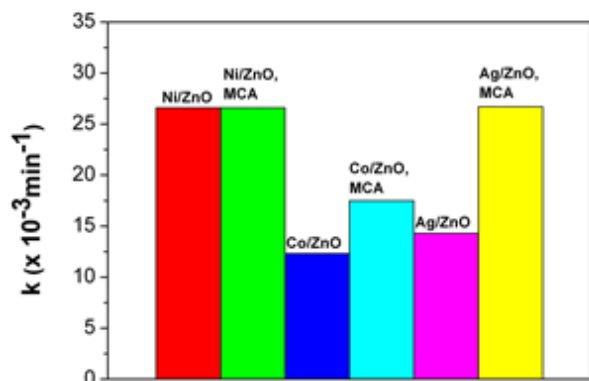


**Fig. 6.** Rate constants  $k$  of the photocatalytic process in the presence of the investigated catalysts under UV-A illumination.

## CONCLUSIONS

Mechanochemical post-synthesis activation of metal-doped (Ag, Co or Ni) ZnO powders was investigated in connection with their photocatalytic activities in degradation of Malachite Green dye. An increased degree of crystallization and decreased crystallite sizes of the samples were observed after mechanochemical activation. The mechanochemical treatment results in formation of a larger number of oxygen defects in the ZnO lattice, which play the role of adsorption sites. Degradation apparent rate constants (pseudo-first order kinetics) are decreasing in the following order: Ag/ZnO-MCA ( $26.7 \times 10^{-3} \text{ min}^{-1}$ ) > Co/ZnO-MCA ( $17.5 \times 10^{-3} \text{ min}^{-1}$ ) > Ag/ZnO ( $14.3 \times 10^{-3} \text{ min}^{-1}$ ) > Co/ZnO ( $12.3 \times 10^{-3} \text{ min}^{-1}$ ). The mechanochemical activation promotes significantly the rate of oxidative reaction of Malachite Green dye discoloration in the case of samples doped with silver.

*Acknowledgements:* The authors gratefully acknowledge financial support by the Bulgarian Science Fund (Contracts DFNI-T-02-16 and DFNI-E-02-2/2014) and the collateral contract between

Bulgarian Academy of Sciences and Serbian Academy of Sciences and Arts 'Development of advanced catalytic systems applicable to chemical and photochemical processes for neutralization of environmental pollution'

## REFERENCES

1. C. Xu, S. De, A. M. Balu, M. Ojeda, R. Luque, *Chem. Commun.*, **51**, 6698 (2015).
2. R. Chauhan, A. Kumar, R. P. Chaudhary, *J. Sol-Gel Sci. Technol.*, **63**, 546 (2012).
3. L. Saiki, D. Bhuyan, M. Saikia, B. Malakara, D. K. Dutta, P. Sengupta, *Appl. Catal. A-Gen.*, **490**, 42 (2015).
4. B. M. Rajbongshia, S. K. Samdarshi, *Mater. Sci. Eng. B*, **182**, 21 (2014).
5. P. Saharan, G. R. Chaudhary, S. Lata, S.K. Mehta, S. Mor, *Ultrason. Sonochem.*, **22**, 317 (2015).
6. S. Senapati, S. K. Srivastava, S. B. Singh, *Nanoscale*, **4**, 6604 (2012).
7. R. Rahimi, J. Shokrayian, M. Rabbani, doi: 10.3390/ecsoc-17-b019.
8. B. Rajbongshi, A. Ramchiary, B. Jha, S. Samdarshi, *J. Mater. Sci.-Mater. Electron.*, **25**, 2969 (2014).
9. Y. Dimitriev, M. Gancheva, R. Iordanova, *J. Alloys Compd.*, **519**, 161 (2012).
10. K. Milenova, I. Avramova, A. Eliyas, V. Blaskov, I. Stambolova, N. Kassabova, *Environ. Sci. Pollut. Res.*, **21**, 12249 (2014).
11. R. Gopinathan, J. Kanhere, J. Banerjee, *Chemosphere*, **120**, 637 (2015).
12. S. Srivastava, R. Sinhaa, D. Roya, *Aquat. Toxicol.*, **66**, 319 (2004).
13. V. Subramanian, E. E. Wolf, P. V. Kamat, *J. Am. Chem. Soc.*, **126**, 4943 (2004).
14. R. Georgekutty, M. K. Seery, S. C. Pillai, *J. Phys. Chem. C*, **112**, 13563 (2008).
15. M. Fallet, S. Permpoon, J. L. Deschanvres, M. Langlet, *J. Mater. Sci.*, **41**, 2915 (2006).
16. A. Lei, B. Qu, W. Zhou, Y. Wang, Q. Zhang, B. Zou, *Mater. Lett.*, **66**, 72 (2012).
17. H. Liu, J. Yang, J. Liang, Y. Huang, C. Tang, *J. Am. Ceram. Soc.*, **91**, 1287 (2008).
18. D. Jassby, J. F. Budarz, M. Wiesner, *Environ. Sci. Technol.*, **46**, 6934 (2012).

# ВЛИЯНИЕ НА МЕХАНОХИМИЧНАТА АКТИВАЦИЯ НА ZnO ДОТИРАН С МЕТАЛ ВЪРХУ ФОТОКАТАЛИТИЧНАТА АКТИВНОСТ ЗА РАЗЛАГАНЕ НА БАГРИЛОТО МАЛАХИТОВО ЗЕЛЕНО

К. И. Миленова<sup>1\*</sup>, К. Л. Захариева<sup>1</sup>, Ал. Ел. Елияс<sup>1</sup>, Ив. А. Аврамова<sup>2</sup>, Ир. Д. Стамболова<sup>2</sup>,  
Вл. Н. Блъсков<sup>2</sup>, Ог. С. Димитров<sup>3</sup>, С. В. Василев<sup>3</sup>, З. П. Черкезова-Желева<sup>1</sup>, Сл. К. Раковски<sup>1</sup>

<sup>1</sup> *Институт по катализ, Българска академия на науките, ул. „Акад. Г. Бончев“, бл. 11, 1113 София, България*

<sup>2</sup> *Институт по обща и неорганична химия, Българска академия на науките, ул. „Акад. Г. Бончев“, бл. 11, 1113 София, България*

<sup>3</sup> *Институт по електрохимия и енергийни системи, Българска академия на науките, ул. „Акад. Г. Бончев“, бл. 10, 1113 София, България*

Постъпила на 28 септември 2015 г.; Преработена на 15 декември 2015 г.

(Резюме)

Изследван е ефектът на механохимичната активация на ZnO дотиран с Ag, Ni или Co върху фотокаталитичната му активност за разлагане на багрилото Малахитово Зелено. Образците са охарактеризирани чрез методите на рентгенова дифракция и рентгенова фотоелектронна спектроскопия. Рентгеновите спектри на фотокатализаторите от ZnO показаха присъствие на вюрцитна фаза. Степента на кристализация нараства, а размерите на кристалитите намаляват силно след механохимична активация. Изчислено е съотношението между кислорода принадлежащ на дефекти и общия кислород за механохимично активираните катализатори от дотиран ZnO и е сравнено със същата величина за нетретираните образци на основата на рентгеновите фотоелектронни спектри.

Скоростта на окислителната реакция водеща до обезцветяване на Малахитово зелено в присъствие на ZnO дотиран с кобалт или сребро нараства след механохимичната им обработка. Ефектът от механохимичната активация е най-силен за дотираните със сребро образци, което се дължи на малкия размер на кристалитите и по-високата степен на кристалност.

## Photocatalytic bleaching of two organic dyes catalysed by La-doped nanosized TiO<sub>2</sub>

A. M. Stoyanova<sup>1\*</sup>, Ts. K. Koleva<sup>1</sup>, A. D. Bachvarova-Nedelcheva<sup>2</sup>, R. S. Iordanova<sup>2</sup>

<sup>1</sup> Medical University, 1 Kliment Ohridski St., 5800 Pleven, Bulgaria

<sup>2</sup> Institute of General and Inorganic Chemistry, Bulgarian Academy of Sciences, Acad. G. Bonchev St., Bldg. 11, 1113 Sofia, Bulgaria

Received September 12, 2015; Revised December 3, 2015

The aim of the present investigation is to synthesize and characterize pure and La-doped TiO<sub>2</sub> and to test as-prepared samples for photocatalytic activity. Doped and undoped samples were prepared by non-hydrolytic sol-gel method from titanium(IV) chloride, benzyl alcohol, and lanthanum(III) nitrate followed by thermal treatment. Lanthanum content in synthesized samples ranged from 0.4 to 5 mol.%. Structure and morphology of the obtained nanopowders were characterized by XRD, IR, and UV-Vis analysis. Average particle sizes of pure and doped TiO<sub>2</sub> were about 6–15 nm and anatase was found to be a dominant crystalline phase in the samples. It was estimated that particle sizes decreased on increasing La content.

The photocatalytic activity of titania samples for degradation of two organic dyes with different chromophores, triphenylmethane dye Malachite Green and xanthen dye Rhodamine B, was studied under UV and visible illumination. Addition of small amounts of La (0.4 and 1 mol.%) to TiO<sub>2</sub> was favourable for the photocatalytic activity under UV irradiation, while doping with 5 mol.% La led to a slower decolouration irrespective of used dye.

**Keywords:** La-doped titanium dioxide, sol-gel, photocatalytic activity.

### INTRODUCTION

Titanium dioxide is one of the most investigated semiconductor photocatalysts for its long-term stability, non-toxicity, and excellent photocatalytic properties. It has been used to solve many environmental problems such as pollution of water, air, and soil. However, titania application is yet limited due to a fast recombination of electron-hole pairs and a large band gap, which corresponds with UV light. Modification of TiO<sub>2</sub> by doping with rare earth metals is a promising approach to improving its photocatalytic performance. Rare earth ion radii are larger than that of Ti<sup>4+</sup>, so they can be distributed mainly on the surface of titania [1]. It is reported that lanthanide ions are able to form complexes with various organic compounds by interaction of their functional groups with lanthanide f-orbitals [2]. Thus, it is expected that organic pollutants could concentrate at the semiconductor surface, which may lead to enhancement of photocatalytic activity.

An enhanced photocatalytic activity was reported for rare earth doped TiO<sub>2</sub> under UV and visible light irradiation in several publications [3–8]. Among the various lanthanide metals examined, La, Ce, Eu, and Gd ions have been used widely [9].

It is well known that the effect of ion doping is strongly dependent on many factors, such as

preparation route, doping method, dopant concentration, etc. For modifying TiO<sub>2</sub> with rare earth elements different techniques have been used: sol-gel technology, hydrothermal method, anodic oxidation, magnetron sputtering, electrospinning, co-precipitation, complexation, etc. [6, 10–17]. Sol-gel procedures are the most popular synthetic methods, which enable researchers to achieve superior compositional product homogeneity at moderate temperatures [15–17]. Among them, due to a slower reaction rate, non-hydrolytic sol-gel syntheses performed in organic solvents allow for better control over particle size and crystallinity degree [16–17].

This paper is a continuation of our previous research on preparation and properties of pure and modified nanosized TiO<sub>2</sub> catalysts by non-hydrolytic sol-gel method [18–25]. In the present work we report on the synthesis, characterization, and photocatalytic properties of La-doped TiO<sub>2</sub> derived by non-hydrolytic sol-gel procedure from titanium(IV) chloride, benzyl alcohol, and lanthanum(III) nitrate, the latter being a rare earth element source. Lanthanum content in the synthesized samples ranged from 0.4 to 5 mol.%. Photocatalytic activities of the synthesized powders were evaluated by degradation of two model organic pollutants under UV-Vis illumination: xanthen dye Rhodamine B (RhB) and triphenylmethane dye Malachite Green (MG). RhB is one of the most

\* To whom all correspondence should be sent  
E-mail: a.stoyanova@mu-pleven.bg

commonly used dyes in textile and paper industry. This dye is now banned from use in foods and cosmetics because it has been found to be potentially toxic and carcinogenic [28,29]. The triphenylmethane dye MG is widely used in aquaculture as a parasiticide and in food, health, textile and other industries. However, it has been reported that this dye can have carcinogenic, genotoxic, and mutagenic effects on fish, mammals, and other animals. Despite being banned in several countries, it is still being used in many parts of the world and poses risks for human health [30]. Therefore, photodegradation of these dyes is important with regard to the environmental cleanup.

## EXPERIMENTAL

### Preparation and characterization of titania catalysts

The starting materials in this study were titanium tetrachloride ( $\geq 99.0\%$ , Fluka) used as a titania precursor, benzyl alcohol ( $\geq 99.5\%$ , Merck), lanthanum(III) nitrate (Aldrich) as a rare earth element source, and absolute ethanol and diethyl ether from Merck. The Rhodamine B dye ( $C_{28}H_{31}ClN_2O_3$ ) was purchased from Fluka while Malachite Green oxalate ( $C_{46}H_{50}N_4.3C_2H_2O_4$ ) was supplied by Sigma. All the chemicals were used without further purification.

Pure and La-doped  $TiO_2$  samples were prepared by means of non-hydrolytic sol-gel method based on the reaction between benzyl alcohol and titanium tetrachloride [26]. The main stages of sol-gel synthesis of lanthanum-modified titania samples are shown in figure 1. The reactions were performed in a regular glass beaker under controlled heating. For the preparation of La-modified titania, initially a proper amount of lanthanum(III) nitrate was dissolved in ethanol and mixed with benzyl alcohol. Then, titanium tetrachloride was slowly added to the beaker with benzyl alcohol at a volume ratio of 1:20 and the resulting sols were heated at  $150^\circ C$  under vigorous stirring for 10 h. Reaction mixtures were left for aging at room temperature for 10–14 days. Obtained white thick suspensions were centrifuged at 5000 rpm for 15 min and the supernatant was discarded by decantation. The precipitates were then washed twice with diethyl ether. After every washing step, the solvent was separated by centrifugation. The collected material was dried in air overnight and then ground into a fine powder. The obtained powders were calcined at  $500^\circ C$  for 2 h. In this way three modified  $xLa/TiO_2$  samples were prepared:  $0.4La/TiO_2$ ,  $1La/TiO_2$ , and  $5La/TiO_2$ , where  $x$  represents La content as mol.%. Pure  $TiO_2$  was prepared

by the same procedure; however, lanthanum solution was replaced by anhydrous ethanol.

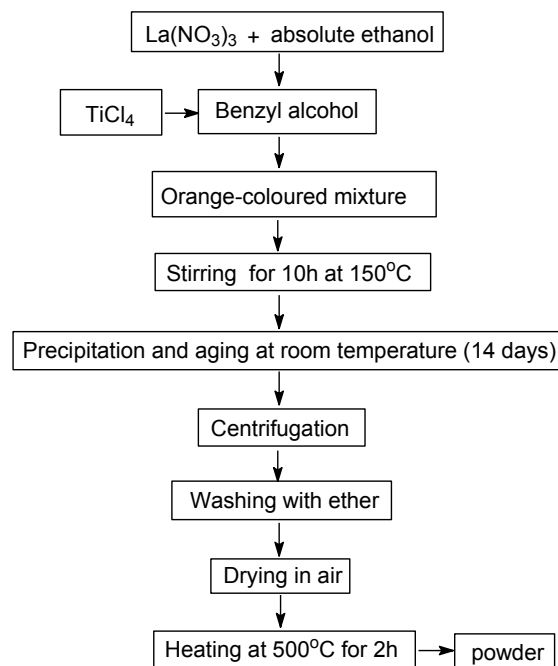


**Fig. 1.** Scheme of non-hydrolytic synthesis of La-doped  $TiO_2$ .

The structure and morphology of the resulting powders were characterized by X-ray diffraction (XRD, Bruker D8 Advance X-ray instrument), infrared (IR) spectroscopy using the KBr pellet method (Nicolet-320, FTIR spectrometer with a resolution of  $\pm 1\text{ cm}^{-1}$ , by collecting 64 scans in the range  $1000\text{--}400\text{ cm}^{-1}$ ), and UV-Vis spectroscopy (Spectrophotometer Evolution 300). Absorption edge and optical band gap were determined following instructions of Dharma et al. [27]. Bandgap energies of the samples were calculated by Planck's equation:  $E_g = hc/\lambda = 1240/\lambda$ , where  $E_g$  is bandgap energy (eV),  $h$  is Planck constant,  $c$  is light velocity ( $\text{m s}^{-1}$ ), and  $\lambda$  is the wavelength (nm) (Table 1).

**Table 1.** Cut-off and optical band gap values for obtained compositions

Sample	Cut-off, nm	$E_g$ , eV
undoped $TiO_2$	388.33	3.19
0.4% La- $TiO_2$	368.61	3.36
1% La- $TiO_2$	364.87	3.39
5% La- $TiO_2$	369.67	3.35

### Photocatalytic activity procedure

The initial concentration of the RhB and MG aqueous solutions was 5 and  $10\text{ mg l}^{-1}$ , respectively. In a typical procedure, a titanium sample (100 mg) was added to a 150-ml dye solution to form suspension. Prior to irradiation, the suspension was magnetically stirred for 30 min in the dark to reach

an adsorption-desorption equilibrium of organic pollutant on the photocatalyst surface. A black light blue lamp (Sylvania BLB 50 Hz 8W T5) was used as a UV radiation source with a peak at 365 nm, and a 500-W halogen lamp (Sylvania) was used as the visible light source. In experiments, UV and visible light lamps were fixed above the treated solution at 10 and 40 cm, respectively. Blank tests were performed with dye solutions without catalysts in order to estimate possibilities for direct photolysis of the dyes.

All photocatalytic tests were performed under magnetic stirring (450 rpm) at a room temperature of 25°C. Aliquot samples of 3 ml were taken out at a regular time intervals from test solutions, centrifuged for 15 min at 5500 rpm, and filtered to remove catalyst particles. The photocatalytic degradation was monitored by measuring the absorbance of clear aliquots on a Jenway 6505 UV-Vis spectrophotometer at the characteristic wavelengths of the dyes: 555 and 618 nm for RhB and MG, respectively. Decolouration efficiency, *DE*, of the photocatalysts was calculated from equation (1):

$$DE = [(A_0 - A_t) / A_0] \times 100, \quad (1)$$

where  $A_0$  is the absorbance at zero time and  $A_t$  is the absorbance at time  $t$ .

## RESULTS AND DISCUSSION

### Characterization of titania samples

XRD patterns of La-doped TiO<sub>2</sub> are shown in figure 2. As is seen, anatase (TiO<sub>2</sub>) (JCPDS 78-2486) is a dominating crystalline phase detected by XRD. No peaks of rutile were observed. Moreover, lanthanum was not observed in the patterns, either. This indicated that La<sup>3+</sup> ions were not incorporated into the TiO<sub>2</sub> crystal lattice to replace Ti<sup>4+</sup>. Obviously, modification by lanthanum cannot enhance a phase transformation of anatase to rutile. Recently, it has been reported that La<sup>3+</sup> dopant could inhibit the A-R phase transportation at high La<sup>3+</sup> concentrations (above 2 at.%) [31]. In our previous investigations, it was established that Fe and N co-doping enhanced rutile crystallization which appeared at lower temperatures (500°C) [32]. Thus, it could be concluded that the doping effect of metal ions on A-R phase transformation is dependent on the physicochemical properties of doping metal ion as well as on its concentration. Average particle sizes of the as-synthesized La-doped TiO<sub>2</sub> samples calculated from diffraction line broadening using Scherrer equation were about 6–15 nm. It was estimated that particle sizes decreased

on increasing La content (Fig. 2). For comparison, the particle size of pure TiO<sub>2</sub> obtained by non-hydrolytic sol-gel method is ~20 nm and these results are published elsewhere [22]. Probably, this is due to the nature of used precursors, experimental conditions as well as to applied non-hydrolytic sol-gel synthesis method [31, 33]. Our results of La-doped TiO<sub>2</sub> phase formation are in good agreement with those reported by other authors [31, 33].

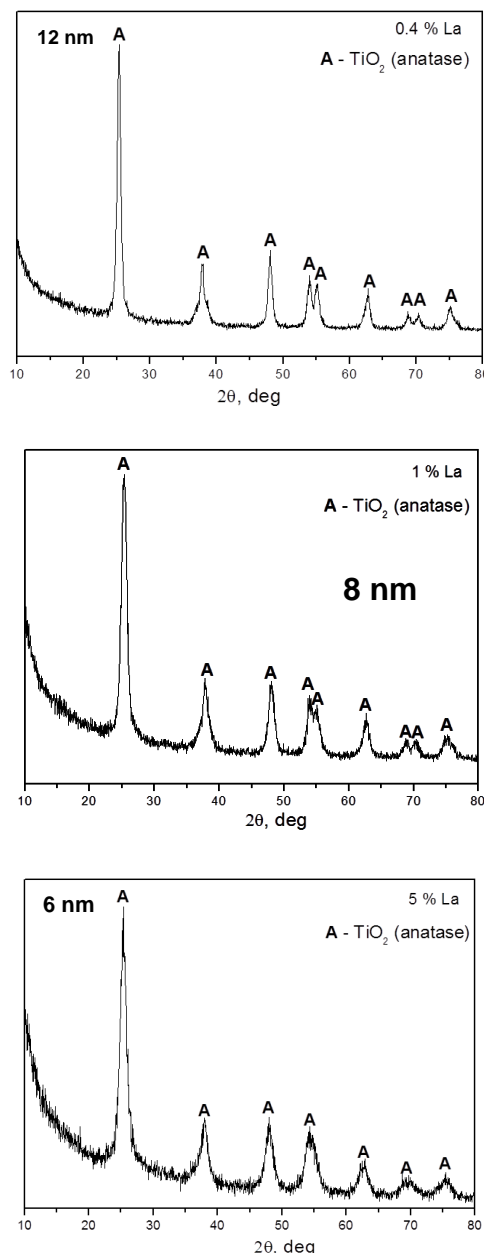
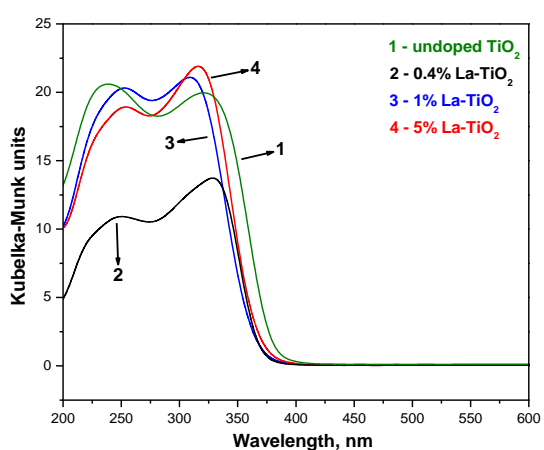
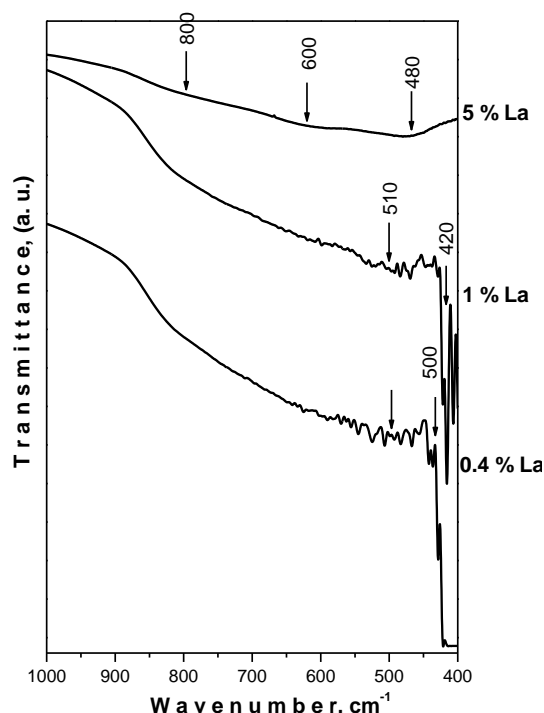


Fig. 2. XRD patterns of La-doped TiO<sub>2</sub>.

The La-TiO<sub>2</sub> powders were investigated by means of IR spectroscopy in the range of 1000–400 cm<sup>-1</sup> (Fig. 3a) where stretching vibrations of the inorganic building units are active. Generally, bands in the range of 600–400 cm<sup>-1</sup> were observed that could be related to vibrations of TiO<sub>6</sub> building units

[23, 34]. No band shifts were observed upon increasing La content.



**Fig. 3.** (a) IR and (b) UV-Vis spectra of La-doped TiO<sub>2</sub>.

UV-Vis diffuse reflectance spectra of La-modified and non-modified TiO<sub>2</sub> samples are shown

in figure 3b. Registered absorption edges and calculated band gap values are given in Table 2. The observed absorption edge of the as-prepared samples varies in the region of 364–369 nm. The UV-Vis spectra of the La-doped TiO<sub>2</sub> samples display a shift of the absorption edge (~20 nm) in comparison with that of undoped TiO<sub>2</sub>. According to Wang et al. [31] the blue shift is attributed to a quantum size effect. Evidently, the La<sup>3+</sup> dopant did not cause any spectral changes. Our blue shifting results of the absorption edge are consistent with reference data [31].

#### Photocatalytic activity

A photocatalytic bleaching effect on the examined dyes was observed during all experiments with synthesized titania samples showing thereby that all these samples have exhibited some photoactivity. The photolysis of both dyes could be neglected, as after 180 min illumination in blank experiments less than 6% and 4% were removed under UV and Vis irradiation, respectively.

The photocatalytic performance varied with dopant content, type of irradiation, and type of model contaminant. Addition of small amounts of La (0.4 and 1 mol.%) to titania was favourable for the photocatalytic activity under UV irradiation, while doping with 5 mol.% La led to a slower decolouration irrespective of used dye (Figs. 4 and 5). Doping with 0.4 and 1 mol.% La improved the photoactivity under visible light illumination toward RhB (Fig. 4) and did not change it toward MG (Fig. 5).

According to many works [35–40], the photocatalytic degradation rate can be described by assuming a pseudo-first order kinetic model (Eq. 2):

$$\ln C_0/C = kt, \quad (2)$$

where  $C_0$  is the initial concentration and  $C$  is the concentration at any time,  $t$ . Semi-logarithmic plots of the concentration data gave straight lines and yielding rate constants from their slopes (Table 2).

**Table 2.** Rate constants ( $k$ ) and decolouration efficiency (DE at 120 min) for dye photodestruction in presence of pure and La-doped TiO<sub>2</sub>

Catalyst sample	UV illumination				Vis illumination			
	RhB		MG		RhB		MG	
	$k \times 10^2 \text{ min}^{-1}$	DE, %	$k \times 10^2 \text{ min}^{-1}$	DE, %	$k \times 10^2 \text{ min}^{-1}$	DE, %	$k \times 10^2 \text{ min}^{-1}$	DE, %
TiO <sub>2</sub>	1.70	86	1.77	88	0.58	50	0.50	46
0.4La/TiO <sub>2</sub>	2.10	76	2.49	95	1.05	69	0.32	31
1La/TiO <sub>2</sub>	3.17	97	1.78	90	1.01	71	0.13	13
5La/TiO <sub>2</sub>	2.10	93	0.86	65	0.54	47	0.01	3

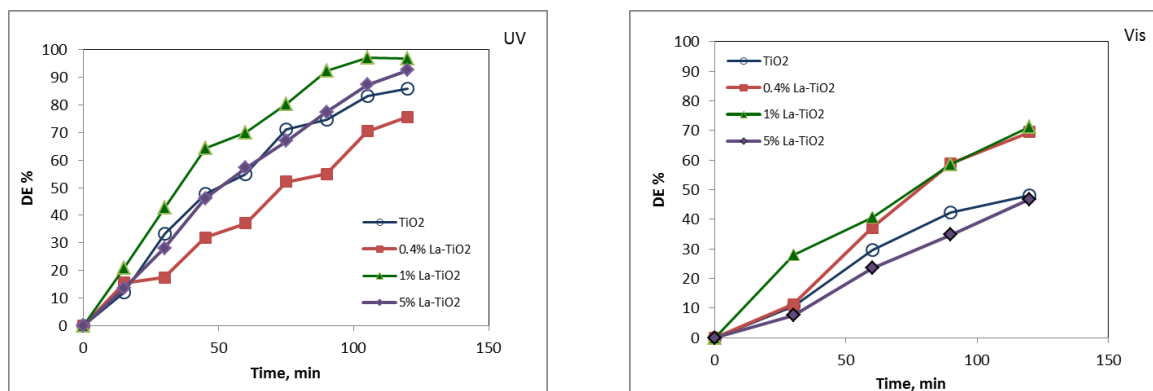


Fig. 4. Photocatalytic activity of La-modified samples against RhB under UV and Vis irradiation.

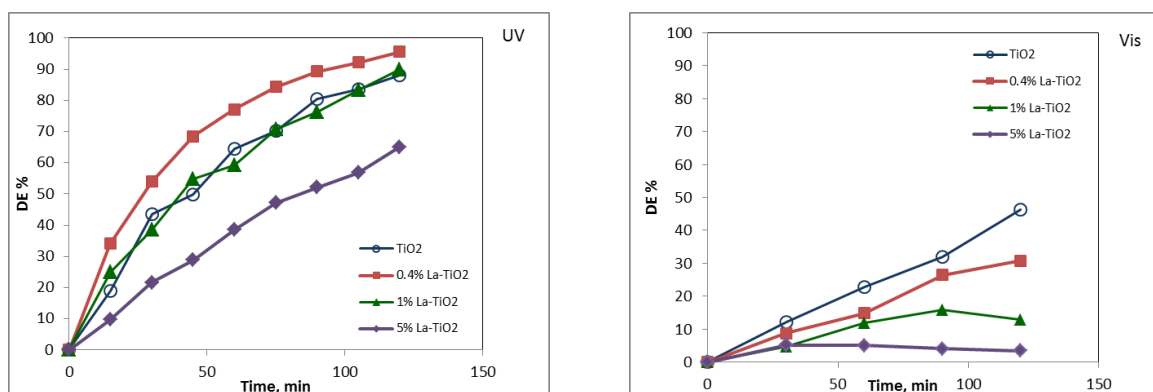


Fig. 5. Photocatalytic activity of La-modified samples against MG under UV and Vis irradiation.

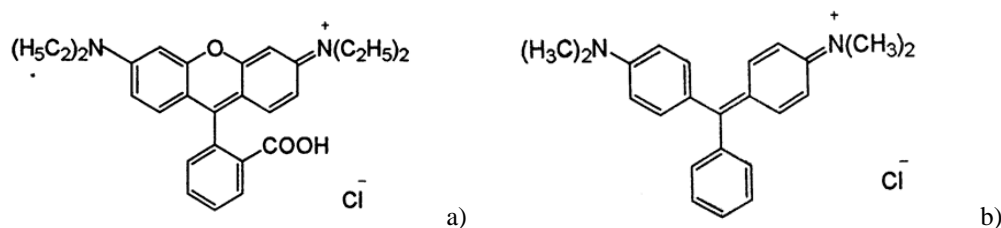


Fig. 6. Structure of model pollutants: a) Rhodamine B, b) Malachite Green

Our results confirm that the amount of dopant plays a significant role in affecting photo-degradation activity and an optimal concentration of dopant should be determined. Titania samples, modified with small amounts of La, exhibited good photocatalytic efficiency probably due to the effect of dopant ions as electron and hole trappers, which leads to suppression of electron-hole recombination and thus stimulating photocatalytic activity. However, surplus doped ions could serve as recombination sites by promoting charge-carrier recombination and doping can become detrimental [9]. Obviously, applying a non-hydrolytic sol-gel procedure and calcination temperature in the present study ensures an optimum doping amount within 0.4–1.0 mol.%, which agrees very well with that reported in the literature [41, 42]. According to some authors, the presence of La ions in the titania can

affect the photocatalytic activity by creating oxygen vacancies and separating charge carriers [43].

In this study, photocatalytic process efficiency was determined not only by the type of titania catalyst and type of irradiation, but also by the chemical structure of the dyes. As can be seen in Figs. 4 and 5 and Table 2, RhB bleaching was faster than that of MG. This can be explained by the structure of the organic pollutants: RhB contains a heterocyclic ring, which is more vulnerable to splitting (Fig. 6).

## CONCLUSIONS

Pure and doped titania nanopowders (6–12 nm) with different amount of La were synthesized by a non-hydrolytic sol-gel route. According to XRD patterns, mainly titania (anatase) was crystallized.

Particle sizes decreased on increasing lanthanum content. Addition of small amounts of La (0.4–1 mol.%) to titania was favourable for the photocatalytic activity under UV irradiation, while doping with 5 mol.% La led to a slower decolouration irrespective of used dye. Doping with 0.4 and 1 mol.% La improved the photoactivity under visible light illumination toward RhB and did not change it toward MG.

*Acknowledgement: The authors are grateful to the Medical University in Pleven for financial support through Contract No7/2015.*

## REFERENCES

1. S. Anandan, Y. Ikuma, V. Murugesan, *Int. J. Photoenergy*, **2012**, 1 (2012).
2. H. Liu, L. Yu, W. Chen, Y. Li, *J. Nanomater.*, **2012**, Article ID 235879, 1 (2012).
3. K. M. Parida, N. Sahu, *J. Mol. Catal. A-Chem.*, **287**, 151 (2008).
4. C.-H. Liang, F.-B. Li, C.-S. Liu, J.-L. Lü, X.-G. Wang, *Dye. Pigment.*, **76**, 477 (2008).
5. A. W. Xu, Y. Gao, H. Q. Liu, *J. Catal.*, **207**, 151 (2002).
6. S. Bingham, W. Daoud, *J. Mater. Chem.*, **21**, 2041 (2011).
7. J. Reszczynska, A. Iwulska, G. Sliwinski, A. Zaleska, *Physicochem. Probl. Miner. Proc.*, **48**, 201 (2012).
8. M. S. Hassan, T. Amna, O.-B. Yang, H.-C. Kim, M.-S. Khil, *Ceram. Int.*, **38**, 5925 (2012).
9. A. S. Weber, A. M. Grady, R. T. Koodali, *Catal. Sci. Technol.*, **2**, 683 (2012).
10. J. Cho, S. Schaab, J. A. Roether, A. R. Boccaccini, *J. Nanopart. Res.*, **10**, 99 (2008).
11. A. Podhorodecki, G. Zatoryb, J. Misiewicz, J. Domaradzki, D. Kaczmarek, A. Borkowska, *J. Electrochem. Soc.*, **156**, H214 (2009).
12. Y. Zhao, C. Li, X. Liu, F. Gu, H. L. Du, L. Shi, *Mater. Chem. Phys.*, **107**, 344 (2008).
13. H. Liu, L. Yu, W. Chen, Y. Li, *J. Nanomater.*, **2012**, 1 (2012).
14. B. Liu, X. Zhao, L. Wen, *Mater. Sci. Eng. B*, **134**, 27 (2006).
15. U. G. Akpan, B. H. Hameed, *Appl. Catal. A-Gen.*, **375**, 1 (2010).
16. M. Niederberger, N. Pinna, *Metal Oxide Nanoparticles in Organic Solvents*, Springer, (2009).
17. D. P. Debecker, P.H. Mutin, *Chem. Soc. Rev.*, **41**, 3624 (2012).
18. M. Stoyanova, M. Sredkova, A. Bachvarova-Nedelcheva, R. Iordanova, Y. Dimitriev, H. Hitkova, Tz. Iliev, *Optoel. Adv. Mater.-RC*, **4**, 2059 (2010).
19. H. Hitkova, A. Stoyanova, N. Ivanova, M. Sredkova, V. Popova, R. Iordanova, A. Bachvarova-Nedelcheva, *J. Optoel. Biomed. Mater.*, **4**, 9 (2012).
20. A. Bachvarova-Nedelcheva, R. Iordanova, A. Stoyanova, R. Gegova, Y. Dimitriev, A. Loukanov, *Centr. Eur. J. Chem.*, **11**, 364 (2013).
21. A. Shalaby, A. Bachvarova-Nedelcheva, R. Iordanova, Y. Dimitriev, A. Stoyanova, H. Hitkova, N. Ivanova, M. Sredkova, *J. Optoel. Adv. Mater.*, **17**, 248 (2015).
22. A. Stoyanova, H. Hitkova, N. Ivanova, A. Bachvarova-Nedelcheva, R. Iordanova, M. Sredkova, *Bulg. Chem. Commun.*, **45**, 497 (2013).
23. A. Stoyanova, H. Hitkova, A. Bachvarova-Nedelcheva, R. Iordanova, N. Ivanova, M. Sredkova, *J. Chem. Technol. Metallurg.*, **48**, 154 (2013).
24. A. Bachvarova-Nedelcheva, R. Gegova, R. Iordanova, A. Stoyanova, Y. Dimitriev, N. Ivanova, *Nanosci. Nanotechnol.*, **13**, 56 (2013).
25. A. Stoyanova, N. Ivanova, R. Iordanova, A. Bachvarova-Nedelcheva, *Nanosci. Nanotechnol.*, **13**, 166 (2013).
26. M. Niederberger, M. H. Bartl, G. D. Stucky, *Chem. Mater.*, **14**, 4364 (2002).
27. J. Dharma, A. Pisal, Perkin Elmer, Inc, Application note.
28. N. Barka, S. Qourzal, A. Assabbane, A. Nounah, Y. Ait-Ichou, *J. Photochem. Photobiol. A-Chem.*, **195**, 346 (2008).
29. X. Shi, X. Yang, S. Wang, S. Wang, Q. Zhang, Y. Wang, *J. Wuhan Univ. Techn.-Mater. Sci. Ed.*, **26**, 600 (2011).
30. S. Srivastava, R. Sinha, D. Roy, *Aquat. Toxicol.*, **66**, 319 (2004).
31. Q. Wang, S. Xu, F. Shen, *Optoel. Adv. Mater.-RC*, **5**, 128 (2011).
32. A. Stoyanova, N. Ivanova, A. Bachvarova-Nedelcheva, R. Iordanova, *Bulg. Chem. Commun.*, **47**, 330 (2015).
33. X. Zhang, G. Zhou, H. Zhang, C. Wu, H. Song, *Transit. Metal Chem.*, **36**, 217 (2011).
34. A. N. Murashkevich, A. S. Lavitskaya, T. I. Barannikova, I. M. Zharskii, *J. Appl. Spectrosc.*, **75**, 730 (2008).
35. U. I. Gaya, A. H. Abdullah, *J. Photochem. Photobiol. C-Photochem. Rev.*, **9**, 1 (2008).
36. O. Carp, C. L. Huisman, A. Reller, *Progr. Solid State Chem.*, **32**, 33 (2004).
37. K. Kabra, R. Chaudhary, R.L. Sawhney, *Ind. Eng. Chem. Res.*, **43**, 7683 (2004).
38. J. M. Herrmann, *Top. Catal.*, **34**, 49 (2005).
39. K. V. Kumar, K. Porkodi, F. Rocha, *Catal. Commun.*, **9**, 82 (2008).
40. M. N. Chong, B. Jin, C. W. K. Chow, C. Saint, *Water Res.*, **44**, 2997 (2010).
41. A.W. Xu, Y. Gao, H.Q. Liu, *J. Catal.*, **207**, 151 (2002).
42. F. B. Li, X. Z. Li, M. F. Hou, *Appl. Catal. B-Environ.*, **48**, 185 (2004).
43. S. Yao, X. Jia, L. Jiao, C. Zhu, Z. Shi, *Indian J. Chem.*, **51A**, 1049 (2012).

# ФОТОКАТАЛИТИЧНО ОБЕЗЦВЕТЯВАНЕ НА ДВЕ ОРГАНИЧНИ БАГРИЛА КАТАЛИЗИРАНО ОТ НАНОРАЗМЕРЕН TiO<sub>2</sub> ДОТИРАН С ЛАНТАН

Анг. М. Стоянова<sup>1\*</sup>, Цв. К. Колева<sup>1</sup>, Алб. Д. Бъчварова-Неделчева<sup>2</sup>, Р. С. Йорданова<sup>2</sup>

<sup>1</sup> *Медицински университет, ул. „Климент Охридски“ 1, 5800 Плевен, България*

<sup>2</sup> *Институт по обща и неорганична химия, Българска академия на науките, ул., Акад. Г. Бончев“, бл. 11, 1113 София, България*

Постъпила на 12 септември 2015 г.; Преработена на 12 декември 2015

(Резюме)

Целта на настоящото изследване е да се синтезират и охарактеризират чист и дотирани с лантан TiO<sub>2</sub> образци и да се изследват фотокаталитичните им свойства. Дотирани и недотирани образци бяха получени чрез нехидролитичен зол-гел метод от титанов(IV) хлорид, бензилов алкохол и лантанов(III) нитрат, с последваща термична обработка. Съдържанието на лантан в образците варира от 0.4 до 5 мол.%. Структурата и морфологията на получените нанопрахове са охарактеризирани чрез РФА, ИЧ и УВ-видима спектроскопия. Относителният размер на частиците на чистия и дотирания TiO<sub>2</sub> е около 6–15 nm и доминиращата кристална фаза в получените образци е анатаз. Установено е, че размерът на частиците намалява с повишаване на съдържанието на лантан.

Фотокаталитичната активност на TiO<sub>2</sub> за разграждане на две органични багрила с различни хромофори – трифенилметановото багрило (Малахитово зелено) и ксантеновото багрило (Родамин Б) беше изследвана при облъчване с ултравиолетова и видима светлина. Добавянето на малко количество лантан (0.4 и 1 мол.%) благоприятства фотокаталитичната активност при облъчване с УВ, докато дотирането с 5 мол.% лантан води до по-бавно обезцветяване, независимо от вида на използваното багрило.

## A DFT study of CO adsorption and dissociation over $\gamma$ -Mo<sub>2</sub>N(111) plane

S. F. Zaman<sup>1,2</sup>

<sup>1</sup>Chemical and Materials Engineering Department, Faculty of Engineering, King Abdulaziz University, P.O. Box 80204, Jeddah 21589, Saudi Arabia

<sup>2</sup>SABIC Chair of Catalysis, Chemical and Materials Engineering Department, Faculty of Engineering, King Abdulaziz University, P.O. Box 80204, Jeddah 21589, Saudi Arabia

Received: 9 October 2015; Revised: 23 November 2015

A theoretical investigation of CO dissociation energy barrier over  $\gamma$ -Mo<sub>2</sub>N(111) plane has been performed using density functional theory. CO dissociation energy possesses a high activation barrier of 67.96 kcal.mol<sup>-1</sup> with an endothermic heat of reaction of 28.87 kcal.mol<sup>-1</sup>, starting with CO molecularly adsorbed on a 3-fold hollow fcc site with an adsorption energy of 35.98 kcal.mol<sup>-1</sup>. The activation barrier is little less, 53.03 kcal.mol<sup>-1</sup>, when CO is molecularly adsorbed on a 3-fold hollow hcp site with an adsorption energy of 34.34 kcal.mol<sup>-1</sup>. For both cases, the C-O bond dissociation process is kinetically unfavourable over the investigated surface. A pronounced electronic effect of ligand nitrogen (N) and underlying molybdenum (Mo) layer during bond formation at the surface was observed.

**Keywords:** CO adsorption,  $\gamma$ -Mo<sub>2</sub>N, activation energy, CO dissociation energy.

### INTRODUCTION

Density functional theory (DFT) is a quantum chemical computational technique, which solves Schrödinger equation to find the minimum energy state of a system comprising a small number of atoms. This computational tool has been successfully used in the field of heterogeneous catalysis, for example studies of catalyst surface electronic properties and adsorption energies of reactant and products, elementary surface reaction steps of potential surface reaction pathways, etc. [1]. In combination with results of catalyst characterization techniques and catalytic tests, theoretical studies at atomic or molecular scale may provide valuable information about intermediate surface compounds formed on catalyst surfaces and their participation in different steps of the reaction mechanism. This computational tool can be very useful in terms of catalyst screening prior to spending time in the research lab for a desired reaction. In addition, it will give valuable information on the electronic behaviour of the surface and performance of the existing catalyst.

Syngas (CO+H<sub>2</sub>) conversion to higher hydrocarbons (Fischer-Tropsch synthesis) and mixed alcohol synthesis is a well-established technology. Fischer-Tropsch synthesis (FTS) is been commercialized in several countries to produce middle distillate products, raw materials for various chemicals, and waxes which undergo further cracking to low carbon chain fuels [2]. Recently researchers are

looking into the conversion of syngas to higher alcohols (HAS), especially C<sub>2</sub> alcohols, which is another contemporary important research area for clean and alternative transportation fuel production and value added raw material for olefin synthesis. A considerable progress has been achieved in recent years in the development of more active, selective, and stable catalysts for these processes. Important characteristics of the reaction mechanism have been revealed. A dependence of technological parameters of FTS on physical and chemical catalyst properties has also been established [2]. Carbon monoxide is a key reagent in FTS and HAS processes. Numerous studies of the reaction mechanism have shown that the non-dissociative adsorption of CO on the catalyst surface is the first step of the reaction mechanism of both the FTS and HAS processes on supported metal catalysts.

Intensive research activities nowadays are devoted to search for new, highly active, and selective catalytic systems for FTS and HAS processes. An indispensable part of these efforts is studying of surface elementary steps of reaction mechanisms by theoretical methods. One of the key issues that should be revealed for each new catalyst system is information on the mechanism of CO participation in the reaction. Since the adsorption of carbon monoxide is the first step of its activation, it is very important to understand how CO predominantly is adsorbed on a catalyst active surface and what type of surface complexes are being formed.

Because dissociative CO adsorption is leading to formation of coke precursors and active oxygen, this

\* To whom all correspondence should be sent:  
E-mail: zfsharif@gmail.com; sfzaman@kau.edu.sa

reaction route should be depressed by selecting catalyst components, on which the CO is adsorbed non-dissociatively. As an effective criterion for such a discrimination, one can use the energy of CO dissociative adsorption on a particular component. Low energy dissociative adsorption would mean that this component is not a suitable catalyst for FTS and HAS processes. At the same time, the energy of CO adsorption can be used as a criterion of the CO hydrogenation ability of a particular metal [3]. Thus, one has to be capable to exclude such components beforehand by suggesting a suitable criterion.

Molybdenum-based catalysts possess a high hydrogenation ability and have been used by many authors as effective catalysts for FTS and HAS from syngas [4–6]. Addition of p orbital ligands to Mo reduces the CO adsorption energies following the sequence Mo > MoP >  $\gamma$ -MoC >  $\delta$ -MoN [7]. The energies of CO dissociative adsorption on MoS<sub>2</sub> and Mo<sub>2</sub>C have been reported earlier [8,9]. The K-MoS<sub>2</sub> system is a well-known catalyst able to produce ethanol from syngas with high selectivity up to 40% [10], whereas Mo<sub>2</sub>C shows a much lower ethanol selectivity [11].  $\gamma$ -Mo<sub>2</sub>N has been used for different reactions, i.e. CO oxidation, HDN, HDO, NH<sub>3</sub> decomposition, etc. and reported for its high activity [12–15], and, in this connection, it may possess some interesting characteristics for CO hydrogenation reactions.

In this study, we report adsorption and dissociation energies of CO over the  $\gamma$ -Mo<sub>2</sub>N(111) plane calculated by using DFT. We have set our focus on finding a preferable adsorption arrangement of CO<sub>ads</sub> and [C<sub>ad</sub>\*+O<sub>ad</sub>\*] and calculate the activation barrier of C-O bond dissociation on a  $\gamma$ -Mo<sub>2</sub>N(111) catalyst.

#### Calculation procedure

The DMol<sup>3</sup> module of Material Studio (version 6.0) from Accelrys Inc. (San Diego, CA, USA) was used to perform the DFT calculations. Accordingly, the electronic wave functions were expanded in numerical atomic basis sets defined on an atomic-centred spherical polar mesh. The double-numerical plus P-function (DNP) of all electron basis set, was used for all the calculations. The DNP basis set includes one numerical function for each occupied atomic orbital and a second set of functions for valence atomic orbitals, plus a polarization p-function on all atoms. Each basis function was restricted to a cut-off radius of 4.4 Å, allowing for efficient calculations without loss of accuracy. The Kohn-Sham equations [16] were solved by a self-consistent

field procedure using PW91 functional with GGA for exchange correlation [17–19]. The techniques of direct inversion in an iterative subspace with a size value of six and thermal smearing of 0.005 Ha were applied to accelerate convergence. Optimization convergence thresholds for energy change, maximum force, and maximum displacement between the optimization cycles were set at 0.00002 Ha, 0.004 Ha/Å, and 0.005 Å, respectively. The k-point set of (1×1×1) was used for all calculations, which help to reduce the computation cost of this large slab/cluster arrangement. The activation energy of interaction between two surface species was identified by complete linear synchronous transit and quadratic synchronous transit search methods [20] followed by TS confirmation through the nudge elastic band method [21–23]. Spin polarization was imposed in all the calculations. The adsorption energy of an element (i.e. molecule or atom) was found according to the following formula:

$$E_{\text{ad}} = E_{\text{slab+element}} - \{E_{\text{empty slab}} + E_{\text{element}}\} .$$

#### Building unit cell structure of $\gamma$ -Mo<sub>2</sub>N crystal

$\gamma$ -Mo<sub>2</sub>N has a cubic B1 type crystal structure belonging to the Fm $\bar{3}$ m space group with lattice parameters a = b = c = 4.14613 Å. The unit cell of Mo<sub>2</sub>N crystal was built following the atomic coordinate position (x, y, z); Mo at (0, 0, 0) and N at (0.5, 0.5, 0.5) according to experimental finding of Bull *et al.* [24]. The studied (111) plane was then cleaved from the unit cell. Further, the cleaved plane was increased to five atomic layers and 4×4 supercell, comprised of total 57 atoms, as shown in Fig. 1. The periodic supercell was converted into a non-periodic cluster. A larger surface area was generated to provide favourable adsorption locations for CO, C, and O species. The  $\gamma$ -Mo<sub>2</sub>N(111) plane has mainly four different adsorption sites, an on-top site, a bridge-bonding site between two Mo atoms and two threefold sites, with an underneath N atom (in 1<sup>st</sup> sublayer), a 3-fold hollow hcp site with an underneath Mo atom (2<sup>nd</sup> sublayer), and a 3-fold hollow fcc site. The underneath N atom layer is located very close to the top Mo layer, only at a 0.736-Å depth while the distance to the next Mo sublayer from the top surface is 2.081 Å, which suggests a pronounced electronic influence/contribution of Mo and N atoms to the top Mo layer. The distance between two surface Mo atoms is 2.942 Å and the angle between the Mo atoms is 60°. The charge on indexed Mo and N atoms of  $\gamma$ -Mo<sub>2</sub>N(111) (Fig. 1) are tabulated in Table 1.

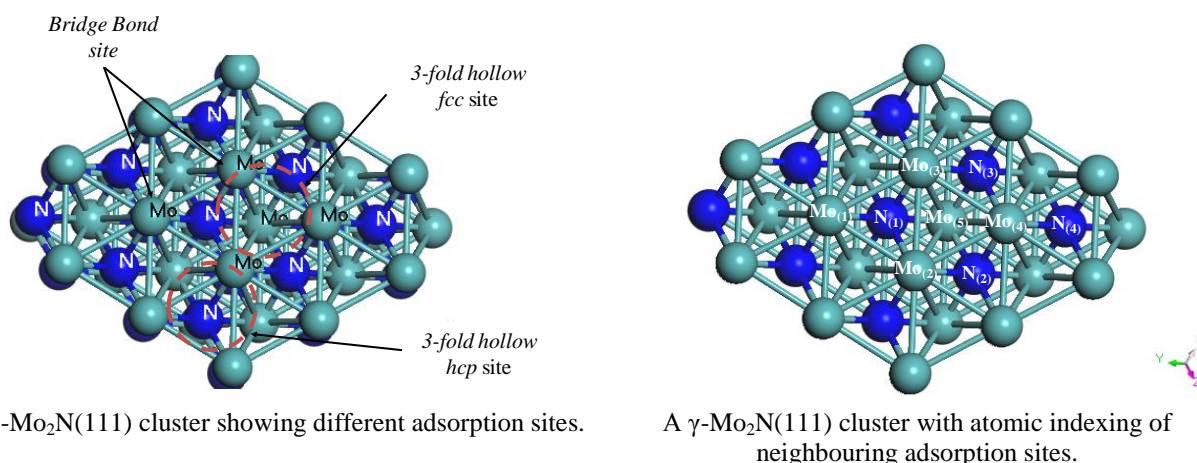
## RESULTS AND DISCUSSION

Adsorption and dissociation energies of CO over  $\gamma$ -Mo<sub>2</sub>N(111) plane

A DFT simulation was conducted for CO adsorption on four different adsorption locations over the  $\gamma$ -Mo<sub>2</sub>N(111) plane, i.e. on-top, bridge-bonding, 3-fold hollow fcc, and 3-fold hollow hcp sites. Adsorption locations are depicted in Fig. 1 and adsorption arrangements and atomic distances from the surface plane are displayed in Table 2. Stable CO adsorption was found for all the above-mentioned arrangements. Carbon monoxide was molecularly adsorbed vertically having the ‘C’ end towards the surface for all the cases, which is common for non-dissociative CO chemisorption on most of the metal

surfaces because the available electron donation orbital ( $5\sigma$ ) is located on the carbon atom of the CO molecule, as explained by Blyholder [25]. Different adsorption arrangements of the CO molecule are explained below.

CO was adsorbed on a Mo<sub>(4)</sub> surface atom as on-top configuration. The obtained energy value of CO adsorption on the  $\gamma$ -Mo<sub>2</sub>N(111) plane as on-top arrangement was  $-30.87 \text{ kcal.mol}^{-1}$  or  $-1.34 \text{ eV}$ . The C-O bond length of non-dissociatively adsorbed CO was found to be equal to  $1.185 \text{ \AA}$ . This length is greater than the molecular CO bond length of  $1.14 \text{ \AA}$ . Therefore, CO adsorption on a  $\gamma$ -Mo<sub>2</sub>N(111) slab makes the C-O bond relaxed. The vibrational frequency of CO on the  $\gamma$ -Mo<sub>2</sub>N(111) plane was found to be  $2663.06 \text{ cm}^{-1}$ .

Fig. 1.  $\gamma$ -Mo<sub>2</sub>N(111) cluster top view.Table 1. Atomic charge distribution over  $\gamma$ -Mo<sub>2</sub>N(111) with adsorbed species.

Atomic index*	Mulliken atomic charge, $e$									
	empty Mo <sub>2</sub> N slab	on-top CO adsorption	bridge CO adsorption	CO adsorption on hcp site	CO adsorption on fcc site	carbon adsorption on fcc site	carbon adsorption on hcp site	oxygen adsorption on fcc site	oxygen adsorption on hcp site	carbon on fcc and oxygen on hcp site
Mo <sub>(1)</sub>	0.561	0.563	0.623	0.633	0.567	0.579	0.666	0.563	0.737	0.772
Mo <sub>(2)</sub>	0.545	0.569	0.584	0.609	0.633	0.676	0.642	0.751	0.711	0.849
Mo <sub>(3)</sub>	0.545	0.573	0.586	0.609	0.633	0.677	0.614	0.751	0.711	0.668
Mo <sub>(4)</sub>	0.496	0.457	0.572	0.508	0.581	0.626	0.524	0.701	0.500	0.632
Mo <sub>(5)</sub>	0.951	0.948	0.948	0.949	0.941	0.941	0.949	0.941	0.951	0.937
N <sub>(1)</sub>	-1.158	-1.158	-1.141	-1.126	-1.154	-1.15	-1.101	-1.155	-1.127	-1.149
N <sub>(2)</sub>	-1.183	-1.187	-1.182	-1.182	-1.183	-1.186	-1.182	-1.193	-1.181	-1.186
N <sub>(3)</sub>	-1.168	-1.168	-1.166	-1.169	-1.163	-1.158	-1.171	-1.165	-1.167	-1.157
N <sub>(4)</sub>	-1.168	-1.17	-1.166	-1.169	-1.163	-1.159	-1.171	-1.165	-1.167	-1.169
C	0.105	0.068	-0.035	-0.089	-0.083	-0.420	-0.403	x	x	-0.575
O	-0.105	-0.186	-0.183	-0.180	-0.180	x	x	-0.595	-0.566	-0.411

\* Atomic indices are according to Fig. 1

For a bridge-bonding configuration of CO, a simulation procedure was performed by binding CO to Mo<sub>(2)</sub> and Mo<sub>(3)</sub> surface atoms, where the carbon atom was bonded to two Mo atoms and the O atom remained on-top of the C atom as a linear arrangement. The adsorption energy of CO on a bridge-bonding site on the  $\gamma$ -Mo<sub>2</sub>N(111) plane was  $-33.22$  kcal.mol<sup>-1</sup> or  $-1.44$  eV. The C-O bond length of non-dissociatively adsorbed CO was found to be equal to  $1.209$  Å, i.e. more relaxed compared to the on-top adsorption configuration. The vibrational frequency of CO for bridged adsorption was found to be  $1769.07$  cm<sup>-1</sup>. For a 3-fold hollow hcp adsorbed configuration of CO, a simulation procedure was performed through bonding the CO to Mo<sub>(1)</sub>, Mo<sub>(2)</sub>, and Mo<sub>(3)</sub> surface atoms with an underneath N<sub>(1)</sub> atom, where the carbon atom was bonded to three Mo atoms and O remained on-top of the C atom as a linear arrangement. CO adsorption on a 3-fold hollow hcp site on the  $\gamma$ -Mo<sub>2</sub>N(111) plane gave an energy value of  $-34.34$  kcal.mol<sup>-1</sup> or  $-1.49$  eV. The C-O bond length of non-dissociatively adsorbed CO was found to be equal to  $1.217$  Å, which is more relaxed compared to the on-top and bridging configurations. The vibrational frequency of CO for this adsorption arrangement was found to be  $2194.47$  cm<sup>-1</sup>. Another simulation was performed for CO adsorption on a 3-fold hollow fcc site by bonding CO to Mo<sub>(2)</sub>, Mo<sub>(3)</sub>, and Mo<sub>(4)</sub> surface atoms with an underneath Mo<sub>(5)</sub> atom, where the carbon atom was bonded to three Mo atoms and O remained on-top of the C atom as a linear species. The energy value of CO adsorption on a 3-fold hollow fcc position on the  $\gamma$ -Mo<sub>2</sub>N(111) plane was  $-35.98$  kcal.mol<sup>-1</sup> or  $-1.56$  eV. The C-O bond length of non-dissociatively adsorbed CO was found to be equal to  $1.217$  Å, which is more relaxed compared to the on-top and bridging configurations but similar to the 3-fold hollow hcp site. The vibrational frequency of CO for this arrangement was found to be  $1844.45$  cm<sup>-1</sup>.

Among all adsorption modes, carbon monoxide was most strongly bonded at a 3-fold fcc position, which may be the preferred adsorption arrangement for CO on the  $\gamma$ -Mo<sub>2</sub>N(111) plane. Yang *et al.* [26] studied the vibrational frequency of CO on a fresh Mo<sub>2</sub>N/Al<sub>2</sub>O<sub>3</sub> catalyst. They assigned infrared bands at  $2045$  and  $2200$  cm<sup>-1</sup> to CO adsorption onto 3-fold hollow hcp sites on the Mo<sub>2</sub>N catalyst. This study also found a very close CO vibrational frequency,  $2194.47$  cm<sup>-1</sup>, for a 3-fold hollow hcp adsorption arrangement but the adsorption energy was little less compared to the 3-fold hollow fcc configuration.

Molecular carbon monoxide adsorption values on the  $\gamma$ -Mo<sub>2</sub>N(111) plane have not been reported so

far in the literature. Flapper *et al.* [27] stated an adsorption energy of  $-1.49$  eV for CO adsorption on a 3-fold site of Mo<sub>2</sub>N(100) plane whereas Liu and Rodriguez [7] reported an adsorption energy value of  $-1.74$  eV for on-top CO on a  $\delta$ -MoN(001) plane.

#### *Electronic charge distribution over the surface*

Electronic charge distribution (Mulliken charge) values are given in Table 1 for the indexed Mo and N atoms of  $\gamma$ -Mo<sub>2</sub>N(111), atom indices are shown in Fig. 1, and for adsorbed C and O atoms. For an on-top adsorbed CO molecule on a Mo<sub>(4)</sub> atom, calculated values of Mulliken atomic charges on C and O were  $+0.068e$  and  $-0.186e$ , respectively. Atomic charges on C and O atoms of a free CO molecule are  $+0.105e$  and  $-0.105e$ , respectively. Reduced charges on C and O atoms indicate that a process of electron back donation from surface molybdenum atoms is taking place. The back donation of electron to the adsorbed CO molecule increases the antibonding orbital population and hence making the C-O bond weaker. At the same time the Mo<sub>(4)</sub> atom, to which CO was bonded, had a decrease in charge from  $+0.496e$  to  $+0.457e$  whereas other close surrounding surface Mo<sub>(1,2,3)</sub> atoms experienced an increase in their positive charge. Charges on underneath Mo<sub>(5)</sub> and N<sub>(1,2,3,4)</sub> atoms did not change to a considerable extent, suggesting their less involvement in electron donation/bonding process. Charge distribution results suggest that the electrons are drawn from other nearby surface Mo atoms to the bonding Mo atom, i.e. Mo<sub>(4)</sub>, and are back donated to CO, which makes the CO bond relaxed and reactive.

For bridge-bonded carbon monoxide on Mo<sub>(2)</sub> and Mo<sub>(3)</sub>, the calculated values of Mulliken atomic charges of C and O were  $-0.035e$  and  $-0.183e$ , respectively, i.e. a decrease in charge value compared to on-top adsorption configuration. Charges on surface Mo<sub>(1,2,3,4)</sub> atoms were increased compared to the empty slab. The increase in charge was less for the Mo<sub>(2)</sub> and Mo<sub>(3)</sub> atoms and more for the Mo<sub>(1)</sub> and Mo<sub>(4)</sub> entities. Charges on the underneath Mo<sub>(5)</sub> and N<sub>(1,2,3,4)</sub> atoms were not changed to a considerable extent, suggesting less involvement in the electron donation/bonding process. Charge distribution results suggest that the electrons are drawn from other surface atoms to the bonding atoms, Mo<sub>(2)</sub> and Mo<sub>(3)</sub>, and are back donated to the carbon monoxide, which makes the CO bond more relaxed as indicated by the increase in C-O bond length.

For 3-fold hollow hcp adsorption of carbon monoxide on Mo<sub>(1)</sub>, Mo<sub>(2)</sub>, and Mo<sub>(3)</sub> atoms, calculated values of Mulliken atomic charges on C and O in the adsorbed CO molecule were  $-0.089e$  and  $-0.180e$ , which is a decrease in charge on the C and

O atoms compared to the bridge bonding configuration. Positive charges on the surface Mo<sub>(1,2,3,4)</sub> atoms were increased compared to the empty slab. The increase in charge was less for the Mo<sub>(4)</sub> atom compared to the Mo<sub>(1)</sub>, Mo<sub>(2)</sub>, and Mo<sub>(3)</sub> atoms to which the CO molecule was bonded. Interesting charge was decreased for the underneath N<sub>(1)</sub> atom from  $-1.158e$  to  $-1.126e$ , which signifies involvement of underneath N atom layer in charge donation and surface bonding process. Charges on underneath Mo<sub>(5)</sub> and N<sub>(2,3,4)</sub> atoms were not changed to a considerable extent, which implies less participation in electron donation/bonding process. Charge distribution results suggest that the electrons are drawn from surface Mo atoms and underneath N atom and back-donated to CO, which makes the CO bond more relaxed as indicated by an increase of the C-O bond length compared to on-top and bridge bonding configurations.

Calculated values of Mulliken atomic charges on C and O atoms of CO molecule adsorbed on a 3-fold hollow fcc site on Mo<sub>(2)</sub>, Mo<sub>(3)</sub>, and Mo<sub>(4)</sub> atoms were  $-0.083e$  and  $-0.180e$ , respectively. Compared to a 3-fold hcp site the charge on the C atom was reduced, while that on the O atom remained the same. Positive charges on surface Mo<sub>(1,2,3,4)</sub> atoms were increased compared to the empty slab. The increase in charge was less for the Mo<sub>(1)</sub> atom compared to the Mo<sub>(2)</sub>, Mo<sub>(3)</sub>, and Mo<sub>(4)</sub> atoms. Charges on underneath Mo<sub>(5)</sub> and N<sub>(1,2,3,4)</sub> atoms changed to a little extent; there was a decrease of positive charge for the Mo<sub>(5)</sub> atom and all the underneath N atoms underwent a decrease in negative charge that indicated their contribution to electron donation and bonding. Charge distribution results suggest that electrons are drawn from surface Mo atoms and underneath N and Mo atoms and are back donated to CO, which makes the CO bond more relaxed as indicated by an increase in CO bond length compared to on-top and bridge bonding sites.

#### *Preferred adsorption location for C and O atoms over $\gamma$ -Mo<sub>2</sub>N(111)*

Before calculating the dissociation energy barrier of CO, the preferred adsorption sites for atomic oxygen (O) and carbon (C) on the  $\gamma$ -Mo<sub>2</sub>N(111) surface were performed by adsorbing C and O atoms separately on the surface and then place them together on the surface, thus building the preferred (lowest energy) surface product configuration of [C<sub>ad</sub>+O<sub>ad</sub>]. Table 2 shows adsorption arrangement for product configuration. For both C and O atoms, the preferred adsorption location was 3-fold hollow fcc and

then 3-fold hollow hcp sites. On-top and bridge bonding adsorption configurations are not possible on  $\gamma$ -Mo<sub>2</sub>N(111).

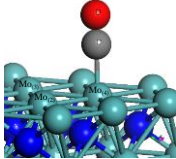
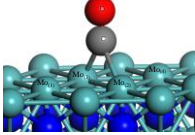
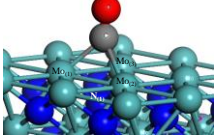
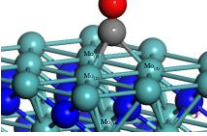
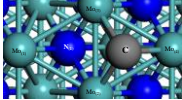
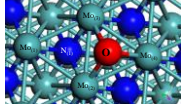
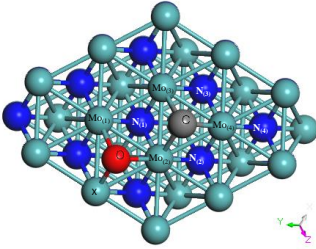
For a 3-fold hollow hcp adsorbed configuration of C atom, a simulation procedure was performed through bonding a C atom to Mo<sub>(1)</sub>, Mo<sub>(2)</sub>, and Mo<sub>(3)</sub> surface atoms with underneath N<sub>(1)</sub> atom. The obtained energy value of C atom adsorption on the  $\gamma$ -Mo<sub>2</sub>N(111) plane was  $-65.45$  kcal.mol<sup>-1</sup> or  $-2.83$  eV. Another simulation was carried out for bonding a C atom to Mo<sub>(2)</sub>, Mo<sub>(3)</sub>, and Mo<sub>(4)</sub> surface atoms with underneath Mo<sub>(5)</sub> atom on a 3-fold hollow fcc site. In this case the energy value of C atom adsorption on  $\gamma$ -Mo<sub>2</sub>N(111) was  $-65.96$  kcal.mol<sup>-1</sup> or  $-2.86$  eV. Therefore, a 3-fold hollow fcc site is more favourable for C atom adsorption than a 3-fold hollow hcp site. Similarly, for an O atom, a simulation was performed by bonding an O atom to Mo<sub>(1)</sub>, Mo<sub>(2)</sub>, and Mo<sub>(3)</sub> surface atoms with underneath N<sub>(1)</sub> atom for a 3-fold hollow hcp configuration. The found energy value of O atom adsorption on the  $\gamma$ -Mo<sub>2</sub>N(111) plane was  $-63.35$  kcal.mol<sup>-1</sup> or  $-2.74$  eV. Further, simulation of adsorbed O atom on a 3-fold hollow fcc site of Mo<sub>(2)</sub>, Mo<sub>(3)</sub>, and Mo<sub>(4)</sub> surface atoms with underneath Mo<sub>(5)</sub> atom was carried out. The adsorption value was  $-65.17$  kcal.mol<sup>-1</sup> or  $-2.82$  eV. Therefore, a 3-fold hollow fcc site is also a favourable adsorption site for O atom.

Simultaneous adsorption of C and O atoms on their preferred locations on the  $\gamma$ -Mo<sub>2</sub>N(111) plane, i.e. both a C atom and an O atom on a 3-fold hollow fcc site, was performed. The adsorption energy of atomic C and O over  $\gamma$ -Mo<sub>2</sub>N(111) was  $-2.77$  eV. The distance between the C and O species on the surface was  $3.11$  Å. Charge distribution showed that both the C and O atoms had a negative charge,  $-0.575e$  and  $-0.411e$ , respectively. It should be noted that non-bonded C and O have  $0e$  charges. Positive charges on all the surface Mo atoms and underneath Mo atoms were increased (a 3-fold hollow fcc site has an underneath Mo atom) and for the underneath N atoms charges were not changed much. Therefore, the main contribution to bonding came from charge donation from surface Mo atoms.

#### *Transition state search for CO dissociation*

A transition state search was performed between a CO molecule adsorbed on a 3-fold hollow fcc site and a product configuration [C<sub>ad</sub>+O<sub>ad</sub>] adsorbed on two different 3-fold hollow fcc sites. A complete Linear Synchronous Transit/Quadratic Synchronous Transit (LST/QST) search was accomplished with a root mean square (RMS) convergence of  $0.002$  Ha/Å.

Table 2. Adsorption energies and surface adsorption arrangement and atomic distances of C and O atoms and CO molecule on  $\gamma$ -Mo<sub>2</sub>N(111) plane.

Adsorbed entity	Adsorption arrangement	Pictorial description	Adsorption energy eV	Atomic distance Å
CO	on-top adsorption on a Mo surface atom		-1.34	$d_{C-O} = 1.185$ $d_{Mo-C} = 2.121$
CO	bridge site adsorption on two surface Mo atoms.		-1.44	$d_{C-O} = 1.209$ $d_{Mo2-C} = 2.29$ $d_{Mo3-C} = 2.29$
CO	3-fold hcp site adsorption on three Mo atoms (underneath N atom)		-1.49	$d_{C-O} = 1.217$ $d_{Mo1-C} = 2.349$ $d_{Mo2-C} = 2.370$ $d_{Mo3-C} = 2.377$
CO	3-fold fcc site adsorption on three Mo atoms (underneath Mo atom)		-1.56	$d_{C-O} = 1.217$ $d_{Mo2-C} = 2.375$ $d_{Mo3-C} = 2.372$ $d_{Mo4-C} = 2.340$
C atom	3-fold fcc site (underneath Mo atom)		-2.86	$d_{Mo2-C} = 2.212$ $d_{Mo3-C} = 2.214$ $d_{Mo4-C} = 2.196$
O atom	3-fold fcc site (underneath Mo atom)		-2.83	$d_{Mo2-O} = 2.212$ $d_{Mo3-O} = 2.214$ $d_{Mo4-O} = 2.196$
C and O atom	adsorption on two different 3-fold fcc sites (underneath Mo atom)		-2.77	$d_{C-O} = 3.119$ $d_{Mo2-C} = 2.225$ $d_{Mo3-C} = 2.204$ $d_{Mo4-C} = 2.160$ $d_{Mo1-O} = 2.195$ $d_{Mo1-O} = 2.223$ $d_{MoX-O} = 2.087$

Dissociation activation barrier was found to be 67.96 kcal.mol<sup>-1</sup> or 2.95 eV, while endothermic reaction energy was +28.87 kcal.mol<sup>-1</sup>. The activation barrier of CO dissociation was quite large compared to carbon monoxide molecular adsorption energy, -35.98 kcal.mol<sup>-1</sup> or -1.56 eV. So the DFT simulation suggests desorption of CO from the surface in molecular form rather than undergoing a CO dissociation step over the  $\gamma$ -Mo<sub>2</sub>N(111) plane. Fig. 2 depicts the transition state of CO dissociation reaction having the surface arrangement of CO at different NEB simulation points. C-O bond length was kept on increasing from 1.22 to 2.09 Å. A transition state

search was also performed for a CO molecule adsorbed on a 3-fold hollow hcp site and [C<sub>ad</sub>+O<sub>ad</sub>] adsorbed on two different neighbouring 3-fold hollow fcc sites. The activation energy was little less compared to CO adsorbed on a 3-fold hollow fcc site as depicted in Fig. 3. Dissociation activation barrier was found 53.03 kcal.mol<sup>-1</sup> or 2.30 eV whereas endothermic reaction energy was +27.13 kcal.mol<sup>-1</sup>. The activation barrier for CO dissociation was still higher than the molecular CO adsorption energy suggesting the same conclusion that CO would prefer to desorb from the surface rather than undergo dissociation, as for the previous one.

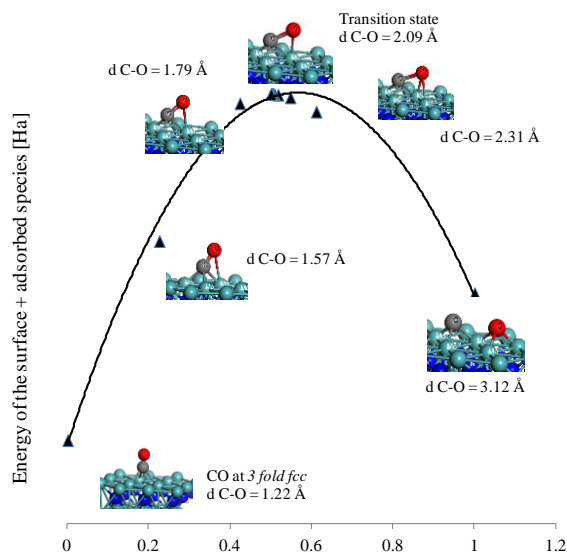


Fig. 2. Transition state search by NEB method for CO dissociation over  $\gamma$ -Mo<sub>2</sub>N(111) for CO adsorbed on a 3-fold fcc location.

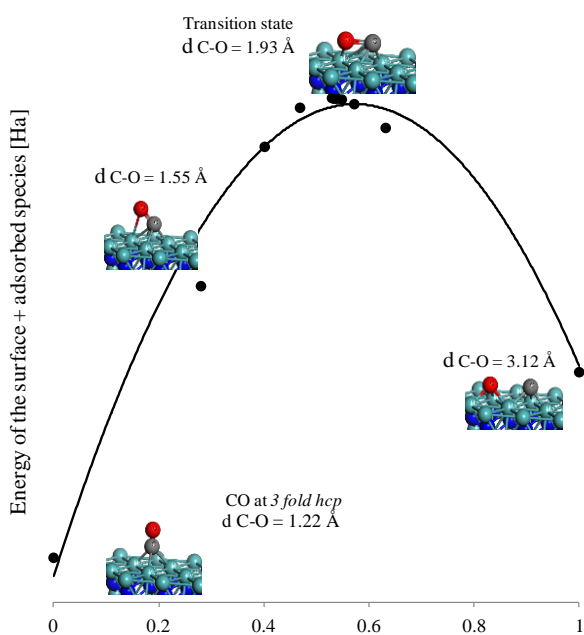


Fig. 3. Transition state search by NEB method for CO dissociation over  $\gamma$ -Mo<sub>2</sub>N(111) for CO adsorbed on a 3-fold hcp location.

Table 3 presents CO dissociation barrier and reaction energies on different molybdenum-based catalysts. Among reported catalysts, the activation barrier varies from low to high values in the following order: Mo<sub>2</sub>C < MoS<sub>2</sub> ≤ Mo<sub>2</sub>N < MoP. Close CO dissociation barrier values for MoS<sub>2</sub> and Mo<sub>2</sub>N suggest similar surface reaction features for CO hydrogenation over these two catalysts.

Table 3. CO dissociation energies for Mo-based catalysts.

Mo surface	Reaction energy, $\Delta E_r$ , kcal.mol <sup>-1</sup>	Activation energy, $\Delta E_a$ , kcal.mol <sup>-1</sup>	Ref.
$\beta$ -Mo <sub>2</sub> C(0001) Mo terminated	-21.91	20.52	[28]
$\beta$ -Mo <sub>2</sub> C(0001) C terminated	-5.99	44.28	[28]
CO <sub>ad</sub> → [C <sub>ad</sub> +O <sub>ad</sub> ] MoS <sub>2</sub> (10 $\bar{1}$ 0) Mo edge	-3.23	59.96	[29]
MoP(100)	62.49	87.17	[30]
MoP(001)	-42.20	92.01	[31]
$\gamma$ -Mo <sub>2</sub> N(111)	28.83	67.96	this work

## CONCLUSIONS

Density functional theory (DFT) was employed to investigate carbon monoxide dissociation energy over  $\gamma$ -Mo<sub>2</sub>N(111) surface. Non-dissociative adsorption of CO on a 3-fold hollow fcc site was favoured on the surface with an adsorption energy of -35.98 kcal.mol<sup>-1</sup>, while the adsorption energy for a 3-fold hollow hcp position was 34.34 kcal.mol<sup>-1</sup>. Both the C and O atoms prefer a 3-fold hollow fcc bonding location. The dissociation activation energy barrier for CO adsorbed on a 3-fold hollow fcc position was 67.96 kcal.mol<sup>-1</sup> while that for CO adsorbed on a 3-fold hollow hcp site was 53.03 kcal.mol<sup>-1</sup>. Hence, the carbon monoxide molecule would prefer to desorb from the  $\gamma$ -Mo<sub>2</sub>N(111) surface rather than undergo dissociative adsorption.

*Acknowledgement:* This work was supported by the Deanship of Scientific Research (DSR), King Abdulaziz University, Jeddah, under grant No. (135-1013-D1435). The authors gratefully acknowledge the DSR technical and financial support.

## REFERENCE

1. J. K. Nørskov, A. P. Frank, S. Felix, T. Bligaard (2010), PNAS early edition, [www.pnas.org/cgi/doi/10.1073/pnas.1006652108](http://www.pnas.org/cgi/doi/10.1073/pnas.1006652108) (2010).
2. S. A. Eliason, C. H. Bartholomew, *App. Catal. A-Gen.*, **186**, 229 (1999).
3. T. Bligaard, J. K. Nørskov, S. Dahl, J. Matthiesen, C. H. Christensen, J. Sehested, *J. Catal.*, **224**, 206 (2004).
4. W. Ma, E. L. Kugler, J. Wright, D. B. Dadyburjor, *Energy Fuels*, **20**, 2299 (2006).
5. A. G. Constant, J.-M. Giraudon, G. Leclercq, L. Leclercq, *App. Catal. A-Gen.*, **260**, 35 (2004).
6. S. F. Zaman, K. J. Smith, *App. Catal. A-Gen.*, **378**, 59 (2010).

- P. Liu, J. A. Rodriguez, *Catal. Lett.*, **91**, 247 (2003).
- M. Huang, K. Cho, *J. Phys. Chem. C*, **113**, 5238 (2009).
- X. R. Shi, J. Wang, K. Hermann, *J. Phys. Chem. C*, **114**, 13630 (2010).
- J. G. Santiesteban, C. E. Bogdan, R. G. Herman, K. Klier, *Proc. 9th Int. Congr. Catal.*, **2**, 561 (1998).
- M. Xiang, D. Li, H. Xiao, J. Zhang, H. Qi, W. Li, B. Zhong, Y. Sun, *Fuel*, **87**, 599 (2008).
- G. Xie, T. Bai, L. An, H. Wang, J. You, *Reac. Kinet. Catal. Lett.*, **65**, 331 (1998).
- C. Sepúlveda, K. Leiva, R. García, L. R. Radovic, I. T. Ghampson, W. J. DeSisto, J. L. García Fierro, N. Escalona, *Catal. Today*, **172**, 232 (2011).
- S. Podila, S. F. Zaman, H. Driss, Y. A. Alhamed, A. A. Al-Zahrani, L. A. Petrov, *Catal. Sci. Technol.* DOI: 10.1039/C5CY00871A (2015).
- S. Li, J. S. Lee, T. Hyeon, K. S. Suslick, *App. Catal. A-Gen.*, **184**, 1 (1999).
- W. Kohn, L. J. Sham, *Phys. Rev.*, **140**, 1133 (1965).
- J. P. Perdew, J. A. Chevary, S. H. Vosko, K. A. Jackson, M. R. Pederson, D. J. Singh, C. Fiolhais, *Phys. Rev. B*, **46**, 6671 (1992).
- A. D. Becke, *J. Chem. Phys.*, **88**, 2547 (1988).
- J. P. Perdew, Y. Wang, *Phys. Rev. B*, **45**, 13244 (1992).
- T. A. Halgren, W. N. Lipscomb, *Chem. Phys. Lett.*, **49**, 225(1997).
- S. Bell, J. S. Crighton, *J. Chem. Phys.*, **80**, 2464 (1983).
- S. Fischer, M. Karplus, *Chem. Phys. Lett.*, **194**, 252 (1992).
- G. Henkelman, H. Jónsson, *J. Chem. Phys.*, **113**, 9978 (2000).
- C. L. Bull, T. Kawashima, P. F. McMillan, D. Machon, O. Shebanova, D. Daisenberger, E. Soignard, E. T. Muromachi, L. C. Chapon, *J. Solid State Chem.*, **179**, 1762 (2006).
- G. Blyholder, *J. Phys. Chem.*, **68**, 2772 (1964).
- S. Yang, C. Li, J. Xu, Q. Xin, *Chem. Commun.*, 1247 (1997).
- G. Frapper, M. Pélissier, J. Hafner, *J. Phys. Chem. B*, **104**, 11972 (2000).
- X. Shi, J. Wang, K. Hermann, *J. Phys. Chem. C*, **114**, 13630 (2010).
- M. Huang, K. Cho, *J. Phys. Chem. C*, **113**, 5238 (2009).
- S. F. Zaman, M. Daous, L. Petrov, *C. R. Acad. Bulg. Sci.*, **66**, 1083 (2013).
- S. F. Zaman, M. Daous, L. Petrov, *C. R. Acad. Bulg. Sci.*, **67**, 1535 (2014).

## ИЗСЛЕДВАНЕ С ТФП НА АДСОРБЦИЯТА И ДИСОЦИАЦИЯТА НА СО ВЪРХУ $\gamma$ -Mo<sub>2</sub>N(111) КРИСТАЛНА РАВНИНА

Ш. Ф. Заман

Департамент по инженерна химия и материали, Факултет по инженерство, Университет Крал Абдулазис, п.к. 80204, Джеда 21589, Саудитска Арабия  
Катедра „Катализ“ на Саудитската основна индустриална корпорация, Департамент по инженерна химия и материали, Факултет по инженерство, Университет Крал Абдулазис, п.к. 80204, Джеда 21589, Саудитска Арабия

Постъпила на 9 октомври 2015 г.; Преработена на 23 ноември 2015 г.

(Резюме)

Проведено е теоретично изследване с теорията на функционала на плътността на енергетичната бариера на дисоциацията на въглероден оксид върху кристалната равнина  $\gamma$ -Mo<sub>2</sub>N(111). Дисоциацията на СО е ендотермична реакция с топлинен ефект 28.87 kcal.mol<sup>-1</sup> и висока енергетична бариера от 67.96 kcal.mol<sup>-1</sup>, започваща с молекулна адсорбция на СО на трицентрови места със стенно центрирана кубична плътна опаковка с енергия на адсорбция 35.98 kcal.mol<sup>-1</sup>. Енергетичната бариера е по-ниска, 53.03 kcal.mol<sup>-1</sup>, когато молекулната адсорбция на СО е върху трицентрови места с хексагонална плътна опаковка с енергия на адсорбция 34.34 kcal.mol<sup>-1</sup>. И в двата случая процесът на дисоциация на СО е кинетически ограничен. Наблюдава се съществен електронен ефект на азотния лиганд и на молибдена от лежащия отдолу слой при образуване на връзки в адсорбционния слой на повърхността.

## Thermochromism of a series of spiroindolinonaphthoxazines

S. Minkovska<sup>1\*</sup>, B. Jeliaskova<sup>2</sup>, S. Rakovsky<sup>1</sup>, T. Deligeorgiev<sup>2</sup>

<sup>1</sup> Institute of Catalysis, Bulgarian Academy of Sciences, Acad. G. Bonchev St., Bldg. 11, 1113 Sofia, Bulgaria

<sup>2</sup> Department of Chemistry and Pharmacy, Sofia University, 1 J. Bourchier Blvd., 1164 Sofia, Bulgaria

Received: October 7, 2015

Five spiroindolinonaphthoxazines, synthesized by the authors, bearing different substituents on the basic skeleton have been studied for their thermochromic properties in solvents of different polarity. The compounds were very polarizable, which led to equilibrium between their colourless closed and coloured open forms in the absence of light at temperatures of 20–60°C. The thermal equilibrium between the ground state populations of the colourless and coloured forms was influenced by solvent polarity as well as by the nature of substituents. The concentration of the open form increased with solvent polarity.

**Keywords:** spirooxazines, thermochromism, thermodynamics

### INTRODUCTION

Spiroindolinonaphthoxazines (SO) are among the most interesting functional dyes with potential application in many new technologies, such as data recording and storage, optical switching, displays, and nonlinear optics [1–15]. These compounds comprise two heterocyclic moieties linked by a tetrahedral spiro-carbon, which prevents them from being conjugated (Scheme 1). As a result, the spiro-compounds are almost colourless or pale yellow since the lowest electronic transition of the molecule occurs in the near UV region. Absorption of UV light gives rise to isomerisation caused by breakage of the spiro linkage C–O and subsequent rotation about the 2-2' C–C bond. The photoisomerized merocyanine (MC) dye molecules absorb in the visible part of the spectrum [1–7].

Irradiation strongly displaces the thermal equilibrium between both forms to the side of open-chain coloured photomerocyanine (MC), but it spontaneously converts to the colourless spiroform (SO) to reach a thermal equilibrium immediately after removing the light. We have recently reported [16–19] on the synthesis and photochromic and solvatochromic properties of a series of spiroindolinonaphthoxazines, both unsubstituted or bearing different substituents on the basic skeleton, and have estimated their metal ion coordination ability. On resuming our investigation of this series of compounds, in the present paper we describe a spectroscopic study of the effect of both solvent and structure on the thermochromic behaviour and equilibrium between SO and MC.

### EXPERIMENTAL

#### Materials

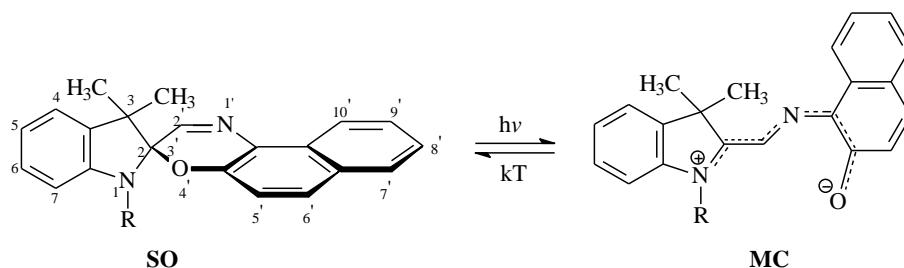
The molecules under study were five spiroindolinonaphthoxazines including four 5'-benzothiazolyl-substituted compounds: 1,3,3-trimethyl-5'-(2-benzothiazolyl)-spiro(indoline-2,3'-[3H]naphth[2,1-b][1,4]oxazine) (**1**); 1-butyl-3,3-dimethyl-5'-(2-benzothiazolyl)-spiro(indoline-2,3'-[3H]naphth[2,1-b][1,4]oxazine) (**2**); 1,3,3-trimethyl-5'-(2-benzothiazolyl)-spironaphth(indoline-2,3'-[3H]naphth[2,1-b][1,4]oxazine) (**3**), and 1-butyl-3,3-dimethyl-5'-(2-benzothiazolyl)-spironaphth(indoline-2,3'-[3H]naphth[2,1-b][1,4]oxazine) (**4**), and one 5'-hydroxy-substituted compound, 1,3,3-trimethyl-5'-hydroxyspiro(indoline-2,3'-[3H]naphth[2,1-b][1,4]oxazine) (**5**).

The compounds (Scheme 2) were prepared and characterized in our laboratory [16, 17]. Solvents were used after distillation.

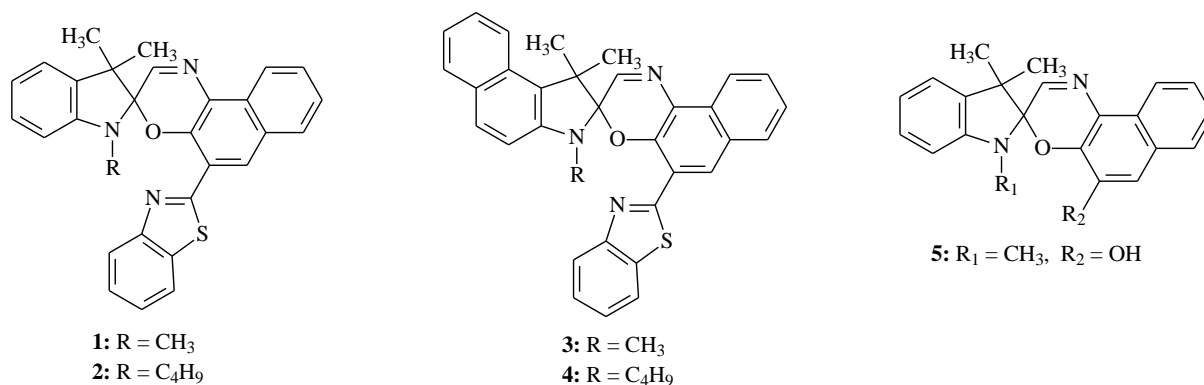
#### Instrumentation

Absorption spectra were taken on a Specord UV-Vis (Carl Zeiss, Jena) spectrophotometer using quartz cells. For absorption measurements at a varying temperature, the reaction cell was enclosed in a thermostatic water jacket placed inside spectrophotometer sample chamber. Spectral changes were recorded at a constant temperature and repeated use of the same solution at temperature intervals of *ca.* 5°C over a temperature range of about 30°C, and waiting for *ca.* 30 min after resetting the temperature control to allow the solution to attain a thermal equilibrium.

\* To whom all correspondence should be sent  
E-mail: stelasmin@ic.bas.bg



Scheme 1



Scheme 2

### Molar absorption coefficients

Spectral characteristics of merocyanines **1–4** in acetone are listed in Table 1. Molar absorption coefficients ( $\epsilon$ ) were calculated by the expression  $\epsilon = \text{colourability}/\Phi_c$  [10, 11] using own data on ‘colourability’ [17] and quantum yield values ( $\Phi_c$ ) of the colour-forming reaction in acetone [19].

**Table 1.** Quantum yield of photocolouration [19] and absorption characteristics of merocyanines 1–4 in acetone

Compound	$\Phi_c$ [18]	$\lambda_{\max}$ , nm [16]	Colourability [16]	$\epsilon$ , M <sup>-1</sup> .cm <sup>-1</sup> *
<b>1</b>	0.75	640	58900	78500
<b>2</b>	0.80	642	72500	90600
<b>3</b>	0.85	655	67600	79500
<b>4</b>	0.90	656	72800	80900

\*this paper

Provided the molar absorption coefficient of the **1–4** open forms is known, the absorbance in the visible region of the non-irradiated concentrated solutions was used in the present study to calculate the thermal equilibrium constant of the spirooxazine-merocyanine systems in acetone.

### Equilibrium constant values

Thermal equilibrium constant values were determined in acetone by measuring the visible absorbance of the open form in relation to its maximum absorption  $K_e = [\text{MC}]/[\text{SO}]$  (Table 1) where the spiroform does not absorb. The equilibrium concentra-

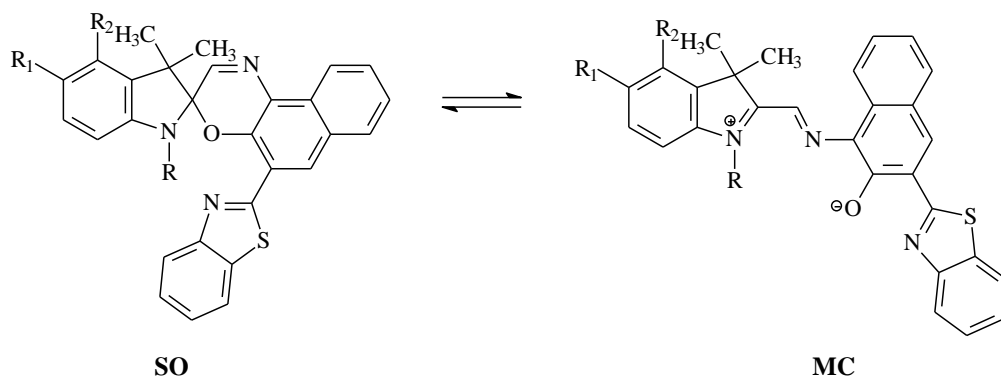
tion of the open form was derived from the equation  $[\text{MC}] = A/\epsilon \cdot b$  using the absorbance  $A$  of MC at  $\lambda_{\max}$  and the molar absorptivity given in Table 1 for  $b = 1$  cm. The equilibrium concentration of the closed spiroform was found by the expression  $[\text{SO}] = c_{\text{SO}} - [\text{MC}]$ , in which  $c_{\text{SO}}$  is the initial concentration of spirooxazine.

## RESULTS AND DISCUSSION

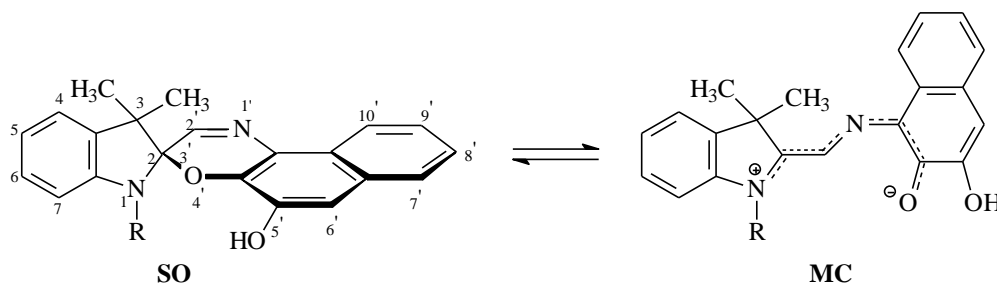
### Thermal equilibrium

We have reported [16–19] that spiroindolinonaphthoxazines **1–5** in polar solvents like acetone, ethanol, or acetonitrile are capable of transformation to their open MC forms in the dark. As a result, solutions of **1–5** ( $\sim 10^{-4}$  mol.dm<sup>-3</sup>) show a low intensity absorption band in the visible region at room temperature denoting that a thermal equilibrium  $\text{SO} \leftrightarrow \text{MC}$  between their open and closed forms given in Schemes 3 and 4 is established. It is affected by changes in solvent polarity at room temperature in the absence of light.

Equilibrium constants derived from the equation  $K_e = [\text{MC}]/[\text{SO}]$  at 25°C in acetone are reported in Table 2 compared with our recently published data [18] evaluated by using rate constants of the forward and back reaction ( $K_e = k_1/k_{-1}$ ). An agreement with the latter can be considered satisfactory since variations of  $K_e$  for the same molecule are within the experimental error.



Scheme 3



Scheme 4

**Table 2.** Equilibrium constants,  $K_e$ , of SO  $\leftrightarrow$  MC in acetone (25°C)

SO	$K_e = k_f/k_r (\times 10^2)$ [18]	$K_e = [\text{MC}]/[\text{SO}]$ ( $\times 10^2$ )*
<b>1</b>	1.69	1.67
<b>2</b>	1.91	1.94
<b>3</b>	4.66	4.60
<b>4</b>	6.04	6.02

\*this paper

The equilibrium constants presented in Table 2 increase on moving from **1** to **4** obviously due to suppression of the thermal ring closure reaction [17] when the benzene substituent in the indoline moiety of **1** and **2** is replaced by naphthalene in **3** and **4** and also when the N-imino  $\text{CH}_3$  group in **1** and **3** is replaced by  $\text{C}_4\text{H}_9$  in **2** and **4**. The combined effect of both substituents gives rise to a decreased rotational freedom upon cyclization yielding decreased  $k_r$  values, while the values of  $k_f$  remain unchanged [19].

### Thermochromism

Visible absorption intensity of **1–5**, observed in polar solvents, increases as the temperature raises (Figs. 1–4), i.e. these molecules exhibit thermochromic properties. For the parent unsubstituted spiroindolinonaphthoxazine (Scheme 1) the coloured band is hardly detectable, even in a saturated solution of polar solvent at 47°C, the absorbance at 600 nm being less than 0.005.

The enthalpy of reaction was evaluated according to the Van't Hoff equation,  $\text{dln}K_e/\text{d}(1/T) = -\Delta H^0/R$ , by measuring the absorbance of the coloured form at several temperatures. Determinations were carried out in the temperature range of 20–80°C, using sample concentrations within  $1 \times 10^{-4} \div 5 \times 10^{-3} \text{ mol}\cdot\text{dm}^{-3}$ . The accuracy can be assumed  $\pm 20\%$ .

Plots of  $\text{ln}K_e$  vs.  $1/T$  for **1–4** in acetone are shown in figure 5 and the obtained  $\Delta H^0$  values are reported in Table 3 along with  $\Delta G^0$  and  $\Delta S^0$  calculated by means of the thermodynamic relationship  $\Delta G^0 = \Delta H^0 - T\Delta S^0$ . Variations of  $\Delta H^0$  from **1** to **4** are within the experimental error.

The reaction entropy is negative, which indicates [7, 8] that the positive contribution to entropy due to increased torsional freedom in the open structure is strongly compensated by solvent reorganization around the more polar merocyanine form.

The constants of thermal equilibrium between SO and MC of compound **5** could not be calculated because the  $\epsilon$  value of its open form was not available and the same was valid about **1–4** in methanol, ethanol, *i*-propanol, *i*-butanol, and acetonitrile. In view of this we have calculated only the enthalpy changes  $\Delta H^0$  by using the expression  $\text{dln}K_e/\text{d}(1/T) = -\Delta H/R$  (Table 4). Plots of  $\text{ln}A$  vs.  $1/T$  are shown in figures 6–10.

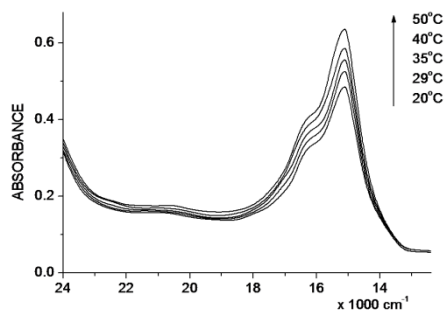


**Fig. 1.** Absorption spectra of  $1 \times 10^{-4}$  M acetone solution of compound **4**.

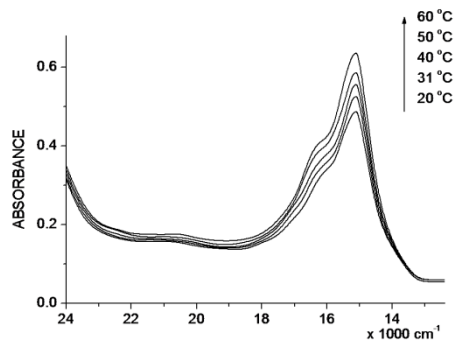


**Fig. 2.** Absorption spectra of  $2.5 \times 10^{-4}$  M methanol solution of compound **2**.

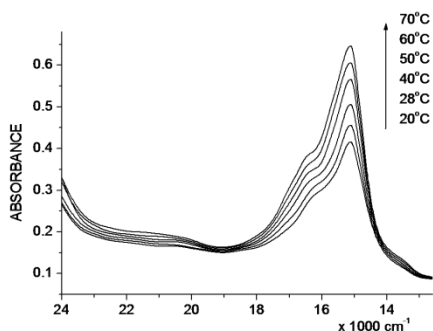


**Fig. 3.** Absorption spectra of  $1 \times 10^{-4}$  M ethanol solution of compound **4**.

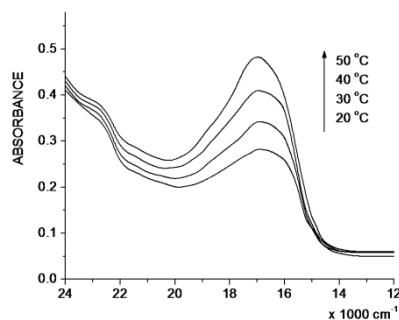


**Fig. 4.** Absorption spectra of  $2.5 \times 10^{-4}$  M *i*-butanol solution of compound **5**.

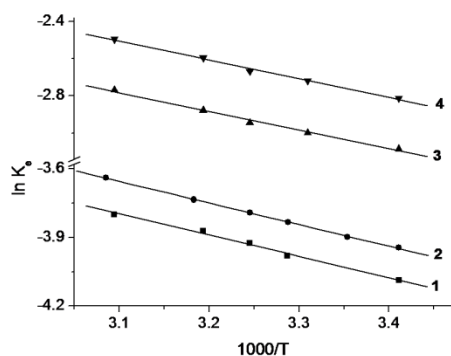


**Fig. 5.** Data ( $\ln K_e$ ) on thermal equilibrium treated according to the Van't Hoff equation in acetone solutions of compounds **1–4**.

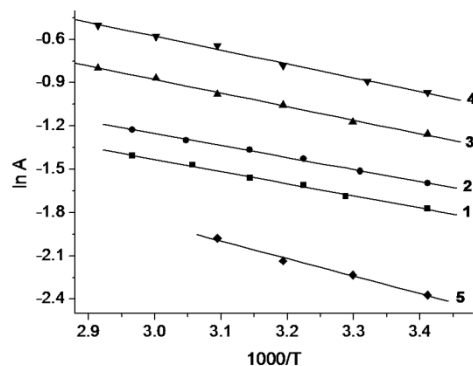


**Fig. 6.** Data ( $\ln A$ ) on thermal equilibrium treated according to the Van't Hoff equation in ethanol solutions of compounds **1–5**.

**Table 3.** Thermodynamic parameters of  $SO \leftrightarrow MC$  in acetone

SO	$\ln K_e$	$\Delta H^0$ kJ mol <sup>-1</sup>	$\Delta G^0$ kJ mol <sup>-1</sup>	$\Delta S^0$ kJ mol <sup>-1</sup>
<b>1</b>	-4.09	7.6	10.0	-34
<b>2</b>	-3.94	7.7	9.6	-33
<b>3</b>	-3.08	8.3	7.5	-26
<b>4</b>	-2.81	8.4	6.9	-23

**Table 4.** Calculated values of  $\Delta H^0$  [kJ mol<sup>-1</sup>] for **1–5** in different solvents for  $SO \leftrightarrow MC$  using the relationship  $d \ln A / d(1/T) = -\Delta H/R$

SO	$\Delta H^0$					
	aceto-nitrile	Acet-one	meth-anol	ethanol	<i>i</i> -pro-panol	<i>i</i> -buta-nol
<b>1</b>	6.7	7.6	6.7	6.6	6.7	5.8
<b>2</b>	6.5	7.7	6.8	6.5	6.7	5.8
<b>3</b>	7.6	8.3	7.8	7.7	8.9	6.5
<b>4</b>	7.9	8.4	8.3	7.8	8.8	6.4
<b>5</b>	11.4	10.4	9.8	11.6	8.2	13.6

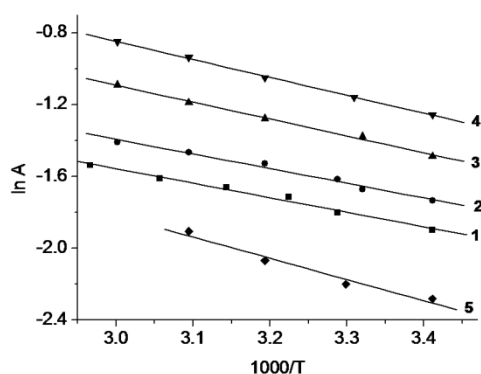


**Fig. 7.** Data ( $\ln A$ ) on thermal equilibrium treated according to the Van't Hoff equation in methanol solutions of compounds 1–5.

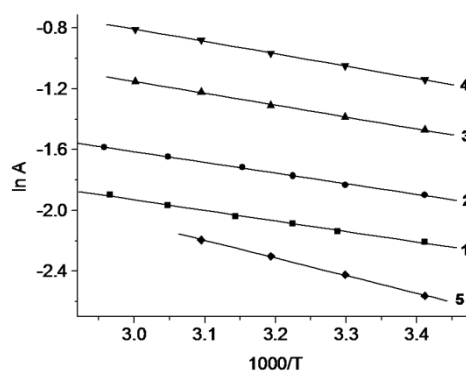


**Fig. 8.** Data ( $\ln A$ ) on thermal equilibrium treated according to the Van't Hoff equation in *i*-butanol solutions of compounds 1–5.

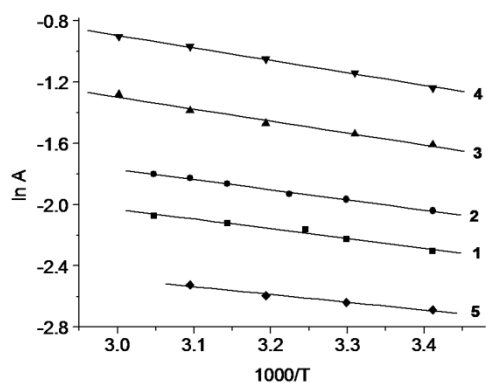


**Fig. 9.** Data ( $\ln A$ ) on thermal equilibrium treated according to the Van't Hoff equation in *i*-propanol solutions of compounds 1–5.

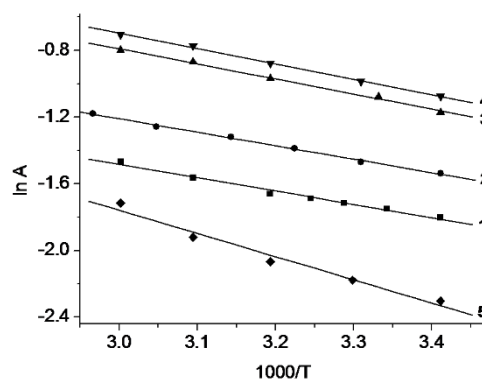


**Fig. 10.** Data ( $\ln A$ ) on thermal equilibrium treated according to the Van't Hoff equation in acetonitrile solutions of compounds 1–5.

## CONCLUSIONS

Five newly synthesized spiroindolinonaphthoxazines bearing different substituents on the basic skeleton were investigated with respect to thermochromism in solvents of different polarity. Thermal reactions involving the cyclic spiroform and the open merocyanine form of the compounds with benzothiazolyl substituent were studied. Acetone was employed as a solvent to determine standard thermodynamic parameters,  $\Delta H^0$ ,  $\Delta S^0$ , and  $\Delta G^0$ , of the reaction. It was found that the opening of the spirocyclic ring was not a spontaneous reaction. Both positive enthalpy changes and  $\Delta S^0$  negative values contributed to the overall positive  $\Delta G^0$  values. Negative standard entropy values were attributed to a better arrangement of the solvent molecules around each open polar MC form in comparison with a starting spirocyclic molecule.

*Acknowledgements:* This work was supported by contract DFNI-TO2/16 of the Bulgarian Science Fund.

## REFERENCES

1. N. Tamai, H. Miyasaka, *Chem. Rev.*, **100**, 1875 (2000).
2. N. Y. C. Chu, in: H. Durr, H. Bouas-Laurent (Eds), *Photochromism: molecules and systems*, Elsevier, Amsterdam, 1990, p. 493.
3. C. B. McArdle (Ed.), *Applied photochromic polymer systems*, Blackie, London, 1992.
4. Tardieu, R. Dumbest, J. Aubard, A. Kellmann, F. Tfibel, A. Samat, R. Guglielmetti, *Helv. Chim. Acta*, **75**, 1185 (1992).
5. A. K. Chibisov, H. Görner, *Phys. Chem. Chem. Phys.*, **3**, 424 (2001).
6. Wilkinson, D. R. Worrall, J. Hobley, L. Jansen, S. L. Williams, A. J. Langley, P. Matousek, *J. Chem. Soc. Faraday Trans.*, **92**, 1331 (1996).

7. G. Favaro, F. Masetti, U. Mazzucato, G. Ottavi, P. Allegrini, V. Malatesta, *J. Chem. Soc. Faraday Trans.*, **90**, 333 (1994).
8. F. Ortica, *Dyes Pigm.*, **92**, 807 (2012).
9. T. Nakabayashi, N. Nishi, H. Sakuragi, *Sci. Progress*, **84**, 137 (2001).
10. J.-L. Pozzo, A. Samat, R. Guglielmetti, D. de Keukeleire, *J. Chem. Soc. Perkin Trans.*, **2**, 1327 (1993).
11. G. Favaro, V. Malatesta, U. Mazzucato, G. Ottavi, A. Romani, *J. Photochem. Photobiol. A-Chem.*, **87**, 235 (1995).
12. A. K. Chibisov, H. Görner, *J. Phys. Chem.*, **103**, 5211 (1999).
13. S. R. Keum, M. S. Hur, P. M. Kazmaier, E. Buncel, *Can. J. Chem.*, **69**, 1940 (1991).
14. H. Kim, H. J. Suh, J. Z. Cui, Y. S. Gal, S. H. Jin, K. Koh, *Dyes Pigm.*, **53**, 251 (2002).
15. H. J. Suh, W. T. Lim, J. Z. Cui, H. S. Lee, G. H. Kim, N. H. Heo, S. H. Kim, *Dyes Pigm.*, **57**, 149 (2003).
16. T. Deligeorgiev, S. Minkovska, B. Jeliaskova, S. Rakovsky, *Dyes Pigm.*, **53**, 101 (2002).
17. S. Minkovska, B. Jeliaskova, E. Borisova, L. Avramov, T. Deligeorgiev, *J. Photochem. Photobiol. A-Chem.*, **163**, 121 (2004).
18. S. Minkovska, M. Fedieva, B. Jeliaskova, T. Deligeorgiev, *Polyhedron*, **23**, 3147 (2004).
19. B. G. Jeliaskova, S. Minkovska, T. Deligeorgiev, *J. Photochem. Photobiol., A-Chem.*, **171**, 151 (2005).

## ТЕРМОХРОМИЗЪМ НА СЕРИЯ СПИРОИНДОЛИНОНАФТОКСАЗИНИ

С. Минковска<sup>1\*</sup>, Б. Желязкова<sup>2</sup>, Сл. Раковски<sup>1</sup>, Т. Делигеоргиев<sup>2</sup>

<sup>1</sup> *Институт по катализ, Българска академия на науките, ул. „Акад. Г. Бончев“, бл. 11, 1113 София, България*

<sup>2</sup> *Факултет по химия и фармация, Софийски университет „Св. Климент Охридски“, бул. „Джеймс Баучер“ 1, 1164 София, България*

Постъпила на 7 октомври 2015 г.

(Резюме)

Термохромните свойства на пет спиронафтоксазина, съдържащи различни заместители в основния скелет на молекулата, са синтезирани в нашата лаборатория и изучени в разтворители с различна полярност. Съединенията са силно поляризуеми, което води до равновесие между безцветната затворена и оцветената отворена форма в интервала от температури (20–60°C) в отсъствие на светлина. Термичното равновесие между основното заселено състояние на безцветната затворена форма и цветната отворена форма зависи както от полярността на разтворителя, така и от природата на заместителите. Концентрацията на отворената форма се увеличава с нарастване полярността на разтворителя.

## Synthesis and study of some novel chelating photochromic spironaphthoxazines

S. Minkovska<sup>1\*</sup>, B. Jeliaskova<sup>2</sup>, S. Rakovsky<sup>1</sup>, T. Deligeorgiev<sup>2</sup>

<sup>1</sup> Institute of Catalysis, Bulgarian Academy of Sciences, Acad. G. Bonchev St., Bldg. 11, 1113 Sofia, Bulgaria

<sup>2</sup> Department of Chemistry and Pharmacy, Sofia University, 1 J. Bourchier Blvd., 1164 Sofia, Bulgaria

Received October 7, 2015

This paper reviews a series of some novel spironaphthoxazines containing chelating functional groups, which have been synthesized and investigated by the authors. Physical and spectroscopic characteristics (UV, <sup>1</sup>H-NMR, and elemental analysis) of these compounds have been determined. Photochromic reactions of the synthesized compounds were studied under continuous UV irradiation in solvents of different polarity. Solvent and structural effects on absorption properties and thermal bleaching kinetics of the photomerocyanines of synthesized spironaphthoxazines were investigated. The photomerocyanines obtained under steady irradiation of spiroindolinonaphthoxazines, containing a hydroxyl substituent in the naphthoxazine moiety, form complexes with Al(III), Cu(II), and Fe(II) in polar solvents, while those containing a benzothiazolyl substituent interact with Co(II), Ni(II), and Zn(II). Complexation of metal ions with the merocyanines induces a slight hypsochromic shift of its visible absorption band and drastically slows down its thermal bleaching in the dark.

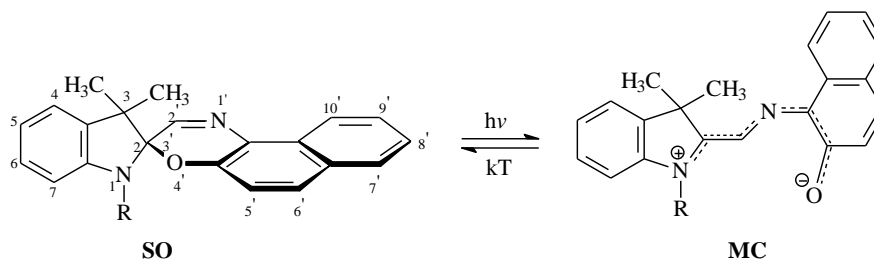
**Key words:** synthesis, photochromism, complexation, spectral properties, kinetics.

### INTRODUCTION

Spirooxazines are a particularly interesting family of photochromic molecules [1, 2] due to their remarkable properties, such as photo-fatigue resistance, strong photocolouration, and fast thermal relaxation [3, 4]. These properties give spiro-oxazines the ability to be applied in many new technologies, for example light filters and optical devices, photochromic liquid crystals, photochromic plastics, photochromic substances useful in lenses, dynamic biosensors and bioelectronic materials, in catalysis, and as metal complex agents [5–14]. The photochromism of these molecules is owing to a photocleavage of the C–O spirobond according to Scheme 1 under UV irradiation and subsequent rotation about a C–C bond to give an open merocyanine (MC) structure (photomerocyanine), which absorbs in the visible region and the molecule is intensively

coloured. The spirooxazines are comprised of two heterocyclic nearly planar moieties (indoline and naphthoxazine) joined by a tetrahedral spiro-carbon which prevents the two  $\pi$  electron systems from conjugation. As a result, the spiro-compounds are almost colourless or pale yellow since the lowest electronic transition of the molecule occurs in the near UV region.

There is a technical interest in photochromic materials based on spiro-compounds [1–14] in which the coloured photomerocyanine once produced cannot revert to the colourless spiro-form, or at least reversion rate is greatly retarded [15, 16]. One way of achieving this is to try to trap the photomerocyanine in a metal-chelated form [17–21] by having suitable substituents in the spiro-compound and metal ions in the solution. This approach has been reported for spiropyranes [17–20] and in single cases for spirooxazines [21, 22].



Scheme 1

\* To whom all correspondence should be sent:

E-mail: stelamin@ic.bas.bg

© 2015 Bulgarian Academy of Sciences, Union of Chemists in Bulgaria

## EXPERIMENTAL

All solvents and starting materials, not synthesized in this laboratory, were commercial products (Sigma Aldrich, TCI Europe) and were used without further purification. Synthesis of spirooxazine compounds **0-6** was carried out in a one- to three-step sequence as depicted in Schemes 2–4 [23].  $^1\text{H}$  NMR spectra of the dyes were recorded in  $\text{CDCl}_3$  on a Bruker 500 MHz spectro-meter.

A 250-W medium-pressure mercury lamp housed in a light box was used for producing coloured forms and absorption spectra were recorded on an Ocean Optics PC2000 fast scanning spectrometer capable of recording the whole absorption spectrum in the visible region in 10 ms using a 1-cm quartz cell. Irradiation was performed in the spectrophotometer holder at right angles to the monitoring beam. Light was homogeneously spread on cell window to avoid stirring [11].

A general procedure for determining photomerocyanine fading kinetics was as follows. A solution of spiro-compound in a suitable solvent, with a concentration sufficient to give an absorbance of ca. 0.8–1.0 at a corresponding  $\lambda_{\text{max}}$ , was exposed to UV light in a quartz cell until the colour was fully developed. SO thermal ring-opening kinetics was measured in the presence of metal ions at a different temperature in the range of 20–50°C about 30 min after having set the temperature control in order to allow initial solution to reach the appropriate temperature in a separate vessel. The ring-closure reaction after photocoloration was monitored directly after switching off light source and scanning the complex between the MC form and the metal ion at the wavelength of maximum absorption ( $\lambda_{\text{compl}}$ ) at 15-s intervals over a period of 20 min at room temperature. First-order rate constants were obtained from linear  $\ln A$  vs. time descending curves. By extrapolation of the obtained  $\ln A/t$  plots to zero time, complex absorbance  $A_0$  at  $t = 0$  was related to

‘colourability’ [11] using the expression  $A_0/c_{\text{SO}} \cdot b$  in which  $c_{\text{SO}}$  is the initial SO concentration and  $b$  is the optical path length.

## RESULTS AND DISCUSSION

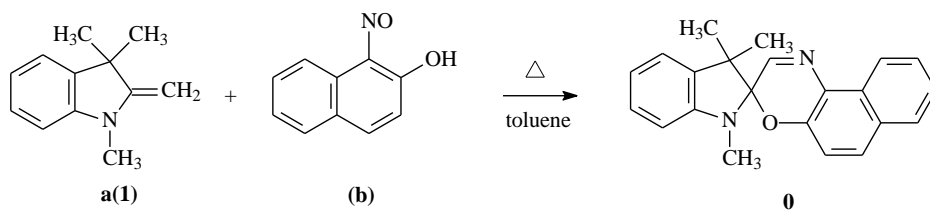
The most common method employed to synthesize spironaphthoxazines is condensation of an alkylidene heterocycle with *o*-nitrosonaphthols in polar organic solvents, such as methanol [8] or chlorinated lower aliphatic hydrocarbons. The present photochromic spironaphthoxazines were prepared by the reaction of 1,3,3-trimethyl-2-methylene indoline, or 1-butyl-3,3-dimethyl-2-methylene indoline, or the corresponding benz[c]indolium perchlorate compounds 1,3,3-trimethyl-benz[c]indolium perchlorate or 1-butyl-3,3-dimethyl benz[c]indolium perchlorate with the matching *o*-nitrosonaphthols [23].

The visible spectra of photomerocyanines **0-6**, acquired by UV irradiation in solvents of different polarity, are characterised by a strong absorption band in the range of 560–660 nm (Table 1). According to data in Table 1, addition of –OH at the 5' position in the naphthoxazine moiety has a minor effect on the visible band of MC derived from compounds **1** and **2** compared to the parent **0**. The effect of benzothiazolyl substituent at the same position reveals a moderate bathochromic shift of 30 to 65 nm in the spectrum of the MC derived from compound **3**. Replacing benzene in the indoline moiety by naphthalene additionally shifts the visible band of the MC originated from compounds **5** and **6** by 15–20 nm to longer wavelengths.

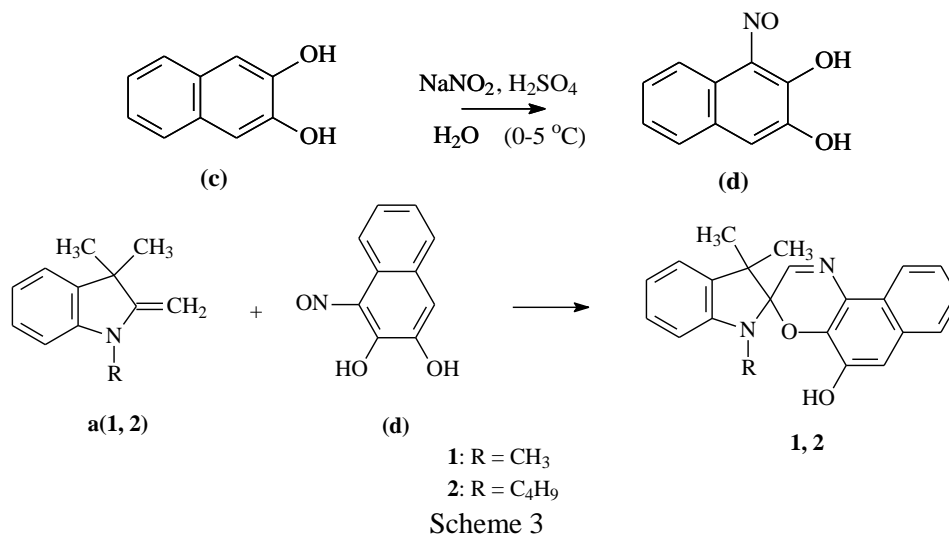
Visible spectra of photomerocyanines derived from compounds **0** and **3-6** are apparently not single absorptions, but show in each case a shorter wavelength shoulder of the main absorption band (Fig. 2) like the spectra of other photomerocyanines of this type [8, 10, 12]. Visible spectra of **1** and **2** reveal only a wide single absorption band (Fig. 3).

**Table 1.** Experimental values of  $\lambda_{\text{max}}$  (nm) and ‘colourability’ ( $\times 10^{-4}$ ) of the visible absorption of photomerocyanines derived from compounds **0-6**

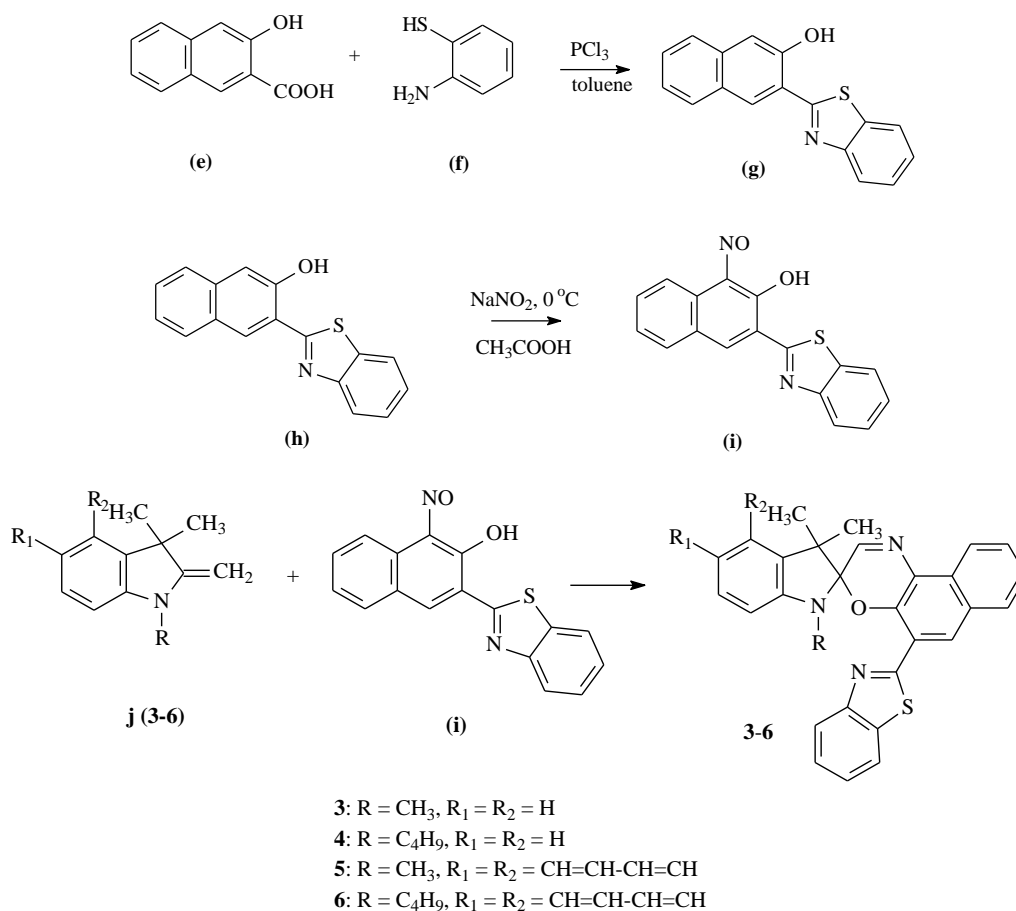
Solvent	$\lambda_{\text{max}}$ (colourability)						
	<b>0</b>	<b>1</b>	<b>2</b>	<b>3</b>	<b>4</b>	<b>5</b>	<b>6</b>
hexane	560 (4.55)	565 (6.87)	570 (6.96)	625 (6.61)	630 (6.84)	642 (6.46)	648 (7.25)
acetone	600 (5.50)	590 (4.27)	595 (4.37)	640 (5.89)	642 (7.25)	655 (6.76)	656 (7.28)
acetonitrile	600 (6.92)	595 (5.79)	597 (5.88)	640 (6.19)	645 (6.98)	658 (7.08)	658 (7.24)
ethanol	610 (5.25)	600 (5.94)	605 (6.32)	642 (7.10)	648 (8.45)	660 (6.82)	660 (8.02)



Scheme 2



Scheme 3



Scheme 4

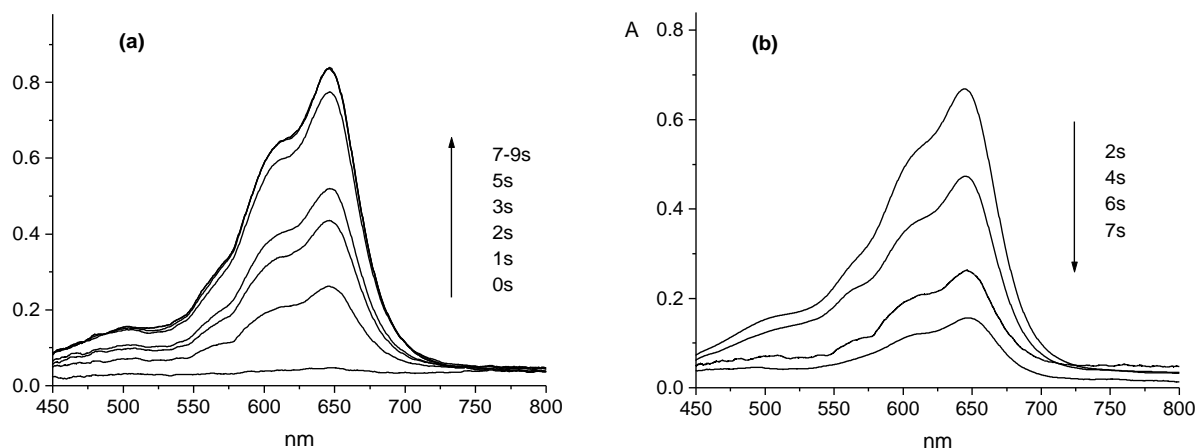


**Fig. 2.** Visible absorption spectra of  $1 \times 10^{-5}$  M hexane solution of **6** taken: upon 0, 1, 2, 3, 5 or 7-9 s UV irradiation (a) and on keeping the irradiated sample for 2, 4, 6, 7, 10, and 15 s in the dark (b).

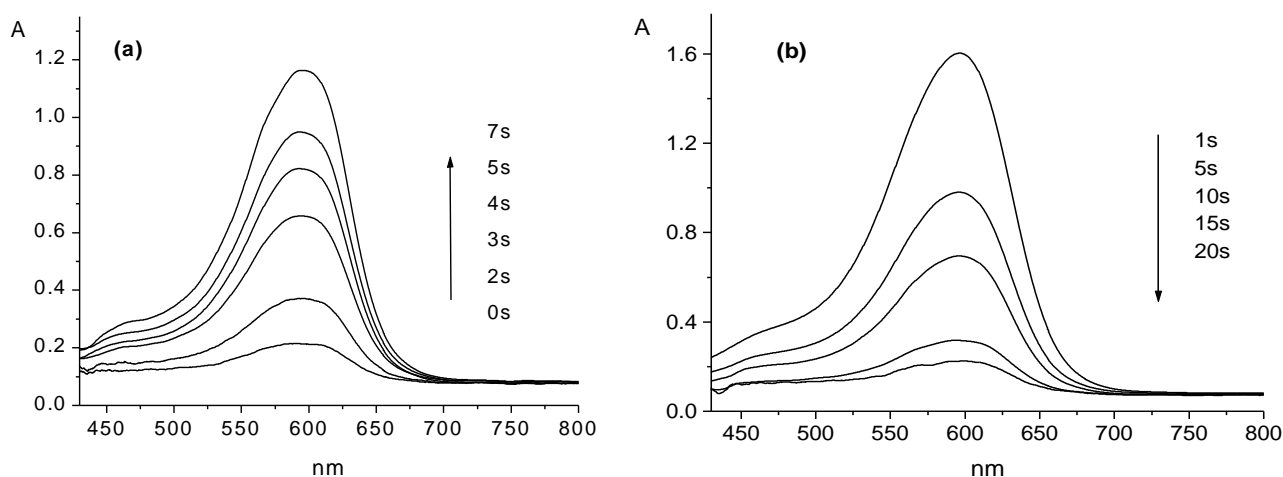


**Fig. 3.** Visible absorption spectra of  $2.5 \times 10^{-5}$  M acetonitrile solution of **1** taken: upon 0, 1, 3, 4, 5, and 7 s UV irradiation (a) and on keeping the irradiated sample for 1, 5, 10, 15, and 20 s in the dark (b).

'Colourability' [9, 11] of photomerocyanines was calculated from the absorbance  $A_0$  obtained by extrapolation to  $t = 0$  of the room temperature linearly descending kinetic curves  $\ln A/t$  (Figs. 4 and 5) taken immediately after UV irradiation. Values of  $A_0/cl$  are displayed in Table 1. Bathochromic shifts given in Table 1 at a higher solvent polarity, positive solvatochromism, are indicative of a better stabilisation of photomerocyanine-excited state relative to the ground state. A high 'colourability' of the visible absorption bands and observed bathochromic shifts of the spectrum at a higher polarity of the medium are consistent with a  $\pi-\pi^*$  character of the singlet excited state of the open forms [10].

Kinetic runs followed immediately after irradiation of **1** or **6** in a range of solvents of different polarity (Figs. 4a,b) show that the thermal ring closure reaction follows first-order kinetics in

concentration of the photomero-cyanine, as the  $\ln A/t$  plots are linear. The slopes of the  $\ln A/t$  curves gave the first-order rate constants,  $k$ . Photomerocyanine relaxation times ( $\tau_{MC-SO}$ ) given in Table 2 were obtained from the first-order rate constants using the expression  $\tau = 1/k$ . Thus, data in Fig. 4a do not indicate any noticeable dependence of the rate of cyclization of photomerocyanine derived from  $-OH$  derivative **1** on solvent polarity and the same is observed about compound **2** and parent unsubstituted compound **0** in Table 2. On the contrary, data in Fig. 4b show that solvent nature has a significant effect on the rate of cyclization of photomerocyanine derived from benzothiazolyl-substituted compound **6** and similar results were obtained for compounds **3-5** in Table 2. In hexane, the merocyanine receives little solvent stabilisation and cyclization is rapid, whereas in acetone and aceto-

nitrile, a relatively higher stabilisation of the polar merocyanine compared to the non-polar spiro-compound is the reason of slower cyclization. The effect is quite pronounced in ethanol, where decolouration reaction is up to 30 times slower than in hexane most probably due to a combined effect of stabilisation of the polar merocyanine and its specific solute-solvent interaction like hydrogen bonding with ethanol. Kinetic runs illustrating the effect of different substituents on colour fading of photomerocyanines in ethanol are presented in Figs. 5a,b. Corresponding values of  $k$  and  $\tau_{\text{MC-SO}}$  are presented in Table 2. According to these values addition of –OH at the 5' position in the naphthoxazine moiety only slightly increases the relaxation time of photomerocyanines derived from compounds **1** and **2**. Addition of benzothiazolyl substituent at the same position has a stronger effect on the rate of cyclization and the value of MC-SO of the photomerocyanine derived from compound **3** is up to 25 times higher than that acquired for parent unsubstituted compound **0**. These results definitively show that the  $\tau_{\text{MC-SO}}$  values vary gradually for **0–6** depending on both structural characteristics and solvent polarity.

Colourless spiro compounds gave no complexes with metal ions. However, the merocyanine form of spirooxazines containing a hydroxyl substituent at the 5' position in the naphthoxazine moiety appeared to form complexes with Al(III), Cu(II), and Fe(II), while those containing a benzothiazolyl substituent interacted with Co(II), Ni(II), Zn(II) in polar solvents.

The visible spectra of photomerocyanines, obtained upon UV illumination of **1** or **2** in polar solvents [46], are characterized by absorption in the

range of 600–620 nm. Irradiation of **1** and **2** in the presence of 1 equivalent of Cu(II), Fe(II) or Al(III) generated a new photo-reversible absorption band in the range of 540–600 nm with band intensity dependent on the  $[\text{M(II),(III)}]/[\text{SO}]$  ratio, the highest effectiveness being at 10 equivalents of added metal ion. The observed  $\lambda_{\text{max}}$  values (Table 3) are slightly blue-shifted and the same was observed at a 10-fold molar excess of M(II),(III). It is obvious that UV irradiation of SO in the presence of a suitable metal ion yields a MC-M(II),(III) complex and this process is considered a photoinduced complexation. Thermal coordination to the metal ion also takes place, giving a complex, which is spectroscopically identical to the photoinduced product. The colouration obtained in the dark becomes more intense upon UV illumination and reverses back to its initial level after switching off the light.

A strong absorption band in the range of 640–660 nm characterizes visible spectra of photomerocyanines, obtained by UV irradiation of **3–6** in acetone [46]. Insertion of Ni(II), Co(II) or Zn(II) generates a new intense photo-reversible absorption band in the range of 610–640 nm. According to the data reported in Table 4 the new absorption band obtained on adding  $5 \times 10^{-5}$  M acetone solution of Ni(II), Co(II) or Zn(II) to equimolar acetone, hexane (or cyclohexane) solutions of **3–6** is slightly blue-shifted, about 25–45 nm for **5** in acetone. The same was observed at a 10- to 250-fold molar excess of M(II). While  $\lambda_{\text{max}}$  depends only moderately on metal ion nature (15–45 nm), the time needed for re-establishing equilibria is sensitive to the metal ion and substantially prolonged compared to non-complexed merocyanine.

**Table 2.** Rate constants  $k$  ( $\times 10^2 \cdot \text{s}^{-1}$ ) of thermal ring closure of photomerocyanines derived from compounds **0–6** and their lifetimes  $\tau_{\text{MC-SO}}$  (s)

solvent	<b>0</b>	<b>1</b>	<b>2</b>	<b>3</b>	<b>4</b>	<b>5</b>	<b>6</b>
hexane	52.5 (2)	18.0 (5)	18.7 (5)	18.0 (5)	18.4 (5)	25.2 (4)	22.5 (4)
acetone	44.7 (2)	16.8 (6)	15.9 (6)	5.4 (19)	5.1 (20)	2.5 (40)	2.1 (48)
acetonitrile	54.6 (2)	15.3 (6)	14.2 (7)	5.2 (19)	5.7 (18)	3.3 (30)	2.8 (36)
ethanol	42.9 (2)	13.6 (7)	12.9 (8)	2.0 (50)	1.9 (53)	1.0 (100)	(125)

**Table 3.** Absorption maxima of complexes obtained upon UV illumination of  $5 \times 10^{-5}$  M solutions of **1** and **2** in the presence of 1 equiv. of metal ion

SO	Solvent	$\lambda_{\text{max}}$ , nm			
		MC	MC-Cu(II)	MC-Al(III)	MC-Fe(II)
<b>1</b>	EtOH/H <sub>2</sub> O	610	595	585	546
	CH <sub>3</sub> COCH <sub>3</sub> /H <sub>2</sub> O	600	590	580	540
<b>2</b>	EtOH/H <sub>2</sub> O	620	600	580	546
	CH <sub>3</sub> COCH <sub>3</sub> /H <sub>2</sub> O	600	590	580	540

**Table 4.** Experimental values of  $\lambda_{\text{max}}$  (nm) and  $\epsilon$  ( $\text{M}^{-1} \cdot \text{cm}^{-1}$ ) of the visible absorption band of Ni(II), Co(II), and Zn(II) complexes with **3–6** in acetone

SO	$\lambda_{\text{max}}$ (nm)		
	MC-Ni(II)	MC-Co(II)	MC-Zn(II)
<b>3</b>	620 (48500)	610 (44500)	600 (36500)
<b>4</b>	625 (51500)	615 (48000)	605 (38500)
<b>5</b>	630 (59000)	620 (54000)	610 (41000)
<b>6</b>	640 (54000)	630 (53500)	620 (40500)

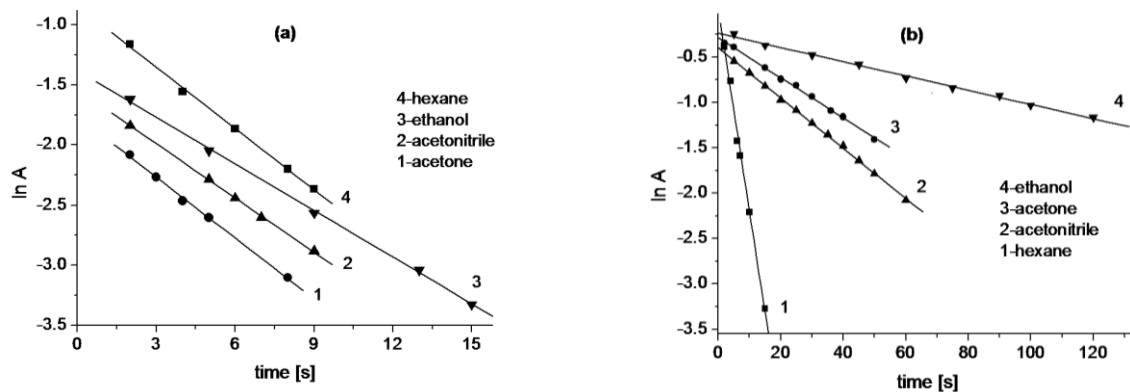


**Fig. 4.** Kinetic runs ( $\ln A$  vs. time) at 600 nm after irradiation of  $1 \times 10^{-5}$  M solutions of **1** (a) and **6** (b) in solvents of different polarity.

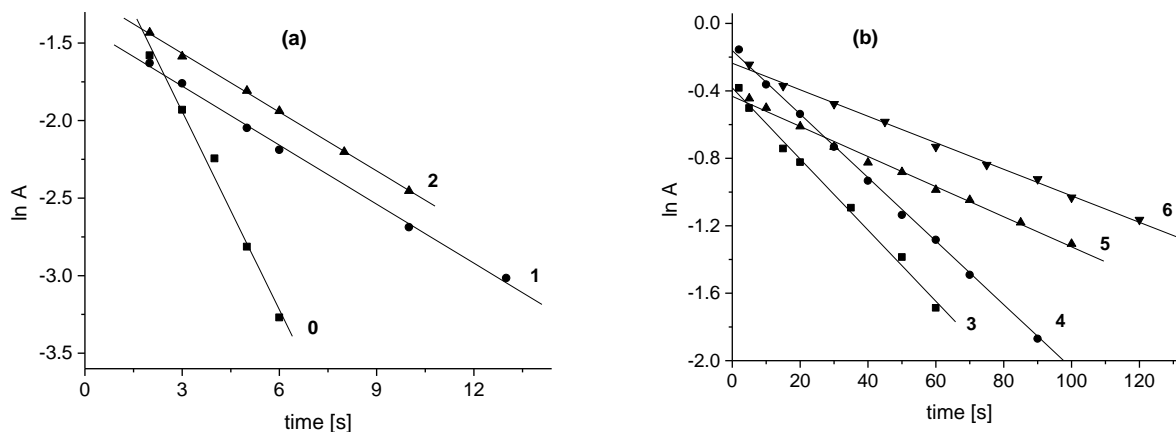


**Fig. 5.** Kinetics runs ( $\ln A$  vs. time) at 600 nm after irradiation of  $1 \times 10^{-5}$  M solutions of **0–2** (a) and **3–6** (b) in ethanol.

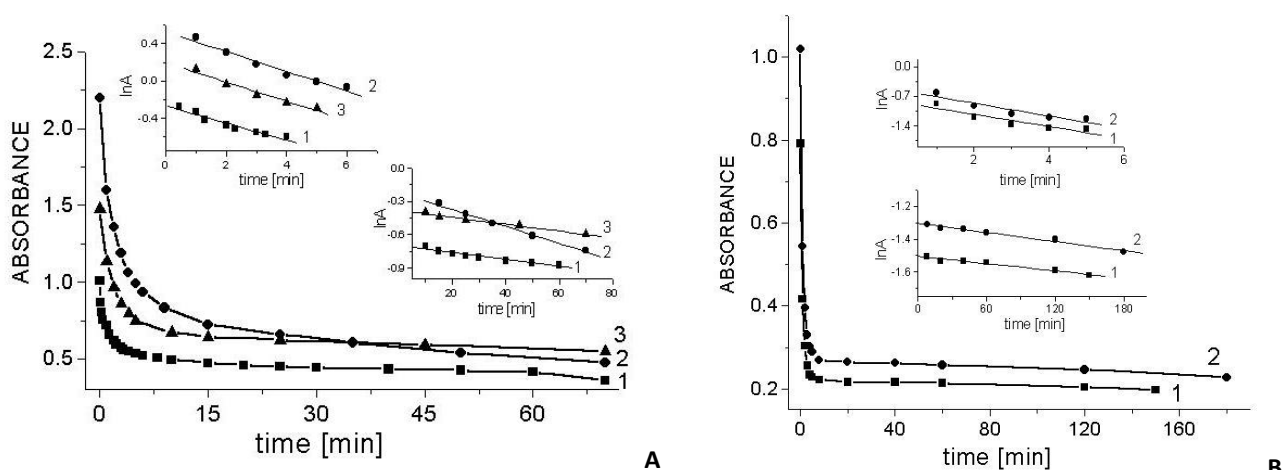


**Fig. 6.** A). Absorbance changes at 590 nm following 15-s UV illumination of an ethanol solution of **1** after insertion of: (1) 0.5 or (2) 10 equivalents of Cu(II) in ethanol and (3) 10 equivalents of aqueous Cu(II). Insets:  $\ln A$  vs. time plots, initial (0.5–6 min) and final (10–70 min); B). Absorbance changes at 600 nm following 15-s UV illumination of an ethanol solution of **2** after insertion of: (1) 0.5 or (2) 1 equivalent of aqueous Cu(II). Insets:  $\ln A$  vs. time plots, initial (1–5 min) and final (10–180 min).

Photoirradiation of the parent-unsubstituted spiroindolinonaphthoxazine (Scheme 1) in the presence of either metal salt [28] induces irreversible photo-degradation without any complexation indicating that the nitrogen atom at the 1' position in the naphthoxazine moiety takes no part in chelation.

In the absence of metal ion, the first-order decay of the photomerocyanines of **1** and **2** occurs with  $k_r \sim 0.1 \text{ s}^{-1}$  [24] and the relaxation time in acetone and ethanol is  $\tau_{\text{MC-SO}} \sim 10 \text{ s}$ . Taking into account that colouring and fading times are important characteristics of the photochromic systems, we have studied the effect of chelation on the kinetics of spiroindolinonaphthoxazine photochromic transformations. A typical picture of bleaching after irradiation of **1** and **2** in the presence of Al(III), Cu(II) or Fe(II) is shown in figures 6A and 6B. Kinetic runs in figure 6A followed at  $k_{\text{compl}}$  immediately after illumination of ethanol (plots 1 and 2) or 1:1 aqueous/ethanol (plot 3) solutions indicate that the photoinduced MC-Cu(II) complex of **1** undergoes spontaneous thermal decolouration. It is first order in concentration of the starting complex as the  $\ln A$  vs. time plots (initial inset in Fig. 6A) are linear ( $q > 0.98$ ) at about 50% of reaction completion. Similar changes are observed in figure 6B for the MC-Cu(II) complex of **2**. A strongly descending part of the curves associated with thermal spiroindolinonaphthoxazine ring closure, analysed by the least squares method, give metal-dependent values of the re-equilibration rate constant  $k_r$  ranging from  $1.5$  to  $2.6 \times 10^{-3} \text{ s}^{-1}$  at  $20^\circ\text{C}$ .

Relaxation times ( $\tau_{\text{com-SO}}$ ) of 5–10 min for **1,2** and of 2–42 min for **3–6** were obtained using the expression  $\tau = 1/k_r$ . The rate constants calculated by the least squares method from the final  $\ln A$  vs. time linear plots are ca.  $5 \times 10^{-5} \text{ s}^{-1}$  for **1** and  $1 \times 10^{-5} \text{ s}^{-1}$  for **2** in 1:1 aqueous/ethanol (up to  $1 \times 10^{-4} \text{ s}^{-1}$  in ethanol).

## CONCLUSION

We have successfully designed and synthesized six novel spiroindolinonaphthoxazines containing chelating functional groups. The photochromic properties of the parent spiroindolinonaphthoxazine were modulated by introduction of substituents at different positions of the molecular framework. A thermal ring closure reaction was strongly suppressed when a benzthiazolyl substituent was attached to the 5' position in the naphthoxazine moiety and benzene was replaced by naphthalene in the indoline fragment. A combined effect of both substituents could be assigned to a decreased rotational freedom upon cyclization. High 'colourability' values (up to  $8.5 \times 10^4$ ) suggest high effectivity of the colour-forming reaction. As a rule,

substituents have stronger influence than solvents and provide an active method of tuning and designing new photochromic molecules. Coordination of Al(III), Fe(II), and Cu(II) with the open MC form of 5'-(hydroxy)spiroindolino(-)naphthoxazines and of Ni(II), Co(II) or Zn(II), with the open MC form of 5'-(benzothiazol-2-yl)spiroindolinonaphthoxazines takes place thermally (slowly) or photochemically in a suitable solvent yielding a reversibly photochromic complex. The thermal build-up reaction ( $\sim 10^{-3} \text{ s}^{-1}$ ) is independent of  $[\text{M(II)}]$ , which implies that ring opening is the rate-determining step. Chelation induces a 10–45-nm hypsochromic shift of the visible absorption band of the photomerocyanine and drastically slows down thermal bleaching in the dark.

*Acknowledgement:* This work was supported by contract DFNI-TO2/16 of the Bulgarian Science Fund.

## REFERENCES

1. S. Maeda, in: Organic Photochromic and Thermochromic Compounds, J. C. Crano, R. J. Guglielmetti (Eds.), Vol. 1, Ch. 2, Plenum Press, New York, 1999.
2. V. Lokshin, A. Samat, A. V. Metelitsa, *Russ. Chem. Rev.*, **71**, 893 (2002).
3. R. C. Bertelson, *Mol. Cryst. Liq. Cryst.*, **246**, 1 (1994).
4. H. Durr, H. Bouas-Laurent (Eds.), Photochromism: Molecules and Systems, Elsevier, Amsterdam, 1990.
5. C. B. McArdle (Ed.), Applied Photochromic Polymer Systems, Blackie, London, 1992.
6. N. Tamai, H. Miyasaka, *Chem. Rev.*, **100**, 1875 (2000).
7. J. C. Crano, R. J. Guglielmetti (Eds.), Organic Photochromic and Thermochromic Compounds, Vols. 1 and 2, Plenum Press, New York, 1999.
8. N. Y. C. Chu, *Can. J. Chem.*, **61**, 300 (1983).
9. S. Kawauchi, H. Yoshida, N. Yamashina, M. Ohira, S. Saeda, M. Irie, *Bull. Chem. Soc. Jpn.*, **63**, 267 (1990).
10. A. Kellmann, F. Tfibel, R. Dubest, P. Levoir, J. Aubard, E. Pottier, R. J. Guglielmetti, *J. Photochem. Photobiol. A-Chem.*, **49**, 63 (1989).
11. G. Favaro, V. Malatesta, U. Mazzucato, G. Ottavi, A. Romani, *J. Photochem. Photobiol. A: Chem.*, **87**, 235 (1995).
12. G. Favaro, F. Masetti, U. Mazzucato, G. Ottavi, P. Allegrini, V. Malatesta, *J. Chem. Soc. Faraday Trans.*, **90**, 333 (1994).
13. C. Bohne, M. G. Fan, Z.-J. Li, Y. C. Liang, J. Luszyk, J. C. Scaiano, *J. Photochem. Photobiol. A-Chem.*, **66**, 79 (1992).
14. J. L. Pozzo, A. Samat, R. Guglielmetti, D. de Keukeleire, *J. Chem. Soc. Perkin Trans.*, **2**, 1327 (1993).
15. S. Janicki, G. B. Schuster, *J. Am. Chem. Soc.*, **117**, 8524 (1995).
16. F. Pina, M. J. Melo, M. Maestri, R. Ballardini, V. Balzani, *J. Am. Chem. Soc.*, **119**, 5556 (1997).

17. L. D. Taylor, J. Nicholson, R. B. Davis, *Tetrahedron Lett.*, **17**, 1585 (1967).
18. J. P. Phillips, A. Mueller, F. Przystal, *J. Am. Chem. Soc.*, **87**, 4020 (1965).
19. H. Görner, A. K. Chibisov, *J. Chem. Soc. Faraday Trans.*, **94**, 2557 (1998).
20. J. T. C. Wojtyk, P. M. Kazmaier, E. Buncel, *J. Chem. Soc. Chem. Commun.*, 1703 (1998).
21. T. Tamaki, K. Ichimura, *J. Chem. Soc. Chem. Commun.*, 1447 (1989).
22. S. V. Paramonov, V. Lokshin, O. A. Fedorova, *J. Photochem. Photobiol. C-Photochem. Rev.*, **12**, 209 (2011).
23. T. Deligeorgiev, S. Minkovska, B. Jeliaskova, S. Rakovsky, *Dyes Pigm.*, **53**, 101 (2002).
24. S. Minkovska, B. Jeliaskova, E. Borisova, L. Avramov, T. Deligeorgiev, *J. Photochem. Photobiol. A-Chem.*, **163**, 121 (2004).
25. S. Minkovska, M. Fedieva, B. Jeliaskova, T. Deligeorgiev, *Polyhedron*, **23**, 3147 (2004).
26. B. G. Jeliaskova, S. Minkovska, T. Deligeorgiev, *J. Photochem. Photobiol. A-Chem.*, **171**, 153 (2005).
27. G. Baillet, G. Giusti, R. Guglielmetti, *Bull. Chem. Soc. Jpn.*, **68**, 1220 (1995).
28. S. Minkovska, K. Kolev, B. Jeliaskova, T. Deligeorgiev, *Dyes Pigm.*, **39**, 25 (1998).

## СИНТЕЗ И ИЗСЛЕДВАНЕ НА НОВИ ХЕЛАТНИ ФОТОХРОМНИ СПИРОНАФТОКСАЗИНИ

С. Минковска<sup>1\*</sup>, Б. Желязкова<sup>2</sup>, Сл. Раковски<sup>1</sup>, Т. Делигеоргиев<sup>2</sup>

<sup>1</sup> Институт по катализ, Българска академия на науките, ул. „Акад. Г. Бончев“, бл. 11, 1113 София, България

<sup>2</sup> Факултет по химия и фармация, Софийски университет „Св. Климент Охридски“, бул. „Джеймс Баучер“ 1, 1164 София, България

Постъпила на 7 октомври 2015 г.

(Резюме)

Статията е обзор върху серия нови спирооксазини, съдържащи различни хелатни функционални групи, които са синтезирани и изследвани в нашата лаборатория. Определени са физичните и спектроскопски характеристики (UV, <sup>1</sup>H-ЯМР и елементарен анализ). Фотохимичната реакция на синтезираните съединения е изследвана при непрекъснато облъчване с УВ светлина в разтворители с различна полярност. Изследвани са ефектът на разтворителя и структурата на съединенията върху абсорбционните свойства и кинетиката на термично обезцветяване на мероцианиновата форма на синтезираните спиронафтоксазини. Фотомероцианините, получени при стационарно облъчване с УВ светлина на спиронафтоксазините, съдържащи хидроксилен заместител в нафт(о)ксазиновата част, образуват комплекси с Al(III), Cu(II) и Fe(II) в полярни разтворители, докато тези, съдържащи бензотиазолилов заместител взаимодействат с Co(II), Ni(II) и Zn(II). Комплексообразването между мероцианиновата форма и металните йони се характеризира със слаб хипсохромен ефект върху абсорбционната ивица във видимата област и значително понижение на скоростта на рециклизация.

## TPS and TPR study of HDS catalysts and process mechanism

I. Shtereva<sup>1\*</sup>, D. Vladov<sup>2</sup>, S. Rakovsky<sup>1</sup>, B. Iliencko<sup>3</sup>

<sup>1</sup> Institute of Catalysis, Bulgarian Academy of Sciences, Acad. G. Bonchev St., Bldg. 11, 1113 Sofia, Bulgaria

<sup>2</sup> University of Chemical Technology and Metallurgy, 8 Kliment Ohridski Blvd., 1756 Sofia, Bulgaria

<sup>3</sup> The Gas Institute, National Academy of Sciences of Ukraine, 39 Degtyarivska St., 03113 Kyiv, Ukraine

Received: September 30, 2015; Revised December 17, 2015

Ni(Co)-Mo/Al<sub>2</sub>O<sub>3</sub> catalysts for hydrodesulphurisation (HDS) process have been studied by means of kinetic, temperature-programmed reduction (TPR), and temperature-programmed sulphidation (TPS) methods. It has been established that on increasing the amount of MoO<sub>3</sub> active phase, and that of NiO promoter, both catalyst activity in the reaction of HDS and selectivity to butane are growing up. Correlations have been established between catalyst activity and TPR peak temperature so as between catalyst activity and TPS peak area. An approach is proposed to predict catalyst activity based on TPR and TPS characteristics. There is experimental evidence confirming a supposition that the active species in the reaction are oxysulphides that are being formed on the surface of the catalyst during activation. At least two types of active sites were found to be present on the surface: hydrogenation and hydrodesulphurization entities, their activity being dependent in a different way on temperature of the TPR peak maximum on activating the catalyst.

**Keywords:** HDS, Ni-Mo/Al<sub>2</sub>O<sub>3</sub> catalysts, TPR, TPS

### INTRODUCTION

Supported Ni(Co)-MoO<sub>3</sub> catalysts are extensively used in hydrotreatment that is one of the most important processes in oil refining. Crude oil fractions treatment in the refineries impose the primary purpose of organic sulphur removal from the stream prior to use as various fuels [1–5]. It is so, as on the one hand, the quality of oil is constantly deteriorating, while on the other hand, the requirements for fuel quality are constantly growing up in view of environmental protection. Since 2005, European Community fuel regulations require sulphur levels less than 10 ppm after 1st January 2009 [6]. It should be noted that 10% of the global market for catalysts are hydrotreating catalysts [7]. The major segment of these catalysts is used for hydrodesulphurization (HDS).

Thomas *et al.* [8] arbitrarily characterize catalyst reducibility by the temperature at which 50% of the transition metal species are reduced. The authors have found that the HDS activity increases on decreasing this temperature. This feature suggests that reduction of the transition metal compounds is a crucial step in the transformation of the oxidic precursor into the sulphided catalyst.

Temperature-programmed reduction (TPR) has been shown to be a sensitive technique to study reducibility and it has been applied successfully for

characterization of CoO/Al<sub>2</sub>O<sub>3</sub>, MoO<sub>3</sub>/Al<sub>2</sub>O<sub>3</sub>, and Co(Ni)-MoO<sub>3</sub> catalysts [9]. A series of temperature-programmed desorption and reduction experiments have been performed over *in-situ* sulphided bare  $\gamma$ -alumina support, alumina-supported monometallic Ni, Mo, and bimetallic NiMo catalysts. Temperature-programmed desorption (TPD) and TPR results were related to active site assignment of nickel- and molybdenum-associated centres in hydrodenitrogenation (HDN) and HDS reactions [10]. The influence of catalyst sulphidability on HDS activity has been studied in detail by Scheffer *et al.* [11]. They proved that active Co-Mo/Al<sub>2</sub>O<sub>3</sub> catalysts are well sulphidable at low temperatures.

Since hydrodesulphurization reactions are carried out in a hydrogen atmosphere, it is tempting to investigate whether a direct correlation exists between the reactivity of various sulphur species registered by TPR and HDS activity [12]. During hydrodesulphurization extra hydrogen is always consumed due to the hydrogenation of unsaturated hydrocarbons. This is often undesirable, because it leads to loss of expensive hydrogen. On the other hand, hydrogenation and hydrocracking will become more important processes in the future as the need for clean fossil fuels has been extended to heavy petroleum fractions and coal [8]. Therefore, in addition to the HDS activities of the catalysts, it is also important to determine their hydrogenation activity.

Many studies have investigated the nature of the active phase in these catalysts [13] and the most

\* To whom all correspondence should be sent  
E-mail: stereva@ic.bas.bg

widely accepted model is that of Co(Ni)-Mo-S proposed by Topsøe *et al.* [14]. In this model, Ni or Co promoters of the active phase are enhancing the activity of sites located at the edges of molybdenum sulphide. Recently, Topsøe has also reported the existence of new sites of metallic character. These sites, located adjacent to the edges in the basal planes of the MoS<sub>2</sub> crystallites, have the ability to perform hydrogenation reactions [15], the latter being a favoured route in hydrodesulphurization. It has been suggested that the more active sites exist in MoS<sub>2</sub> crystallites of more than one slab. However, they can also exist in one slab crystallites having only weak interaction with the support [16]. The existence of these active sites and prevention of inactive species formation can be achieved by carefully controlling the metal-sulphur interaction during catalyst activation. Therefore, it is important to determine precisely the temperature of sulphidation of the catalyst during activation. The easiest way to do this is by using temperature-programmed sulphidation (TPS) data on the catalyst samples.

## EXPERIMENTAL

### Catalysts preparation

A series of alumina-supported NiO-MoO<sub>3</sub>/Al<sub>2</sub>O<sub>3</sub> catalysts (12, 15, 18 wt.% MoO<sub>3</sub>, and 2, 3, 4 wt.% NiO) were prepared by consecutive impregnation of  $\gamma$ -Al<sub>2</sub>O<sub>3</sub> (Cherok, surface area of 128 m<sup>2</sup> g<sup>-1</sup>) with an aqueous solution of (NH<sub>4</sub>)<sub>6</sub>Mo<sub>7</sub>O<sub>24</sub>·4H<sub>2</sub>O (Merck), followed by impregnation with an aqueous solution of Ni(NO<sub>3</sub>)<sub>2</sub>·6H<sub>2</sub>O (Acros Organics). In each impregnation step, the suspensions were stirred continuously at ambient temperature for 6 h, dried at 70°C under constant stirring for 2 h, further drying at 120°C, and finally calcined 4 h at 500°C. The amounts of ammonium heptamolybdate and nickel nitrate were so calculated as to obtain compositions of desired formulation.

### Catalytic activity measurements

The model reaction of thiophene hydrodesulphurization was carried out in a continuous flow reactor. Catalyst amount was 0.5 g and a sieve fraction of 0.25–0.50-mm size was used. A measure of HDS activity of the catalyst was accepted to be the rate of thiophene decomposition, while the rate of *n*-butane (b) formation was taken as a measure for hydrogenation activity. HDS and hydrogenation activities in the reaction were determined after *in situ* preliminary activation of each catalyst sample in a flow mixture of 10% H<sub>2</sub>S in H<sub>2</sub> at 400°C for 2 h. The reaction was carried out in a continuous flow reactor at ambient pressure and excess of hydrogen.

The liquid reactant was fed into the reactor by means of a Gilson 302 piston pump. Gas feed rates were regulated and controlled by a Matheson flow regulator. The catalytic activity of the samples was measured at 300, 350, and 400°C. The reactor was directly connected by means of a 6-way valve to a gas chromatograph equipped with a thermal conductivity detector. Separation of the reaction products was performed on two GC columns. One of them had a length of 2 m and was filled with 10% Carbowax 1500 on Chromosorb to separate unreacted thiophene from the reaction products. The second column had a length of 8 m and was filled with 20%  $\beta\beta'$ -oxydipropionitrile on Diatomite, which separated the products of the reaction. GC-identified compounds were: unconverted thiophene, *n*-butane, 1-butene, *cis*-2-butene, *trans*-2-butene, and hydrogen sulphide. Thiophene conversion rate was selected to be a criterion for evaluating HDS activity, while the rate of *n*-butane formation was a measure of hydrogenation (HYD) activity. Before measurements, steady state conditions were attained at each reaction temperature for 2 h. Experimental confirmation that the reaction is proceeding in the kinetic region was obtained by calculating Weisz's criterion, which was less than unity.

### TPR and TPS measurements

The specific temperature of reduction of the various phases in the oxide form of the catalyst samples was determined by the method of temperature-programmed reduction. The reducing mixture containing 10% H<sub>2</sub> in argon was deoxygenated over a Pt/asbestos filter at 130°C, dried in a molecular sieve 5A filter and then fed into a tubular quartz reactor at a flow rate of 25 cm<sup>3</sup>.min<sup>-1</sup>. The TPR started from room temperature and the temperature was increased linearly at a ramp of 10 grad.min<sup>-1</sup> up to 600°C. The amount of catalyst sample charged in the reactor was 0.1 g. The TPR setup was equipped with a thermal conductivity detector. A scheme of the experimental setup is presented in figure 1.

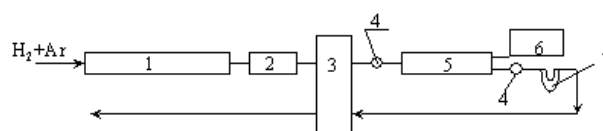


**Fig. 1.** Experimental set-up for temperature-programmed reduction: 1 – Matheson electronic mass flow regulator, 2 – Pt/asbestos catalyst and molecular sieve (0.5 nm), 3 – thermal conductivity detector; 4 – six-way valve, 5 – catalytic reactor placed in an oven, 6 – micro-processor-controlled thermal regulator, 7 – water trapping unit for evolved vapour during reduction.

In TPS experiments, reduced catalyst samples were cooled down to room temperature and TPS was carried out with similar equipment. 10% H<sub>2</sub>S were added to the reaction mixture and the heating procedure followed the conditions at which the TPR run had been conducted.

## RESULTS AND DISCUSSION

TPR measurements were conducted to determine catalyst reducibility. Figure 2 displays patterns of 12% MoO<sub>3</sub>/Al<sub>2</sub>O<sub>3</sub> samples promoted by 2, 3, and 4% NiO. All the runs were carried out up to the temperature, which is actually used in the HDS process (600°C). TPR profiles of samples having 15% and 18% MoO<sub>3</sub> had the same appearance with peak maxima shifted to lower temperatures by increasing NiO content but also on increasing MoO<sub>3</sub> content.

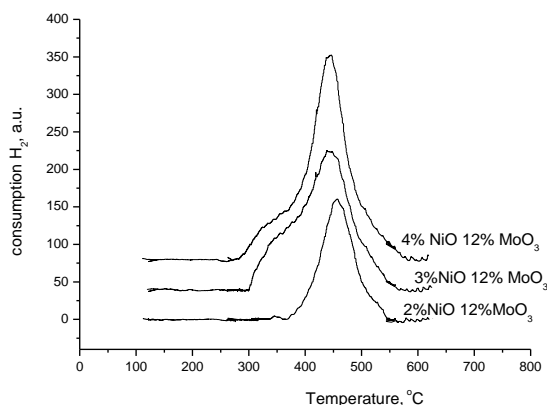


**Fig. 2.** TPR patterns of 12% MoO<sub>3</sub>/Al<sub>2</sub>O<sub>3</sub> promoted by 2, 3, and 4% NiO.

It is seen that by increasing NiO content the reduction occurred at lower temperatures, while the peak area was growing up. It should be noted here that in our previous studies with the same catalyst samples [17, 18] it was found that the rate of thiophene decomposition and the selectivity to butane formation increased with the increase in nickel content. An enhanced catalyst activity on increasing promoter amount has also been observed in the case of Co-Mo-Al<sub>2</sub>O<sub>3</sub> catalysts [11]. Brito and Laine have assigned a TPR peak at 457°C in Ni-Mo-Al<sub>2</sub>O<sub>3</sub> to reduction of octahedrally coordinated Mo<sup>6+</sup> ions of a Ni-Mo-O phase [19]. Accordingly, the peaks observed in this study at 441, 445, and 457°C of the 12% MoO<sub>3</sub>/Al<sub>2</sub>O<sub>3</sub> catalyst samples promoted by 2, 3, and 4% NiO, respectively, we assign to reduction of this species. TPR patterns of 15 and 18% MoO<sub>3</sub>/Al<sub>2</sub>O<sub>3</sub> catalyst samples, also promoted by 2, 3, and 4% NiO, demonstrated a peak in the same temperature interval, but it was shifted to lower temperatures with the increase of MoO<sub>3</sub> content.

Figure 3 represents dependences of sample HDS activity on the TPR peak maximum attributed to reduction of octahedrally coordinated Mo<sup>6+</sup> ions of a Ni-Mo-O phase in 2, 3, and 4% NiO-promoted 18% MoO<sub>3</sub>/Al<sub>2</sub>O<sub>3</sub> catalyst samples at reaction temperatures of 300, 350, and 400°C. The dependences have similar appearance at the three temperatures of HDS reaction. It is seen that activities of samples of greater nickel content, i.e. lower temperatures of the TPR maxima, are higher.

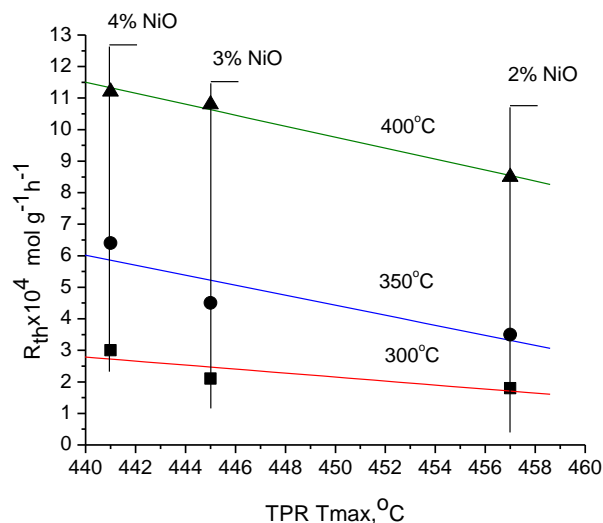


**Fig. 3.** Dependence of thiophene decomposition rate at various reaction temperatures on peak maximum in TPR patterns of NiO-promoted 18% MoO<sub>3</sub>/Al<sub>2</sub>O<sub>3</sub> catalysts.

At selected reaction temperatures, the rate of thiophene decomposition is increased on decreasing the temperature of reduction of the active phase. This is experimental evidence for suggested mechanism of reduction of these catalysts put forward on the basis of quantum chemical calculations [20]. According to the proposed mechanism, during the first step of catalyst activation, i.e. reduction, hydrogen is bonded to the oxygen entities of the MoO<sub>3</sub> phase to liberate H<sub>2</sub>O and thus an oxygen vacancy is formed on the surface. Sulphur is chemisorbed on the so formed vacancy during the second step of the activation process, namely sulphidation. Certainly, a lower temperature of reduction will contribute to the formation of more vacancies thus increasing catalyst activity. This result is also in agreement with an established higher activity of catalysts, for which 50% reduction is occurring at a lower temperature [8]. In our case, for the samples of different composition, this dependence had the same character as that of active samples having a higher content of Ni and Mo.

Another important for the industry characteristics of these catalysts is their hydrogenation activity. Figure 4 illustrates dependence of the butane

formation rate on the temperature of peak maximum in the TPR pattern of the same catalyst samples.

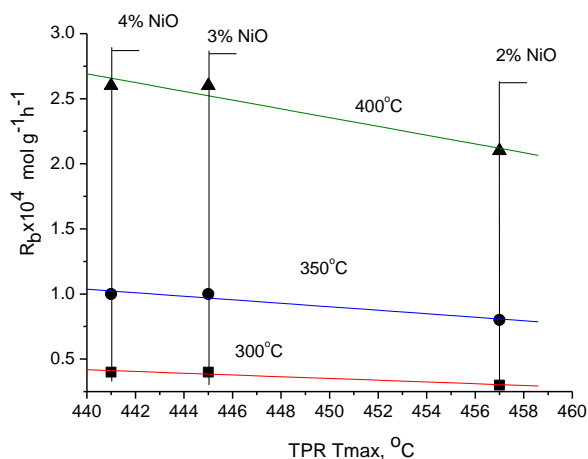


**Fig. 4.** Dependence of butane formation rate at various reaction temperatures on the temperature of peak maximum in TPR patterns of NiO-promoted 18% MoO<sub>3</sub>/Al<sub>2</sub>O<sub>3</sub> catalysts.

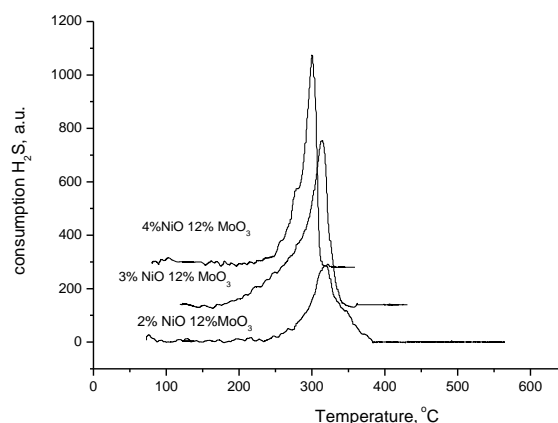
Comparing the tendencies shown in figures 3 and 4 it is seen that both the HDS and hydrogenation activities are decreasing with the increase in temperature of the peak maxima during TPR analysis of the catalyst samples, but the slopes are different. It is evident that the two processes take place on two types of active sites on the catalyst surface in agreement with a supposition of Radomyski [21]. According to this author, thiophene is adsorbed on one type of active sites and then it decomposes into butenes and H<sub>2</sub>S, but if it is adsorbed on another type of active sites, at first, it is hydrogenated into tetrahydrothiophene and the latter is decomposed into the products of the reaction.

The effect of sulphidation during catalyst activation was also studied with respect to changes of properties. Figure 5 represents TPS patterns of 12% MoO<sub>3</sub>/Al<sub>2</sub>O<sub>3</sub> samples promoted by 2, 3, and 4% nickel oxide.

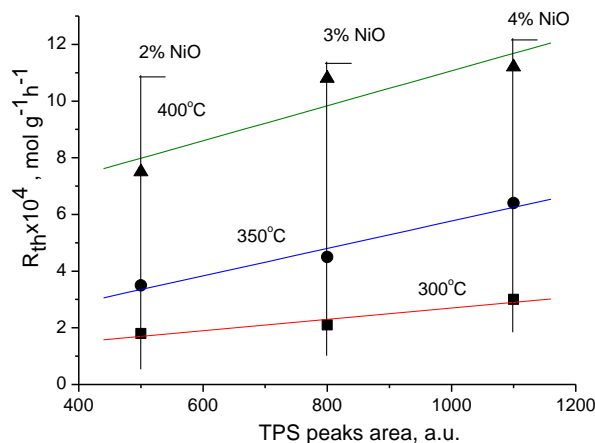
The increase in NiO content gives rise to an increase of the TPS peak area and a shift of the peak maximum to a lower temperature. The same kind of dependence was also observed with samples of higher MoO<sub>3</sub> content (15 and 18%). The increase in MoO<sub>3</sub> quantity led also to peak shifts to lower temperatures if samples of the same NiO content were compared.

Figure 6 illustrates dependences of thiophene decomposition rate at a reaction temperature of 300, 350, and 400°C on TPS peak area of 12% MoO<sub>3</sub>/Al<sub>2</sub>O<sub>3</sub> catalyst samples promoted by various quantities of NiO (2, 3, 4%). It is seen that an increase in the TPS peak area resulting from the increase of nickel amount in the catalyst sample

leads to a higher HDS activity. Similar dependences were observed with other promoted MoO<sub>3</sub>/Al<sub>2</sub>O<sub>3</sub> samples containing 15 and 18% MoO<sub>3</sub>.



**Fig. 5.** TPS patterns of 12% MoO<sub>3</sub>/Al<sub>2</sub>O<sub>3</sub> catalyst samples promoted by 2, 3, and 4% NiO.



**Fig. 6.** Dependences of thiophene decomposition rate at various reaction temperatures on peak area of TPS profiles of NiO-promoted 12% MoO<sub>3</sub>/Al<sub>2</sub>O<sub>3</sub> catalyst samples.

The increase in TPS peak area comes as a result of an increase in sulphur quantity chemisorbed on the surface of these catalysts. This dependence was observed with all reaction temperatures studied. Our results are a new experimental evidence supporting the reaction mechanism of thiophene hydrodesulphurization over a Mo catalyst proposed on the basis of molecular orbital calculations [22]. According to this mechanism, the thiophene molecule is adsorbed *via* the sulphur atom on a vacancy between two Mo atoms of the oxysulphide, which is being formed on the catalyst surface during activation. The C–S bond in the adsorbed thiophene is weakened and after an attack by hydrogen molecule this bond is broken. Butane and butenes are liberated as well as hydrogen sulphide. It is evident that according to this reaction mechanism the increase in sulphur amount

(in the oxysulphide) on the catalyst surface would lead to enhanced activity.

For all the studied catalyst samples an increase in the hydrogenating activity (expressed as the rate of butane formation) was also observed on increasing sulphur content in the catalyst. This correlation has a similar character but a lower slope if compared to the changes in HDS activity (Fig. 7).

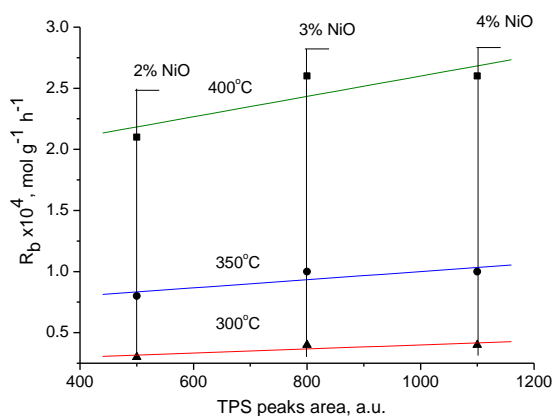


**Fig. 7.** Dependence of the butane formation rate at various reaction temperatures on the peak area in TPS patterns of NiO-promoted 12% MoO<sub>3</sub>/Al<sub>2</sub>O<sub>3</sub> catalysts samples.

Thus, the effect of sulphur on catalyst activity for hydrogenation and HDS once again suggests that at least two types of sites occur on the surface of the activated catalysts, which are responsible for hydrogenation and hydrodesulphurization reactions. These results are further confirmation of earlier formulated suggestion during a study of the effect of catalyst pretreatment on catalyst activity and selectivity [23].

## CONCLUSIONS

The first step in HDS of sulphur-containing organic compounds on Ni-Mo catalysts involves adsorption *via* the sulphur atom on a vacancy at the catalyst surface. During catalyst activation at least two types of active sites are being formed on the surface responsible for hydrogenation and hydrodesulphurization reactions. The activity and selectivity of these catalysts can be predicted based on TPR and TPS data.

*Acknowledgement:* The authors are grateful to Dr. A. Dotzeva for technical assistance in carrying out part of the experiments.

## REFERENCES

1. H. Topsøe, B. S. Clausen, F. E. Massoth, *Catalysis Science and Technology*, Vol. 11, Eds. J. R. Anderson, M. Boudart, Springer, Berlin, 1996.
2. D. D. Whitehurst, T. Isoda, I. Mochida, *Adv. Catal.*, **42**, 345 (1998).
3. A. N. Startsev, *Catal. Rev.-Sci. Eng.*, **37**, 353 (1995).
4. R. R. Chianelli, M. Daage, M. J. Ledoux, *Adv. Catal.*, **40**, 177 (1994).
5. R. Prins, V. H. J. de Beer, G. A. Somorjai, *Catal. Rev.-Sci. Eng.*, **31**, 1 (1989).
6. S. Eijsbouts, A. A. Battistone, C. C. van Leerdam, *Catal. Today*, **130**, 361 (2008).
7. C. J. H. Jacobsen, E. Tornqvist, H. Topsøe, *Catal. Lett.*, **68**, 179 (1999).
8. R. Thomas, E. M. van Oers, V. H. J. de Beer, J. Medema, J. A. Moljin, *J. Catal.*, **76**, 241 (1982).
9. P. Arnoldy, M. C. Franken, B. Scheffer, J. A. Moulijn, *J. Catal.*, **96**, 381 (1985).
10. L. Zhang, G. Karakas, U. S. Ozkan, *J. Catal.*, **178**, 457 (1998).
11. B. Scheffer, E. M. van Ders, P. Arnoldy, V. H. J. de Beer, J. A. Moulijn, *Appl. Catal.*, **25**, 303 (1986).
12. P. J. Mangnus, A. Piezebos, A. D. van Langeveld, J. A. Moulijn, *J. Catal.*, **151**, 178 (1995).
13. V. A. J. Ramirez, L. C. Caero, P. C. Villalon, A. Gutierrez-Alejandre, *Catal. Today*, **250**, 60 (2015).
14. H. Topsøe, *Appl. Catal. A-Gen.*, **322**, 3 (2007).
15. H. Topsøe, B. Hinnemann, J. K. Nørskov, J. V. Lauritsen, F. Besenbacher, P. L. Hansen, G. Hytoft, R. G. Egeberg, K. G. Knudsen, *Catal. Today*, **205**, 12 (2005).
16. G. Murali Dhar, B. N. Srinivas, M. S. Rana, M. Kumar, S. K. Maity, *Catal. Today*, **86**, 45 (2003).
17. Ch. Vladov, A. Eliyas, A. Dotzeva, I. Shtereva, L. Dimitrov, L. Spasov, N. Houbenov, L. Petrov, in: *Heterogeneous Catalysis (Proc. 9<sup>th</sup> Int. Symp. Heterogen. Catal., Varna, Bulgaria)*, L. Petrov, Ch. Bonev, G. Kadinov, Eds., Institute of Catalysis, 2000, p. 555.
18. A. A. Dotzeva, Ch. D. Vladov, L. A. Petrov, *Bulg. Chem. Ind.*, **79**, 21 (2008).
19. J. Brito, J. U. Laine, *J. Catal.*, **139**, 540 (1993).
20. Ch. Vladov, N. Neshev, L. Petrov, D. Shopov, in: *Heterogeneous Catalysis (Proc. 5<sup>th</sup> Int. Symp. Heterogen. Catal., Varna, Bulgaria)*, D. Shopov, A. Andreev, A. Palazov, L. Petrov, Eds; Institute of Catalysis, 1983, Part 2, p. 479.
21. B. Radomyski, J. Szczygiel, J. Tranczynski, *Appl. Catal.*, **25**, 295 (1986).
22. N. Neshev, Ch. Vladov, L. Petrov, D. Shopov, *Z. Phys. Chem. Neue Folg.*, **136**, 231 (1983).
23. L. Petrov, Ch. Vladov, D. Shopov, V. Fribova, L. Beranek, *Collect. Czech. Chem. Commun.*, **48**, 691 (1983).

## ИЗСЛЕДВАНЕ С ТПР И ТПС НА КАТАЛИЗАТОРИ ЗА ХДС И МЕХАНИЗЪМ НА ПРОЦЕСА

Ис. Щерева<sup>1\*</sup>, Д. Владов<sup>2</sup>, Сл. Раковски<sup>1</sup>, Б. Илъенко<sup>3</sup>

<sup>1</sup> *Институт по катализ, Българска академия на науките, ул. „Акад. Г. Бончев“, бл. 11, 1113 София, България*

<sup>2</sup> *Химикотехнологичен и металургичен университет, бул. „Климент Охридски“ 8, 1756 София, България*  
*Институт за газ, Национална академия на науките, Киев, Украйна*

Постъпила на 30 септември 2015 г.; Преработена на 17 декември 2015 г.

(Резюме)

Чрез кинетични изследвания, температурно програмирана редукция (ТПР) и температурно програмирано сулфидиране (ТПС) са изследвани Ni(Co)-MoO<sub>3</sub>/Al<sub>2</sub>O<sub>3</sub> катализатори за хидродесулфуриране (ХДС). Установено е, че при увеличаване на количеството на активната фаза (MoO<sub>3</sub>) и на промотора (NiO) активността на катализатора в реакциите на ХДС и хидриране на бутан се увеличават. Установена е зависимост между температурата на максимума на ТПР пика, площта на ТПС пика и активността на катализаторите. Предложен е начин за предсказване на активността на катализаторите по техните ТПР и ТПС характеристики. Експериментално е потвърдено предположението, че активни в реакцията са оксисулфиди, образувани на повърхността на катализатора при неговото активиране. Установено е наличието на поне два типа активни центрове на каталитичната повърхност – хидриращи и хидродесулфуриращи, чиято активност корелира по различен начин с температурата на максимума на ТПР пика.

## CONTENTS

<i>Preface</i> .....	3
V. Iliiev, D. Tomova, A. Eliyas, S. Rakovsky, M. Anachkov, L. Petrov, Enhancement of the activity of TiO <sub>2</sub> -based photocatalysts: a review .....	5
T. S. Tsoncheva, I. G. Genova, N. Scotti, V. Dal Santo, N. Ravasio, Unconventional ‘chemisorption-hydrolysis’ vs ‘impregnation’ technique for preparation of nanodispersed copper on mesoporous ceria and zirconia .....	12
R. Palcheva, B. Pawelec, E. Gaigneaux, J. L. Fierro, S. Damyanova, Redox properties of ceria-alumina oxides .....	19
A. M. Ali, M. A. Daous, L. A. Petrov, Role of Mn in supported Au-Mn/TOS Catalysts .....	25
A. Braga, J. B. dos Santos, S. Damyanova, J. M. C. Bueno, XANES and EXAFS study of supported CoNi catalysts for ethanol steam reforming .....	34
S. Todorova, A. Ganguly, A. Naydenov, H. Kolev, I. Yordanova, M. Shopska, S. Mondal, G. Kadinov, S. Saha, A. K. Ganguli, Nanosized cobalt oxides modified with palladium for oxidation of methane and carbon monoxide .....	42
A. I. Naydenov, Catalytic decomposition of ozone: from laboratory fixed bed reactor to design of adiabatic monolithic reactor .....	49
Ts. Lazarova, P. Tzvetkov, V. Tumbalev, S. Atanassova-Vladimirova, G. Ivanov, A. Naydenov, D. Kovacheva, Complete oxidation of methane on Pd-substituted perovskite LaCu <sub>0.5</sub> Mn <sub>0.5</sub> O <sub>3</sub> .....	54
N. Stoeva, I. Spassova, R. Nickolov, G. Atanasova, M. Khristova, Effect of carbon in cobalt-silica-carbon composite catalysts for NO reduction by CO .....	59
M. V. Gabrovska, R. M. Edreva-Kardjieva, M. G. Shopska, D. A. Nikolova, L. P. Bilyarska, D. Crişan, M. Crişan, Purification of hydrogen-rich streams from CO <sub>2</sub> by methanation .....	66
M. Shopska, S. Todorova, I. Yordanova, S. Mondal, G. Kadinov, Comparative analysis of the catalytic behaviour in CO oxidation of iron containing materials obtained by abiotic and biotic methods and after thermal treatment .....	73
M. G. Shopska, G. B. Kadinov, J. Briančin, I. D. Yordanova, H. G. Kolev, M. Fabián, Preparation of Fe-Pd/Al-Si-O catalyst using biogenic iron of cultivated <i>Leptothrix</i> genus bacteria .....	79
N. G. Kostova, E. Dutkova, A. Eliyas, E. Stoyanova-Eliyas, M. Fabián, P. Balaž, Mechanochemical synthesis, characterization and photocatalytic activity of CdS/TiO <sub>2</sub> composites in air purification .....	87
A. E. Eliyas, I. D. Stambolova, V. N. Blaskov, D. Stoyanova, K. I. Milenova, L. D. Dimitrov, M. G. Shipochka, O. S. Dimitrov, Preparation of ZnO photocatalysts by copolymer Pluronic-assisted hydrothermal process .....	94
K. L. Zaharieva, K. I. Milenova, Z. P. Cherkezova-Zheleva, A. E. Eliyas, B. N. Kunev, I. G. Mitov, Photocatalytic properties of ferrite/activated carbon composites for degradation of Malachite Green in aqueous medium .....	99
K. L. Zaharieva, K. I. Milenova, V. Rives, R. Trujillano, Z. P. Cherkezova-Zheleva, A. E. Eliyas, M. P. Tsvetkov, B. N. Kunev, I. G. Mitov, Mixed cobalt-copper ferrite-type materials: synthesis and photocatalytic efficiency in degradation of Reactive Black 5 dye under UV-light irradiation .....	105
K. I. Milenova, K. L. Zaharieva, A. E. Eliyas, I. A. Avramova, I. D. Stambolova, V. N. Blaskov, O. S. Dimitrov, S. V. Vassilev, Z. P. Cherkezova-Zheleva, S. K. Rakovsky, Influence of mechanochemical activation of metal-doped ZnO on its photocatalytic activity in degradation of Malachite Green dye .....	112
A. M. Stoyanova, Ts. K. Koleva, A. D. Bachvarova-Nedelcheva, R. S. Iordanova, Photocatalytic bleaching of two organic dyes catalysed by La-doped nanosized TiO <sub>2</sub> .....	118
S. F. Zaman, A DFT study of CO adsorption and dissociation over $\gamma$ -Mo <sub>2</sub> N(111) plane .....	125
S. Minkovska, B. Jeliaskova, S. Rakovsky, T. Deligeorgiev, Thermochromism of a series of spiroindolinonaphthoxazines .....	133
S. Minkovska, B. Jeliaskova, S. Rakovsky, T. Deligeorgiev, Synthesis and study of some novel chelating photochromic spironaphthoxazines .....	139
I. Shtereva, D. Vladov, S. Rakovsky, B. Iliencko, TPS and TPR study of HDS catalysts and process mechanism .....	147

СЪДЪРЖАНИЕ

<i>В. Илиев, Д. Томова, Ал. Елияс, Сл. Раковски, М. Аначков, Л. Петров</i> , Повишаване на активността на фотокатализатори на основата на $TiO_2$ : Обзорна статия .....	11
<i>Т. С. Цончева, Из. Г. Генова, Н. Скоти, Вл. Дал Санто, Н. Равазио</i> , Нестандартен метод на „хемосорбция-хидролиза” и метод на „импрегниране” за получаване на нанодисперсна мед върху мезопорести цериев диоксид и циркониев диоксид .....	18
<i>Р. Палчева, Б. Павелец, Е. Геньо, Х. Л. Г. Фиеро, С. Дамянова</i> , Окислително-редукционни свойства на $SeO_2-Al_2O_3$ оксиди .....	24
<i>А. М. Али, М. А. Даус, Л. А. Петров</i> , Роля на мангана в нанесени Au-Mn/TOS катализатори .....	33
<i>А. Брага, Х. Б. Сантос, С. Дамянова, Х. М. К. Буено</i> , Изучаване на нанесени CoNi катализатори за реформиране на етанол с водна пара с помощта на рентгенова абсорбционна спектроскопия .....	41
<i>С. Тодорова, А. Гангули, Ант. Найденов, Хр. Колев, Ил. Йорданова, М. Шопска, С. Мондал, Г. Кадинов, С. Саха, А. К. Гангули</i> , Наноразмерен кобалтов оксид модифициран с паладий за окисление на метан и въглероден оксид .....	48
<i>Ант. Ил. Найденов</i> , Каталитично разлагане на озон – от лабораторен реактор с неподвижен слой към оразмеряване на монолитен адиабатен реактор .....	53
<i>Цв. Лазарова, П. Цветков, В. Тумбалева, С. Атанасова-Владимирова, Г. Иванов, Ант. Найденов, Д. Ковачева</i> , Пълно окисление на метан върху заместен с паладий перовскит $LaCu_{0.5}Mn_{0.5}O_3$ .....	58
<i>Н. Стоева, Ив. Спасова, Р. Николов, Г. Атанасова, М. Христова</i> , Влияние на въглерода в кобалт-силикатно-въглеродни композитни катализатори за редукция на NO с CO .....	65
<i>М. В. Габровска, Р. М. Едрева-Кърджиева, М. Г. Шопска<sup>1</sup>, Д. А. Николова, Л. П. Билярска<sup>1</sup>, Д. Кришан, М. Кришан</i> , Очистване на богати на водород газове от $CO_2$ чрез метаниране .	72
<i>М. Шопска, С. Тодорова, Ил. Йорданова, С. Мондал, Г. Кадинов</i> , Сравнителен анализ на каталитичното поведение в окисление на CO на желязо-съдържащи материали получени с абиотични и биотични методи и след термична обработка .....	78
<i>М. Г. Шопска, Г. Б. Кадинов, Я. Бриянчин, Ил. Д. Йорданова, Хр. Г. Колев, М. Фабиан</i> , Синтез на катализатор Fe-Pd/AL-Si-O съдържащ биогенно желязо чрез култивиране на бактерии от рода <i>Leptothrix</i> .....	86
<i>Н. Г. Костова, Ер. Дуткова, Ал. Елияс<sup>1</sup>, Ем. Стоянова-Елияс, М. Фабиан, П. Балаж</i> , Механохимичен синтез, охарактеризиране и фотокаталитична активност на CdS/ $TiO_2$ композити за очистване на замърсен въздух .....	93
<i>Ал. Ел. Елияс, Ир. Д. Стамболова, Вл. Н. Блъсков, Д. Стоянова, К. И. Миленова, Л. Д. Димитров, М. Г. Шипочка, Ог. С. Димитров</i> , Хидротермално получаване на фотокатализатори от ZnO с помощта на кополимер Плуроник .....	98
<i>К. Л. Захариева, К. И. Миленова, З. П. Черкезова-Желева, Ал. Ел. Елияс, Б. Н. Кунев, Ив. Г. Митов</i> , Фотокаталитични свойства на композити ферит/активен въглен за разграждане на Малахитово Зелено във водна среда .....	104
<i>К. Л. Захариева, К. И. Миленова, В. Ривес, Р. Трухилиано, З. П. Черкезова-Желева, Ал. Ел. Елияс, М. П. Цветков, Б. Н. Кунев, Ив. Г. Митов</i> , Смесени кобалт-медни материали от феритен тип – синтез и фотокаталитична активност в разграждането на Реактивно Черно 5 багрило при UV облъчване .....	111
<i>К. И. Миленова, К. Л. Захариева, Ал. Ел. Елияс, Ив. А. Аврамова, Ир. Д. Стамболова, Вл. Н. Блъсков, Ог. С. Димитро, С. В. Василев, З. П. Черкезова-Желева, Сл. К. Раковски</i> , Влияние на механохимичната активация на ZnO дотиран с метал върху фотокаталитичната активност за разлагане на багрилото Малахитово зелено .....	117
<i>Анг. М. Стоянова, Цв. К. Колева, Алб. Д. Бъчварова-Неделчева, Р. С. Йорданова</i> , Фотокаталитично обезцветяване на две органични багрила катализирано от наноразмерен $TiO_2$ дотиран с лантан .....	124
<i>Ш. Ф. Заман</i> , Изследване с ТФП на адсорбцията и дисоциацията на CO върху $\gamma-Mo_2N(111)$ кристална равнина .....	132

<i>Ст. Минковска, Б. Желязкова, Сл. Раковски, Т. Делигеоргиев, Термохромизъм на серия спироиндолинонафтоксазини .....</i>	<i>138</i>
<i>Ст. Минковска, Б. Желязкова, Сл. Раковски, Т. Делигеоргиев, Синтез и изследване на нови хелатни фотохромни спирооксазини .....</i>	<i>146</i>
<i>Ис. Щерева, Д. Владов, Сл. Раковски, Б. Ильенко, Изследване с ТПР и ТПС на катализатори за ХДС и механизъм на процеса .....</i>	<i>152</i>

